

**Search for new resonances in the four-lepton
channel and implementation of the LED integrator
panel for the PROMETEO system in the ATLAS
Tile Calorimeter**



Onesimo Mtintsilana

Supervisor:

Prof. Bruce Mellado

Co-supervisor:

Dr. Mukesh Kumar

A thesis submitted to the Faculty of Science, University of the Witwatersrand,
Johannesburg, in fulfilment of the requirements for the degree of

Doctor of Philosophy

3 June 2024

Declaration

I declare that this dissertation is my own, unaided work. It is being submitted for the Degree of Doctor of Philosophy at the University of the Witwatersrand, Johannesburg. It has not been submitted before for any degree or examination at any other University.

Onesimo Mtintsilana

3 June 2024

A handwritten signature in black ink, consisting of a stylized, cursive letter 'M' with a horizontal line extending to the right.

Abstract

The Large Hadron Collider (LHC) has transformed our understanding of fundamental particles and forces, notably with the seminal discovery of the Higgs boson in 2012, which completed the Standard Model (SM) of particle physics. Despite its success, the SM leaves numerous unanswered questions, motivating a quest for new physics. This thesis explores three main avenues:

Firstly, it investigates the possibility of an extended Higgs sector or alternative SM extensions, focusing on heavy ZZ resonances that decay into four leptons. Using a dataset of 139 fb^{-1} from proton-proton collisions at the LHC, this study explores both gluon-gluon fusion and vector-boson fusion production mechanisms. Although no significant signal for a new resonance is observed, upper limits on the production cross section of spin-0 or spin-2 particles are established. These limits provide constraints on specific theoretical models, such as Type-I and Type-II two-Higgs doublet models for spin-0 resonances, and the Randall-Sundrum model for spin-2 resonances. Intriguingly, the combined results of ATLAS and CMS for Run 2 and Run 3 data in the final state of 4 leptons exhibit an excess around 250 GeV, reaching a significance of 2.4σ which is in the region of interest of the multi-lepton anomalies..

In the second part, the analysis extends to heavy boson decays resulting in a final state with four leptons, specifically focusing on the R boson or the A boson decays into a combination of the SM Higgs boson and another boson, denoted S , which further decays into dark-matter candidates. No evidence contradicting SM predictions is found, yielding stringent upper limits on the production cross-sections of these hypothesised bosons and their branching ratios at a 95% confidence level.

Lastly, the thesis highlights advancements in Higgs boson studies and new particle discovery potential in the upcoming High-Luminosity LHC era starting in 2029, emphasising improvements to the ATLAS detector electronics, particularly the integration of a new LED Integrator Panel within the Prometeo portable readout module system, enabling precise calibration and monitoring of individual detector components.

Acknowledgements

The journey to completing this thesis has been made possible by the collective wisdom, guidance, and unwavering support of many remarkable individuals. Reflecting on my journey, I am reminded of three profound Xhosa expressions that resonate deeply with my experience. *Intaka yakha ngoboya benye*, loosely translating to 'a bird builds its nest with another's feathers', symbolises the necessity of support in achieving one's goals. *Akukho qili linokuzikhotha umhlana*, meaning 'no genius can lick its own back', underscores the value of collaboration. Lastly, *Inyathi ibuzwa kwabaphambili*, 'enquire from those ahead where the buffalo has been sighted,' highlights the importance of seeking wisdom and guidance from those before us.

With those words, I extend my heartfelt gratitude to Prof. Bruce Mellado, my supervisor since my M.Sc. days. His expertise in particle physics has been a beacon of knowledge and inspiration throughout my research journey. Our weekly meetings, echoing the ethos of "Talk to people", have significantly shaped my approach to both academic and personal challenges. I also extend my thanks to Dr. Mukesh Kumar and Dr. Xifeng Ruan, whose guidance has been crucial throughout my doctoral studies. If there are any errors in this dissertation, as surely there must be, they are the fault of these other supervisors- most likely Bruce Mellado, because he supervised my PhD and should have trained me better :).

The first part of my thesis, centred on experimental work with the TileCal group at CERN, benefitted greatly from Dr. Jalal Abdallah's technical advisement and Pavle Tsotskolauri's support during late-night coding sessions. My appreciation also goes to all TileCal members, especially Gulio, for his support during Testbeam nightshifts, and Irakli, for the much-needed braai post-nightshifts, among many others whose contributions have been invaluable.

In the second part of my thesis, focused on work with the ATLAS HZZ group, Dr. Theodota Lagouri's guidance since my MSc has been instrumental. Her wisdom, which extends beyond academic boundaries, has been a constant source of motivation and belief. I also acknowledge Gaetano Barone, William Leight, Panagiotis Bellos, Abdualazem Fadol, and Mzwandile

Thabete for their collaboration. My colleagues and friends at the School of Physics at Wits have enriched this journey with shared memories, laughter, and profound conversations.

I am deeply grateful to my colleagues at the South African Institute of Physics and the Women Physics Forum (WiPiSA). Dr. Brian Masara's mentorship has imparted numerous life lessons. I am equally grateful to Dr. Rosinah Modiba 'Rose' for her mentorship, friendship, and motherly presence in all WiPiSA activities. My appreciation also extends to Ndanga, Queen, and Tebogo for their remarkable partnership.

Umbulelo ongazenzisiyo kuNontutuzelo, umama wam nakubantwana basekhaya uLwandile, uTulani, noSandisiwe ongasekhoyo. Uthando, inkuthazo, ukuzidina, ukukholelwa okungangqiyi kwenu kum, nomonde wenu kundinike amandla nokomelela okungakumbi kwaza kwakhokelela empumelelweni yam. Ndiyazingca ngani maqobokazana.

Ndibamba ngazibini kuni zihlobo zenene nakuni zizalwane, enkosi ngenkxaso nenkuthazo yenu, nibe ngumthombo wolomelelo novuyo lwam.

Lo msebenzi ndiwunikezela ngothando ndineenkumbulo ezintle ngabo bonke abo bathe baqaqamba okweenkwenkwezi bendikhanyisela endleleni, bayakuhlala bekho ezingcingeni zam nangona bengasekho nje phezulu kwalo umagad'ahlabayo.

Kusana luka mama u'Siwe', obehlekisa enothando, qhubeka ube njengesibane ube nje-gesikhanyiso. Siwe, besinolwalamano olomeleleyo, nangona ungasekho, umoya wakho ungumhlobo wam osekhosi. Iinkumbulo zam ngawe zingumthombo wamandla zindiphembelela ukuba ndiqhubeke ndibheke phambili, zindikhumbuza ngokomelela nobuhle bobomi. Ndiyakukhumbula kakhulu kwaye ndiyakuthanda.

Kutatomkhulu nomakhulu wam endibathandayo, abandizalela umama ondizalayo, ubulumko, uthando nesikhokelo senu sibe ngumlumiso neentsika endithe ndayama ngazo endleleni nasebuntwini bam. Nenze ngako konke nindixhonxa, nindixoxa nindenza umntu nindilungiselela ingomso. Nibe sisibonelo esihle nolutho kum ngexesha lokudla kwenu ubomi, ndifunde nto kuni ngamandla othando, ukunyamezela phantsi koxinizelelo olumandla, ukuzithoba phantsi kwamanzithinzithi obom.

KuNandi umzala wam, ugqwesile ntombozana wenza wabetha ngaphaya, ubungasenguye umzala koko ubungudade wethu omkhulu nqo. Ukhawuleze wasithela dad'ethu wasishiya sithe ca izisini. Nangona kunjalo siyabulela kuba usishiye nomzila omhle owalatha ubukhalipha novelwano olundenza ndizive ndithabatheka kakhulu.

Ninonke nishiye umtshithi ongasayi kucimeka entliziyweni yam. Kungenxa yeenkumbulo ezintle endinazo ngani endibone ukuba wonke lo msebenzi ndiwunikezele egameni lenu. Ndibuhlungu ke kuba aniyi kubakho ukuze sibhiyoze kunye. Le mpumelelo asiyam kuphela koko ikwaluzuko endinizukisa ngalo ndikwanithulela umnqwazi ngokuzijul' ijacu nindinika uthando, iimfundiso, nindishiyela umzila othe tye nongasayi kuze ulibaleke. Nam ke ndithembisa ukwenza kangangoko ndisenza umahluko esizweni nanjengoko nani nenzile kobam ubom. Ndiyanikhumbula kwaye ndiyanithanda kakhulu.

Kwimimoya yabaphantsi, ooRhadebe, ooBhungane, ooNdlebele zombini. Kude kwaba lelixhaphetsu nindibheleka, nindibonisa indlela, nindikhusela, nikwandikhanyisela endleleni yam, ndiyakusoloko ndibulela egameni lenu.

Icamagu livumile!

This research was conducted at CERN in Geneva, Switzerland. The financial support from the National Research Foundation and the Department of Science and Technology, through the SA-CERN consortium, is gratefully acknowledged.

List of Publications

Journal Articles

1. **ATLAS Collaboration.** (2024). “Search for heavy resonances in final states with four leptons and missing transverse momentum or jets in pp collisions at $\sqrt{s} = 13$ TeV with the ATLAS detector.” *submitted to JHEP*. [arXiv:2401.04742 \[hep-ex\]](https://arxiv.org/abs/2401.04742)
2. **ATLAS Collaboration.** (2021). “Search for heavy resonances decaying into a pair of Z bosons in the $\ell^+\ell^-\ell'^+\ell'^-$ and $\ell^+\ell^-\nu\bar{\nu}$ final states using 139 fb^{-1} of pp collisions at $\sqrt{s} = 13$ TeV with the ATLAS detector.” *Eur. Phys. J. C*, 81, 332. [DOI:10.48550/arXiv.2009.14791y](https://doi.org/10.48550/arXiv.2009.14791y)

Conference Papers

1. **Mtintsilana, O.,** Abdallah, J., Tsotskolauri, P., and Mellado, B. (2022). “Implementation of the LED Integrator panel for the Prometeo system in the ATLAS Tile Calorimeter.” In *Proceedings of the 66th Annual Conference of the South African Institute of Physics (SAIP2022)*, pages 517-522. [ISBN: 978-0-6397-4426-1](https://doi.org/10.1088/1742-6596/2022/1/012001)
2. **Mtintsilana, O.,** Fadol, A., Tlou, H., Mellado, B., and Ruan, X. (2021). “Search for a heavy pseudo-scalar decaying into a Z boson and another heavy scalar boson leading to four lepton final states in pp collisions at $\sqrt{s} = 13$ TeV with the ATLAS detector.” In *Proceedings of the 65th Annual Conference of the South African Institute of Physics (SAIP2021)*, pages 145-150. [ISBN: 978-0-620-97693-0](https://doi.org/10.1088/1742-6596/2021/1/012001)
3. Tlou, H., Fadol, A., Mellado, B., **Mtintsilana, O.,** and Ruan, X. (2021). “Search for heavy resonances in the $\ell^+\ell^-\ell^+\ell^-$ final state in association with missing transverse energy using pp collisions at $\sqrt{s} = 13$ TeV with the ATLAS detector.” In *Proceedings*

of the 65th Annual Conference of the South African Institute of Physics (SAIP2021), pages 126-131. [ISBN: 978-0-620-97693-0](#)

4. **Mtintsilana, O.**, Lagouri, T., and Mellado, B. (2019). “Electron isolation studies in $H \rightarrow ZZ \rightarrow 4\ell$ analysis using the ATLAS detector.” In *Proceedings of the 64th Annual Conference of the South African Institute of Physics (SAIP2019)*. Submitted for publication.
5. **Mtintsilana, O.**, and Lagouri, T. (2018). “Studying the Effects of Pileup on the Leptonic Properties in the $H \rightarrow ZZ \rightarrow 4\ell$ Channel Using the ATLAS Detector.” In J. Engelbrecht (Ed.), *Proceedings of the 63rd Annual Conference of the South African Institute of Physics (SAIP2018)*, pages 110-115. [ISBN: 978-0-620-85406-1](#).

Internal Notes

1. Abidi, SH., et al. (2018). “Event selection and background estimation in the $H \rightarrow ZZ \rightarrow 4\ell$ channel at $\sqrt{s}=13$ TeV - Final Run 2 Analysis.” *Tech. Rep.*. [ATL-COM-PHYS-2018-1710](#)

Ndithanda ukuthi kudadewethu omncinci ongasekhoyo uSandisiwe, endimkhumbula nendimxabise kakhulu entliziyweni yam, umoya wakho uyaqhubeka undikhokela kwaye uyandikhuthaza yonke imihla. Ndiyakuthanda ngokunzulu yaye ndiyakukhumbula.

Kubatshana bam abahle endibathandayo, uLerato, uMangaliso, uMivuyo, uKhayone, kunye noNakhane – ningumthombo wovuyo nokhanyo ebomini bam. Ndingwenela ukuba oluphando lungabi ngumfuziselo nje wohambo lwam kwizifundo zam kuphela kodwa lubengumhlahla ndlela wekamva lenu eliqaqambileyo. Ulonwabo namaphupha enu andinika amandla nokhuthazo lokufuna ukuphumelela emagqabini kuyo yonke into endiyenzayo.

Table of contents

List of Publications	xi
List of figures	xxi
List of tables	xxxii
Nomenclature	xxxiii
1 Introduction	1
1.1 Fundamental Physics and the Universe	2
1.1.1 Manuscript Organisation	3
1.2 Phenomenology of the Standard Model	4
1.3 Fundamental SM particles	5
1.4 Mathematical description	7
1.5 The Brout-Englert-Higgs Mechanism	8
1.5.1 Exploring the Properties of the Higgs Boson	11
1.5.2 Experimental Limits from LEP	12
1.6 The Multi-lepton Anomalies	14
1.6.1 Description of the Theoretical Model	15
1.6.2 Multi-lepton Anomalies Observed at the LHC	16

1.6.3	Low Mass Range (95 GeV)	16
1.6.4	High Mass Range (152 GeV)	17
2	Experimental Setup	19
2.1	CERN and LHC	19
2.2	The concept of Luminosity	24
2.3	The ATLAS detector	25
2.3.1	Layout and coordinate system	27
2.3.2	Inner Detector	28
2.3.3	Calorimeters	30
2.4	Muon Spectrometer	32
2.4.1	Magnetic Field System in ATLAS	33
2.5	Trigger and Data Acquisition System	33
2.6	The Tile Calorimeter	35
2.6.1	TileCal architecture	35
2.6.2	TileCal mechanics and optical readout	35
2.6.3	TileCal Readout Electronics	38
2.6.4	Requirements for the HL-LHC	40
3	Implementation of the LED Integrator Panel within the PROMETEO System for ATLAS TileCal	43
3.1	General purpose	44
3.2	The PROMETEO functions and usage	46
3.2.1	Usage during Assembly	46
3.2.2	Usage during Installation and Maintenance	49
3.3	Physical Description of the Prometeo	49

3.3.1	Portable Low Voltage Power Supply for TileCal MDs	49
3.3.2	Portable High Voltage Power Supply	50
3.3.3	LED driver card and LEDs	51
3.3.4	Readout System: CPM and Mini-Carrier	51
3.3.5	Readout and configuration	51
3.3.6	The PROMETEO Software	53
3.3.7	IPBus Server	54
3.4	System Tests	55
4	Physics Object Reconstruction	59
4.1	Electron	59
4.1.1	Electron Reconstruction	59
4.1.2	Electron Identification	60
4.2	Muon	61
4.2.1	Muon Reconstruction	61
4.2.2	Muon Identification	62
4.3	Jets	63
4.4	The Missing Transverse Momentum	66
5	Event Classification and Background Modelling in search for $H \rightarrow ZZ \rightarrow 4\ell$	71
5.1	Analysis Overview	72
5.2	Data and simulation	72
5.2.1	Data	72
5.3	Simulation	74
5.3.1	Simulation of signal	74
5.3.2	Simulation of background	75

5.4	Efficiency studies for electrons and muons	76
5.4.1	Efficiency of the electron identification	76
5.4.2	Efficiency of the muon identification	78
5.5	Event selection	81
5.5.1	Trigger configuration	81
5.5.2	Physics objects selection	81
5.5.3	Selection criteria for physics objects	83
5.6	The effects of pileup	85
5.6.1	Motivation	85
5.6.2	The role of the analysis framework	87
5.6.3	Results	88
5.7	Electron Isolation	93
5.7.1	Motivation	93
5.7.2	Calorimeter-based isolation	94
5.7.3	Track-based Isolation	96
5.7.4	Particle Flow Isolation	97
5.7.5	Performance studies of the WPs	99
5.7.6	Optimisation of isolation criteria and final results with scale factors	105
5.7.7	Tag and Probe with $Z \rightarrow ee$	106
5.7.8	Discussion on experimental systematic uncertainties	106
5.7.9	Efficiency and scale factor results	107
6	Exploring higher-mass ZZ resonances in the 4ℓ final states	111
6.1	Research Analysis Outline	112
6.2	Event Selection	114
6.3	Background estimation	114

6.4	Signal and background simulation	116
6.4.1	Signal simulation	116
6.4.2	Background Simulation	117
6.5	Systematic uncertainties	118
6.5.1	Experimental systematic uncertainties	119
6.5.2	Effect of systematic uncertainties on signal shape parameterisation	119
6.5.3	Systematic assessment of theoretical uncertainties	120
6.6	Results	122
6.6.1	Statistical Approach and Systematic Uncertainty Analysis	122
6.6.2	Cut-Based Analysis	122
6.6.3	Results for the cut-based analysis	123
6.6.4	General Results	124
6.7	Interpretations	126
6.7.1	Spin-0 Resonances	127
6.7.2	Spin-2 resonances	129
6.8	Combined results	129
7	Heavy Resonance Searches in 4ℓ and E_T^{miss}/Jets final state	133
7.1	Analysis Overview	134
7.2	Data and simulated event samples	135
7.3	Analysis Strategy	137
7.3.1	$R \rightarrow SH \rightarrow 4\ell + E_T^{\text{miss}}$ Signal Optimisation	137
7.4	Signal and Background modelling	139
7.5	Results	140

8	Conclusions	147
8.1	The Integrator Panel on the Prometeo Software	147
8.2	Isolation Studies for 4ℓ searches	148
8.3	Searches for heavy resonances in the 4ℓ final state	149
8.4	Searches for heavy resonances in the 4ℓ final state and E_T^{miss} or jets	149
	References	151

List of figures

1.1	Representation of the 12 fermions (quarks & leptons), their interactions with the three fundamental forces (strong, EM, weak), and the role of gauge bosons and the Higgs field in the model. Taken from Ref. [11].	6
1.2	Potential of the scalar field	9
1.3	Higgs boson production cross section in pp collisions as a function of the center-of-mass energy. Taken from Ref. [29]	11
1.4	Feynman diagrams for the four main production modes of the Higgs boson at the LHC, created by the author.	13
1.5	The p -value dependence on the hypothesized S' mass in low-mass search channels. Taken from Ref. [63].	17
1.6	The p -values for individual high-mass search channels and their combined analysis, presented with and without the μe signal. Taken from Ref. [63].	18
2.1	The overall layout of the CERN accelerator complex as of summer 2022. Figure taken from Refs. [76].	21
2.2	Schematic layout of the LHC, highlighting the two counter-rotating proton beams within the machine's eight arc sections and eight straight sections. Figure taken from Refs. [77].	22
2.3	Cutaway view of a Large Hadron Collider (LHC) dipole bending magnet, highlighting key components [79] from Refs. [77].	23

2.4	Total integrated luminosity delivered to ATLAS is illustrated in green, while the portion recorded by ATLAS is represented in yellow. The luminosity certified for physics analysis is denoted in blue for the years 2015 to 2018. Taken from [85].	25
2.5	ATLAS detector diagram showing the different subdetector systems and four people to demonstrate the size. Taken from Ref [86].	26
2.6	A transverse section of the ATLAS detector showing the three main sub-systems: the calorimeter, the tracker and the muon spectrometer. The paths and interactions of different particles with the detector are shown. Figure taken from [87].	27
2.7	Definition of pseudorapidity (η) and the scheme of polar (θ) and azimuthal (ϕ) angles. The polar angle θ is shown for various pseudorapidity values, and the azimuthal angle ϕ is defined as the angle around the beam axis, perpendicular to the polar angle plane.	28
2.8	Schematic representation of a particle traversing the three subdetectors of the ATLAS Inner Detector: the pixel detector, the semiconductor tracker (SCT), and the transient radiation tracker (TRT). Taken from Ref [88].	29
2.9	The structure of the ATLAS calorimeter, taken from Ref [80].	30
2.10	Cross-sectional representation of the ATLAS Muon Spectrometer (MS), showing the high precision tracking chambers, trigger chambers, and superconducting air-core toroid magnets. Taken from Ref [91].	32
2.11	Schematic of the ATLAS trigger and Data Acquisition System. CP (Cluster Processor), JEP (Jet/Energy Processor), L1Topo (Level-1 Topological Processor), ROD (Read-Out Driver), ROS (Read-Out System), and Tier-0. Taken from Ref [92].	34
2.12	Integration diagram of the TileCal's mechanical and optical elements. Scintillating tiles, fibres, and PMT's are shown for visualisation of energy capture and light collection. This figure is taken from Ref [97].	36
2.13	Tile Calorimeter Module Segmentation: Granularity in Depth and η . Left: Central Barrel, Right: Extended Barrel. Taken from Ref [97].	37

2.14	Block diagram of the tile-calorimeter readout electronics, including the TTC (Timing, Trigger, and Control) system for synchronization and control. Taken from Ref [97].	38
2.15	TileCal 3-in-1 card schematic showing key functionalities including signal shaping and amplification, and calibration injection. Taken from Ref [99].	40
3.1	Illustration of Photomultiplier Tube (PMT) Block Elements. Numbered in red, the components are designated as follows: (1) MainBoard (MB), which manages overall signal processing and control functions, (2) PMT Blocks, which convert scintillation light into electrical signals, (3) DaughterBoard (DB), which interfaces with the PMTs to handle signal processing and digitization, and (4) High-Voltage (HV) Distribution Board (positioned beneath).	44
3.2	Logical sketch of the PROMETEO sub-components, illustrating the connections between the Central Processor Module (CPM)/ PreProcessor (PPr), Photomultiplier Tube (PMT) blocks, MiniDrawers (MDs), DaughterBoards (DBs), and MainBoards (MBs). The sketch also indicates the integration with the Timing, Trigger, and Control (TTC) system.	45
3.3	Light tight box for the phase-2 PMT test stand showing 12 PMT-Blocks on the tray. At the top, PROMETEO box prototype.	47
3.4	Tile Calorimeter SD low voltage supply topology. Image developed by Sergiu from the TileCal community, not published.	49
3.5	High Voltage Power Supply. Image taken by the author of this thesis.	50
3.6	Compact Processing Module version 2. Image developed by Fernando from TileCal community, not published.	52
3.7	Block diagram of the main firmware blocks used for the PROMETEO system. Image developed by Fernando from TileCal community, not published.	53
3.8	PROMETEO Graphical User Interface (GUI). High Voltage Power Supply. Image taken by the author of this thesis.	54

3.9	Results of the Integrator Panel installed in the PROMETEO GUI [109]. The Y-axis represents the ADC counts. High Voltage Power Supply. Image taken by the author of this thesis.	57
3.10	LED Shape Panel. The Y-axis represents the ADC counts. High Voltage Power Supply. Image taken by the author of this thesis.	58
4.1	Sketch of pp -collision and resulting collimated spray of particles, a jet. Taken from Ref. [119].	63
4.2	The jet transverse momentum resolution as determined in dijet MC events for calorimeter jets and particle flow jets. Simulated pile-up conditions are similar to the data-taking in 2012. Taken from Ref. [123].	64
4.3	The jet transverse momentum response distribution as determined in dijet MC events for calorimeter jets and particle flow jets. Two different p_T bins are shown: (a) $40 < p_T < 50$ GeV and (b) $120 < p_T < 130$ GeV. Simulated pile-up conditions are similar to the data-taking in 2012. Image taken from [123] .	66
4.4	The resolutions of p_x^{miss} and p_y^{miss} are depicted for various jet selections and p_T^{miss} working points (WPs). The analysis employs flow jets and the <i>Tight</i> p_T^{miss} WP, based on SM MC simulations, specifically using SHERPA for the $Z \rightarrow \mu\mu$ event generation with the corresponding selection applied. The error bars represent the statistical uncertainty of the MC. The lower panels' y-axis labels use 'incl.' for inclusive jet selection, 'sel.' for the specific jet selection being analysed and 'WP' for the working point. 'True' denotes quantities derived from MC simulations. Taken from [128].	68
4.5	The p_x^{miss} and p_y^{miss} resolution for different p_T^{miss} working points as a function of μ in 4.5a or N_{PV} in 4.5b. A $t\bar{t}$ selection is applied in 4.5a and 4.5b. PFlow jets are used. The error bars include the statistical uncertainty of MC. In the y-axis label of the lower panels, 'incl.' refers to the inclusive jet selection, 'sel.' to the alternate jet selection under consideration and 'WP' to the working point under consideration. 'True' refers to MC-generated quantities. Taken from [128].	69

- 5.1 Average number of interactions per bunch crossing in proton-proton collisions at 13 TeV measured by ATLAS from 2015 to 2018. Higher values indicate higher collision density. The total integrated luminosity for this period is also given. Image taken from [130]. 73
- 5.2 The efficiency of electron identification in data for electrons with $E_T > 30$ GeV, presented as a function of the average number of interactions per bunch crossing. The analysis includes Loose, Medium, and Tight operating points. Efficiencies are derived from $Z \rightarrow ee$ events using data from 2017. The $\langle\mu\rangle$ distribution is depicted as a shaded histogram. The lower panel illustrates the ratio of data to simulation, including total uncertainties. Taken from Ref. [152]. 77
- 5.3 Electron identification efficiency in $Z \rightarrow ee$ events as a function of E_T (left) and η (right) for Loose, Medium, and Tight operating points. Efficiency ratios from $J/\psi \rightarrow ee$ and $Z \rightarrow ee$ events are applied to $Z \rightarrow ee$ simulations. Inner uncertainties are statistical, and total uncertainties include both statistical and systematic components added in quadrature. The bottom panels in both plots show the data-to-simulation ratios. Adapted from Ref. [152]. 78
- 5.4 Comparison of muon reconstruction and identification efficiencies for *Loose*, *Medium*, and *Tight* selection criteria. The left plot illustrates the efficiencies derived from the $J/\psi \rightarrow \mu\mu$ events as a function of p_T , while the right plot presents the efficiencies of the $Z \rightarrow \mu\mu$ events versus η for muons with $p_T > 10$ GeV. The predicted efficiencies are shown with open markers, and the results of the collision data are indicated by filled markers. Statistical uncertainties, when significant, are represented by error bars. The bottom panel shows the relationship between measured and predicted efficiencies, including both statistical and systematic uncertainties. 79
- 5.5 Evaluation of muon reconstruction and identification efficiencies for *Medium* criteria using $J/\psi \rightarrow \mu\mu$ and $Z \rightarrow \mu\mu$ events, plotted as a function of p_T for muons within $0.1 < |\eta| < 2.5$. Statistical uncertainties are shown by error bars when they are not negligible. The bottom panel provides the ratio of the measured efficiencies to the predicted ones, accounting for both statistical and systematic uncertainties. 80

5.6	Shape comparisons between mc16a and mc16d for m_{Z_1} and $m_{4\ell}$ for only the 4μ final state. The error bars in the ratio plots represent the statistical uncertainties in the ratio of the event counts.	90
5.7	Shape comparisons between mc16a and mc16d for $m_{4\ell}$ and m_{Z_1} for only the 4μ final state. The error bars in the ratio plots represent the statistical uncertainties in the ratio of the event counts.	91
5.8	Shape comparisons between mc16a and mc16d for m_{Z_1} and $m_{4\ell}$ for only the $2\mu 2e$ final state. The error bars in the ratio plots represent the statistical uncertainties in the ratio of the event counts.	92
5.9	Layout of the E_T^{topocone} variable.	95
5.10	A diagram of the p_T^{cone} variable.	97
5.11	Results of significance scans on the track isolation for ggH production for various values of the reducible background uncertainty and pileup (μ). Figures with 100% background uncertainty are shown in Figs. 5.11a, 5.11b, and 5.11c; those with 200% are shown in Figs. 5.11d, 5.11e, and 5.11f. . . .	100
5.12	Results of significance scans on the track isolation for ttH production for various values of the reducible background uncertainty and pileup with with 100% background uncertainty for Figs. 5.12a, 5.12b, and 5.12c and 200% for Figs. 5.12d, 5.12e, and 5.12f.	101
5.13	Comparison of transverse momentum isolation within a cone of radius 0.3 ($p_T^{\text{varcone30}}$) to transverse energy in a cone of radius 0.2 ($E_T^{\text{topocone20}}$) for 4μ events in ggH, ttH, $t\bar{t}$, and Z + jets production processes.	102
5.14	Correlation between transverse momentum isolation within a cone of radius 0.3 ($p_T^{\text{varcone30}}$) and particle flow calorimeter isolation (neflowisol20) for 4μ channels in ggH, ttH, $t\bar{t}$, and Z + jets production.	103
5.15	ggH	104
5.16	VBF	104
5.17	Efficiency vs. average number of interactions ($\langle\mu\rangle$) for signal and background samples for several isolation WPs for the ggH and VBF processes. The error bars in the ratio plot (bottom panel) represent the statistical uncertainty in the efficiency measurements relative to the FixedCutLoose working point.	104

- 5.18 Electron identification efficiencies for the Tight WP. 108
- 5.19 Electron identification efficiencies for the Medium Identification WP. 109
- 6.1 The lowest order Feynman diagrams of the SM processes $q\bar{q} \rightarrow ZZ$ and $gg \rightarrow ZZ$ in a pp collider. 115
- 6.2 Muon systematic effects for ggF signal with $m_H = 200$ GeV for the 4μ channel. 120
- 6.3 The p_0 value as a function of m_S in the NWA for the cut-based analysis, combining all categories. The first plot covers the mass range from 200 to 800 GeV, while the second plot spans from 800 to 1800 GeV. 125
- 6.4 Depictions of the $m_{4\ell}$ distributions in the 4ℓ background final states are presented for both the ggF-MVA-low classification and the 4ℓ final states within the VBF-MVA-enriched category. Figure taken from Ref. [122]. . . . 126
- 6.5 Upper limits (95% CL). The solid black line represents the observed limits. The shaded areas in green and yellow indicate the one- and two-standard deviation uncertainties around the expected limits. The dashed lines represent the individual expected limits for each search channel. Refer to Figs. 6.5a and 6.5b for additional details on the ggF and VBF channels, respectively. Taken from Ref. [122]). 128
- 6.6 Limits on $\sigma_{ggF} \times B(H \rightarrow ZZ)$ with additional heavy scalar (1%/5% width). Black: observed limit. Green/yellow bands: $\pm 1/\pm 2\sigma$ uncertainties. Dashed lines: individual search expectations. Taken from Ref. [122]. 128
- 6.7 Exclusion contours for 2HDM Type-I/II vs. $\cos(\beta - \alpha)$ and $\tan \beta$ at $m_H = 220$ GeV. The bands represent predicted uncertainty ($\pm 1\sigma, \pm 2\sigma$), shaded area denotes observed exclusion. Taken from Ref. [122]. 130
- 6.8 This figure displays the upper limit of the cross section times branching fraction at a 95% confidence level. The black line represents the observed constraints, while the shaded regions in green and yellow depict the one and two standard deviation uncertainty ranges, respectively. Additionally, a red line shows the theoretical predictions for the mass of the Kaluza-Klein graviton, $m(G_{KK})$. Taken from Ref. [122]. 131

- 6.9 The p -values for ATLAS (Run 2 and Run 3) and CMS (Run 2) data and their combined analysis, presented for the 4 lepton final state channels.¹ 132
- 7.1 Heavy boson generation through ggF. Figure 7.1a represents the process $R \rightarrow SH \rightarrow 4\ell + E_T^{\text{miss}}$, and Figs. 7.1b and 7.1c represent $A \rightarrow ZH \rightarrow 4\ell + X$, where X encompasses $j\bar{j}/\ell^\pm\ell^\pm/\nu\bar{\nu}$. Image taken from Ref. [191]. . 135
- 7.2 Two-dimensional plots showing the mass differences of the (a) $R \rightarrow SH \rightarrow 4\ell + E_T^{\text{miss}}$ and (b) $A \rightarrow Z(\rightarrow X)H(\rightarrow 4\ell)$ and $A \rightarrow Z(\rightarrow 2\ell)H(\rightarrow 2\ell)$ models. The mass differences are represented by the z -axis as $m_R - m_H$ or $m_A - m_H$. The z -axis also represents E_T^{miss} for these models, indicating that the signal is not varying when the mass of S is below 200 GeV. Different colors represent different values of the missing transverse energy. 136
- 7.3 Distribution for the $R \rightarrow SH \rightarrow 4\ell + E_T^{\text{miss}}$ signal comparing to the different background components of the Missing transverse energy. Each signal is normalised to the total number of background to get better comparison with the background. 138
- 7.4 Figure 7: Two-dimensional scan of the $p_T^{4\ell}$ and E_T^{miss} significance for the $R \rightarrow SH \rightarrow 4\ell + E_T^{\text{miss}}$ signal in the zero central jets region. The z -axis shows the significance calculated using s/\sqrt{b} (top) and $s/\sqrt{s+b}$ (bottom). The High- E_T^{miss} scans are displayed on 7.4a and 7.4c, and Low- E_T^{miss} on 7.4b) and 7.4d. 139
- 7.5 The $m_{4\ell}$ distributions of the interpolated (blue) and simulated (black-filled point) signals. The lower panels show the ratio between the interpolated and simulated histograms. The plots are only shown in SR1 for illustrative purposes. The upper panels display the normalised distribution to compare the shapes, and the lower panels display the ratio, which should ideally be close to 1 if the interpolation is accurate. Taken from Ref. [191]. 140
- 7.6 Search for $R \rightarrow SH \rightarrow 4\ell + E_T^{\text{miss}}$ across SRs: background (blue) vs. potential signal (red, 500 GeV RH-neutrino, 300 GeV Higgs, upper limit 25.0 fb). Error bars: statistical, hatched areas: systematic uncertainties. Lower panel: Bin-by-bin significance. Taken from Ref. [191]. 142

-
- 7.7 **a** presents local p_0 -values in the plane of (m_H, m_R) for the decay process $R \rightarrow SH \rightarrow 4\ell + E_T^{miss}$, with m_S at 160 GeV. **b** illustrates the same in the (m_H, m_A) plane for the decay $A \rightarrow ZH \rightarrow 4\ell + X$. Taken from Ref. [191]. 144
- 7.8 Comparing observed (left) and expected (right) limits on $gg \rightarrow R/A \rightarrow 4\ell$ searches, with $m_S = 160$ GeV. Solid/dashed lines show 95% confidence limits for $R \rightarrow SH$ and $A \rightarrow ZH$ across the $(m_H, m_{R/A})$ planes. 145

List of tables

1.1	Multi-lepton anomalies. Taken from Ref. [56].	16
5.1	$H4\ell$ decay channel yields (2015-2017) post-selection, $m_{4\ell}$ range: 140-180 GeV. The event yields are weighted events.	89
5.2	Comparison of yields and significances for different isolation criteria, with reducible ($\ell\ell\mu\mu$) background calculated via Monte Carlo simulation and signal extracted from simulation.	104
5.3	Change in the rate at which ggF events are reconstructed using the new ‘FixedCutPFlowLoose’ isolation WP for each MC simulation campaign, with and without the data-MC isolation efficiency scale factors. The error bars in the ratio plot (bottom panel) represent the statistical uncertainty in the efficiency measurements.	110
6.1	List of RS graviton Monte Carlo samples.	117
6.2	Summary of the effects of the experimental systematic uncertainties on the Crystal Ball + Gaussian parameters: μ (mean of the distribution), σ_G (standard deviation of the Gaussian component), and σ_C (standard deviation of the Crystal Ball component) for ggF production at $m_H = 200$ GeV, 800 GeV, and 2000 GeV. The errors are symmetrised for simplicity.	121
6.3	Simulated background event yields (weighted) and their systematic uncertainties in the 4ℓ channel, after fit to the background-only Asimov data.	123
6.4	Background event estimates (weighted) after accounting for uncertainties, using the defined selection criteria.	123

-
- 6.5 Scaling factors for simulated ZZ events, derived from background-only fit and categorized by final state and signal region. Total uncertainties (statistical and systematic) included. MVA categories use the 4ℓ channel. 124
- 6.6 Comparison of observed (3275) vs. predicted 4ℓ events ($m_{4\ell} > 200$ GeV). The predictions assume a background-only scenario and incorporate uncertainties. 126
- 7.1 Event yields following fit adjustment for $m_{4\ell} > 200$ GeV, encompassing uncertainties and comparing observed values with predicted values. Normalisation factor μ_{ZZ}^{norm} applies to $q\bar{q} \rightarrow ZZ$ and $gg \rightarrow ZZ$ backgrounds. Additional backgrounds such as $q\bar{q} \rightarrow ZZ$ (EW), $t\bar{t}$, $t\bar{t} + Z$, $t\bar{t} + jets$, and WZ , along with the VVV process, were fixed to their SM predictions. . . . 141
- 7.2 Relative impact of major uncertainty components on the final signal cross section values determined through model fitting. The table presents results for three mass points in the context of the $R \rightarrow SH \rightarrow 4\ell + E_T^{miss}$ and $A \rightarrow ZH \rightarrow 4\ell + X$ signal analyses. Each bar represents the sum of squared upward and downward variations ($\Delta\sigma$) in the cross section due to a specific uncertainty, divided by the best fit cross section value (σ) for that particular signal. 143
- 7.3 Observed and expected upper limits at 95% CL on the product of three cross sections: $\sigma(gg \rightarrow A)$, $\mathcal{B}(A \rightarrow ZH)$, and $\mathcal{B}(H \rightarrow ZZ)$, for various LWA signals. These results are compared with the NWA. 145

Nomenclature

Greek Symbols

η Pseudo-rapidity

γ Gamma Photon

ℓ Lepton

μ Muon

Other Symbols

\mathcal{L} Luminosity

m_T Transverse mass

p_0 Local Probability

pp Proton-Proton

σ Standard Deviation

Acronyms / Abbreviations

2HDM Two-Higgs Doublet Model

AD Active Dividers

ADC Analogue-to-Digital Converter

ALICE A Large Ion Collider Experiment

ATLAS A Toroidal LHC Apparatus

BSM Beyond the Standard Model

CERN European Organisation for Nuclear Research

CIS Charge Injection System

CL Confidence Level

CM Center-of-Mass

CMS Compact Muon Solenoid

CPM Central Processor Module

DAQ Data Acquisition

DBs Daughterboards

DCS Detector Control System

DM Dark Matter

ECAL Electromagnetic Calorimeter

FCAL Forward Calorimeter

FE Front-End

GBT GigaBit Transceiver

GeV Giga electron Volt

ggF Gluon-Gluon fusion

GUI Graphical User Interface

HCAL Hadronic Calorimeter

HL-LHC High Luminosity Upgrade of the LHC

HLT High Level Trigger

HV High Voltage

ID Inner Detector

L1 Level 1 Trigger

LAr Liquid Argon

LED Light Emitting Diode

LEP Large Electron Positron

LHCb LHC beauty

LHC Large Hadron Collider

LINAC2 Linear Accelerator 2

LS1 Long Shutdown 1

LS2 Long Shutdown 2

LS3 Long Shutdown 3

MBs MainBoards

MDs MiniDrawers

MeV Mega electron Volt

MoEDAL Monopole and Exotics Detector At the LHC

MS Muon Spectrometer

PMT Photomultiplier Tube

PPr PreProcessor

PROMETEO Portable ReadOut Module for Tile ElectrOnics

PSB Proton Synchrotron Booster

PS Proton Synchrotron

QCD Quantum Chromodynamics

QFT Quantum Field Theory

RF Radio Frequency

RMS Root Mean Square

SD Super Drawer

SFs Scale Factors

SM Standard Model

SPS Super Proton Synchrotron

TeV Tera electron Volt

TileCal Tile Calorimeter

UX15 ATLAS Cavern

VBF Vector Boson Fusion

VDC Volts Direct Current

Chapter 1

Introduction

The development of particle accelerators pushed forward the science of particle physics; this then led to the discovery of new particles that were not included in the so-called "particle zoo" at that time. A theoretical framework was needed to describe these particles from an elementary level. A theory soon emerged that was known as the Standard Model (SM) of particle physics. However, the history of physics is beyond the aim of this thesis; our knowledge of nature and the universe advanced from understanding the motion and dynamics of important objects like planets, stars, and galaxies to a point where today we question what matter is made up of at the most fundamental level. The SM theorem is the current description of the fundamental structure of matter and the fundamental forces that govern all known phenomena. Section 1.2 contains a brief introduction to the SM as a theoretical background for the work done in this thesis. The fundamental particles are also discussed; then an introduction to the Lagrangian field theory is given in Section 1.4 which is followed by the existence of SM Higgs boson in Section 1.5. Finally, extensions and alternatives to the SM are briefly mentioned in Section 1.6.

Akukho Nkwali'iphandel'el'enyeye,
ephandel'enyeye yenethole.

E.W.M Mesatywa.

1.1 Fundamental Physics and the Universe

Modern fundamental research in physics sits at the precipice of expanding our understanding of the cosmos. This unwavering pursuit, driven by humanity's inherent curiosity, has fuelled our ongoing search to comprehend the composition of the universe and the forces that bind it. The seeds of physics were sown in this desire to dissect the inherent complexity of phenomena and unravel the "why" behind their existence. Particle physics, a cornerstone of this endeavour, delves into the realm of the smallest, most fundamental constituents of nature, from the interplay of electromagnetism to the enigmatic building blocks of matter. The past century has witnessed a cascade of breakthroughs in this domain, exemplified by Ernest Rutherford's discovery of the atomic nucleus [1]. These milestones have paved the way for increasingly sophisticated theories that govern fundamental particles and their interactions. Although advancing technology or solving specific problems may not be the immediate goal of fundamental research, its long-term influence on human self-awareness and daily life has been profound and pervasive. Modern medicine, for instance, relies on the insights of particle physics which have revolutionised medical imaging and guided cancer treatment strategies. Similarly, the Internet, in its contemporary form, emerged as an unexpected but potent consequence of fundamental research conducted at the European Organisation for Nuclear Research (CERN).

These technological advancements, in turn, catalyse the refinement of existing scientific methods, further enriching our understanding of the universe. This cyclical interplay between fundamental research and technological progress propels humanity's exploration of the cosmos ever forward, one groundbreaking discovery at a time. To this day, the SM in particle physics stands as a pivotal theory, elucidating fundamental aspects of the universe's structure. Conceived in the 1960s, its development was propelled by a series of experimental insights. In the SM, the unification of electromagnetism, strong, and weak nuclear forces is achieved within the Quantum Field Theory (QFT) framework. This integration effectively accounts for both the force mediators, known as bosons, and the constituents of matter, identified as fermions. The SM demonstrates remarkable accuracy in predicting particle interactions and even anticipating the existence of undiscovered particles. The SM has demonstrated remarkable predictive power. A cornerstone of this success is the discovery of a massive particle consistent with the long-sought Higgs boson. Confirmed in 2012 at the world's most powerful particle accelerator, the Large Hadron Collider (LHC), by independent experiments ATLAS [2] and CMS [3], this particle's mass of approximately 125 GeV aligns remarkably well with SM predictions. By 2012, the SM had developed into a robust framework that

showed remarkable consistency with experimental observations. Nevertheless, the SM is acknowledged as not being a complete theory for describing all aspects of the universe. One notable limitation is its failure to incorporate Dark Matter (DM), a mysterious component that, according to cosmological studies, constitutes the majority of the universe's matter. Furthermore, it lacks a mechanism for gravitational interaction. This gap in the SM, while highlighting its limitations, does not significantly affect collider experiments, where gravity's influence is minimal. Discrepancies arising from the SM's incompleteness suggest the existence of new physics beyond its current framework. Models aiming to elucidate this Beyond the Standard Model (BSM) physics are typically constructed in a way that adheres to SM predictions demonstrably consistent with experimental observations. A popular scenario involves extending the Higgs boson sector. While various Higgs field expansion proposals exist, all introduce an additional neutral boson resembling the SM particle. The Large Electron-Positron (LEP) experiment previously conducted a comprehensive search for the SM-like Higgs boson below 125 GeV, implying that any additional boson could be heavier [4]. Therefore, the heavy-neutral Higgs boson serves as a prime target in the quest for new physics.

1.1.1 Manuscript Organisation

This dissertation investigates the possible existence of a heavy Higgs boson beyond the Standard Model (SM), using data collected by the ATLAS detector at the LHC during Run 2 (2015-2018), specifically focusing on the four-lepton decay channel. This decay mode, known for its high precision measurements, offers enhanced sensitivity to detect narrow resonances, potentially revealing new physics phenomena. Notably, the four-lepton channel played a crucial role in the groundbreaking discovery of the SM Higgs boson in 2012. Importantly, the search for a heavier Higgs boson is conducted using a model-independent approach, avoiding any assumptions about the specific properties of potential new particles. This method establishes a broad constraint on the particle production rate, which can be further interpreted within various reference models. This document aims to concisely present the key aspects of the author's participation in the ATLAS collaboration. Section 1.2 introduces the SM and the theories of new potential physics. Subsequently, Chapter 2 discusses the experimental setup underpinning this research, encompassing a detailed account of the LHC's design and functioning, as well as an examination of the ATLAS experiment. Furthermore, Chapter 3 details the author's contributions to the Tile Calorimeter (TileCal) as part of the High Luminosity Upgrade of the LHC (HL-LHC), with a specific focus on the implementation of the LED Integrator panel in the Prometeo system. Chapter 4 delves into the methodologies

used for the reconstruction and identification of particles in the ATLAS detector. Furthermore, Chapter 5 delves into the selection of events and the estimation of the background for the final state of 4-leptons, including isolation studies carried out by the author. The search for an additional Higgs boson is elaborated in Chapter 6, while Chapter 7 expands on this search by incorporating analyses involving missing transverse momentum (E_T^{miss}) or jets, to which the author contributed. Lastly, Chapter 8 offers a succinct summary and conclusion of the research documented in this thesis.

1.2 Phenomenology of the Standard Model

The SM [5], [6] stands as the cornerstone of modern particle physics, providing a remarkably comprehensive framework for understanding the fundamental constituents of the universe and their interactions. Built during the 20th century, it reached its current formulation in the 1970s through the groundbreaking work of Glashow, Salam, and Weinberg [7–9]. The predictive power and explanatory capacity of the SM are well established, with accurate predictions and successful explanations of a vast array of experimental findings. At its core, the SM leverages the framework of quantised Yang-Mills theory [10] to offer a unified description of three fundamental forces: ¹ the strong nuclear interaction, the weak nuclear interaction, and electromagnetism. This unification is achieved through a specific Lagrangian formalism implemented within QFT. Furthermore, the SM's Lagrangian exhibits gauge invariance, a crucial property stemming from its underlying symmetry group.

$$SU(3)_C \times SU(2)_L \times U(1)_Y. \quad (1.1)$$

Units and Conventions

In this thesis, the units for various physical quantities are expressed according to standard conventions in high-energy physics. Specifically:

- Transverse momentum (p_T) is measured in GeV/c.
- Mass is expressed in GeV/ c^2

¹Gravitational force is measured to be very weak hence it is not included in the SM. It is applicable on the Planck scale of order 10^{19} GeV and in the context of the Grand Unification Theory [5].

These units account for the factor of the speed of light (c). Throughout this work, it is assumed that c is set to 1 (natural units) unless otherwise stated. This convention simplifies the notation and is common in theoretical and experimental high-energy physics.

1.3 Fundamental SM particles

Elementary particles, considered the fundamental building blocks of matter in physics, comprise the world around us. From molecules composed of atoms to protons, neutrons, and electrons, the analysis reveals a hierarchical structure. While electrons constitute the fundamental level (lacking composition from other particles), protons and neutrons exhibit a composite nature, built from additional elementary particles. The SM categorises these elementary particles into three groups: fermions, gauge bosons, and scalar bosons. The diversity of elementary particles predicted by the SM arises from various combinations of unique representations, as depicted in Fig. 1.1.

Fermions

The visible matter around us consists of twelve point-like particles with spin of $1/2$, known as fermions. These particles adhere to Fermi-Dirac statistics and obey the Pauli exclusion principle. Each fermion has a corresponding antiparticle with identical mass but opposite quantum numbers. Figure 1.1 categorises fermions into two families: quarks and leptons. Leptons are further classified into six "flavours" arranged in three generations of increasing mass, with the lightest and most stable in the first generation (Fig. 1.1). Each generation of leptons includes a negatively charged lepton and its associated neutral partner, the neutrino. The neutrino's mass remains unknown, but evidence suggests that neutrinos change their "flavour" during propagation (neutrino oscillation) due to misalignment of flavour and mass eigenstates, confirming nonzero neutrino mass. Similarly to leptons, quarks exist in six "flavours" (Fig. 1.1) divided into three generations of increasing mass [12, 13]. Uniquely among fermions, quarks possess an intrinsic conserved property called the "colour charge" [14], enabling their interaction through the strong force mediated by gluons. This charge comes in three types: red, blue, and green. Consequently, the SM includes 18 quarks and their antiparticle counterparts. Quantum Chromodynamics (QCD) dictates that colour-charged particles cannot exist as free entities; this phenomenon is known as "color confinement" [15]. Therefore, quarks and gluons are confined within colourless bound states,

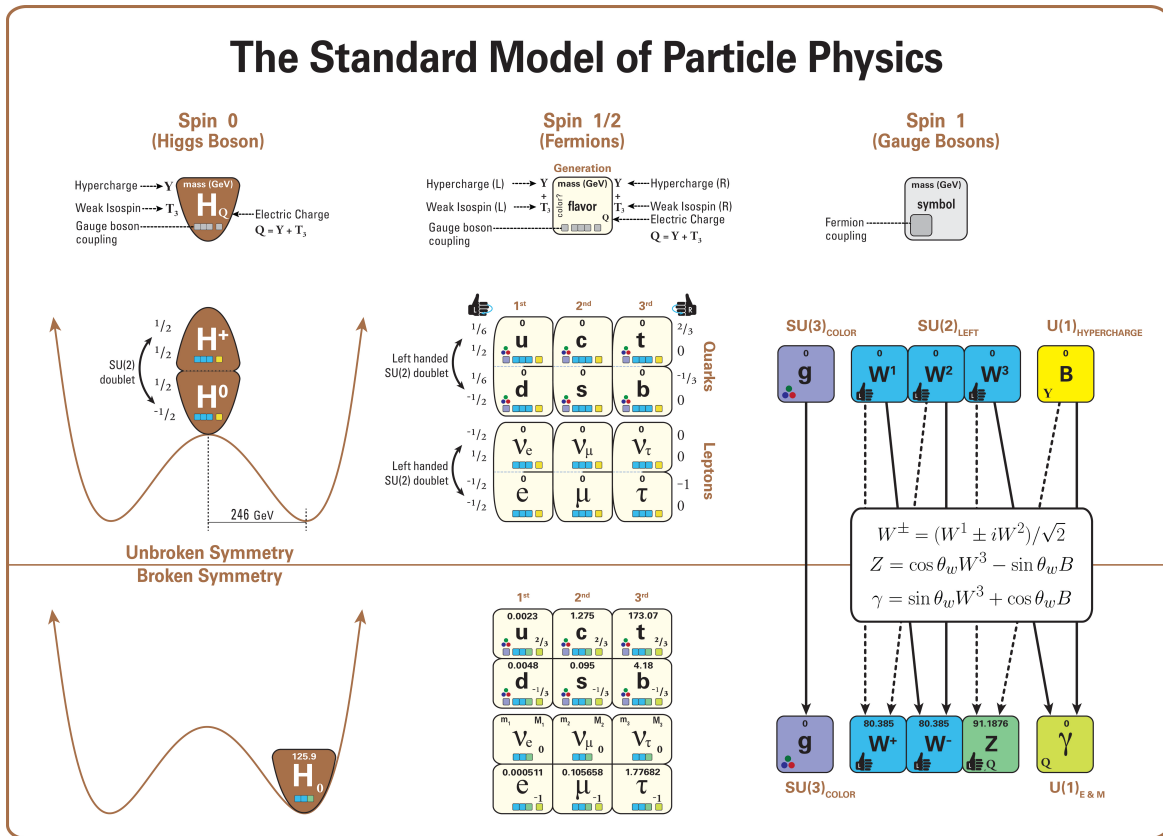


Fig. 1.1 Representation of the 12 fermions (quarks & leptons), their interactions with the three fundamental forces (strong, EM, weak), and the role of gauge bosons and the Higgs field in the model. Taken from Ref. [11].

called hadrons. Three combined quarks form a baryon, while recent observations by the LHCb experiment suggest the existence of four- and five-quark states [16–18].

Bosons

Bosons play a crucial role in the SM by acting as messengers of the fundamental forces. These force carriers come in two varieties: gauge bosons, possessing a spin of 1, and the Higgs boson, with a spin of 0. Gauge bosons mediate electromagnetic, weak, and strong interactions. They include the gluon (strong force), the W^+ and W^- bosons and the Z boson (weak force), and the photon (electromagnetic force). On the other hand, the Higgs boson arises from the Higgs boson mechanism, a theoretical framework within the SM that explains how fundamental particles acquire mass.

1.4 Mathematical description

Lagrangian field theories arise from the concept of interactions that are governed by gauge symmetries. QCD is derived from the symmetry group $SU(3)_C$ and describes quark interactions, mediated by gluons that carry the colour charge. The Lagrangian QCD is given by:

$$\mathcal{L}_{QCD} = \bar{\psi}(i\gamma^\mu D_\mu - m)\psi - \frac{1}{4}\mathbf{G}_{\mu\nu}\mathbf{G}^{\mu\nu}. \quad (1.2)$$

The electromagnetic and weak interactions (responsible for processes such as the decay of neutrons and muons) are unified in the electroweak (EW) gauge theory and the $SU(2)_L \times U(1)_Y$ symmetry group is the underlying symmetry of the EW theory. This gives rise to the following EW Lagrangian:

$$\mathcal{L}_{EWK} = \bar{\psi}(iD_\mu - m)\psi - \frac{1}{4}\mathbf{W}^{\mu\nu} \cdot \mathbf{W}_{\mu\nu} - \frac{1}{4}B^{\mu\nu}B_{\mu\nu}. \quad (1.3)$$

Despite the unparalleled success and great deal of predictive power of the SM, there is, however, a glaring problem with the theory; its massless form is in contradiction with experimental observations; Z and W boson masses (91.2 GeV and 80.4 GeV respectively) were detected at CERN by the UA1 and UA2 experiments in 1983 [19–22]. Furthermore, fermions have a clear mass as reported in Refs. [23] and a consequence of massive gauge bosons would explicitly violate the gauge symmetry. The riddle of the origin of gauge boson masses remained questionable until 2012, when the discovery of the Higgs boson was independently confirmed by ATLAS [2] and CMS [3] experiments at CERN. The Higgs boson, which is the last particle of the SM is a manifestation of Spontaneous Symmetry Breaking (SSB) in the EW sector, delivering mass to other W and Z bosons.

To summarise, the SM Lagrangian may be written as the sum of three parts:

$$\mathcal{L}_{SM} = \mathcal{L}_{QCD} + \mathcal{L}_{EWK} + \mathcal{L}_H, \quad (1.4)$$

where \mathcal{L}_H describes the Higgs boson section of the Lagrangian which is written as:

$$\mathcal{L}_H = (D^\mu\Phi^\dagger)(D_\mu\Phi) - \mu^2\Phi^\dagger\Phi - \lambda(\Phi^\dagger\Phi)^2. \quad (1.5)$$

The following section describes how SSB leads to the prediction of this new particle.

1.5 The Brout-Englert-Higgs Mechanism

This summer I have discovered
something totally useless.

Peter Higgs, 1964

Building upon the initial assertion that all particles were once considered to be massless, the introduction of mass would apparently violate the local symmetry of the underlying theory. However, this apparent paradox was resolved by the Brout-Englert-Higgs (BEH) mechanism, proposed independently by P.W. Higgs, F. Englert, and R. Brout, and by G.S. Guralnik, C.R. Hagen, and T.W.B. Kibble [24–26]. This mechanism, through spontaneous symmetry breaking (SSB), reintroduces mass terms in an $SU(2)$ invariant form. This is achieved by adding a complex scalar field, ϕ (Higgs field), to the Lagrangian. Crucially, a nonzero vacuum expectation value (v) of ϕ preserves gauge invariance while spontaneously breaking the symmetry.

The Higgs field is represented as a $SU(2)_L$ doublet, expressed as:

$$\Phi = \begin{pmatrix} \phi^+ \\ \phi^0 \end{pmatrix} = \frac{1}{\sqrt{2}} \begin{pmatrix} \phi_1 + i\phi_2 \\ \phi_3 + i\phi_4 \end{pmatrix}, \quad (1.6)$$

with a Lagrangian of:

$$\mathcal{L}_\phi \equiv \mathcal{L}_{Higgs} = (D_\mu \phi)^\dagger (D^\mu \phi) - V(\phi). \quad (1.7)$$

The general potential, $V(\phi)$, which describes the evolution of ϕ , is depicted in Fig. 1.2 and depends on the parameters λ and μ^2 . It is constrained by the requirement of $SU(2)_L \times U(1)_Y$ symmetry and renormalizability, leading to the chosen form:

$$V(\phi) = \mu^2 \phi^\dagger \phi + \lambda (\phi^\dagger \phi)^2 \quad \text{with } \lambda > 0. \quad (1.8)$$

The existence of a minimum is crucial for the field to have a ground state, which requires a positive λ . However, there are two potential forms depending on the choice of μ^2 . A positive μ^2 places the ground state in the centre of the potential (all ϕ components equal 0), leading to a unique stable minimum. On the contrary, a negative μ^2 results in an unstable ground state at $\phi = 0$, prompting the field to move towards the minimum as shown in Fig. 1.2. Notably, the

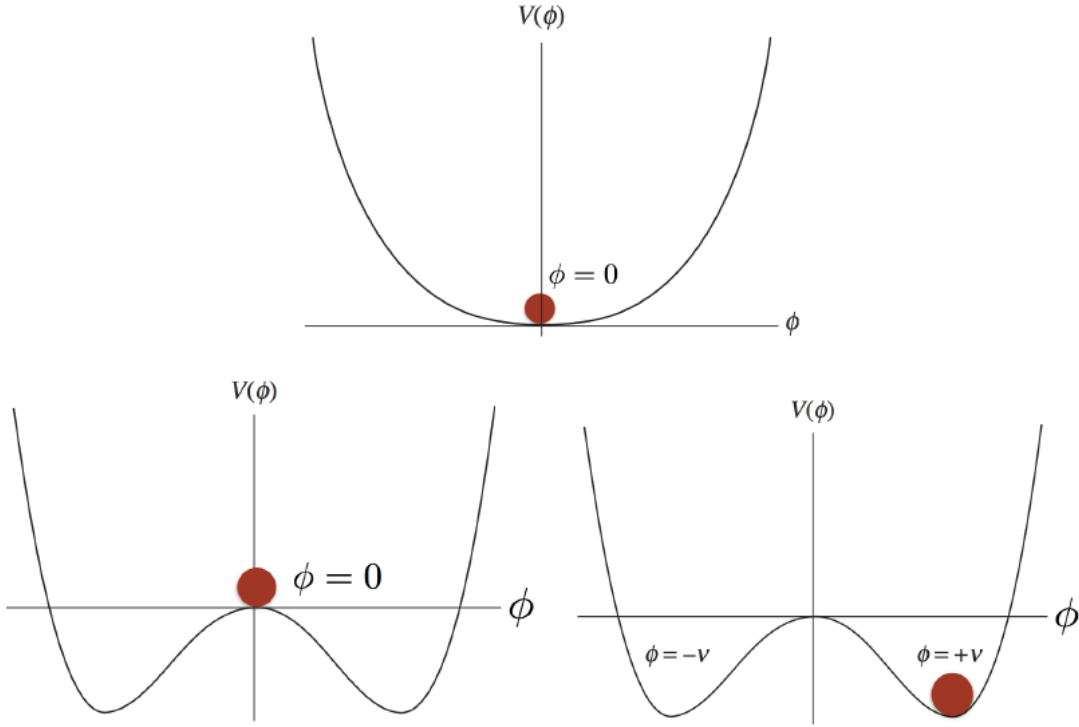


Fig. 1.2 Lagrangian potential: top without symmetry breaking case for $\mu^2 > 0$; bottom symmetry breaking for case for $\mu^2 < 0$. The bottom left indicates that the minimum potential is not $\langle \phi \rangle = 0$, the bottom left shows the minimum potential breaking the symmetry. Figure reproduced using Ref. [27]

symmetry can be spontaneously broken by choosing one of the infinitely degenerate ground states lying on a hypersphere defined by:

$$|\phi|^2 = -\frac{\mu^2}{2\lambda}, \quad (1.9)$$

illustrated in the lower right part of Fig. 1.2. The *vev* is denoted as $v = \sqrt{-\mu^2/\lambda}$, and a specific minimum is chosen as:

$$\langle \phi \rangle = \frac{1}{\sqrt{2}} \begin{pmatrix} 0 \\ v \end{pmatrix}. \quad (1.10)$$

This corresponds to $\phi_3 = v$, and all other ϕ components are equal to 0. This spontaneous symmetry breaking of the Higgs field gives rise to four independent scalar fields, analogous

to Goldstone's theorem [28], where continuous symmetry breaking produces a massless scalar (Goldstone boson). In the SM, three of the scalar fields generate mass terms for the three weak gauge bosons, whereas the fourth one gives rise to a Higgs boson. This Higgs boson is electrically neutral, has even charge parity (CP), and is a scalar boson (which means it has spin-0). It will be referred to throughout the remainder of this work as the SM Higgs boson. Expanding the field in the radial direction with the parameterisation of Equation 1.10 generates:

$$\phi = \frac{1}{\sqrt{2}} \begin{pmatrix} 0 \\ v + H(x) \end{pmatrix}, \quad (1.11)$$

where $H(x)$ is a massive scalar boson, known as the Higgs field. Inserting equation 1.10 will produce the Higgs boson with the following mass:

$$m_H = \sqrt{2}\mu = v\sqrt{2\lambda}. \quad (1.12)$$

The couplings between the W and Z bosons and the Higgs field lead to the generation of terms corresponding to the following masses:

$$m_W = \frac{1}{2}gv, \quad (1.13)$$

and

$$m_Z = \frac{m_W}{\cos\theta_W}, \quad (1.14)$$

together with the variables that explain the interactions between the Higgs boson and the gauge bosons. Fermion masses m_f are also generated through the Higgs boson mechanism, known as *Yukawa couplings*, and are given by:

$$m_f = \lambda_f \frac{v}{\sqrt{2}}. \quad (1.15)$$

Here, λ_f represents the Yukawa coupling constant specific to a particular fermion "f". This constant dictates the strength of the interaction between that fermion and the Higgs field, ultimately influencing the fermion's mass. In simpler terms, a stronger Yukawa coupling (higher λ_f) signifies a more significant interaction with the Higgs field, resulting in a heavier fermion. The Fermi constant G_F is calculated exactly in muon decays [28] and can be linked to the vacuum expectation value (VEV) through:

$$v = (\sqrt{2}G_F)^{-1/2} = 246 \text{ GeV}. \quad (1.16)$$

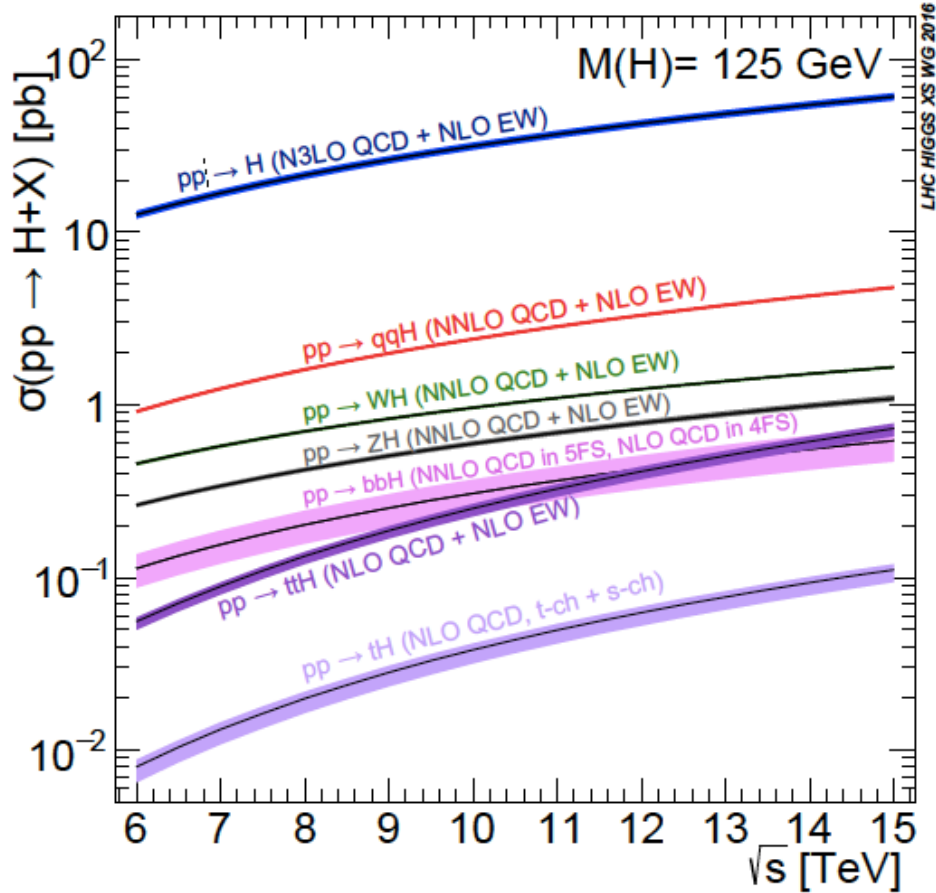


Fig. 1.3 Higgs boson production cross section in pp collisions as a function of the center-of-mass energy. Taken from Ref. [29]

The Higgs boson mechanism contributes to the completion of the SM Lagrangian, and, as seen in the latter equations, the Higgs boson is an adjustable parameter in the SM. Its precise measurement is crucial because its mass determines the production cross sections and decay branching ratios of the Higgs boson.

1.5.1 Exploring the Properties of the Higgs Boson

Extensive efforts have been devoted to the detection of the Higgs boson at various accelerator facilities,² but direct identification remained elusive. As a result, the LHC was constructed, which will be discussed in Chapter 2, primarily to test the predictions of the SM and explore the phenomena Beyond the SM (BSM). Following indirect searches at TeVatron and LEP,

²These include the Stanford Linear Collider (SLC) [30] at SLAC, the Large Electron-Positron Collider (LEP) [31] at CERN, and the TeVatron [32] at Fermilab.

the LHC, during its first run, accumulated sufficient luminosity to observe a particle, as elaborated in Section 1.4, consistent with the SM Higgs boson, which has a mass of $m_H = 125.09 \pm 0.21(\text{stat}) \pm 0.11(\text{syst.})$ GeV [33]. Figure 1.3 provides a visual representation of the various mechanisms through which the Higgs boson can be produced in proton-proton (pp) collisions.

1.5.2 Experimental Limits from LEP

The Large Electron-Positron Collider at CERN was instrumental in setting stringent limits on the Higgs boson mass prior to the operation of the LHC. During the course of its operation, the four LEP collaborations, ALEPH, DELPHI, L3, and OPAL, collected a total of 2461 pb^{-1} of e^+e^- collision data at center-of-mass energies ranging from 189 to 209 GeV. These data were meticulously analysed to search for the SM Higgs boson. The combined analysis from the four LEP experiments tested two hypotheses: the background hypothesis and the signal plus background hypothesis. This rigorous statistical examination led to the establishment of a lower bound on the Higgs boson mass at the 95% confidence level. The results did not show a significant excess over the background expectation, setting a lower limit of $114.4 \text{ GeV}/c^2$ for the Higgs boson mass [34].

In particular, at a Higgs boson mass of $115 \text{ GeV}/c^2$, an excess was observed by the ALEPH experiment that was consistent with Higgs boson production. However, the confidence level indicating consistency with the background hypothesis was 0.09, while the confidence level indicating consistency with the signal plus background hypothesis was 0.15. The LEP results significantly influenced subsequent Higgs boson search strategies, particularly at the LHC, by defining the mass range that needed to be explored. These results also set upper bounds on the HZZ coupling for various hypothetical Higgs boson masses and decay properties, thereby narrowing down the parameters for future searches. The comprehensive data and advanced analytical techniques developed during the LEP experiment extended the sensitive range of the Higgs boson searches beyond initial expectations, laying a robust foundation for the eventual discovery at the LHC.

Higgs Boson Production Mechanisms

The Large Hadron Collider (LHC) collided protons at center-of-mass energies ranging from $\sqrt{s} = 7 \text{ TeV}$ to 8 TeV during Run 1 (2010-2013) and at $\sqrt{s} = 13 \text{ TeV}$ during Run 2 (2015-2018). During Run 2, approximately 8 million Higgs bosons were produced [35]. This translates

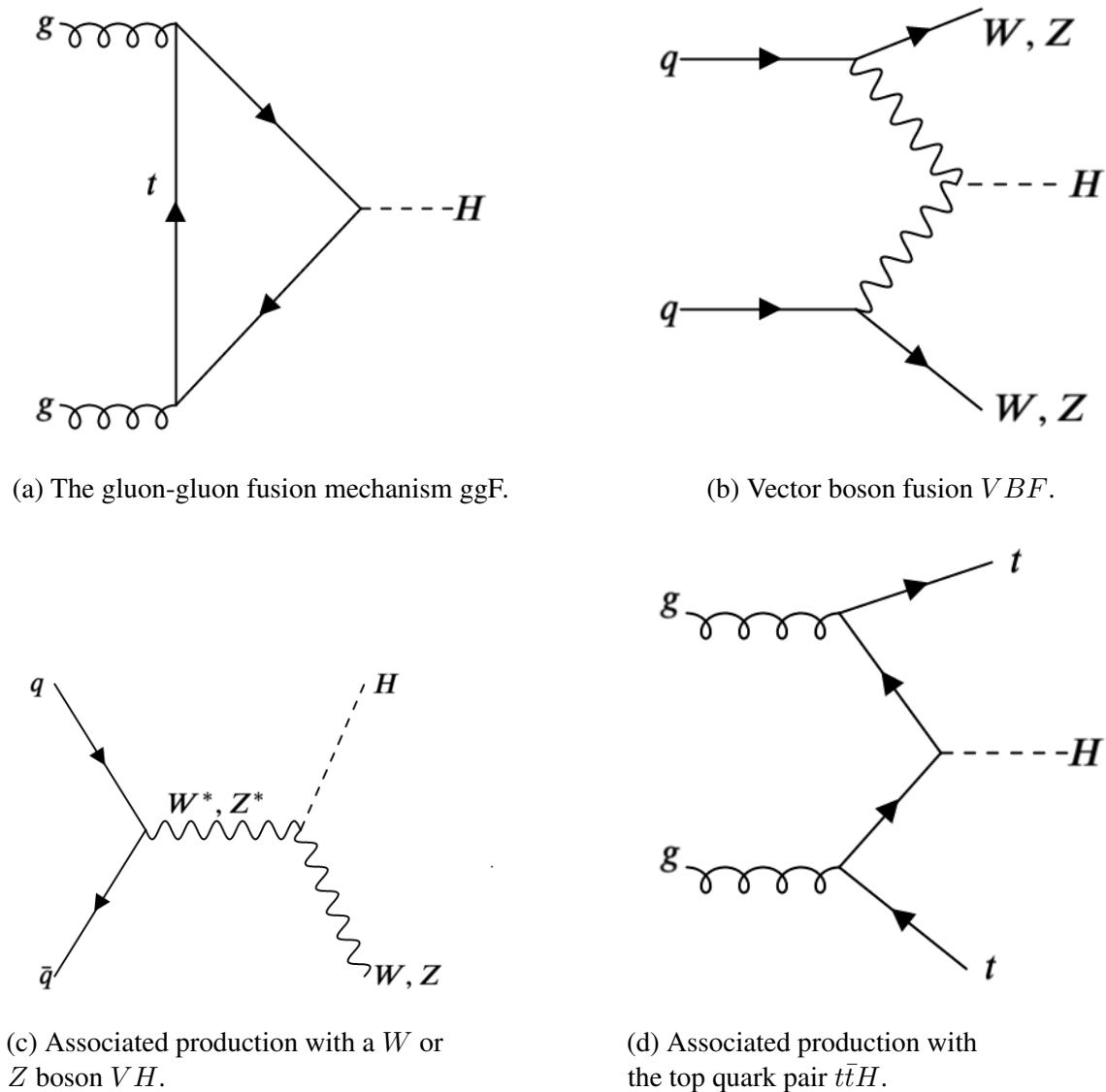


Fig. 1.4 Feynman diagrams for the four main production modes of the Higgs boson at the LHC, created by the author.

to a remarkable production rate of roughly one Higgs boson every two seconds. Among the various production mechanisms, the dominant Higgs boson production mechanism is the gluon-gluon fusion (ggF), which contributes to roughly 87% of the Higgs boson production. As depicted in Fig. 1.4a, gluons, being massless, do not directly couple to the Higgs boson. Instead, the interaction occurs through quark loops, with the top quark's contribution dominating due to its significantly stronger coupling. As shown in Fig. 1.3, the predicted ggF cross-sections reach approximately 50 pb at $\sqrt{s} = 13$ TeV, indicated by the blue curve. Following the ggF in significance is vector boson fusion (VBF), responsible for

6.9% of the LHC Higgs boson production. This process, illustrated in Fig. 1.4b, involves two incoming quarks that emit oppositely charged W bosons or Z bosons that subsequently fuse via a t-channel to create the Higgs boson. A defining characteristic of VBF production is the presence of two highly energetic jets emerging in the forward direction. These jets, characterised by large pseudorapidity and invariant mass, serve as prominent indicators of this production mode. The corresponding VBF cross sections exhibit a range from 1 pb to 3.8 pb, which increases as \sqrt{s} goes from 7 TeV to 13 TeV.

The third most dominant production mechanism is associated production with vector bosons, closely resembling the primary Higgs boson production mode at LEP. Here, an off-shell vector boson, produced from the annihilation of a quark-antiquark pair, emits the Higgs boson to transition to an on-shell state. This process, termed Higgsstrahlung, results in a final state containing the Higgs boson alongside an on-shell vector boson, as depicted in Fig. 1.4c. Although contributing less frequently (around 2.6% for WH and 1.7% for ZH), the $b\bar{b}$ Higgs boson decay channel in this mode offers valuable separation from background processes. The corresponding cross-sections range from 0.4 pb to 1.5 pb at $\sqrt{s} = 7$ TeV to 13 TeV. Finally, associated production with top or bottom quarks, illustrated in Fig. 1.4d, represents the least frequent production mechanism, occurring at a rate of roughly 0.9%. This process involves the emission of a Higgs boson alongside a top or bottom quark pair, initiated by gluons or other quarks. At the LHC, $t\bar{t}H$ and $b\bar{b}H$ production cross-sections range from 0.13 pb to 0.5 pb at $\sqrt{s} = 7$ TeV to 13 TeV.

1.6 The Multi-lepton Anomalies

Although the discovery of the Higgs boson has 'capped' the SM in its long string of successes in describing physical phenomena, several puzzling phenomena exist that cannot be explained within the framework of the SM. Many theoretical arguments for the existence of BSM physics arise because the SM, for example, cannot account for the observations of DM established at cosmological scales, nor for the non-vanishing neutrino masses required by neutrino oscillations, since in the SM neutrinos are necessarily massless. Therefore, the incompleteness of the SM has led the particle physics community to search for a plethora of BSM physics models. Recent studies of growing excesses in pp collisions at the LHC [36] suggest that introducing additional scalar bosons to the SM could explain several anomalies observed in LHC data. Of particular interest here is the BSM scenario considered in Refs. [37–45]. In this scenario, additional scalars H , S , and S' are introduced within an

effective model, with the aim of explaining several Run 1 data anomalies. Specifically, the model allows H to decay into Sh , SS , and hh . The performance of the model against the ATLAS and CMS data sets is discussed in detail in Ref. [37]. This model suggests production and decay modes of these scalars that could have significant signals at the LHC, which could be tested with newer and statistically more precise datasets.

1.6.1 Description of the Theoretical Model

The hypothesis was formulated to address the shortcomings of the SM in explaining certain observed phenomena. This model introduces a new heavy scalar boson, H , with a mass of approximately 270 GeV. The scalar H is hypothesised to decay into pairs of lighter scalars, specifically S and S' , and the SM Higgs boson, h . The scalar S is proposed to decay into vector bosons, predominantly W^+W^- , ZZ , and possibly hh pairs, which subsequently decay into leptons or jets. The motivation for introducing these additional scalars includes explaining anomalies such as non-resonant opposite-sign dilepton events and the excess of events involving b -jets. The scalar S has a proposed mass around 150 GeV and decays primarily into W^+W^- pairs, leading to leptonic final states ($\ell = e, \mu$). This decay chain can explain observed non-resonant opposite-sign dilepton events with or without accompanying b -jets [40]. The scalar S' , on the other hand, is proposed to have a mass of approximately 95 GeV and decays into $b\bar{b}$, accounting for the observed excesses involving b -jets [46].

This model incorporates several free parameters, including the masses and coupling strengths of the scalars H , S , and S' . Specifically, the model introduces a single parameter β_g^2 , which is the scale factor for the production cross section of the heavy scalar H . The mass of H is determined to be $m_H = 272_{-9}^{+12}$ GeV. The interactions of H with the top quark (t) and the heavy vector bosons (W^\pm and Z) are controlled by free parameters: β_g for the $H - t - t$ interaction and β_V for the $H - V - V$ interaction. The model assumes a small coupling of H to pairs of weak vector bosons ($\beta_V = 0$), focusing on the dominant production mode via ggF. Other production modes include single top (tH) and double top associated production (ttH). The decay mode $H \rightarrow Sh$ is given a 100% branching ratio in the model, with S further decaying into vector bosons or the SM Higgs boson. The degrees of freedom are constrained by fitting the model to experimental data from the LHC, particularly the ATLAS and CMS collaborations. The statistical likelihood function $L(\beta_g^2|\theta)$ is constructed to account for the systematic uncertainties and variations in the measurements. The best-fit value of β_g^2 is determined by minimising the likelihood function, providing a flexible framework to explain the observed multi-lepton anomalies.

Final state	Characteristics	SM backgrounds	Significance
$\ell^+\ell^- + (b - \text{jets})$ [42],[47],[48]	$m_{\ell\ell} < 100 \text{ GeV}$ (1b, 2b)	$t\bar{t}, Wt$	$> 5\sigma$
$\ell^+\ell^- + \text{no jet}$ [40],[49]	$m_{\ell\ell} < 100 \text{ GeV}$	W^+W^-	$\approx 3\sigma$
$\ell^\pm\ell^\pm, 3\ell + (b\text{-jets})$ [50],[51],[52]	Moderate H_T	$t\bar{t}W^\pm, t\bar{t}t\bar{t}$	$> 3\sigma$
$\ell^\pm\ell^+, 3\ell(\text{no } b\text{-jet})$ [44],[53],[54]	In association with h	$W^\pm h(125), WW, WZ$	$\gtrsim 4\sigma$
$Z(\rightarrow \ell\ell), (\text{no } b\text{-jet})$ [42],[55]	$p_T^Z < 100 \text{ GeV}$	ZW^\pm	$> 3\sigma$

Table 1.1 Multi-lepton anomalies. Taken from Ref. [56].

1.6.2 Multi-lepton Anomalies Observed at the LHC

Recent LHC data have revealed several anomalies involving multilepton final states. Table 1.1 summarises the observed multilepton excesses and their characteristics.

These anomalies are compatible with the direct production of a scalar H (mass $\approx 270 \text{ GeV}$) decaying dominantly into pairs of lighter scalars S . A subset of these anomalies involves non-resonant, opposite-sign, different-flavour dileptons (with or without b -jets), suggesting that S decays into $W^+W^- \rightarrow \ell^+\ell^-$, where $\ell = e, \mu$, potentially indicating a mass of $150 \pm 5 \text{ GeV}$ [40]. Ref. [57] suggests that the sidebands of the SM Higgs boson analyses in ATLAS [58] and CMS [59] have an excess at a narrow scalar resonance (mass $\approx 151 \text{ GeV}$) produced in association with leptons and b -jets. Furthermore, CMS has reported potential excesses for a new neutral scalar S' with a mass of $\approx 95 \text{ GeV}$ [46]. It should be noted that some of these anomalies are accompanied by b -jets, which could be consistent with the $S' \rightarrow b\bar{b}$ decay channel. Although previous ATLAS analyses [60] did not rule out this potential signal, the latest result [61] indicates a weaker limit than expected. In particular, a previous LEP measurement suggests $\ell^+\ell^- \rightarrow Z^{(*)} \rightarrow S'Z$ with $Z \rightarrow b\bar{b}$ [34], and CMS found a possible excess of resonant τ pair production at a similar mass [62].

1.6.3 Low Mass Range (95 GeV)

Incorporating recent ATLAS and CMS analyses published after 2021, a combined analysis was performed. This combined analysis produced a significantly stronger signal: assuming a simplified model with five degrees of freedom (DOF), a value of approximately 5σ was found for m_S around 152 GeV . Furthermore, combining excesses for the existence of a scalar

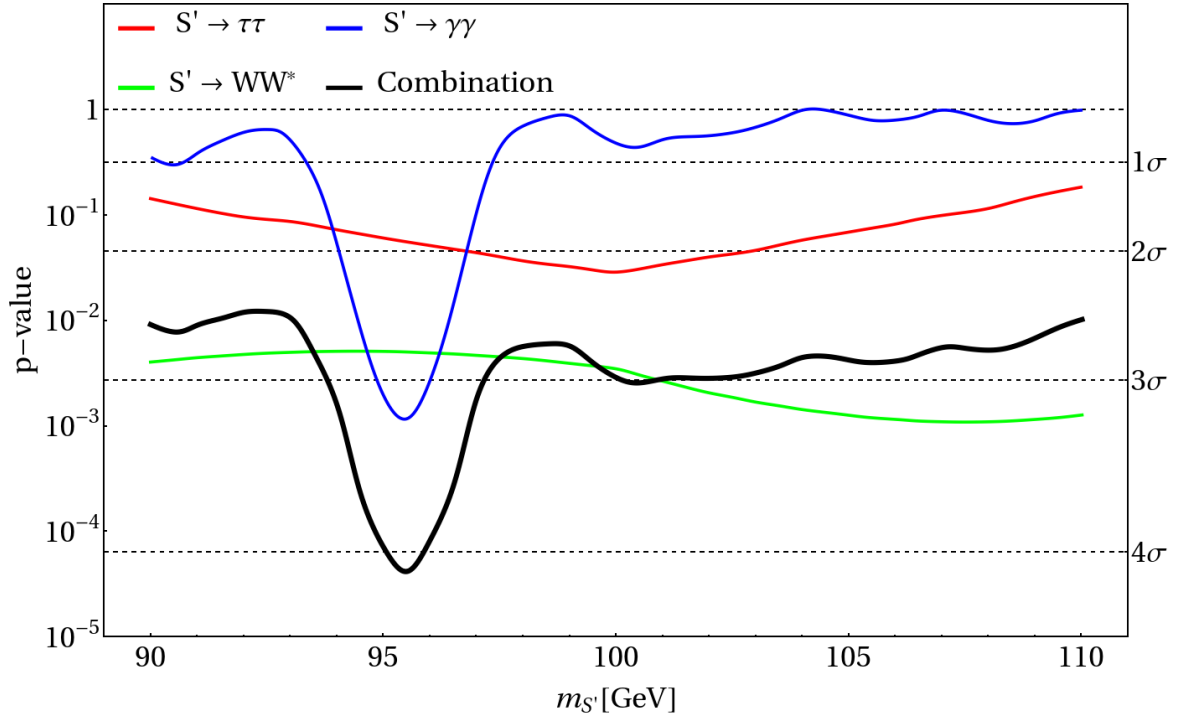


Fig. 1.5 The p -value dependence on the hypothesized S' mass in low-mass search channels. Taken from Ref. [63].

particle, S' , with a mass of approximately 95 GeV, a preference of 3.8σ was observed over the hypothesis of the SM. This finding opens the possibility of a decay chain, $H \rightarrow SS'$, which could explain the observed multilepton anomalies. In this scenario, the decay of the S particle would be the source of leptons, while the S' particle would be responsible for the b -quarks. Finally, the absence of a signal for the decay process $S \rightarrow ZZ^* \rightarrow 4\ell$ suggests that the S particle might be the neutral component of an $SU(2)$ triplet [64–67], as previously motivated by the average W mass measurement [68–70].

1.6.4 High Mass Range (152 GeV)

Section 1.6 introduces a simplified model featuring a scalar boson (H) directly produced by ggF. The model assigns the H boson a mass of 270 GeV. This choice aligns with the motivation drawn from multilepton anomalies. The model includes the decay of H into two lighter scalars, one of which is off-shell (denoted SS^*). An assumption of SM-like properties was made for S , implying that its branching ratios mirror those of a hypothetical SM Higgs boson with the same mass [29, 71]. Initially, an additional branching ratio to invisible final states was incorporated, resulting in a two-DOF combination. Focusing solely

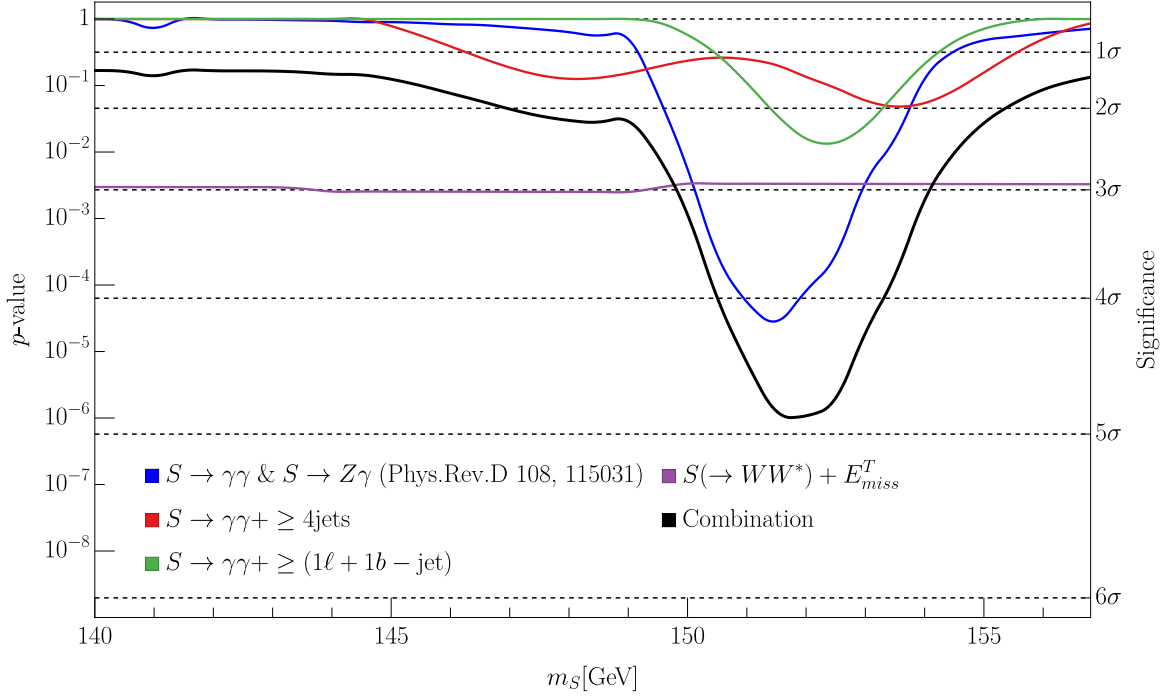


Fig. 1.6 The p -values for individual high-mass search channels and their combined analysis, presented with and without the μe signal. Taken from Ref. [63].

on the on-shell S in the $\gamma\gamma$ and $Z\gamma$ channels, data up to 2021 were combined, leading to the blue line in Fig. 1.6. This curve corresponds to a global significance peak of 4.7σ at 152 GeV. The trial factor, which accounts for the variation in signal resolutions and the mass range (140-155 GeV), adjusted this down to 3.8σ . Subsequently, this result was combined with the results of the second 152 GeV combination. Independent of the analysis above, a separate search for narrow resonances within the sidebands of the SM Higgs boson investigations revealed a potential excess for a ≈ 151 GeV scalar [57]. Integrating recent ATLAS and CMS data released after 2021 into this combination further strengthened the evidence. Assuming a simplified five-DOF model, a significance of $\approx 5\sigma$ was achieved for $m_S \approx 152$ GeV. Furthermore, the excesses for the existence of a ≈ 95 GeV scalar S' were pooled, which produced a preference for the new scenario over the SM hypothesis at a level of 3.8σ . This opens the door to a potential decay chain where H transitions to SS' , providing an explanation for multilepton anomalies.

Chapter 2

Experimental Setup

This chapter concisely outlines the key characteristics of the LHC accelerator and the ATLAS detector. It focuses on analyses derived from data collected during the data acquisition phases 2015-2018. From 10 December 2018 to 5 July 2022, the LHC was offline for extensive updates, enhancing its ability to handle collisions at energies up to 13.6 TeV with a maximum data intake of 300 fb^{-1} . Subsequent developments anticipate a tenfold increase in the LHC's interaction rate, attributed to the forthcoming HL-LHC upgrade. The contents of this chapter are organised as follows, as noted below: Section 2.1 details the LHC's principal features and operational history until 2018. Section 2.3 presents a detailed examination of the ATLAS experiment, including its subdetectors, and Section 2.6 focuses on the role of the TileCal in ATLAS.

Imbovane iyalithwala inyiki.

E.W.M Mesatywa.

2.1 CERN and LHC

The research documented in this thesis was conducted at CERN,¹ an eminent European particle physics research facility established in 1954. Situated on the Franco-Swiss border near Geneva, CERN's workforce exceeds 17,000, with a significant portion, over 13,000,

¹Originally an acronym for 'Conseil Européen pour la Recherche Nucléaire,' CERN now stands as an independent designation for the European Organisation for Nuclear Research, or 'Organisation Européenne pour la Recherche Nucléaire' in French.

being researchers in particle physics. This entity epitomises international collaboration, hosting staff from more than 110 nationalities. These professionals are representatives of their home institutions from more than 70 countries around the world or are among the approximate 5% directly employed by CERN [72]. At CERN, researchers are engaged in delving into the fundamental constituents of matter, using the world's largest and most potent particle accelerator, the LHC. Constructed at CERN, near Geneva, the LHC is a dual-ring superconducting hadron accelerator and collider, which occupies the tunnel previously used by the LEP Experiment [73]. This 26.7 km tunnel, crossing the Franco-Swiss border, varies in depth from 50 m near Lac Lemman to 175 m beneath the Jura Mountains. LEP's limitations, primarily due to synchrotron radiation capping its maximum energy at 209 GeV, led to the conception of a more powerful collider. The idea for the LHC was first formalised in Lausanne, Switzerland, in March 1984 [74], a collaborative effort spearheaded by CERN and the European Committee for Future Accelerators (ECFA). The endorsement by the CERN Council in December 1994 marked the beginning of LEP's decommissioning in 2000, paving the way for the construction of the LHC, which was completed in 2008 [75]. The LHC was engineered for pp collisions at CM energies reaching up to 14 TeV and heavy ion (lead-lead) collisions peaking at 5.5 TeV per nucleon. Figure 2.1 shows a schematic layout of the accelerator complex.

In Fig. 2.2, the geometric structure of the LHC is depicted, illustrating that its design deviates from a true circular shape. This deviation consists of a configuration of eight arcs coupled with eight straight sections, each extending 528 m, known as insertions. Within these arcs, the LHC's intricate magnetic system is primarily housed, comprising 9593 superconducting magnets. Central to this system are the 1232 main dipole magnets, critical for directing the proton beams. These magnets are capable of producing a magnetic field approximately 8.3 T in strength, a magnitude that exceeds the Earth's magnetic field by a factor of 10,000. To achieve such a feat, conventional electromagnets are insufficient; hence, an alloy of Niobium-Titanium (NbTi) is employed. To operationalise these magnets, they are cooled to an ultra-low temperature of 1.9 K using superfluid helium-4. This cooling method enables the magnets to conduct an impressive current of 11,700 A. Complementing the main dipole magnets are other magnetic components with higher multipole orders, such as quadrupoles and sextupoles, as mentioned in Ref. [78]. These components are instrumental in focusing the beams and rectifying various beam-related anomalies. Further details on the design details of the LHC's primary dipole magnet are visually represented in Fig. 2.3.

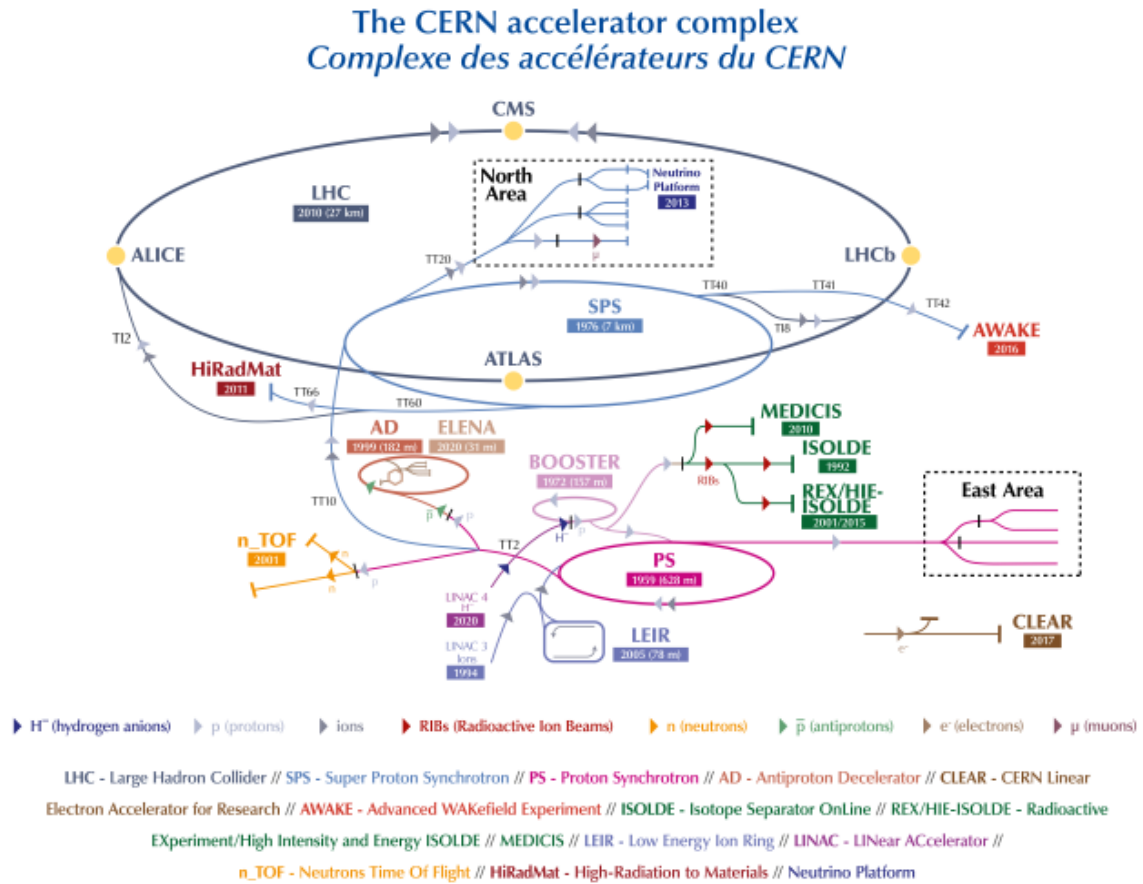


Fig. 2.1 The overall layout of the CERN accelerator complex as of summer 2022. Figure taken from Refs. [76].

The LHC injects beams of protons for collision experiments through a multi-stage acceleration process. This journey begins with the extraction of protons from a source of gaseous hydrogen. A specialised ion source strips electrons, creating a beam of bare protons. These protons are initially accelerated in the 30 m long LINAC2 to an energy of 50 MeV. The Proton Synchrotron Booster (PSB), a 160-meter circular accelerator, further boosts their energy to 1.4 GeV. The next stage involves the Proton Synchrotron (PS), a larger synchrotron with a 628-meter circumference. Here, protons reach an energy of 25 GeV before injection into the final accelerator, the Super Proton Synchrotron (SPS). This 6.9-km ring accelerates them to 450 GeV, the injection energy for the LHC. The LHC operates with counter-rotating beams, requiring separate injection points for each direction. Due to limitations in the preceding accelerators, multiple injections are needed to fill the LHC. Protons then circulate at 450 GeV until achieving stable beam conditions, a process taking approximately two

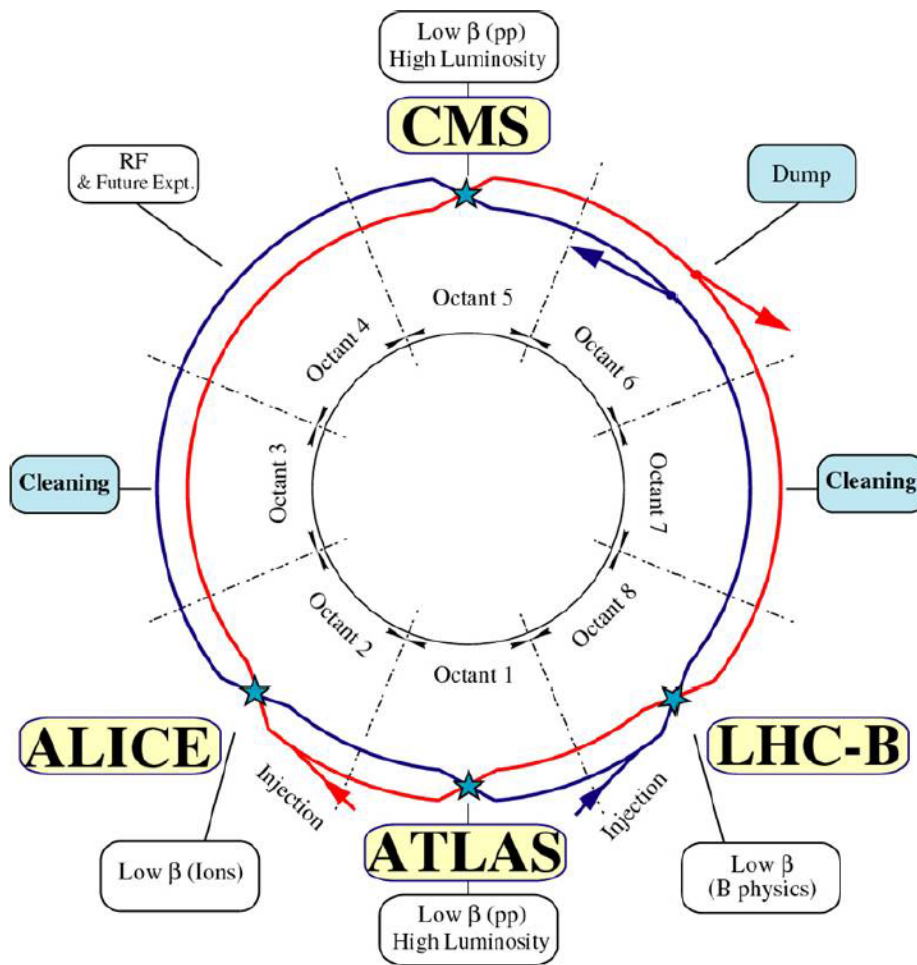
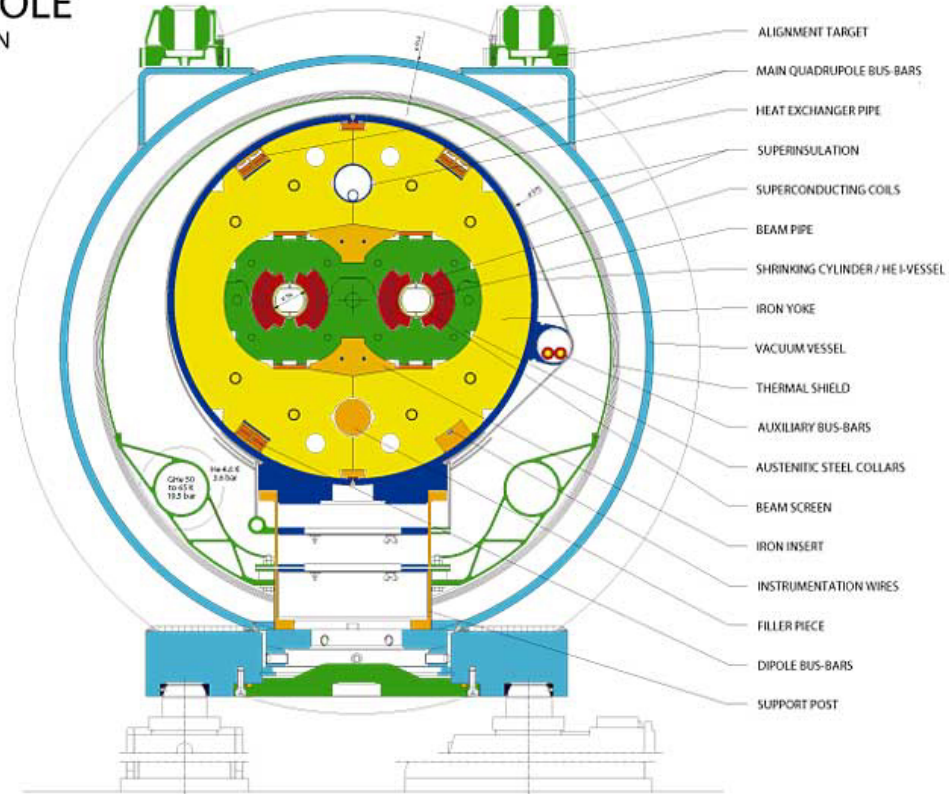


Fig. 2.2 Schematic layout of the LHC, highlighting the two counter-rotating proton beams within the machine's eight arc sections and eight straight sections. Figure taken from Refs. [77].

hours for collisions at 6.5 TeV. Once the LHC is sufficiently filled, the proton acceleration process begins, driven by eight superconducting radio frequency (RF) cavities located in each beam path. Acceleration is achieved by incrementally increasing the frequency of RF oscillations. However, the maximum energy attainable within the LHC is bound by the tunnel's circumference and current technological capabilities. The protons within the LHC do not form a continuous stream, but are organised into discrete units known as bunches, each containing over 10^{11} protons. These bunches are accelerated at regular intervals by an accelerating electromagnetic field generated in the RF cavities. The cavities oscillate at a frequency of 400.8 MHz, and given the LHC's circumference, there are approximately 35640 potential slots, termed "RF buckets". Not every bucket is filled with particles; typically, only every tenth bucket contains a bunch, resulting in a minimum inter-bunch interval of 25 ns,

LHC DIPOLE CROSS SECTION



CERN AC/DI/MM — 2001/06

Fig. 2.3 Cutaway view of a Large Hadron Collider (LHC) dipole bending magnet, highlighting key components [79] from Refs. [77].

equivalent to a bunch length of 7 m. Under nominal conditions, the LHC beams consist of 2808 proton bunches, spaced 25 ns apart.

At the time of writing, the beams were brought into collision in four interaction regions, where the experiments ² were located, as shown in Fig. 2.1. The LHC experiments encompass a suite of detectors designed to explore diverse physics phenomena. ATLAS (A Toroidal LHC ApparatuS) [80] and CMS (Compact Muon Solenoid) [81] detectors, classified as general purpose, are optimised for a broad spectrum of investigations. These include high-precision measurements of SM particles, the Higgs boson, and top quarks, alongside searches for new physics beyond the SM, such as supersymmetry or exotic states. Specialised detectors targeting specific physics goals complement these general-purpose experiments. The LHCb

²Throughout this thesis, the terms "detector" and "experiment" will be used interchangeably. This reflects the established nature of the research, where the detectors function as a synecdoche, representing the extensive collaboration of physicists, engineers, and other personnel who have contributed to their development and operation for many years.

(LHC beauty) detector [82], with its asymmetric design, concentrates on studying rare decays of beauty particles and the composition of matter and antimatter in the universe. ALICE (A Large Ion Collider Experiment) [82], another specialised detector, utilises heavy-ion collisions to recreate conditions similar to the early universe, enabling the exploration of quark-gluon plasma. In addition, three smaller detectors installed at the LHC focus on targeted measurements. TOTEM (TOtal, elastic and diffractive cross-section measurements) [82], positioned near the CMS detector, and LHCf (LHC forward) [83], situated further along the beamline on both sides of ATLAS, concentrate solely on protons that experience minimal deflection during collisions. Finally, MoEDAL (Monopole and Exotics Detector at the LHC) [84], located near LHCb, aims to detect hypothetical particles such as magnetic monopoles and highly ionising stable particles. This thesis will delve specifically into the ATLAS experiment, as detailed in Section 2.3.

2.2 The concept of Luminosity

The primary objective of the particle accelerator is to facilitate collisions at an optimal rate, with the aim of achieving the highest attainable CM energy. The collision-induced event frequency per second can be quantified as:

$$N_{events} = \mathcal{L} \times \sigma_{events}, \quad (2.1)$$

where σ_{events} represents the event cross-section, and \mathcal{L} denotes the accelerator's luminosity. It is noteworthy that luminosity is directly influenced by the beam's parameters, as expressed in the following equation:

$$\mathcal{L} = \frac{\langle \mu \rangle \times n_b \times f_r}{\sigma_{total}}. \quad (2.2)$$

In the context of the LHC, luminosity determination involves assessing several factors: the average number of inelastic collisions per bunch crossing $\langle \mu \rangle$, as visualised in Fig. 2.4, the frequency of bunch crossings per time unit, represented by $n_b \times f_r$, and the aggregate inelastic cross-section for pp collisions σ_{total} . This calculation integrates all relevant processes outlined in the Feynman diagrams.

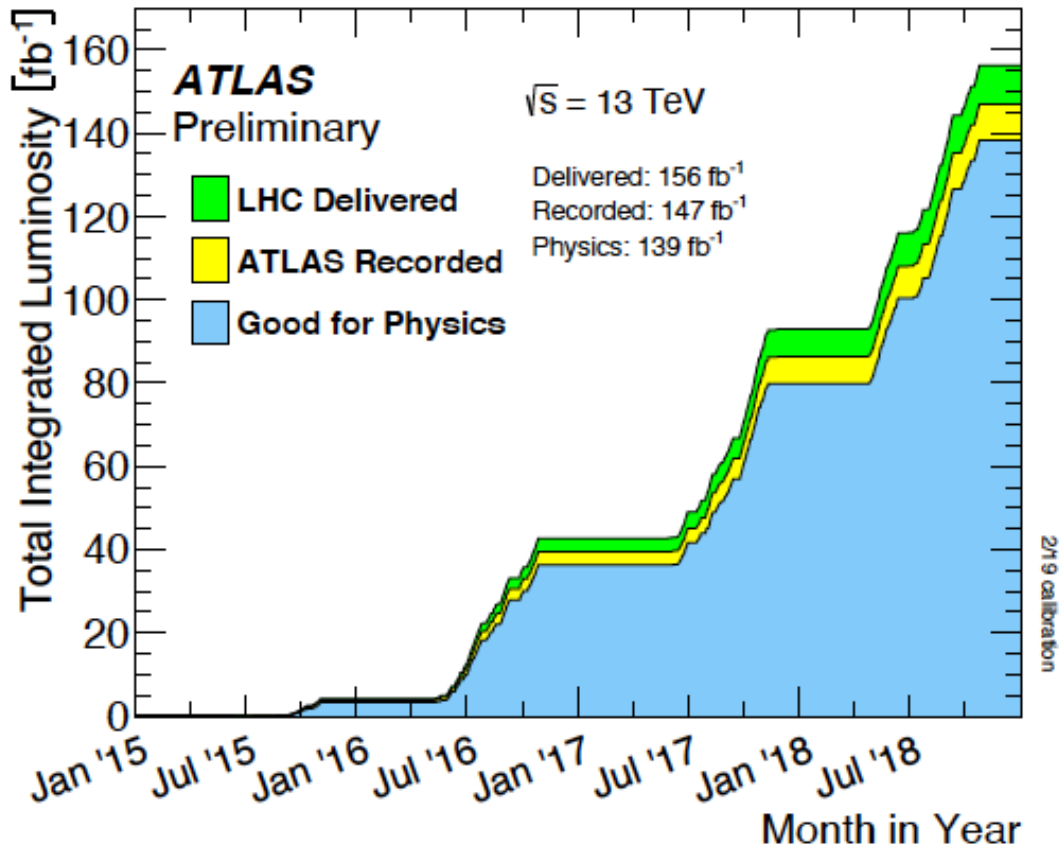


Fig. 2.4 Total integrated luminosity delivered to ATLAS is illustrated in green, while the portion recorded by ATLAS is represented in yellow. The luminosity certified for physics analysis is denoted in blue for the years 2015 to 2018. Taken from [85].

2.3 The ATLAS detector

Accelerator-based investigations have significantly advanced our understanding of the minutiae of matter; yet, they represent just one facet of the complex realm of high-energy physics. Equally crucial is the role of sophisticated particle detectors, which are essential for interpreting high-energy collision events. These detectors, consisting of multiple components, are adept at measuring various event characteristics, leading to the identification and analysis of various particles and their decay products. For instance, segments of a contemporary detector are tailored to assess particle energies and momenta, while also differentiating among particle types. This integrated approach facilitates the reconstruction of collision events, allowing the isolation of individual particles for a detailed examination. Among these versatile experimental setups, ATLAS, as highlighted in Fig. 2.5, is strategically positioned at one of

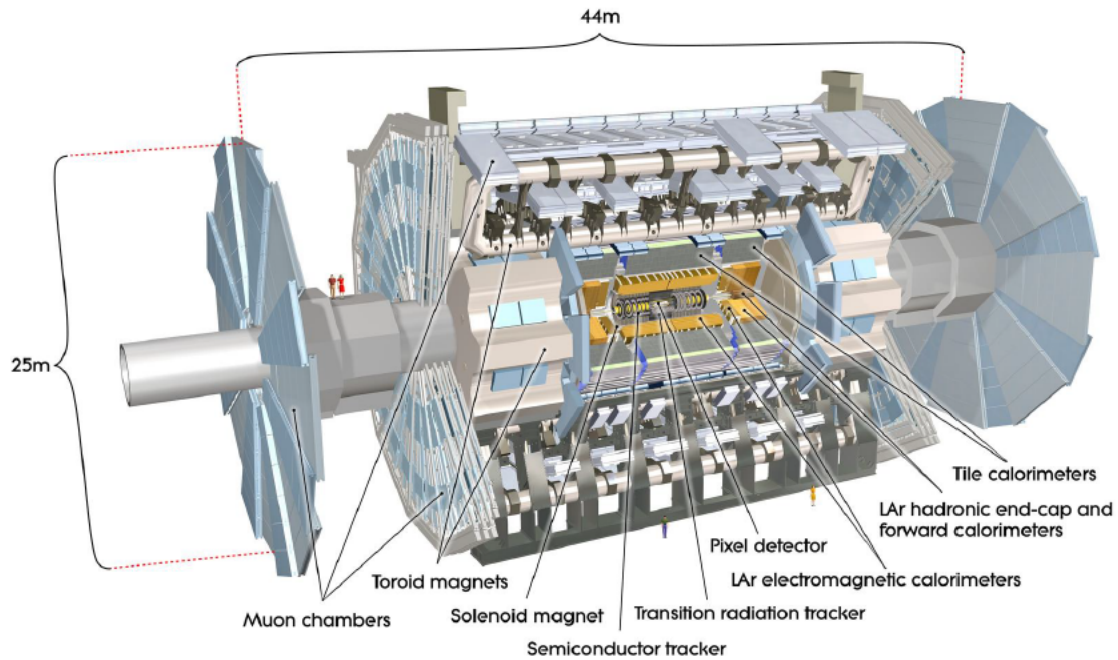


Fig. 2.5 ATLAS detector diagram showing the different subdetector systems and four people to demonstrate the size. Taken from Ref [86].

the LHC interaction points. As detailed in Ref. [80], ATLAS stands as the most voluminous detector ever constructed for particle collider experiments, boasting cylindrical dimensions of 46 m in length, 25 m in diameter, and a mass of 7000 tonnes. Primarily used to test pp , pPb , $PbPb$, and other collisions with hadrons, this thesis concentrates exclusively on pp collision analysis. The ATLAS detector comprises three principal sections, each of which is tasked with detecting specific aspects of collision events. The rationale for this modular design lies in the need for each section to measure different particle properties. These components are arranged sequentially, ensuring that the particles traverse each layer. The presence of a particle becomes evident either through measurable interaction with the detector or via decay into detectable particles. The ATLAS detector, as detailed in Fig. 2.6, is structured into three primary segments: the Inner Detector (ID) closest to the collision point, followed by the calorimeter, and finally the outermost Muon Spectrometer (MS). Subsequent subsections will dive into these components individually, beginning with an introduction to the detector's coordinate system.

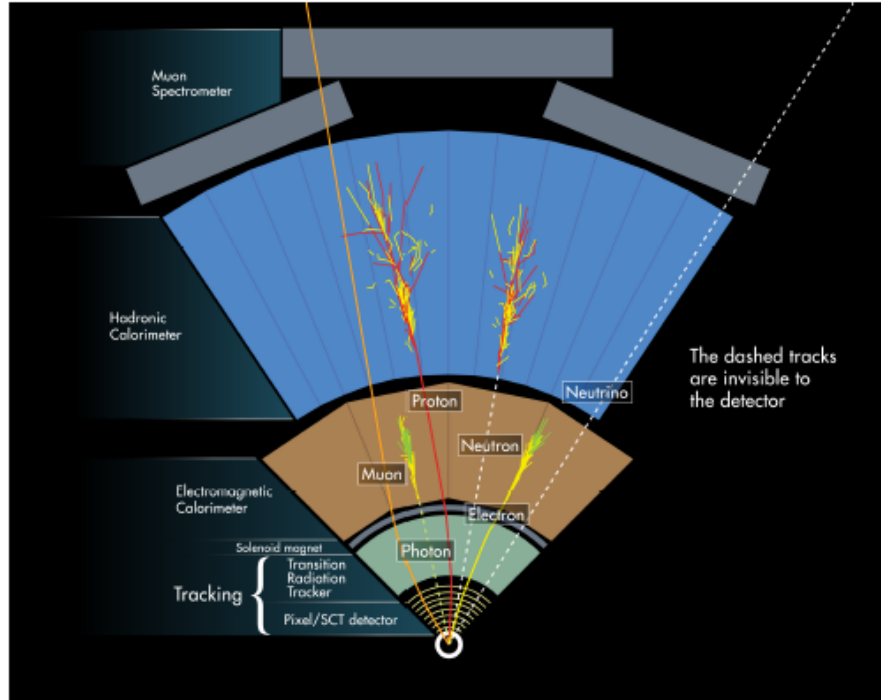


Fig. 2.6 A transverse section of the ATLAS detector showing the three main sub-systems: the calorimeter, the tracker and the muon spectrometer. The paths and interactions of different particles with the detector are shown. Figure taken from [87].

2.3.1 Layout and coordinate system

In the context of the ATLAS experiment, a right-handed Cartesian coordinate framework is used consistently. At the particle collision point, which is also the central point of this system, the Z-axis is aligned along the beam pipe. The plane defined by the X and Y axes, orthogonal to the beam, is known as the transverse plane. In this context, the terms "transverse momentum" and "transverse energy" are introduced, represented as p_T and E_T , respectively. This transverse plane is also describable by cylindrical coordinates, which encompass $r - \phi$ parameters. In this setup, the azimuthal angle of the X-axis ϕ circumnavigates the beam pipe and the beam width is determined by the radial coordinate r . The polar angle θ , originating in the positive direction of the Z axis, is another critical measure. Consequently, transverse momentum and energy are mathematically expressed as $p_T = p \cdot \sin \theta$ and $E_T = E \cdot \sin \theta$. Pseudo-rapidity, denoted as η , is another important parameter used in the analysis of particle collisions. It is defined as:

$$\eta = -\ln(\tan(\theta/2)) \quad (2.3)$$

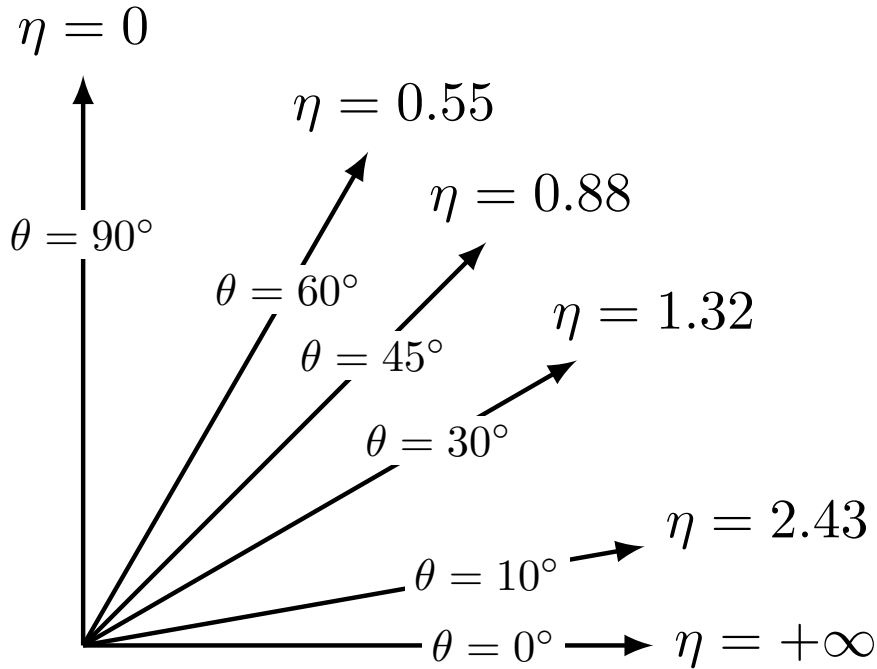


Fig. 2.7 Definition of pseudorapidity (η) and the scheme of polar (θ) and azimuthal (ϕ) angles. The polar angle θ is shown for various pseudorapidity values, and the azimuthal angle ϕ is defined as the angle around the beam axis, perpendicular to the polar angle plane.

This measure is particularly useful because differences in pseudorapidity are invariant under Lorentz boosts along the beam axis. Figure 2.7 illustrates the relationship between pseudo-rapidity, the polar angle θ , and the azimuthal angle ϕ .

In the defined $\eta - \phi$ space, the angular separation between entities, denoted as ΔR , is calculated using the formula $\sqrt{\Delta\eta^2 + \Delta\phi^2}$. Given the predominant momentum in the Z direction due to colliding beams, p_T becomes a constrained parameter and hence a critical parameter for analysis. Notations such as E_T , p_T , and m_T frequently signify quantities measured within this transverse plane.

2.3.2 Inner Detector

Within a 2-Tesla magnetic field, the ID, depicted in Fig. 2.8, plays a crucial role in meticulously reconstructing the trajectories of charged particles. It boasts complete azimuthal coverage and extends up to an absolute pseudorapidity of 2.5. The ID comprises three subdetectors: a pixel detector, a silicon strip tracker (SCT), and a transition radiation tracker (TRT). The pixel detector excels at measuring the three-dimensional spatial coordinates (x , y , z) of charged

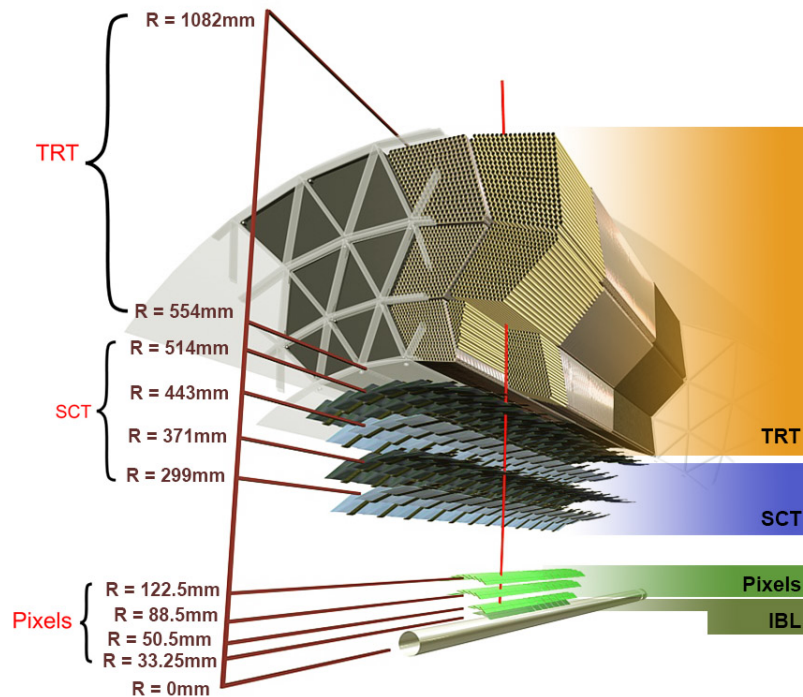


Fig. 2.8 Schematic representation of a particle traversing the three subdetectors of the ATLAS Inner Detector: the pixel detector, the semiconductor tracker (SCT), and the transient radiation tracker (TRT). Taken from Ref [88].

particle interactions. The SCT, designed with pairs of single-sided sensors in a back-to-back configuration, guarantees the acquisition of eight precise hits per particle track. Meanwhile, TRT averages about 35 hits per track within a pseudo-rapidity of 2.0. The Insertable B-Layer (IBL) [89] plays a critical role in the ATLAS detector's ability to distinguish hadronized bottom quarks from other particles like converted photons and electrons. Installed in 2014 after a major shutdown, this fourth layer of the pixel detector sits at a mere 3.2 cm from the beam pipe, significantly closer than the original B-layer. This strategic positioning enhances the detector's sensitivity, enabling more precise measurements and ultimately contributing to deeper insights into subatomic interactions. Integration of IBL improved track and vertex precision in Run 2, particularly under conditions of higher luminosity, while also alleviating radiation-induced deterioration in the primary innermost layer. In particular, IBL has increased primary vertex resolution by 28% and reduced uncertainty in the impact parameter by 25%. This improvement leads to a 1.9 times higher rejection rate for light jets while maintaining a 60% efficiency for identifying B-hadrons in top-antitop ($t\bar{t}$) events. Comprehensive details of tracking performance are available in Ref. [90]. In terms of the

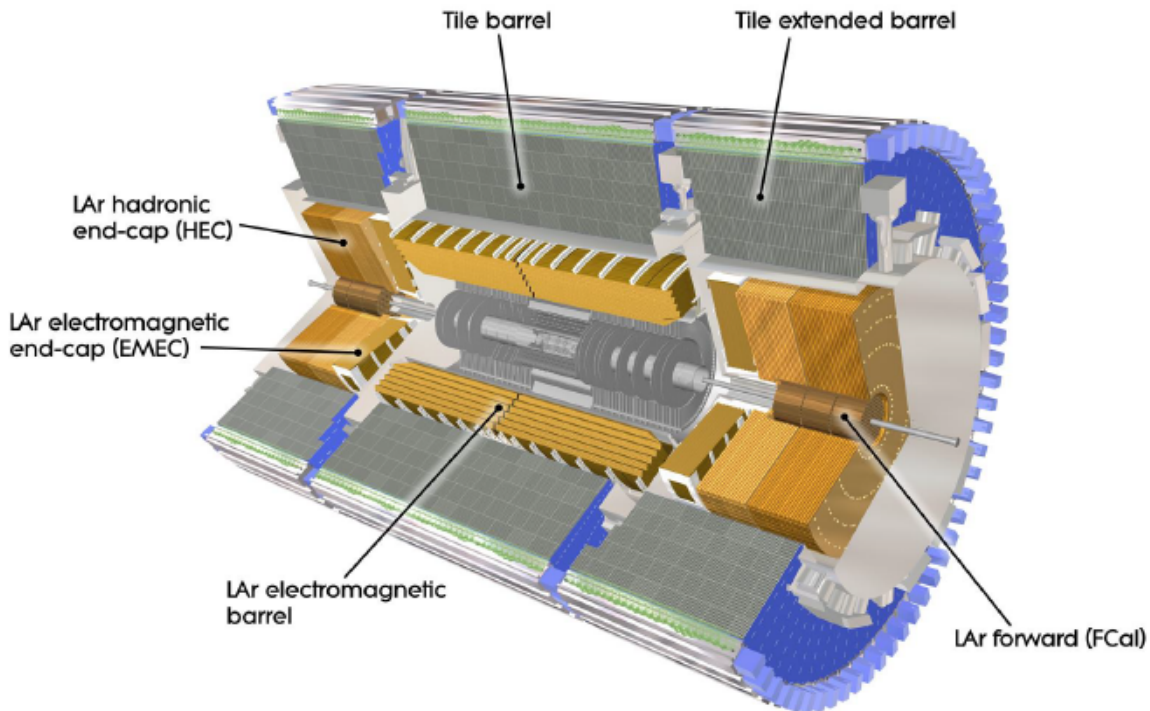


Fig. 2.9 The structure of the ATLAS calorimeter, taken from Ref [80].

precision of measuring the momentum of charged particles, the ID maintains a high resolution, characterised by $\sigma/p_T = 0.05\% p_T \oplus 1\%$.

2.3.3 Calorimeters

The ATLAS detector calorimeter system, depicted in Fig. 2.9, comprises three distinct components: the electromagnetic calorimeter (ECAL), the hadronic calorimeter (HCAL), and two forward calorimeters (FCAL). The ECAL, which is responsible for measuring electron and photon energies, sits at the core, surrounded by the HCAL. Two FCALs extend the detector's coverage to $|\eta| < 4.9$, enabling particle detection across a wider range. Each calorimeter uses a granular η - ϕ segmentation for precise measurement of the shower profile, while its depth is divided into three layers to facilitate the analysis of the longitudinal development of the shower. The active material within these layers absorbs the energy deposited by the particles, while the passive material ensures complete energy containment within the detector volume.

Electromagnetic Calorimeter

ECALs with high granularity are used to cover η up to an absolute value of 3.2. These ECALs employ lead as the absorber and liquid argon (LAr) as the active medium. The central barrel of the ECAL encompasses a pseudo-rapidity range up to 1.475 and consists of three layers for sampling. The end cap regions, referred to as EMECs, are structured differently: two layers cover the range of 1.375 to 1.5 and 2.5 to 3.2 in pseudorapidity, while three layers are used for the range of 1.5 to 2.5. In particular, the strip layer, or the initial barrel layer, is characterised by its fine segmentation, which enhances particle recognition capabilities. The subsequent layer primarily absorbs the energy from electrons and photons. The final layer aims to address energy leakage in cases of high-energy particle showers. Additionally, a pre-sampler layer located in both the barrel (for pseudo-rapidity less than 1.52) and the end-cap regions (between 1.5 and 1.8 in pseudo-rapidity) plays a crucial role in measuring energy before it reaches the main ECAL. The unique accordion design of the ECAL ensures seamless and uninterrupted coverage in the ϕ dimension. However, particle collisions at high-energy accelerators are not isolated events. The phenomenon in which multiple proton-proton collisions occur within a very short time window at the detector is known as pile-up.

Within the precision physics-dedicated region of pseudo-rapidity less than 2.5, where the inner detector and the ECAL intersect, the calorimeter exhibits enhanced segmentation. This feature is particularly advantageous for the precise measurements of electrons and photons. During the 25 ns pile-up interval, the LAr readout's sensitivity extends to 24 preceding bunch crossings, potentially leading to out-of-time pile-up effects. To counteract this, a bipolar signal shaping technique is employed, which produces both positive and negative outputs. This method is effective in averaging the pile-up signal to zero, optimising the read-out system for operations with a 25 ns bunch spacing.

Hadronic and Forward Calorimeters

The HCAL extends its ability to detect particles to a wider range of angles, reaching up to 3.2 units in pseudo-rapidity. This is achieved by using two different techniques in distinct regions. In the central region, where the pseudorapidity is less than 1.0, the HCAL uses a similar design to the ECAL. This design employs steel plates ("absorbers") interspersed with plastic scintillator tiles (referred to as "Tile"). However, the HCAL is specifically optimised for detecting hadrons, unlike the ECAL, which is designed for electromagnetic interactions. This thesis focuses on TileCal, which is discussed in detail in Section 2.6. Its rapid read-out

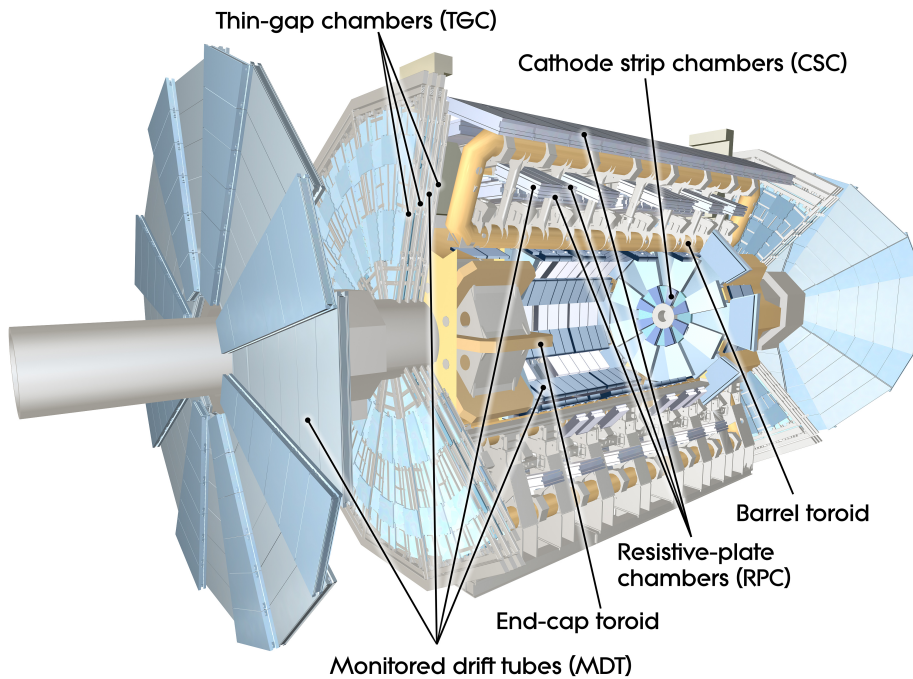


Fig. 2.10 Cross-sectional representation of the ATLAS Muon Spectrometer (MS), showing the high precision tracking chambers, trigger chambers, and superconducting air-core toroid magnets. Taken from Ref [91].

makes it less susceptible to out-of-time pile-up effects. Beyond the central region, HCAL adopts a different approach. An extended barrel ($0.8 < |\eta| < 1.7$) and an end-cap region ($1.5 < |\eta| < 3.2$) utilise LAr as the active material, with copper absorbers for electromagnetic measurements and stainless steel for hadronic interactions. These regions feature three and four sampling layers, respectively, for improved energy resolution. Furthermore, scintillator detectors fill the gap between the central barrel and the extended barrel ($0.85 < |\eta| < 1.51$). Finally, the FCAL covers the forward region ($3.1 < |\eta| < 4.9$). Employing LAr as the active medium, FCAL uses optimised copper absorbers for electromagnetic measurements and tungsten absorbers for hadronic interactions.

2.4 Muon Spectrometer

The Muon Spectrometer (MS) is positioned at the outermost layer of the ATLAS detector and plays a critical role in the identification and reconstruction of muons. As shown in Fig. 2.10, the MS features high precision tracking chambers for accurate muon trajectory measurements, trigger chambers for efficient event selection, and powerful superconducting air-core toroid

magnets for momentum determination. The MS operates within the pseudorapidity (η) range of -2.7 to 2.7 , achieved through a combination of a central barrel covering the η range of -1.05 to 1.05 and two end-cap regions that extend the coverage to -2.7 and 2.7 , respectively. Determining muon momentum hinges on a sophisticated magnetic field system composed of three large superconducting air-core toroid magnets. For $\eta < 1.4$, the massive barrel toroid bends the muon trajectories inward. Meanwhile, two smaller end-cap magnets take over this task in the $1.6 < \eta < 2.7$ region, bending the muons outward. A seamless transition occurs between $1.4 < \eta < 1.6$, where both the barrel and the end-cap magnets contribute to bending. The MS also houses a variety of diverse active components tailored for specific purposes. The resistive plate chambers handle the event trigger and track position measurements for $\eta < 1.05$, while Thin Gap Chambers take charge of these tasks in the $1.0 < \eta < 2.4$ region. Throughout the entire η range of the MS, the monitor tube chambers (MDTs) guarantee precise momentum measurements. In particular, cathode strip chambers replace MDTs as the innermost layer in the $\eta < 2.0$ region. The spacing between the muon chambers ranges from 30 mm to 60 mm, ensuring high measurement accuracy throughout the system. This intricate combination of components allows the MS to play a vital role in unraveling the mysteries of particle collisions at the ATLAS experiment.

2.4.1 Magnetic Field System in ATLAS

The ATLAS detector features a complex and powerful magnetic field system designed to measure the momentum of charged particles accurately. The system includes three large superconducting air-core toroid magnets: one central barrel toroid and two smaller end-cap toroids. The central barrel toroid, which spans the central region of the detector, is responsible for bending the trajectories of particles with pseudorapidity (η) less than 1.4. In the regions where η ranges from 1.6 to 2.7, the end-cap toroids take over the bending task. The transition between these regions, from 1.4 to 1.6 in η , involves contributions from both the barrel and end-cap magnets, ensuring a seamless and effective momentum measurement.

2.5 Trigger and Data Acquisition System

In Run 2 of the LHC, proton bunch collisions occurred at a frequency of 40 MHz, with a time interval of 25 ns. If we were to consider recording each of these bunch crossings with an initial event size of 1.5 MB, the resultant data output would exceed a staggering 60 TBs per second. This volume is clearly unmanageable and unsuitable, given that most LHC collisions

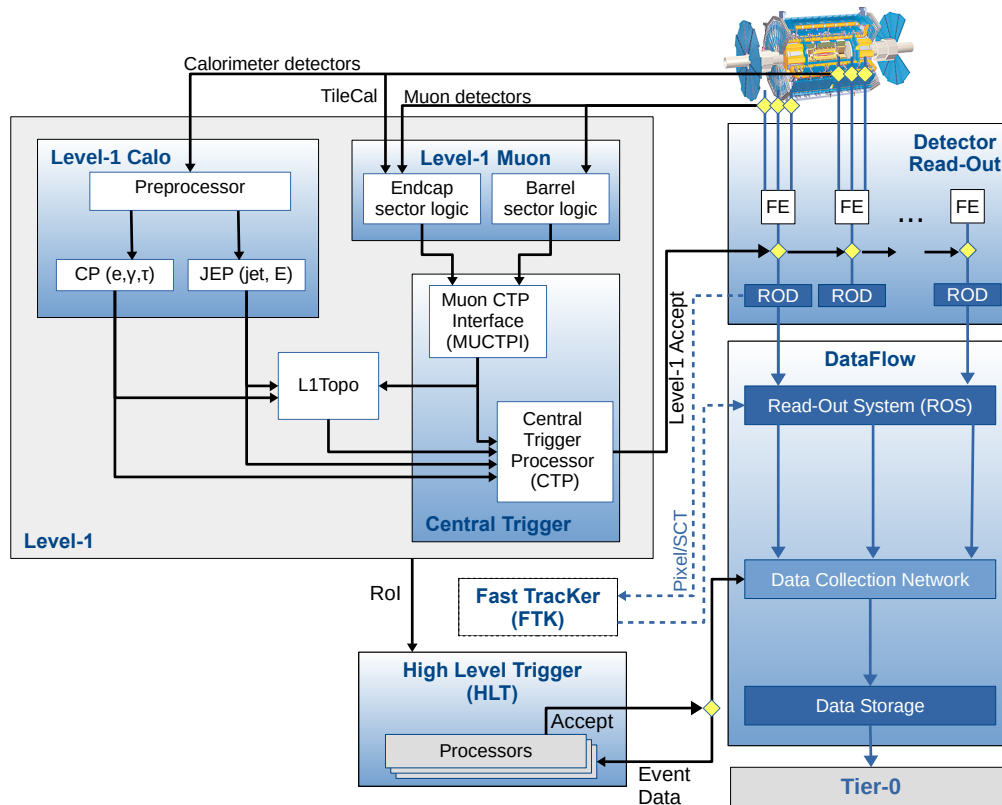


Fig. 2.11 Schematic of the ATLAS trigger and Data Acquisition System. CP (Cluster Processor), JEP (Jet/Energy Processor), L1Topo (Level-1 Topological Processor), ROD (Read-Out Driver), ROS (Read-Out System), and Tier-0. Taken from Ref [92].

involve parton scattering, wherein the captivating physics of the electroweak scale is absent. To address this challenge, a two-tier trigger system is employed [93]. This system uses a hardware-based first level, the Level-1 Trigger (L1), which employs simplified calorimeter and tracking algorithms to efficiently reduce the event rate by a factor of 200. The L1 trigger makes rapid decisions within a mere $2.5 \mu\text{s}$ of the bunch crossing, prompting the transmission of data from the detector's front-end boards. Subsequently, the second level, called the High Level Trigger (HLT) [94], takes over as a software-based trigger. It conducts more intricate tracking procedures to reconstruct pertinent physical quantities in regions of interest. If an event meets the criteria, the HLT accepts it and stores it in the data repository. This process results in a significant rate reduction, bringing it down to approximately 1.5 kHz from an initial 100 kHz. Subsequently, these selected events are forwarded to the CERN Computing Network Tier 0 for a thorough reconstruction. For a visual representation of the trigger and data acquisition (DAQ) system, see Fig. 2.11.

2.6 The Tile Calorimeter

This section presents a detailed discussion of the TileCal architecture and TileCal readout electronics.

2.6.1 TileCal architecture

The TileCal detector (Fig. 2.9) forms the central component of the ATLAS hadronic calorimeter system [95, 96]. Contributing approximately 30% to jet energy capture, it plays a crucial role in various measurements, including:

- **Jet energy:** Accurate determination of jet energy is critical for understanding particle interactions.
- **Missing energy:** Undetected particles can contribute to missing energy, providing clues about dark matter or other exotic phenomena.
- **Jet substructure:** Analysing the internal structure of jets can reveal information about the underlying particle interactions.
- **Electron isolation:** : Distinguishing electrons from other particles relies on identifying their isolation within the detector and this work is covered in detail in Chapter 5.7
- **Triggering :** Selecting relevant events for further analysis requires efficient and accurate triggers based on various detector signals, including muon information.

TileCal is segmented into four distinct subdetectors:

- **Central long barrels (LBA, LBC):** Occupy the detector's core region, encompassing radii between 2.28 m and 4.23 m. Stretching 2.82 m in length, they offer pseudo-rapidity coverage up to 1.6.
- **End-cap barrels (EBA, EBC):** These extend the coverage to higher pseudo-rapidities, reaching 2.91 m in length. They share the same inner and outer radii as the central barrels.

2.6.2 TileCal mechanics and optical readout

TileCal, a sampling calorimeter composed of steel and plastic scintillator plates (Fig. 2.12), employs approximately 460,000 scintillators on each side, read out by wavelength-shifting

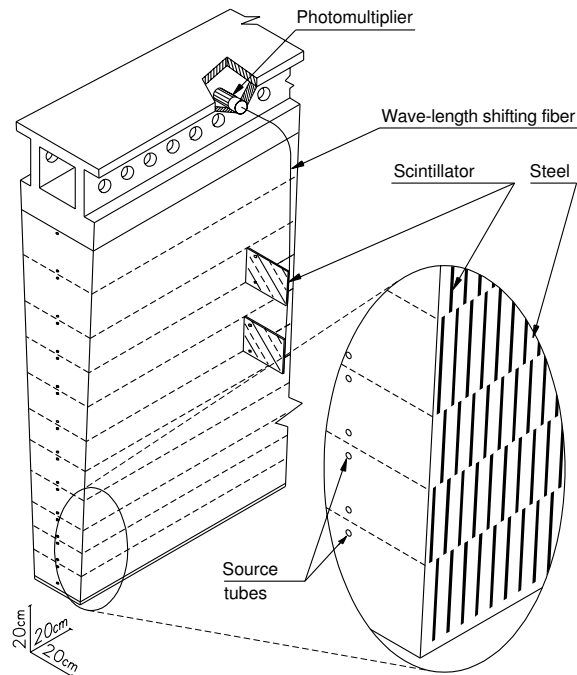


Fig. 2.12 Integration diagram of the TileCal's mechanical and optical elements. Scintillating tiles, fibres, and PMT's are shown for visualisation of energy capture and light collection. This figure is taken from Ref [97].

(WLS) fibres bundled into cells, and detected by photomultiplier tubes (PMTs). Comprising 4670 cells with dual PMT readout, TileCal exhibits radial segmentation into three layers, labelled "A", "BC", and "D". At a $\eta = 0$, these layers have interaction lengths of 1.4, 3.9, and 1.8, respectively. The detector granularity in pseudo-rapidity and azimuthal angle amounts to approximately 0.1×0.1 . This granularity defines "towers" formed by grouping layers A and B with C and D (A-B/C-D), which are currently employed in the fast trigger system (Fig. 2.13).

Additionally, TileCal reads out scintillators ("E cells") between the Long Barrel (LB) and Extended Barrel (EB), including E1-E2 "gap" and E3-E4 "cryostat" scintillators to measure the escaping electromagnetic energy. Minimum Bias Trigger Scintillators (MBTS) at higher η values monitor minimum bias event rates, luminosity during van der Meer scans, and electron identification. In particular, E3-E4 scintillators restore lost electron/converted-photon resolution in the 1.2-1.6 rapidity range.

The First Long Shutdown (LS1) modifications to several E4 scintillators, introducing additional "E4'" scintillators, extend this coverage to a rapidity of 1.72. In TileCal, the azimuthal structure (64 modules) uses water-cooled electronic drawers located at the outermost radius

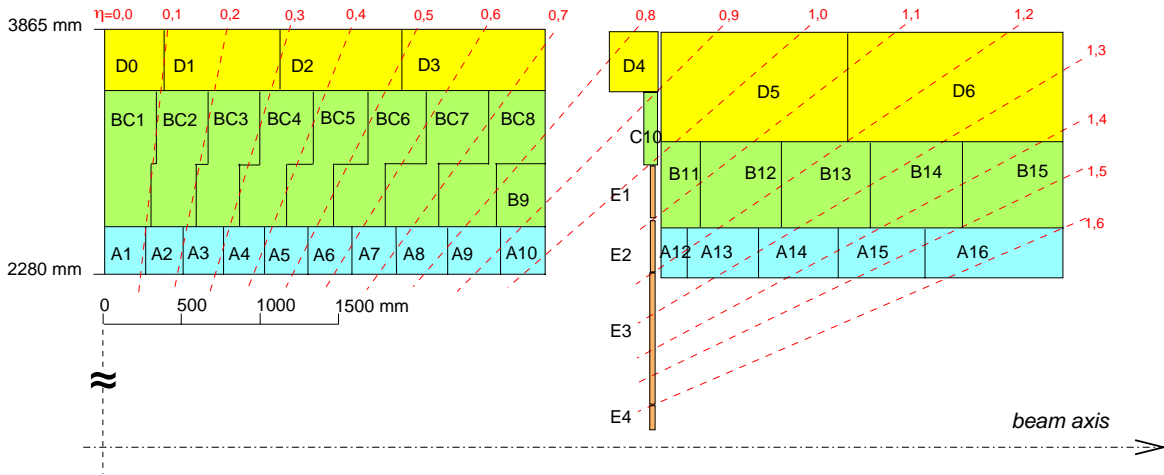


Fig. 2.13 Tile Calorimeter Module Segmentation: Granularity in Depth and η . Left: Central Barrel, Right: Extended Barrel. Taken from Ref [97].

for servicing. Low-voltage power supplies (the "fingers") (LVPs) located at the drawer ends provide power. Radiation shielding from calorimeter steel protects most electronics, with the exception of the more susceptible LVPS, known to experience neutron-induced latch-up during Run 1. The front-end electronics handle critical functions: summing PMT signals for a fast analogue trigger, digitising PMT signals, integrating continuous PMT current for low-light measurements (radioactive source calibration and minimum bias events), serialising data for back-end transmission, and supporting a 16-bit dynamic range. The calorimeter is required to accurately detect and measure the energy of various particles. This includes identifying single muons that deposit minimal energy (around 400 MeV) in the central detector region and exhibit a consistent response for high-energy jets reaching several TeV. Temperature and voltage monitoring are vital to maintain optimal performance and are achieved through a CAN-bus interface integrated with the overall detector control system. Calibration is based on three key methods:

- **Local charge injection system (CIS):** This method directly injects a known amount of charge into the front-end electronics to assess its response and gain calibration factors.
- **Laser Calibration System:** This system directs precisely controlled laser pulses into the PMTs to calibrate their light sensitivity and gain.
- **Cs 137 Radioactive Source:** A dedicated source containing Cs 137, which emits gamma rays with a well-defined energy spectrum, traverses the entire calorimeter volume. The response to this source is used to calibrate the energy response across the detector.

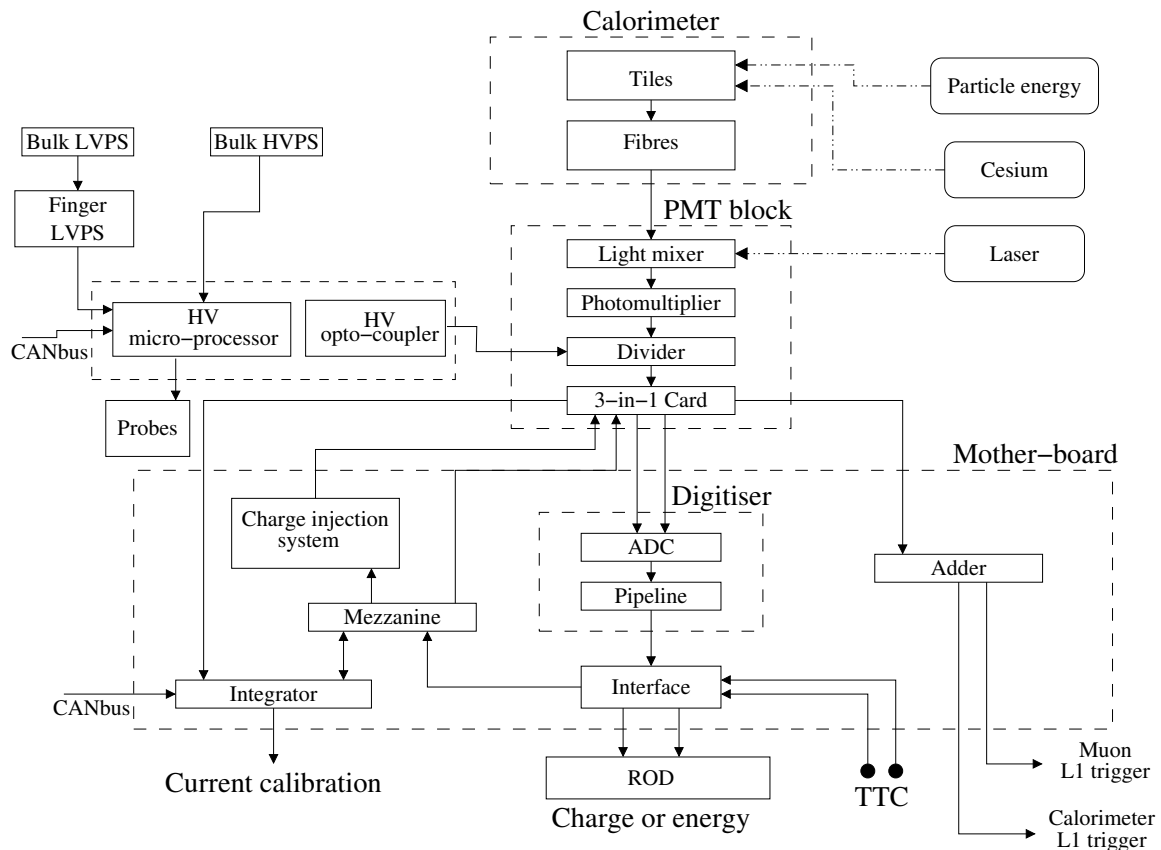


Fig. 2.14 Block diagram of the tile-calorimeter readout electronics, including the TTC (Timing, Trigger, and Control) system for synchronization and control. Taken from Ref [97].

2.6.3 TileCal Readout Electronics

The TileCal readout electronics play a crucial role in the transformation of analogue signals generated by PMTs into digitised data for analysis. As depicted in Fig. 2.14, the system comprises several key components:

PMT block

Situated within drawers adjacent to the PMT, each channel houses a dedicated PMT block responsible for converting scintillation light into electrical signals. The block consists of:

- **Photomultiplier Tube**

As detailed in Ref. [98], this device amplifies weak scintillation light into measurable electrical pulses.

- **Light Mixer**

This element acts as a bridge between the fibre-optic bundle and the PMT, ensuring uniform illumination across the photocathode.

- **High Voltage Divider**

Located at the PMT's terminal, this component distributes the high-voltage supply to the respective dynode stages.

- **3-in-1 Card**

Named for its multifaceted functionalities, this card sits on the PMT's anode. Figure 2.15 illustrates its internal circuitry. Its key functions include:

- **Signal Shaping and Amplification:** The PMT signal is split into two branches, each undergoing independent amplification with a gain ratio of 1:64. This "bi-gain" architecture allows for accurate measurement of a broad energy range, from a few MeV to TeV. The low-gain (LG) branch feeds the analogue trigger system, while the high-gain (HG) branch provides the primary data sample.
- **Calibration Injection:** The card injects a programmable signal into the circuit, enabling the calibration of the analogue-to-digital converters (ADCs) via the TileCal CIS.
- **Slow Integration and Monitoring:** The integrator processes signals from the cesium calibration system and measures the average anode current generated by minimum-bias events, providing valuable insight into detector performance.

Motherboard

This layer beneath the PMT block supplies low-voltage power and digital control signals to the 3-in-1 card.

Digitizer Board

Situated in the middle, this board digitises the amplified and shaped analogue signals received from the 3-in-1 card. Every 25 ns, a dedicated Data Acquisition Module on the board uses 10-bit ADCs to convert high- and low-gain signals, ensuring accurate measurement throughout the energy range.

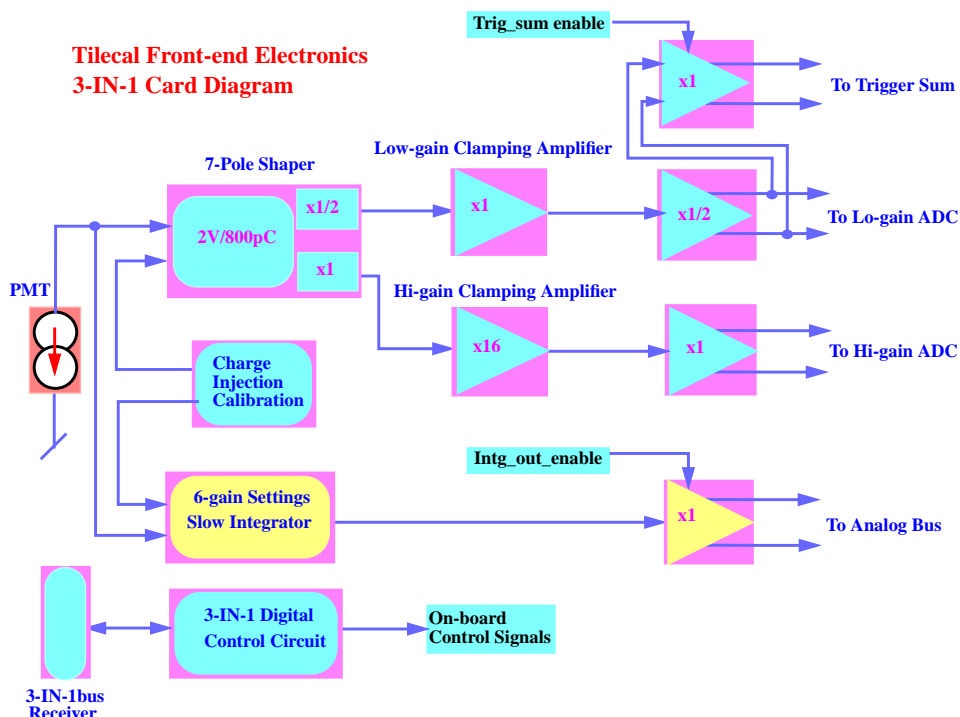


Fig. 2.15 TileCal 3-in-1 card schematic showing key functionalities including signal shaping and amplification, and calibration injection. Taken from Ref [99].

Interface Board

As the outer layer, this board transmits the digitised data to the back-end electronics and manages communication with the TTC (Timing, Trigger and Control) system, which synchronises the detector's timing and control signals.

2.6.4 Requirements for the HL-LHC

The Large Hadron Collider is currently undergoing a significant upgrade known as the High-Luminosity LHC (HL-LHC) project. Scheduled to begin operation in 2029, this project aims to significantly enhance the LHC's capabilities by increasing its instantaneous luminosity by a factor of five compared to its nominal design value (Ref. [100]). To accommodate the demands of the HL-LHC environment, the TileCal requires new electronics capable of handling a 1 MHz trigger rate, increased ambient radiation levels, and maintaining optimal

performance under high pile-up conditions. Therefore, both the TileCal on- and off-detector electronics will be replaced during the 2026-2028 shutdown [101]. Although the high luminosity of the HL-LHC presents exciting opportunities for exploring various physics phenomena, it also poses significant challenges for the detector and data acquisition systems due to anticipated increases in trigger rates and detector occupancy. In response to these challenges, Chapter 3 introduces a portable system specifically designed to validate new on-detector readout functionalities tailored for the HL-LHC environment. This portable system will play a crucial role in ensuring the successful operation of TileCal on the upgraded LHC and maximising the scientific potential of the HL-LHC programme.

Chapter 3

Implementation of the LED Integrator Panel within the PROMETEO System for ATLAS TileCal

The HL-LHC presents challenges to the ATLAS detector, including increased radiation exposure and higher pile-up that compromise trigger selection. To address these, almost all TileCal electronics will be upgraded during Phase II. During assembly, installation, and maintenance, a portable system is needed to validate new on-detector readout functionality. Prometeo, an improvement to the MobiDICK system used in LS 1 and 2, fulfils this role. This chapter delves into the PROMETEO system, a crucial component of the TileCal detector. Section 3.1 introduces the PROMETEO and its intended role within TileCal, while Section 3.2 explores its specific functionalities and applications. Subsequently, Section 3.3 provides a concise overview of the core components of the Prometeo. Finally, Section 3.4 concludes by summarising the comprehensive system tests carried out to validate the performance of the Prometeo.

Akukho mfula ungahlokomiyu.

E.W.M. Mesatywa.

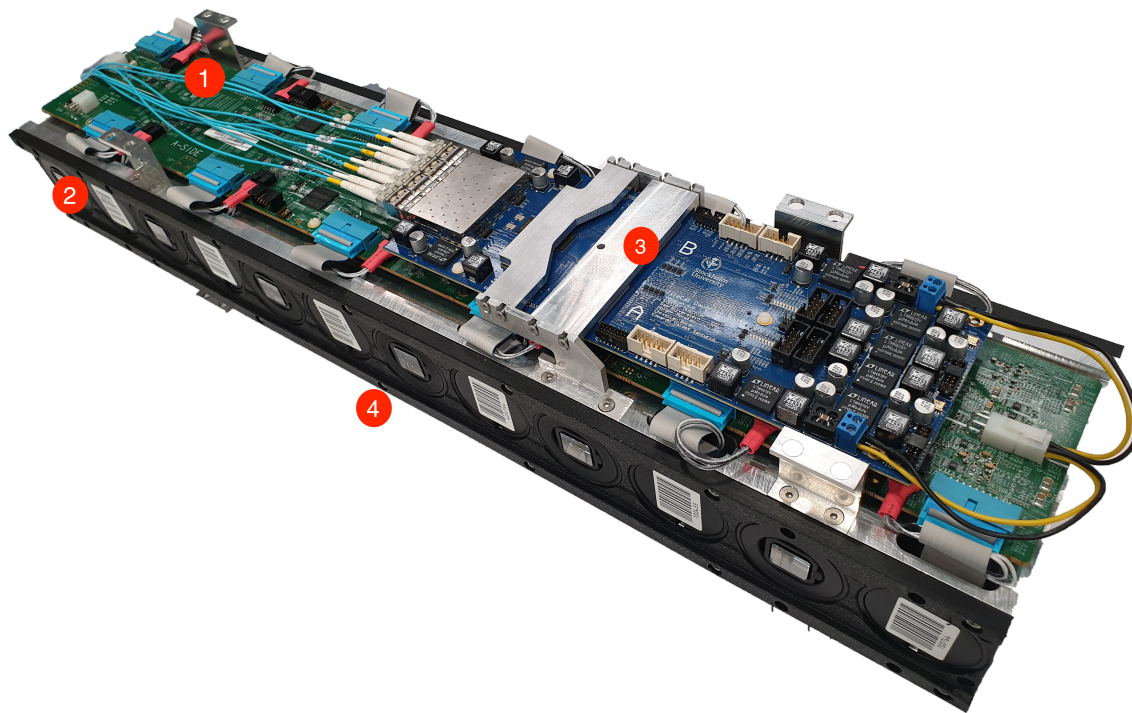


Fig. 3.1 Illustration of Photomultiplier Tube (PMT) Block Elements. Numbered in red, the components are designated as follows: (1) MainBoard (MB), which manages overall signal processing and control functions, (2) PMT Blocks, which convert scintillation light into electrical signals, (3) DaughterBoard (DB), which interfaces with the PMTs to handle signal processing and digitization, and (4) High-Voltage (HV) Distribution Board (positioned beneath).

3.1 General purpose

The Portable ReadOut Module for Tile ElectRONics (PROMETEO) is a portable test bench designed to certify the Front-End (FE) electronics of the TileCal at the High-Luminosity Large Hadron Collider (HL-LHC). It offers high throughput by simultaneously reading all digitised samples from 12 channels at the LHC bunch crossing frequency and evaluating data quality in real time. The design takes advantage of the features of the established Mobile Digital Integrator and Controller for Calorimeters version 4 (MobiDICK4) test bench [102]. The PROMETEO facilitates various functionalities as shown in Fig. 3.1, including testing connections with MiniDrawers (MDs), DaughterBoards (DBs) [103], and

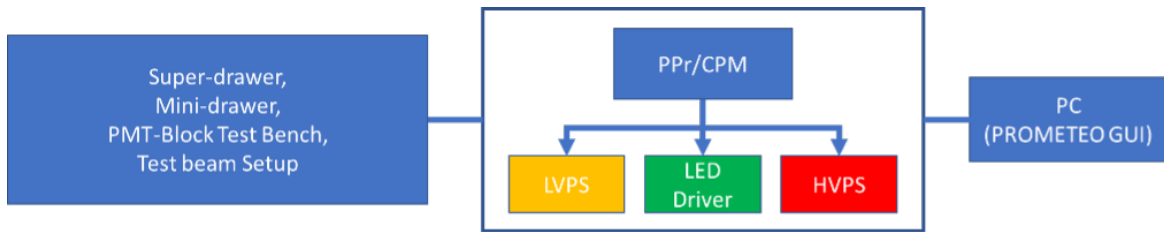


Fig. 3.2 Logical sketch of the PROMETEO sub-components, illustrating the connections between the Central Processor Module (CPM)/ PreProcessor (PPr), Photomultiplier Tube (PMT) blocks, MiniDrawers (MDs), DaughterBoards (DBs), and MainBoards (MBs). The sketch also indicates the integration with the Timing, Trigger, and Control (TTC) system.

MainBoards (MBs) [104], evaluating Photomultiplier Tubes (PMTs) and evaluating charge injection linearity. MiniDrawers are smaller, modular versions of the larger SuperDrawers (SDs) used in the TileCal, containing all necessary electronics for signal processing in a compact form. DaughterBoards are electronic boards that interface with the PMTs to handle signal processing and digitisation, while MBs manage the overall signal processing and control functions. Photomultiplier Tubes convert the light from scintillating tiles into electrical signals, which are then processed by the FE electronics.

To emulate physics pulses and probe PMT block responsiveness, an integrated light-emitting diode (LED) system generates light pulses. A dedicated PMT block test stand enables the simultaneous testing of 12 PMT blocks (corresponding to one MD). Figure 3.2 shows a logical sketch of the PROMETEO subcomponents. Subsequent sections delve into the PROMETEO's functions and usage, the Integrator software, and the obtained results.

The Portable ReadOut Module for Tile ElectrOnics (PROMETEO) system, designed for in situ certification of the TileCal on-detector electronics at the HL-LHC, serves as an independent and autonomous test-bench. This comprehensive system incorporates all components necessary for verifying the functionality of TileCal's on-detector electronics. PROMETEO's capabilities encompass a variety of functions including interfacing with MDs, DBs, and MBs, integration of FENICS cards, PMTs, and the assessment of various operational aspects such as Link Status and Reset, Cyclic Redundancy Check, Pedestal, Charge Injection Linearity, and Charge Injection Shape. Furthermore, to evaluate the PMT blocks' response to light pulses, PROMETEO requires an LED system capable of simulating physics pulses. The PMT block test stand, capable of testing up to 12 PMT blocks simultaneously (equivalent to one MD), is crucial for analysing their response to light. Additionally, the SD test stand allows for the examination of an entire SD within a light-tight environment, assessing the reaction of each PMT to the LED-generated light pulses. SuperDrawers are assemblies of

multiple MDs that cover an entire TileCal module, providing the necessary infrastructure for signal processing.

The PROMETEO system requires several key components: a portable Low Voltage Power Supply (LVPS) to power the FE within the MD, a portable High Voltage (HV) system capable of supplying 600 - 900 V to the Active Dividers (AD) [105] in PMT blocks, and an LED system to stimulate the PMTs. Moreover, readout electronics that replicate the off-detector electronics are required, specifically to read and interpret digital signals from the DBs on the MDs. This is achieved through a scaled-down version of the off-detector readout electronics anticipated in Phase-2, incorporating a single Central Processor Module (CPM) and an MD board. This segment of the PROMETEO also facilitates the sending of commands and the configuration of the FE electronics. In addition, the system includes software to read and modify the configuration of the FE electronics, conduct charge injection runs, pedestal runs, and noise measurements for both precision and integrator readout, as well as light injection ("LED") runs. The software also extracts channel characteristics from calibration runs, such as slopes in charge injection runs, noise and pedestal in pedestal runs, and pulse shapes in charge injection and LED runs. In addition, it verifies the status of the readout link and generates detailed reports on digital readout errors. To further evaluate PMT blocks and their light response, it is essential to have a dedicated PMT block test stand, containing a PMT block black box and specialised trays for the MB, DB, and HV bus board [98]. The PROMETEO controls and reads out the FE electronics, HV, LV, and light-pulse generation for this test stand. Similarly, for testing the entire SDs light response, a dedicated SD black box is required. In this context, the PROMETEO ensures control and readout of the FE electronics and provides HV, LV, and light pulse generation for the SD test stand.

3.2 The PROMETEO functions and usage

3.2.1 Usage during Assembly

The functionality tests described in this section are performed on assembled PMT-Blocks during the TileCal module assembly phase in building 175 (B175) at CERN, as shown in Fig. 3.3. This dedicated area receives and stores certified electronic components from participating institutes prior to assembly.

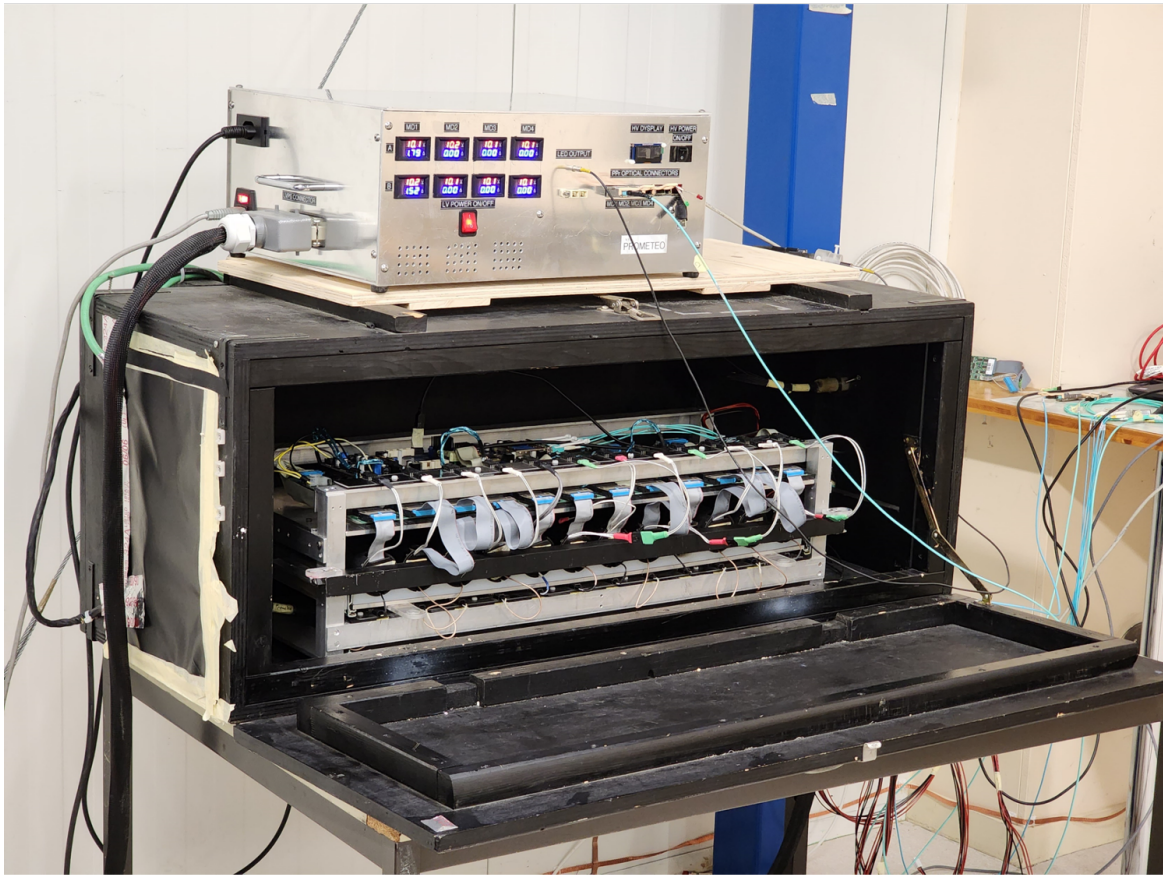


Fig. 3.3 Light tight box for the phase-2 PMT test stand showing 12 PMT-Blocks on the tray. At the top, PROMETEO box prototype.

PMT-Block test stand

The PMT-Block test stand serves solely to certify assembled blocks' proper operation, not to characterise individual PMTs. The characteristics of PMTs are measured prior to issuance for those that require it, specifically for new PMTs and a selected portion of existing PMTs. The initial step in MD assembly includes the preparation of up to 12 PMT-Blocks, each equipped with an Active Divider (AD) and a Front-End board for the New Infrastructure with Calibration and Signal Shaping (FENICS) card [98]. The FENICS card is the front-end board that shapes and pre-amplifies PMT signals. These PMT-Blocks, once assembled, are installed and examined on a PMT test stand capable of holding 12 PMT-Blocks, as illustrated in Fig. 3.3. The test stand comprises a light-tight black box for cable management and a tray that accommodates the PMT-Blocks alongside specific MainBoard (MB), DaughterBoard (DB), and High-Voltage (HV) bus boards.

Once installed on the test stand, the PMT-Blocks receive HV, LV, and light pulses. The PROMETEO portable HV connects to the HV bus board, which supplies HV to the PMT-Blocks. Its LED system delivers light pulses to the PMTs, while its portable LV powers the MB. The connection to the DB is established via readout fibres. The tests carried out include low- and high-gain LED runs, pedestal and charge injection assessments, and evaluations of linearity, noise, gains, and data transmission accuracy in slow and fast read-out channels.

Mini-Drawer Assembly Testing

The PROMETEO further contributes to the assembly process by facilitating the certification of completed MDs. Each MD comprises a MB, a DB, and 12 PMT-Blocks. This certification occurs after individual PMT-Block verification using the dedicated tests and their subsequent installation and connection within an MD alongside a DB, MB, and HV bus board. After the installation and connection of the PMT-Blocks in an MD, calibration runs, excluding LED, are performed for pedestal and charge injection in both slow and fast readout chains. In this context, The PROMETEO supplies LV power to the MD front-end electronics (MB and DB), HV power to the HV bus board, and performs readout of the 12 channels via the DB. Measurements include evaluating linearity, noise, gain, and data integrity in all channels and gains.

SuperDrawer Assembly and Testing

After certification of four (or three) MDs, a long (extended) barrel SD is assembled. The assembled SD is then carefully placed within a dedicated light-tight black box designed to ensure optimal routing for readout fibres, LED fibres, LV cables, and HV cables. In this application, the PROMETEO system plays a crucial role by supplying HV power to all 45 PMTs (or 32 PMTs in extended barrel modules with three MDs), LED light to all PMTs, LV power to all four MDs (or three MDs in extended barrel modules) and performing readout of up to 45 PMTs (or 32 PMTs and readout channels in extended barrel modules with three MDs). Once securely positioned within the black box, the SD undergoes the full calibration suite, encompassing pedestal, charge injection, and LED runs in both slow and fast readout modes.

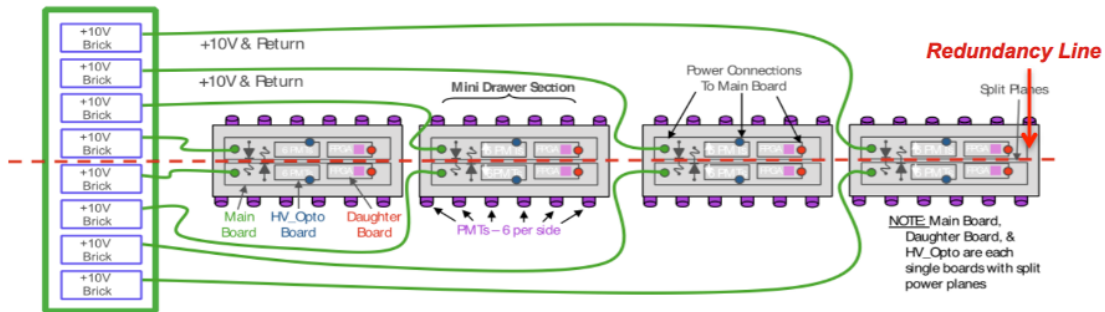


Fig. 3.4 Tile Calorimeter SD low voltage supply topology. Image developed by Sergiu from the TileCal community, not published.

3.2.2 Usage during Installation and Maintenance

In-situ SuperDrawer and MiniDrawer Tests

During the TileCal installation in the maintenance periods of Long Shutdown 3 (LS3) and HL-LHC, the PROMETEO serves within the ATLAS cavern (UX15) to certify or recertify the SD inserted in the calorimeter. Its portable HV, LV, and LED system allows for certification even when essential services such as LV, HV, off-detector electronics, or the laser system are unavailable. The requirements for this application mirror those described in Section 3.2.1 for the SD test stand.

Surface-level Tests

Occasionally, maintenance periods require the return of faulty MDs or SDs to the surface assembly building for rework. In such cases, the PROMETEO facilitates the re-certification of reassembled SDs and MDs. These procedures mirror the operations described in Sections 3.2.1 and 3.2.1, although they were performed on reworked modules rather than newly assembled ones.

3.3 Physical Description of the Prometeo

3.3.1 Portable Low Voltage Power Supply for TileCal MDs

The FE electronics of the TileCal require a power supply of 10 ± 2 VDC (Volts Direct Current) for operation. To facilitate testing during various stages, including the PMT-Block test

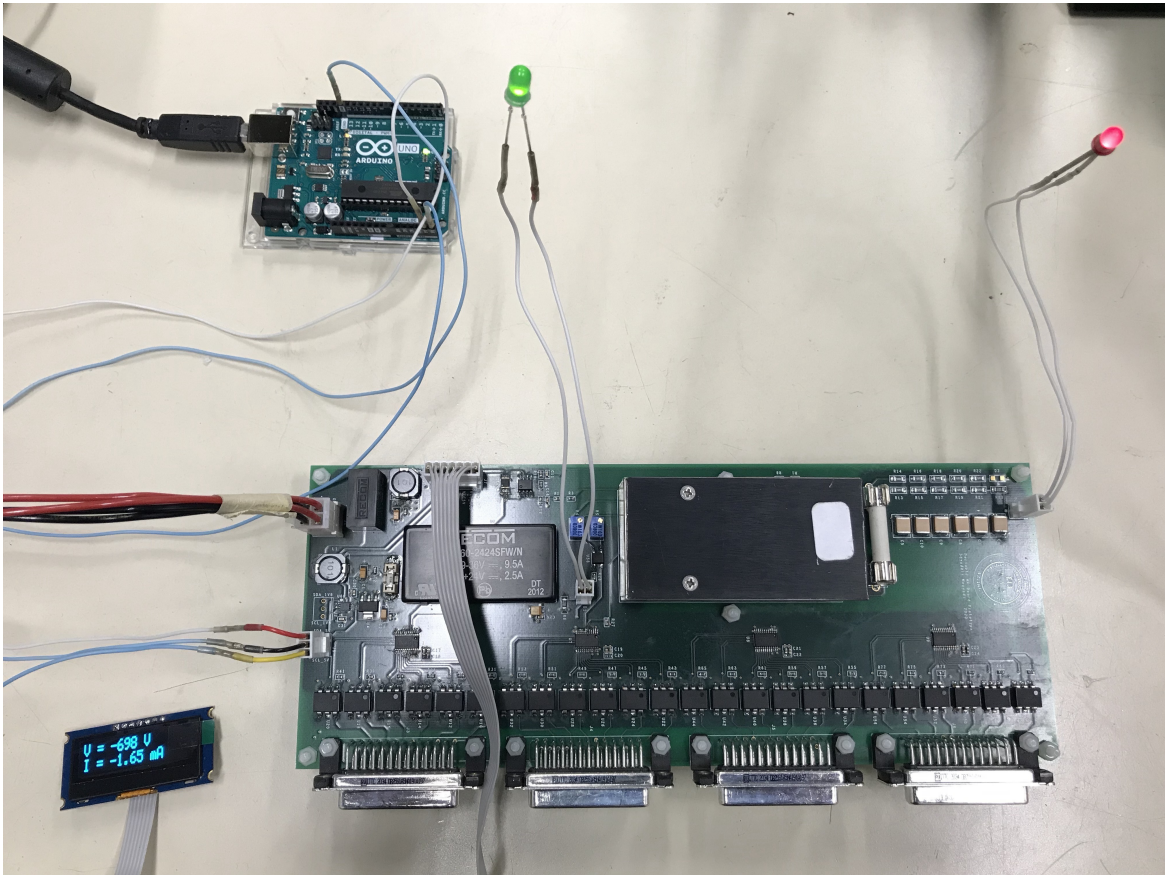


Fig. 3.5 High Voltage Power Supply. Image taken by the author of this thesis.

stand, SD test stand, and PROMETEO tests, a portable and configurable LV power supply is essential. This section details the solutions implemented for both LV and HV power delivery.

For LV power, the ROAL RCB1200 series [106] was chosen as a suitable option due to its high-density configuration with eight independent channels, each capable of providing adjustable voltage. These channels use output module B, a specific module within the RCB1200 series that enables voltage adjustment within the range of 4.5 to 15 V, delivering up to 150 W per MD. This configuration closely replicates the real-world operating conditions of the SDs tested (see Fig. 3.4). Therefore, a portable 8 output power supply with 10 Vdc and 10 A per channel was considered optimal for LV power delivery during TileCal testing.

3.3.2 Portable High Voltage Power Supply

A dedicated High Voltage Power Supply (HVPS) (see Fig. 3.5) has been developed specifically for the Prometeo, capable of delivering up to 900 V for powering PMT-Blocks. The HVPS

board is constructed as a four-layer entity, measuring 10 cm by 25 cm. Four HV DB-25 connectors efficiently distribute high voltage to individual MDs.

The HVPS itself is powered by a readily available 12 V (Advanced Technology Extended (ATX)) power supply. For operational control, the I²C protocol (Inter-Integrated Circuit) is used, which facilitates communication with the CPM or other I²C-capable processors. In simpler terms, the I²C protocol allows the CPM to send control signals to the HVPS board, enabling functions such as voltage adjustments and power management. Additionally, the HVPS incorporates an LCD display for real-time voltage and current monitoring. To ensure compatibility between different voltage standards, the HVPS board includes a voltage translator, enabling seamless I²C communication with both 5 V and 3.3 V systems.

3.3.3 LED driver card and LEDs

The LED driver card is a crucial component of the PROMETEO system, responsible for testing the functionality of PMT blocks. Physically connected to the CPM and controlled by PROMETEO software, it operates on the basis of the Kapustinsky LED Pulser circuit [107]. This circuit, characterised by its simplicity and 20 ns operating range, forms the basis for the new LED driver design.

3.3.4 Readout System: CPM and Mini-Carrier

The PreProcessor (PPr) Demonstrator module, integral to the first version of the PROMETEO system, is designed for single TileCal module readout and operation. On the contrary, the second version will use a CPM capable of handling up to two TileCal modules, as shown in Fig. 3.6. The CPM acts as the central readout unit for the final PPr system in the ATLAS Tile Phase II Upgrade. Each PPr module comprises an Advanced Mezzanine Card hosting an Xilinx UltraScale KU115 FPGA with 48 GTH transceivers (Gigabit Transceiver for High-Speed) and six Samtec FireFly optical modules. High-quality clock recovery is achieved through a Silicon Labs SI5345 jitter cleaner, which feeds the high-speed transceivers responsible for communication with on-detector electronics.

3.3.5 Readout and configuration

Tests are conducted from an external computer, interfacing with either the PPr Demo or CPM via a Gigabit Ethernet (GbE) port utilising the IPbus protocol. Fig. 3.7 shows a firmware block diagram implemented in the PROMETEO PPr Demonstrator for the operation of the

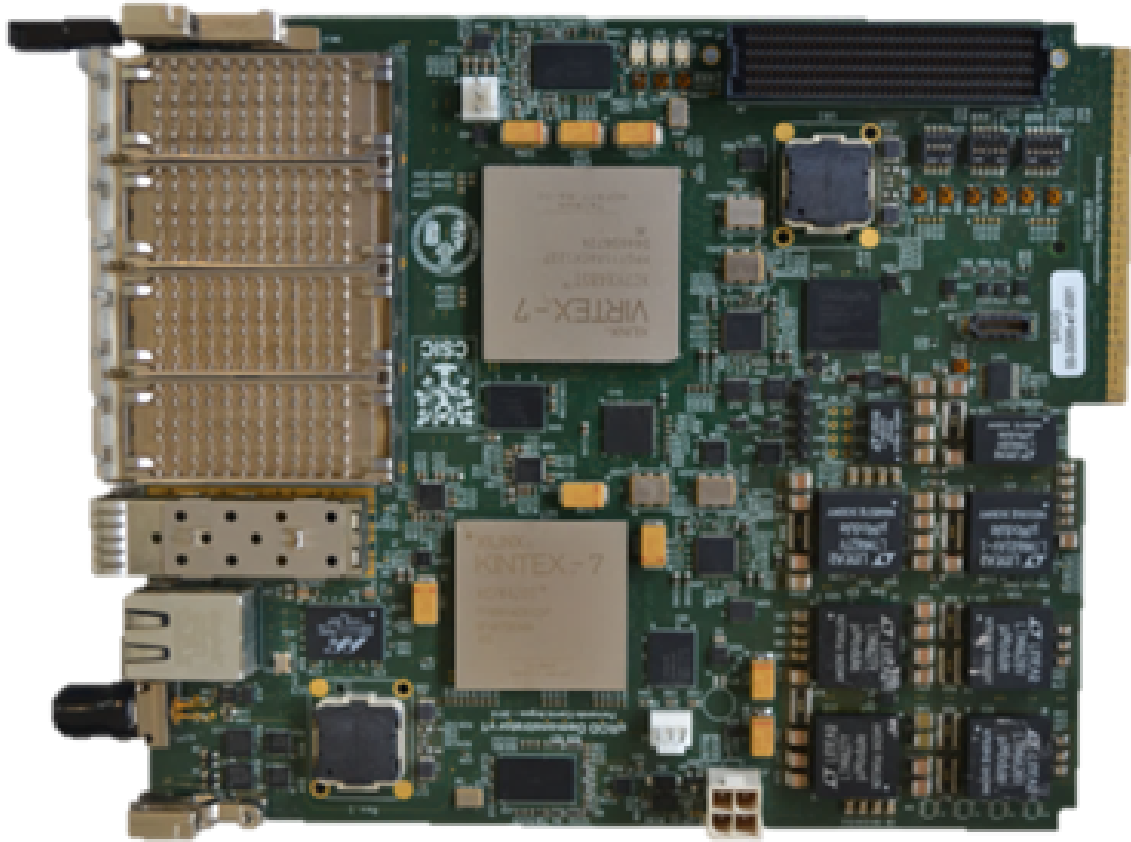


Fig. 3.6 Compact Processing Module version 2. Image developed by Fernando from TileCal community, not published.

PROMETEO system. The PPr Demonstrator uses 16 bidirectional high-speed links, adhering to the GigaBit Transceiver (GBT) protocol, for communication between the FE electronics and itself. It receives configuration and trigger commands from the PROMETEO software through a GbE port. These commands, which are aimed at configuring the FE electronics, are decoded in the Virtex 7 FPGA and transmitted via downlinks. Furthermore, PROMETEO software sends specific test commands to PPr to control and configure the LVPS, HVPS, and LED systems through I²C ports. In terms of data readout, the Virtex 7 FPGA continuously acquires event data for each bunch crossing via uplinks (16 per TileCal module). In addition, it extracts integrator, monitoring and data samples from the input GBT stream, timestamping them with the corresponding bundle crossing identifier. PMT data samples are stored in 96 pipeline memories, one for each gain and channel, with a depth of 12.8 μs . When receiving an internal trigger acceptance signal from the PROMETEO software, the selected events are extracted from the pipelines and transferred via the GbE port to the external computer where the PROMETEO software is executed.

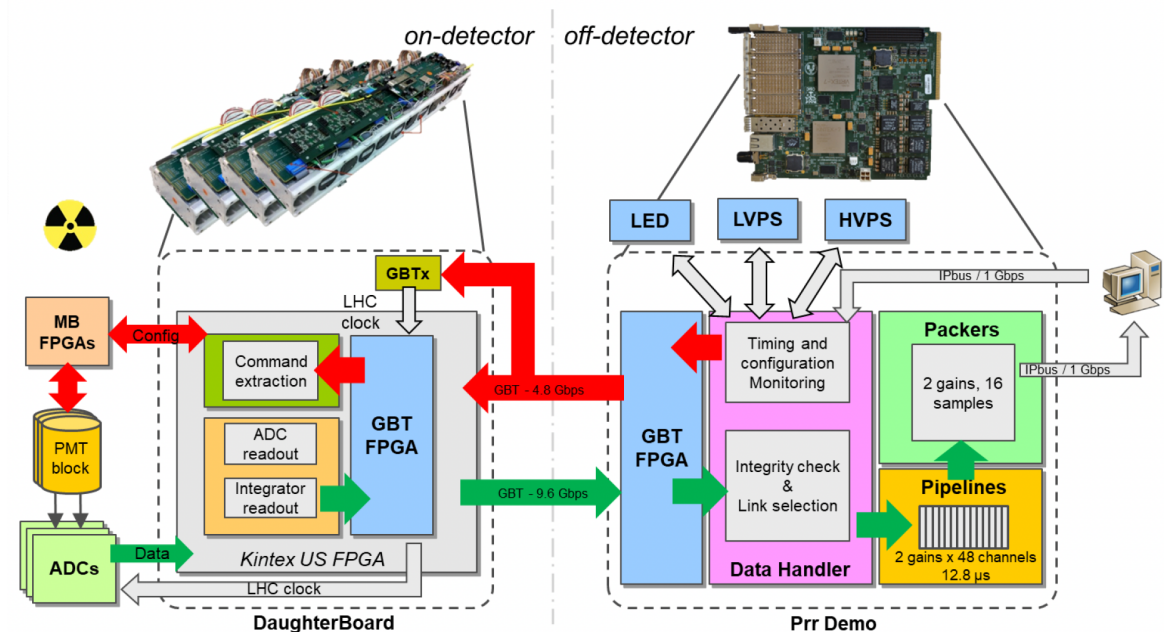


Fig. 3.7 Block diagram of the main firmware blocks used for the PROMETEO system. Image developed by Fernando from TileCal community, not published.

3.3.6 The PROMETEO Software

The PROMETEO Web interface as shown in Fig. 3.8 is the primary software used to perform certification tests and visualise their results. This interface operates on a client-server model, where PROMETEO functions as the server. Communication occurs through a VHDL module (Very High Speed Integrated Circuit (VHSIC) Hardware Description Language) over Ethernet, which supports the IPbus protocol [108]. The client, using a modular framework with panel plug-ins for specific MD tests, connects via UDP. This client-driven architecture grants direct control over the server's functionalities, allowing for on-the-fly modifications. The interaction between the software and the server via the IPbus protocol facilitates read and write tasks on designated memory addresses or FIFO memory [108]. The firmware maintains a list of registers, allowing for the configuration of commands, status, data position, sample count, calibration parameters, and other crucial elements. The system performs various tests targeting potential malfunctioning components. These assessments are vital for identifying defects in components such as PMTs, DACs, ADCs, or issues in interconnections and power supplies.

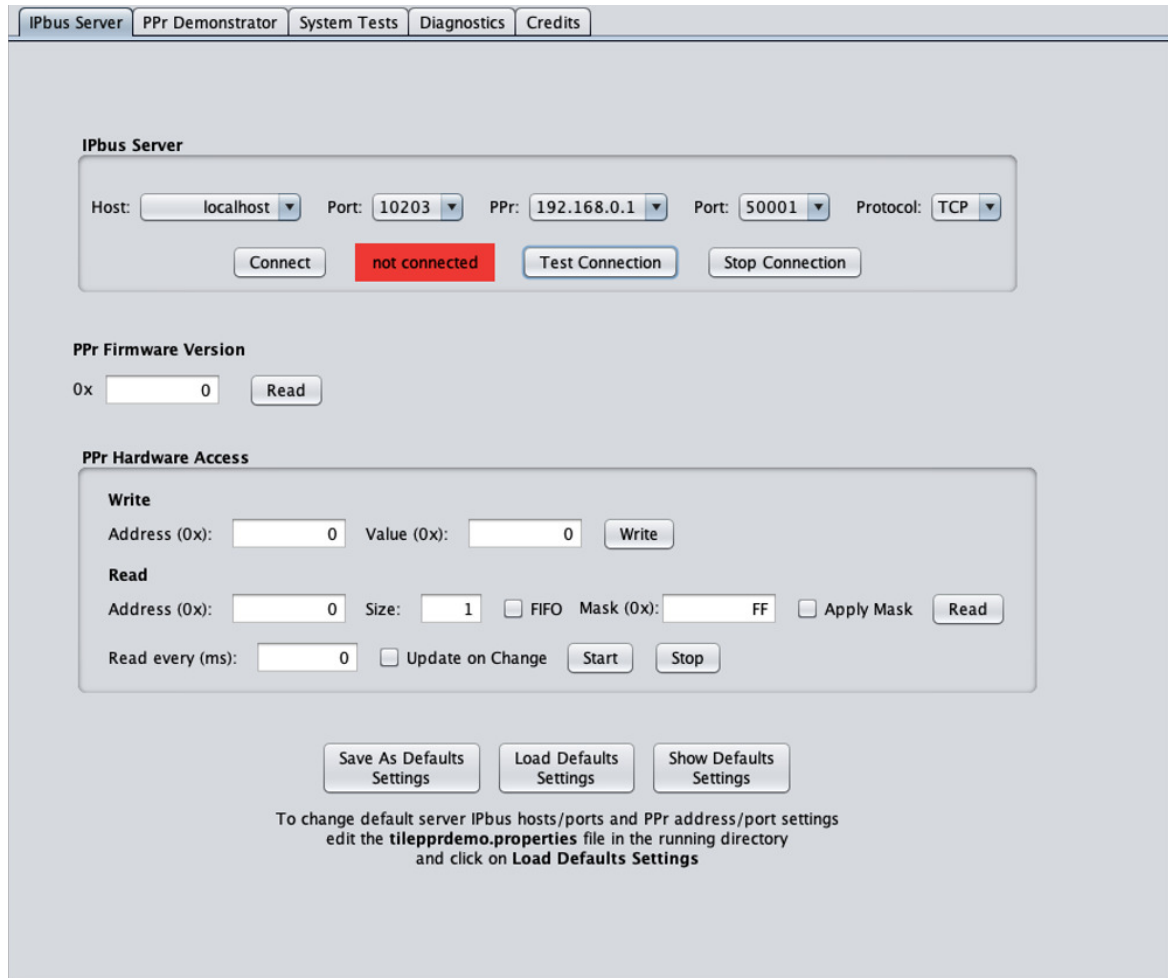


Fig. 3.8 PROMETEO Graphical User Interface (GUI). High Voltage Power Supply. Image taken by the author of this thesis.

3.3.7 IPBus Server

IPbus software is implemented in C++ and provides a Python extension for enhanced scripting capabilities, often used to develop new tests. Alternatively, users can employ the Java Graphical User Interface (GUI) (Fig. 3.8) to manage interactive test results. Both the C++ core and the Python extension are platform-independent, while the Java GUI is compatible with all operating systems. At its core, the software comprises algorithms that transform IPbus protocol commands into functions for MD testing. Users can test MD communication, manipulate FE cards, LEDs, and HV power, and store/retrieve data from FIFO or address-specific memory. In particular, the Integrator tests for the new system have been redeveloped, and the results are presented in Section 3.4.

3.4 System Tests

Integrator

The integrator is printed on a circuit board that is connected to the Front End board for the New Infrastructure with Calibration and signal Shaping (FENICS). FENICS is the very front-end board that shapes and preamplifies the PMT signals. In addition to the integrator, this board contains a fast digital signal processor for processing collision events of interest in physics, and it delivers a portion of the ATLAS Level 1 Calorimeter trigger signals. A panel for the integrator, as shown in Fig. 3.9, has been added and tested on the PROMETEO GUI. The total number of gains added to this panel is six, but only the results for Gain 2 are shown in panel (G2). This test was carried out on MD 1, and the 12 channels produced consistent results. This was then repeated for Gain 2 and the remaining three min-drawers, for which no deviations were found. To avoid saturation, the integrator gain can be selected by choosing one of six pre-configured resistors that also specify the integration time. The user can set the frequency, sample number, MD to read, gains, and events for each measurement step using this panel. The six gains were tested, and no discrepancies were detected.

Charge Injector System (CIS) Linearity

The CIS calibration system is based on injecting known charge values into the readout electronics through dedicated capacitors and a 4096 DAC controlled by the ADC. This simulated physics signal establishes the relationship between the peak response amplitude (ADC counts) and the injected charge (pC), calibrating each ADC in units of ADC counts/pC. This calibration facilitates the verification and identification of errors in the readout chains, allowing individual calibration of single ADC outputs for each PMT within every 3-in-1 module. Therefore, the CIS linearity panel, specifically tests the linearity of the charge injection process. This test verifies the presence of a pulse within predefined bands for both low- and high-gain settings. Users can configure the charge value, sampling number, MD, and BC to be read, gain settings, and the number of events for each measurement step through this panel.

LED Shape

The PROMETEO LED Driver submodule, described in Section 3.2, plays a crucial role in evaluating the functionality of PMT blocks. This functionality is assessed through the integration and testing of an LED Shape panel shown in Fig. 3.10 on the GUI. The panel,

powered by an LED driver, allows for the evaluation of light injection across 12 PMT blocks. Adjustable LED voltage (5-30 V) allows for light intensity modulation. System testing included high- and low-gain (LG) settings. The LG data for MD 1, which encompasses 11 tested channels, are displayed on the panel. In particular, no inconsistencies were observed during the LED Run test.

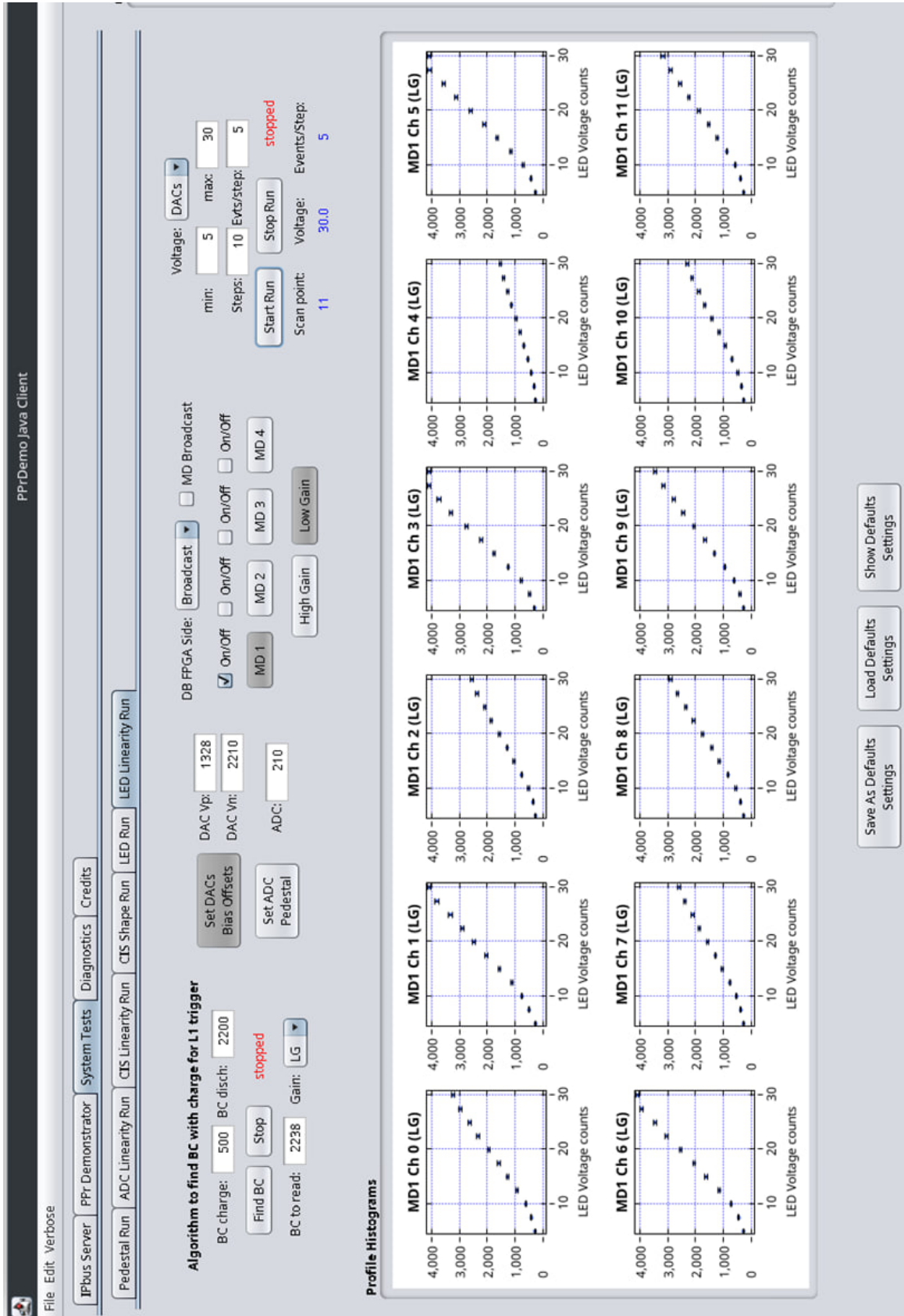


Fig. 3.9 Results of the Integrator Panel installed in the PROMETEO GUI [109]. The Y-axis represents the ADC counts. High Voltage Power Supply. Image taken by the author of this thesis.

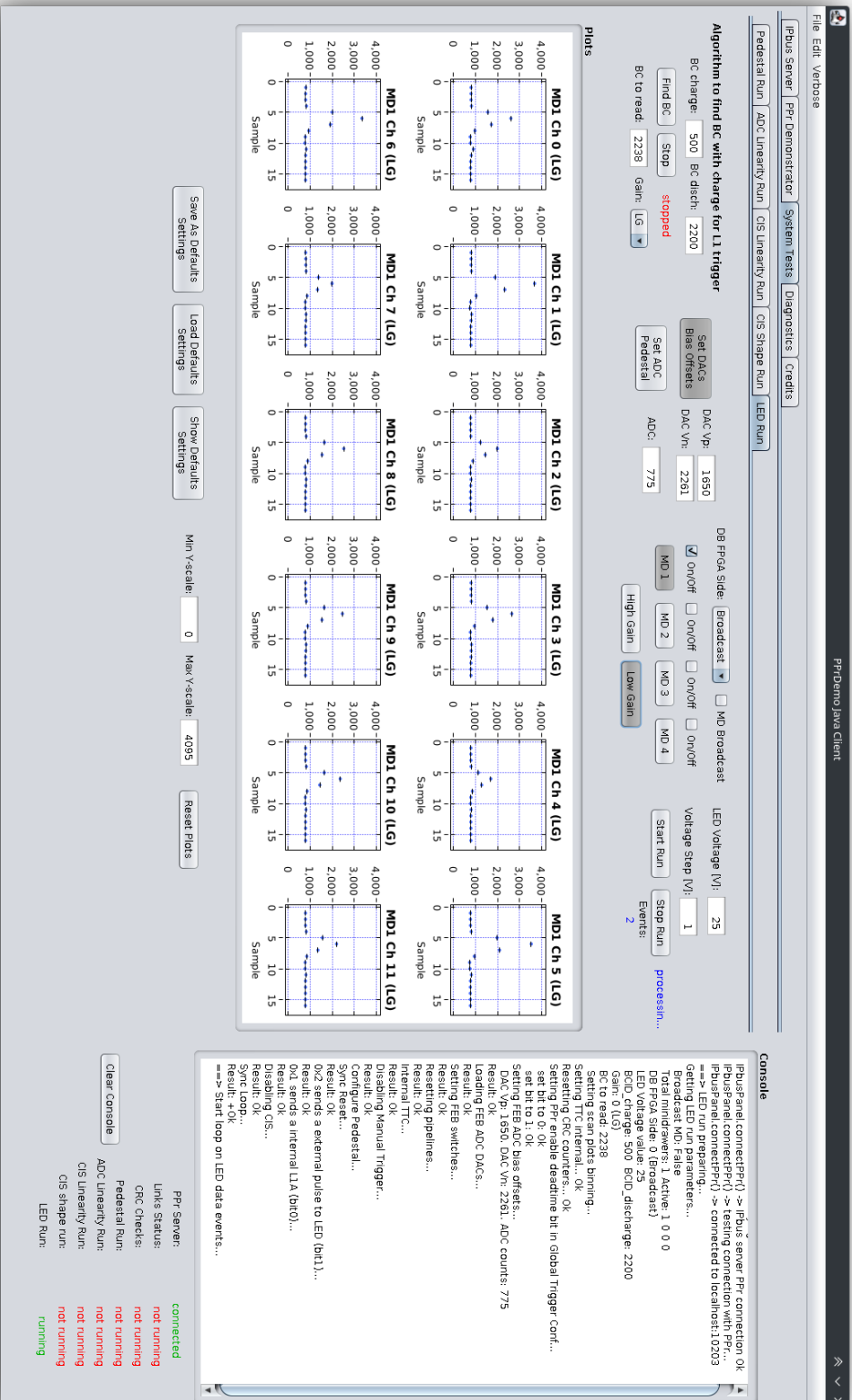


Fig. 3.10 LED Shape Panel. The Y-axis represents the ADC counts. High Voltage Power Supply. Image taken by the author of this thesis.

Chapter 4

Physics Object Reconstruction

The analysis presented in this thesis aims to identify the presence of a heavy scalar within the 4 lepton final state, which requires the reconstruction of both electrons and muons. This reconstruction is based on the selection of events.¹ These selected events are then subjected to a process known as reconstruction, in which raw detector signals are transformed into identifiable "physics objects" for further analysis. The details of this reconstruction procedure will be elaborated on in subsequent sections.

Inkonyana ikhethwa kusakhanya.

E.W.M Mesatywa.

4.1 Electron

4.1.1 Electron Reconstruction

The energy deposits in the ECAL are used to identify electrons. These deposits are grouped into clusters based on their topological connectivity within the ECAL and neighbouring hadronic calorimeters. To be classified as an electron, each cluster must be associated with at least one ID track. It is important to note that the clustering algorithm used has evolved since Run 1. Notably, Run 1 employed a fixed-size "sliding-window" technique, as detailed in Ref. [110]. In contrast, Run 2 has adopted a more sophisticated approach based

¹The ensemble of particles produced in the final state after every proton collision is called an event.

on topological cell clustering. This method offers a key advantage: the ability to capture low-energy bremsstrahlung photons and, through their association with the parent electron or converted photon, form larger "super-clusters." A comprehensive description of the current algorithm can be found in Ref. [111].

A new technique is used to reconstruct electron trajectories using a method based on dynamic clustering of topological cells. This method significantly improves the precision of electron energy measurements, particularly for electrons emitting bremsstrahlung photons. Detailed information on these changes can be found in Ref. [112]. Electrons are selected with a p_T exceeding 4.5 GeV and η less than 2.47. This relaxed selection ("loose" working point) ensures a high efficiency in identifying genuine electrons: exceeding 90% for $p_T > 30$ GeV and reaching around 96% for $p_T > 60$ GeV, as documented in Ref. [112].

4.1.2 Electron Identification

Electron candidates reconstructed from energy deposits in the calorimeter require further discriminatory measures to distinguish them from backgrounds such as hadronic jets and converted photons [113]. The key variables for this differentiation include hits in the silicon detectors, particularly the innermost layers such as the Insertable B-Layer (IBL) and a likelihood discriminant based on the distribution of high-threshold hits in the TRT tracker. Heavy-flavour backgrounds arise from particles containing heavy quarks, such as charm or bottom quarks. These backgrounds are significant because heavy-flavour quarks can produce secondary particles that mimic electron signals in the detector. For instance, bottom quarks (b-quarks) can decay into hadrons and leptons, including electrons, which then contribute to the background. Additionally, the longer lifetimes of heavy-flavour hadrons mean they can travel some distance from the collision point before decaying, complicating the identification process. To improve the rejection of heavy-flavour backgrounds, two additional variables have been incorporated into the likelihood function: the transverse impact parameter ($|d_0|$) and its significance ($|d_0|/\sigma_{d_0}$). The transverse impact parameter measures the distance of closest approach of the track to the primary vertex in the plane transverse to the beamline, while its significance normalizes this distance by its uncertainty, providing a more robust measure.

These variables are crucial because tracks from heavy-flavour decays typically have larger impact parameters compared to tracks from primary electrons originating directly from the interaction point. By incorporating these variables, the likelihood function can more effectively distinguish genuine electrons from those arising from heavy-flavour decays.

These variables are combined into working points (WPs) [114, 115] to optimize the trade-off between signal efficiency and background suppression. Three levels of identification, LooseLH, MediumLH, and TightLH, are defined based on their respective signal electron efficiencies at 100 GeV for E_T : 96%, 94%, and 90% [114]. The $H4\ell$ analysis, presented in Chapter 5, uses a loose working point (WP) with a p_T -dependent efficiency ranging from 90% at 20 GeV to 96% for p_T above 60 GeV.

The resolution of electron candidates is another critical parameter in their identification. In the central region of the detector, the electron energy resolution is significantly influenced by the performance of the EM calorimeter and the precision of the track-cluster matching. For electrons with $E_T > 7$ GeV and $|\eta| < 2.47$, the resolution is optimised using sophisticated algorithms that balance the contributions from the calorimeter and tracking detectors. According to Ref. [111], the electron energy resolution achieves an accuracy of approximately 1-2% for high-energy electrons, with some dependence on the pseudo-rapidity and energy of the electron.

4.2 Muon

4.2.1 Muon Reconstruction

During pp collisions at the LHC, muons arise primarily from the decay of top-quark-antiquark pairs ($t\bar{t}$) and the decay of W and Z bosons. Muons possess unique properties. Notably, they deposit minimal ionisation energy within the calorimeter, allowing them to pass through it and reach the dedicated muon spectrometer. While they leave tracks in the detector, they are not trapped within its volume due to their minimal interaction with matter. The identification process of these muons involves the integration of track candidates, which are formed independently in both the muon spectrometer (MS) and the inner detector (ID), as detailed in the reference literature [116]. This process is crucial for the reconstruction of muon objects. The ATLAS detector is specifically designed to accurately identify muons and precisely measure their momenta. To be considered within the detector acceptance range, muon candidates must have an η less than 2.5. The detector uses four distinct identification WPs: "VeryLoose," "Loose," "Medium," and "Tight." The 4ℓ analysis, in particular, employs the "Loose" WP, achieving an efficiency of 98.5%. The amalgamation of MS and ID tracks is facilitated through various algorithms, resulting in four categorisations of muons, as explained in subsequent references [117, 116]:

- The combined muons originate from both ID and MS tracks. A global fit is applied to these tracks, beginning in the MS and extending back to the ID, to form the combined track.
- Segment-tagged muons are initially ID tracks, which are designated as muon tracks if they align with at least one local track segment in the Monitored Drift Tubes or Cathode Strip Chambers within the MS. These are typically used when muons do not traverse the entire MS due to a lower p_T or a trajectory through regions of the MS lacking instrumentation.
- Calorimeter-tagged muons are characterised by the absence of muon hits on the muon spectrometer. Instead, these are ID tracks correlated with energy deposits in the calorimeters, indicative of a minimally ionising particle. They are used primarily in analyses covering regions where MS instrumentation is limited, specifically at $|\eta| < 0.1$.
- Extrapolated or Stand-Alone muons rely solely on track candidates from the MS. These tracks are loosely required to originate from the interaction point and are used in the $2.5 < \eta < 2.7$ range, a region not covered by the ID, thus extending the acceptance of muon reconstruction.

Recent improvements in muon reconstruction algorithms, as detailed in Ref. [118], help minimise the number of incorrectly identified tracks. The chosen "loose" muon identification criteria ensure that at least 98% of genuine muons with a p_T of 5 GeV are correctly identified. This efficiency improves further to 98.5% for muons with even higher p_T values as reported in Ref. [118].

4.2.2 Muon Identification

Muons are differentiated into prompt and non-prompt categories based solely on their origin, while maintaining high acceptance rates for prompt muons. This distinction plays a crucial role in suppressing background contributions. A small difference between the momentum-to-charge ratio (q/p) measured in the Inner Detector (ID) and the Muon Spectrometer (MS) is a key criterion for background rejection, expressed as follows:

$$\frac{|q/p_{ID} - q/p_{MS}|}{\sqrt{\sigma_{ID}^2 + \sigma_{ME}^2}} < 7. \quad (4.1)$$

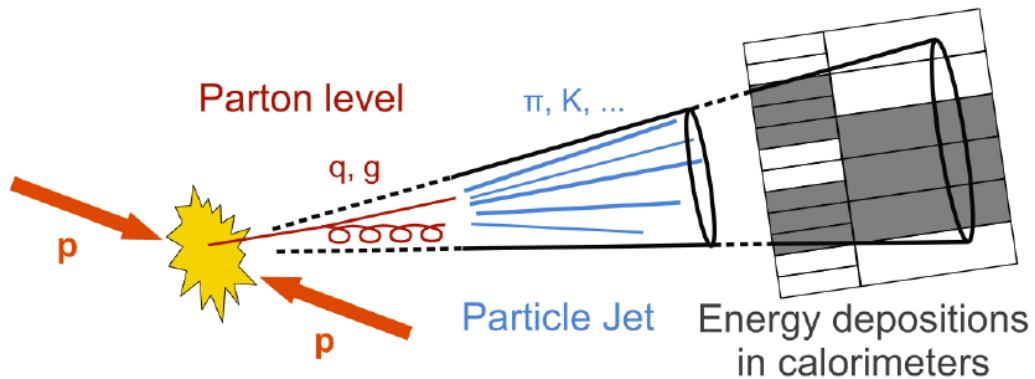


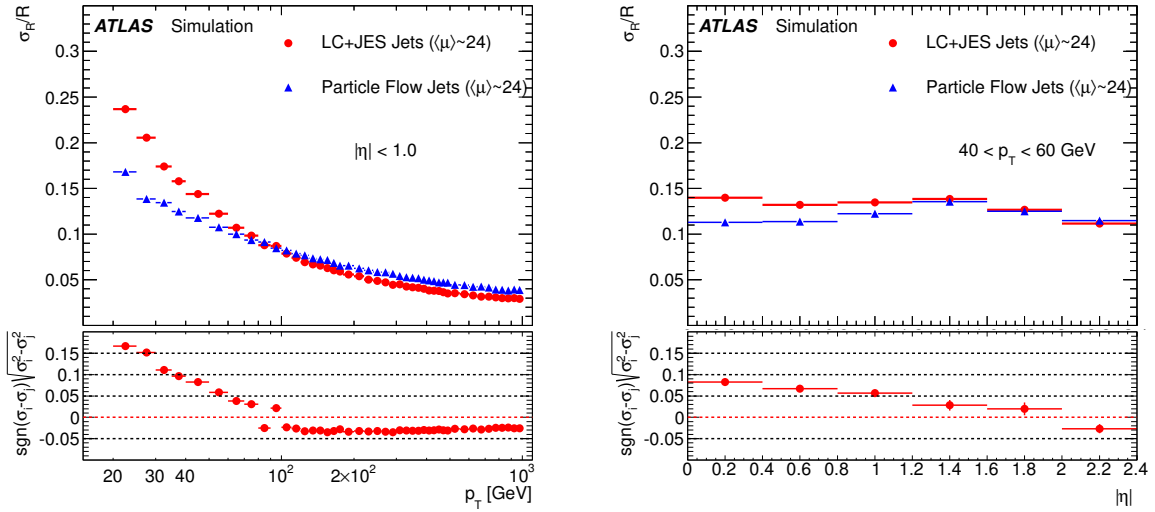
Fig. 4.1 Sketch of pp -collision and resulting collimated spray of particles, a jet. Taken from Ref. [119].

In this context, σ_{ME} refers to the variance of the measurement of the momentum-to-charge ratio for extrapolated muons (ME). These muons are reconstructed on the basis of only the MS track and a loose requirement on compatibility with the originating from the interaction point (IP). The parameters of the muon track are defined in the IP, accounting for the estimated energy loss in the calorimeters. Generally, the muon must traverse at least two layers of MS chambers, with three layers required in the forward region. ME muons extend the acceptance for muon reconstruction into the region $2.5 < |\eta| < 2.7$, which is not covered by ID.

This selection is implemented through a set of quality requirements tailored to each type of muon. Non-prompt muons originate from in-flight decays of charged hadrons, primarily pions and kaons, often leading to discrepancies between their track parameters in the ID and MS. This high performance is achieved through a "Loose" muon identification category, encompassing both "medium" muons and those identified using the calorimeter (calo-tagged) or inner tracker segments (segment-tagged) in the forward region ($\eta < 0.1$) where tracking is limited.

4.3 Jets

Building on previous research [120, 121], particle collisions create fundamental particles called partons (quarks and gluons). These invisible entities cannot be directly observed because of their strong interaction with other particles and their inability to exist independently (colour confinement). As a result, they rapidly transform into a spray of visible particles called hadrons. At high energies, these hadrons tend to travel in narrow, cone-shaped



(a) The jet transverse momentum resolution as a function of p_T for jets with $|\eta| < 1.0$.

(b) The jet transverse momentum resolution as a function of $|\eta|$ for jets with $40 < p_T < 60$ GeV.

Fig. 4.2 The jet transverse momentum resolution as determined in dijet MC events for calorimeter jets and particle flow jets. Simulated pile-up conditions are similar to the data-taking in 2012. Taken from Ref. [123].

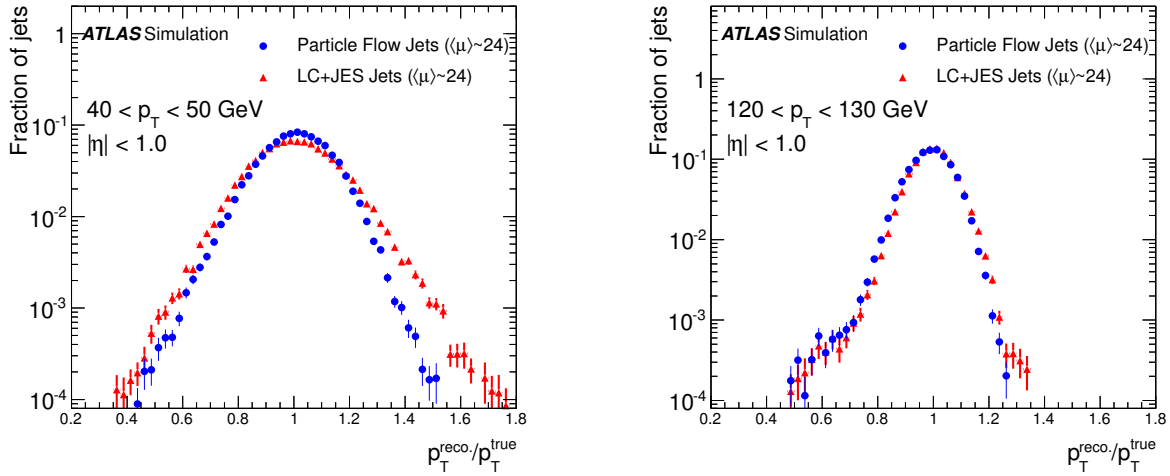
regions, known as jets. Although jets primarily deposit their energy within the dedicated HCAL, in contrast to the typically point-like deposits of electrons in the electromagnetic calorimeter, this analysis employs the "anti- k_T algorithm" [120] implemented in the widely used software FastJet [122] for jet reconstruction. This algorithm takes advantage of signals from individual detector cells with positive energy as its starting point. In this specific analysis focused on final states with four leptons, jets must have a minimum transverse momentum exceeding 30 GeV and must be detected within a specific angular region defined by pseudorapidity less than 4.5. In addition to reconstructing jets, we also search for jets containing "bottom quarks" (b -quarks), known as b -jets. A multivariate algorithm [113] is used for this identification. These b -jets are crucial for various measurements, including studies of top quark physics and the decay of the Higgs boson to b -quarks. The jets were reconstructed using the anti- k_t algorithm with a radius parameter of 0.4, followed by corrections to calibrate them to particle-level energy scales. These objects form the basis for subsequent jet analyses. The reconstructed jets were subjected to further refinements. Their four momenta were corrected for various factors, including calorimeter response and pile-up effects [124]. Furthermore, only jets with a significant p_T that is greater than 30 GeV and pseudo-rapidity within the detector coverage ($|\eta| < 4.5$) were considered. Pile-up contamination within $|\eta| < 2.5$ was minimised using a dedicated jet-vertex tagger technique [125, 126]. Events

were required to have at least one reconstructed vertex with two or more associated tracks, each exceeding $p_T > 500$ MeV, to ensure good quality tracking and reduce ambiguity. The primary vertex, defined by the highest sum of associated track momenta (p_T^2), was used for further analysis. Overlaps between leptons and jets were addressed by prioritising muons over electrons when sharing the same track, particularly for combined or extrapolated muons. Finally, to minimise ambiguities, jets within a cone of radius $\Delta R = 0.24$ around electrons and $\Delta R = 0.1$ around muons were removed, reflecting their respective spatial resolutions.

The largest expected benefit of using particle flow reconstruction as input to jet-finding is an improvement in the jet energy and angular resolution for low- p_T jets. The jet resolution achieved with particle flow methods is compared with that attained using standard calorimeter jet reconstruction. The relative jet transverse momentum resolution for particle flow and calorimeter jets is shown as a function of jet transverse momentum and pseudo-rapidity (see Figure 4.2). Particle flow jets perform better than calorimeter jets at transverse momenta of up to 90 GeV in the central region, benefiting from the improved scale for low- p_T hadrons and intrinsic pile-up suppression. However, at high transverse momenta, the particle flow reconstruction performs slightly worse than the standard reconstruction due to the dense core of a jet posing a challenge to tracking algorithms and the degree of confusion during the cell subtraction stage. However, particle flow jets do not introduce significant tails in the response at low or high p_T , demonstrating their reliability in maintaining jet resolution.

In addition to improving the p_T resolution of the jets, the particle flow algorithm is expected to enhance the angular resolution of jets. This improvement is attributed to three key effects. First, using tracks to measure charged particles results in significantly better angular resolution for individual particles than the resolution obtained using topological clusters because the tracker's angular resolution is superior to that of the calorimeter. Second, the four-momentum track can be determined at the perigee, before the charged particles have spread out by the magnetic field, thus improving the ϕ resolution for the jet. Third, the suppression of charged pile-up particles should also reduce mismeasurements of the jet direction. At low p_T , where these effects are most significant, improvements are observed in both η and ϕ resolutions (see Figure 4.3).

Figure 4.3 shows the angular resolution in η and ϕ as a function of the reconstructed jet transverse momentum for particle flow and calorimeter jets. It is determined from the standard deviation of a Gaussian fit over $\pm 1.5\sigma$ to the difference between the values of η and ϕ for the reconstructed and matched truth jets in the central region. At low p_T , significant improvements are seen in both η and ϕ resolutions for particle flow jets compared



(a) The jet transverse momentum response distribution as determined in dijet MC events for calorimeter jets in the $40 < p_T < 50$ GeV bin. Simulated pile-up conditions are similar to the data-taking in 2012.

(b) The jet transverse momentum response distribution as determined in dijet MC events for particle flow jets in the $120 < p_T < 130$ GeV bin. Simulated pile-up conditions are similar to the data-taking in 2012.

Fig. 4.3 The jet transverse momentum response distribution as determined in dijet MC events for calorimeter jets and particle flow jets. Two different p_T bins are shown: (a) $40 < p_T < 50$ GeV and (b) $120 < p_T < 130$ GeV. Simulated pile-up conditions are similar to the data-taking in 2012. Image taken from [123]

to calorimeter jets, demonstrating the improved performance of the particle flow algorithm in maintaining accurate jet direction measurements.

4.4 The Missing Transverse Momentum

In the LHC, when protons collide, the tiny particles inside them (partons) are assumed to travel directly towards each other, with their motion confined to the path of the beams. In an ideal world, the total momentum of the particles after a collision should be perfectly balanced in all directions. However, limitations in our detectors and the existence of invisible particles like neutrinos make directly measuring this balance impossible. This is why, after a collision, the missing momentum is not zero and shows up as a quantity called missing transverse energy, or E_T^{miss} [127].

The transverse plane is used in these measurements because it is perpendicular to the beam axis. Since the initial momentum along the beam axis is not precisely known due to the partonic structure of the proton, focusing on the transverse plane eliminates uncertainties

associated with the longitudinal components. Technically, E_T^{miss} is the amount of energy "missing" in the collision, calculated by adding the transverse momentum (p_T) of all particles detected in the event and then flipping the sign (making it negative). This equation is shown below:

$$E_T^{\text{miss}} = \left| \sum_{i=1}^{N_{\text{objects}}} \vec{p}_{T,i} \right|. \quad (4.2)$$

This discrepancy arises from various factors that influence the total p_T . In particular, neutrinos, which interact only through the weak force, escape detection. They traverse the detector without leaving tracks or energy deposits, their presence being inferred only from the imbalance in final-state energy. Component-wise, this imbalance can be measured as:

$$\begin{aligned} E_{x(y)}^{\text{miss}} &= E_{x(y)}^{\text{miss},e} + E_{x(y)}^{\text{miss},\gamma} \\ &\quad + E_{x(y)}^{\text{miss},\tau} + E_{x(y)}^{\text{miss},\text{jets}} \\ &\quad + E_{x(y)}^{\text{miss},\mu} + E_{x(y)}^{\text{miss},\text{soft}}. \end{aligned} \quad (4.3)$$

Each term $E_{x(y)}^{\text{miss},i}$ (where i represents electrons, photons, taus, jets, or muons) quantifies the missing energy associated with the respective object. Additionally, $E_{x(y)}^{\text{miss},\text{soft}}$ captures the soft term, reconstructed from p_T of tracks not associated with any hard objects but originating from the primary vertex. Accurate determination of E_T^{miss} requires careful calibration of all contributing objects.

An important measure for the quality of the E_T^{miss} reconstruction is the resolution. For $Z \rightarrow \ell\ell$ events, the p_x^{miss} and p_y^{miss} are approximately Gaussian-distributed around zero, except for events with very large $\sum p_T$ or noise. To understand the impact of pile-up on p_T^{miss} resolution, Figure 4.4 shows the p_x^{miss} and p_y^{miss} resolutions in MC simulations satisfying the $Z \rightarrow \mu\mu$ selection, binned in the variables N_{PV} and μ . The resolution degrades as the amount of pile-up increases, but improves significantly as events containing jets are vetoed. Figure 4.5 illustrates the resolution dependence on different working points for MC simulations that satisfy various selections, indicating that tighter working points effectively reduce the contamination of fake p_T^{miss} . These figures confirm that the p_T^{miss} resolution in the MC simulation represents the data well, with resolutions that agree within error bands that include the statistical, luminosity and detector uncertainties of the MC.

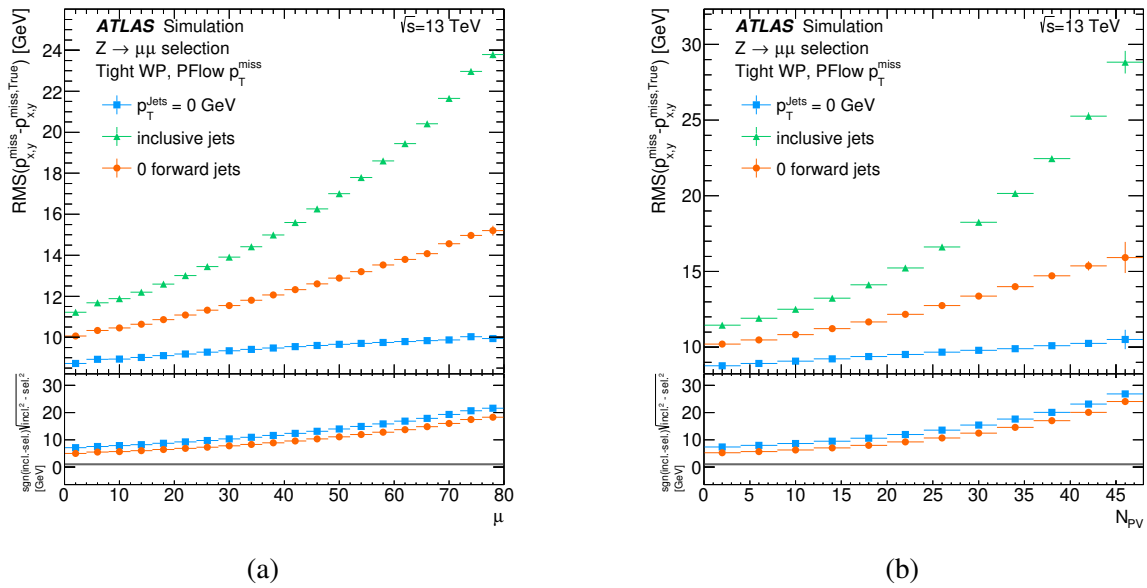


Fig. 4.4 The resolutions of p_x^{miss} and p_y^{miss} are depicted for various jet selections and p_T^{miss} working points (WPs). The analysis employs flow jets and the *Tight* p_T^{miss} WP, based on SM MC simulations, specifically using SHERPA for the $Z \rightarrow \mu\mu$ event generation with the corresponding selection applied. The error bars represent the statistical uncertainty of the MC. The lower panels' y-axis labels use 'incl.' for inclusive jet selection, 'sel.' for the specific jet selection being analysed and 'WP' for the working point. 'True' denotes quantities derived from MC simulations. Taken from [128].

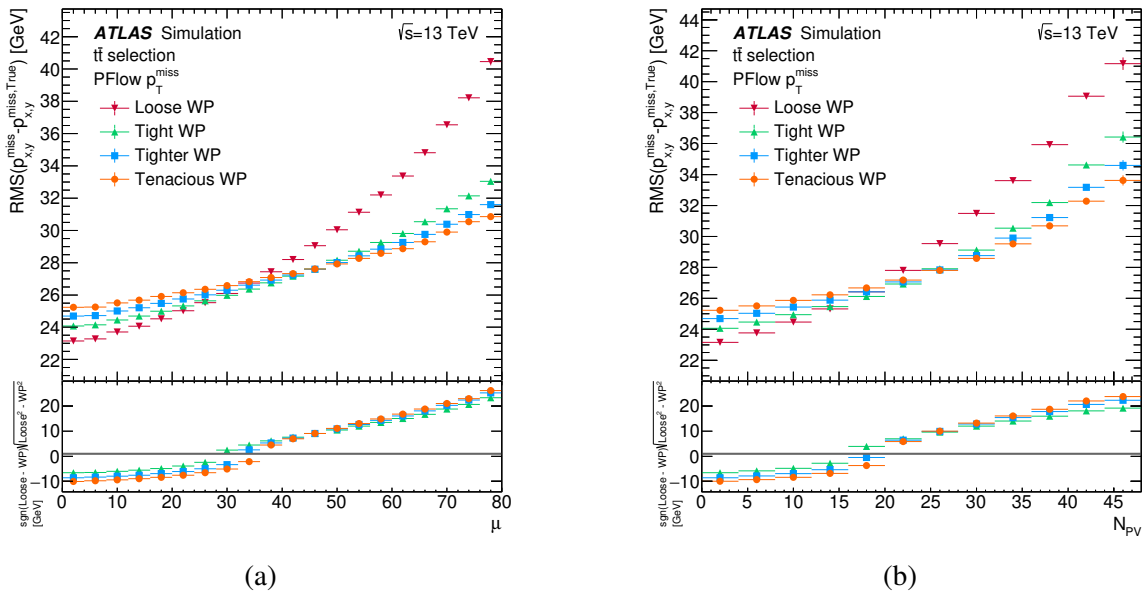


Fig. 4.5 The p_x^{miss} and p_y^{miss} resolution for different p_T^{miss} working points as a function of μ in 4.5a or N_{PV} in 4.5b. A $t\bar{t}$ selection is applied in 4.5a and 4.5b. PFlow jets are used. The error bars include the statistical uncertainty of MC. In the y-axis label of the lower panels, 'incl.' refers to the inclusive jet selection, 'sel.' to the alternate jet selection under consideration and 'WP' to the working point under consideration. 'True' refers to MC-generated quantities. Taken from [128].

Chapter 5

Event Classification and Background

Modelling in search for $H \rightarrow ZZ \rightarrow 4\ell$

This chapter focuses on a critical aspect of the analysis: the categorisation of events and the identification of background contributions for the decay channel of a heavy Higgs boson (H) into two Z bosons, leading to the 4ℓ final state. It begins with an in-depth analysis of the 4ℓ final state channel in Section 5.1. The subsequent Section 5.2 elaborates on the data and simulation techniques utilised. This study relies heavily on accurate reconstruction of muon and electron objects as well as on the construction of physical events. Section 5.4 delves into the details of the performance and efficiency studies for electrons and muons. Section 5.5 provides a systematic description of the selection criteria used to identify events of interest. Section 5.6 investigates the effects of pile-up on leptons, highlighting significant contributions made in this area. The manuscript concludes with Section 5.7, which thoroughly investigates electron isolation, underscoring the author's pivotal role in this essential element of the research.

Isiziba siviwa ngodondolo.

E.W.M Mesatywa.

5.1 Analysis Overview

The approach used to choose events and estimate the background in the $H \rightarrow ZZ \rightarrow 4\ell$ decay channel is described in this section. These methodologies are crucial for characterising the Higgs boson, including its mass, off-shell signal strength, and interactions through fiducial and differential cross sections, as well as Effective Field Theory (EFT) couplings. Further analyses explore the four-lepton invariant mass distribution $m_{4\ell}$ and search for potential heavy Higgs-like bosons. This analysis uses a data set corresponding to proton-proton (pp) collision events recorded at a centre-of-mass (CM) energy of $\sqrt{s} = 13$ TeV during the period 2015-2018. The dataset has an integrated luminosity of approximately 139 fb^{-1} . The four-lepton channel, where ℓ and ℓ' represent electrons or muons, offers exceptional sensitivity over a wide mass range due to its precise reconstruction and clean final-state signature. Events are categorised into four distinct final states: $4e$, 4μ , $2e2\mu$ and $2\mu2e$. In particular, the key distinction between the last two channel categories lies in selecting the first two leptons with a dilepton-invariant mass closest to that of the Z boson. The primary background comes from ZZ processes. In instances where $m_H < 180$ GeV, a significant background is also observed from Z with jets, $t\bar{t}$, and WZ production. This background predominantly stems from the decay of hadrons containing bottom or charm quarks or from jets that are misidentified. Additionally, triboson events also account for a minor background component. Subsequently, Section 5.6 introduces the pile-up studies from which the author had a significant contribution, and lastly, Section 5.7 introduces the electron isolation studies in the $H4\ell$ analysis, which were again performed by the author.

5.2 Data and simulation

5.2.1 Data

Commencing operations at the LHC in May 2015, pp collisions were produced, with proton beams at individual energies of 6.5 TeV, yielding a CM energy of 13 TeV and a bunch spacing of 25 ns. ¹ In particular, a fractional data set of 0.13 fb^{-1} , obtained with a 50 ns bunch spacing, is excluded from the primary dataset. Before this, the LHC operated at lower CM energies, specifically 7 TeV in 2010 and 2011, and 8 TeV in 2012 and 2013. Subsequent to an initial commissioning phase, the ATLAS experiment began data acquisition for physics

¹The analysis excludes 2015 data collected with the 50 ns bunch spacing (0.13 fb^{-1}), ensuring consistency with the rest of the data collected at the standard 25 ns spacing.

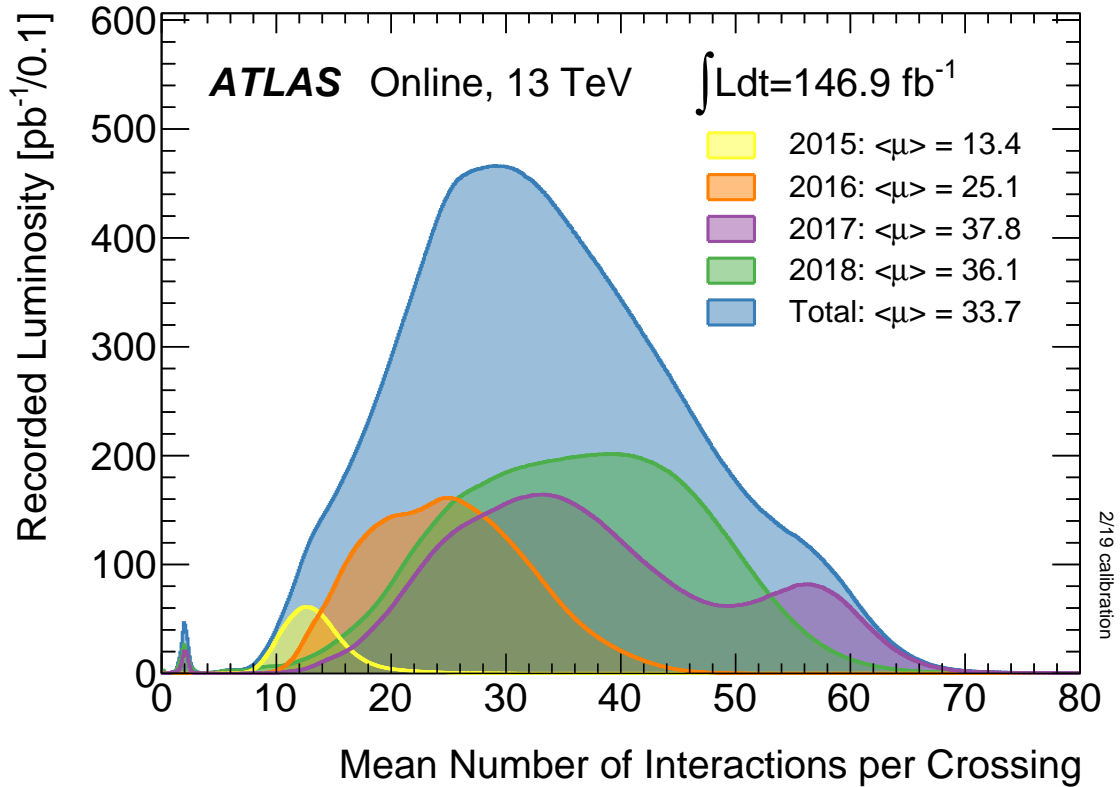


Fig. 5.1 Average number of interactions per bunch crossing in proton-proton collisions at 13 TeV measured by ATLAS from 2015 to 2018. Higher values indicate higher collision density. The total integrated luminosity for this period is also given. Image taken from [130].

analysis purposes in August 2015. The research presented in this thesis is based on data collected between August 2015 and October 2018. During this operational period, ATLAS experienced a gradual increase in peak and average pile-up levels, with the highest pile-up in 2018 reaching around 90. Throughout the entirety of Run 2 at the LHC, the overall efficiency of data collection was 95.76% [129]. The pile-up distribution for these data sets is illustrated in Fig. 5.1.

Data reconstruction was carried out using Athena Release 21.2 [131]. Throughout this timeframe, ATLAS received an integrated luminosity of 156 fb^{-1} from the LHC, as indicated in Fig. 2.4. Among these, 147 fb^{-1} were successfully recorded, with $(139.0 \pm 2.4) \text{ fb}^{-1}$ deemed suitable for subsequent physics analyses.² The combined integrated luminosity for Run 2 was determined with an uncertainty of $\pm 2.4 \text{ fb}^{-1}$ ($\pm 1.7\%$) [132].

²This corresponds to the integrated luminosity of the luminosity blocks that meet the criteria of the Good Runs Lists.

5.3 Simulation

The methodology for simulating events integrates various approaches in different analyses. These events, which encompass both signal and background processes, are essential for multiple aspects of the analysis, including background modelling, acceptance calculations, and systematic uncertainty estimations. Initially, events are generated using a Monte Carlo (MC) approach, a numerical integration method that determines the probability of process occurrence. This involves generating events based on perturbative theoretical frameworks that employ an array of generators for this purpose. In the simulation of particle interactions within the ATLAS detector, the comprehensive ATLAS simulation framework [133] is used, functioning within the Geant4 framework [134]. Subsequently, the responses of the simulated detector are digitised and reconstructed within the ATHENA framework [131].

To accurately model experimental conditions, signal and background events were generated using dedicated ATLAS MC simulation campaigns: mc16a, mc16d, and mc16e. These campaigns replicate the data-taking characteristics and pile-up scenarios for 2015-16, 2017, and 2018, respectively. A key aspect of these simulations was the pile-up reweighting process. This involved adjusting events to ensure consistency with the mean interactions occurring per bunch crossing. This approach ensures that the high-mass signal and SM background events generated in the simulation closely resemble the actual data collected.

5.3.1 Simulation of signal

A variety of theoretical frameworks BSM propose the existence of heavy particles with potential decay into pairs of bosons, specifically in diboson final states. The following is an overview of a specific group of these models that theorise the existence of a substantial ZZ resonance. These models are significant for their implications in the field of particle physics, offering potential insights into the behaviour and characteristics of particles beyond those currently known in the SM.

Heavy Higgs-like Scalar

This analysis relied on the POWHEG-BOX v2 event generator [135] to produce simulated signal samples for the narrow-width approximation (NWA). NWA is used when the decay width of a particle is much smaller than its mass, allowing the propagator to be approximated as a delta function. This simplifies calculations by factorising the production and decay processes. This choice leverages the precision of next-to-leading-order (NLO) calculations within the

framework of Quantum Chromodynamics (QCD), which include one-loop corrections and real emission processes, providing more accurate and reliable predictions compared to leading-order (LO) calculations, which only include the primary interactions.

To accurately model subsequent particle interactions, hadron formation, and decays, particularly for the final state of the Higgs boson with four leptons, the simulations were coupled with PYTHIA8 [136]. This software handles the parton showering and hadronization processes. Additionally, the decay of the bottom and charm quarks was further simulated using EvtGen v1.2.0 [137]. In particular, the hard-scattering processes within these simulations employed the set of LO CT10 parton distribution function set [138]. To ensure a comprehensive analysis, both the ggF and VBF production modes were simulated separately for various discrete Higgs boson mass values.

For NWA signals, the masses ranged from 200 to 2000 GeV with 100 GeV increments up to 1000 GeV, and thereafter, increments of 200 GeV, including additional samples at 2400 and 3000 GeV for extrapolation validation. In contrast, heavy Higgs boson production (denoted as H) in the ggF mode under the Low Width Approximation (LWA) was simulated with NLO accuracy using MADGRAPH5_MC@NLO v2.3.2 [139]. LWA is applicable when the width of the resonance is small but is not negligible compared to its mass. Simulations were performed with natural widths of $\Gamma_H = 0.15m_H$, $\Gamma_H = 0.05m_H$, and $\Gamma_H = 0.1m_H$ at various mass points to validate the $m_{4\ell}$ distribution parametrization.

Furthermore, spin-2 graviton simulations were performed within both the Randall–Sundrum (RS) framework and the bulk RS model, using MADGRAPH5 interfaced with PYTHIA8. These graviton samples were generated with the value of the k/\bar{M}_{Planck} parameter set to 1. For the bulk RS model, the NNPDF2.3 LO PDF set with $\alpha_s = 0.130$ [140] was used. The width of these resonances was closely correlated with the k/\bar{M}_{Planck} coupling, resulting in gravitational widths of approximately 6% of the graviton mass. This approach to sample generation was carefully designed to ensure compatibility with previous analyses and to thoroughly explore a broad spectrum of theoretical predictions within the RS models.

5.3.2 Simulation of background

The background processes relevant to the 4ℓ channel were carefully considered, including the diboson (ZZ), the triboson (VVV), the Z + jets, the $t\bar{t}$ and the $t\bar{t}V$ processes. To accurately model the decay channels of bottom and charm quarks, the simulation used the software EvtGen v1.2.0 for the hadronization process. For the $q\bar{q} \rightarrow ZZ$ process,

generation was carried out using SHERPA v2.2.2. This choice ensured the use of NNPDF3.0 PDF for hard scattering processes, achieving the precision of NLO in the calculation of matrix elements for the final states of 0 and 1 jet according to the SHERPA v2.2.2 standards. LO accuracy was used for the final states of the 2- and 3-jets, as appropriate for their respective contributions. Parton showers were simulated within SHERPA's internal shower algorithm [141], and events were merged in the NLO using a combination of MePs [142], Comix [143], and OPENLOOPS [144–146] matrix element generators to achieve a high level of precision in the modelling of multi-jet final states.

Furthermore, the simulation of $gg \rightarrow ZZ$ production, which includes the production of SM Higgs bosons and associated interference effects, used a combination of SHERPA v2.2.2 and OPENLOOPS. In LO, the matrix elements for the jet 0 and 1 were calculated and harmonised with the SHERPA parton showers. The electroweak (EW) $q\bar{q} \rightarrow ZZ$ process, specifically with two additional jets through vector-boson scattering, was generated with the same versions of SHERPA and NNPDF3.0 at NLO. The production of a single Z boson in conjunction with jets was simulated using SHERPA v2.2.2. In this simulation, elements of the NLO matrix were considered for interactions involving up to two partons, while LO calculations were applied for configurations involving up to four partons. The merging of these calculations was achieved through the use of COMIX and OPENLOOPS. VVV backgrounds were generated with SHERPA v2.2.1, while the $t\bar{t} + Z$ background with four prompt leptons was simulated using MADGRAPH5_MC@NLO. POWHEG-BOX v2 interfaced with PYTHIA v6.428 [147] and the PERUGIA 2012 [148] set handled parton showering, hadronization, and QED radiative corrections via PHOTOS [149]. The τ decays were modelled with TAUOLA [150, 151].

5.4 Efficiency studies for electrons and muons

5.4.1 Efficiency of the electron identification

The electron identification efficiency is evaluated at three operating points: Loose, Medium, and Tight. These are optimised in nine bins of $|\eta|$ and 12 bins of E_T , ensuring that the reconstructed electrons meet the predefined likelihood discriminant criteria. The discriminant thresholds are determined using simulated events, where electromagnetic shower quantities and track-cluster variables are adjusted to match the distribution seen in real data. To maintain stable background rejection, the discriminant threshold is linearly adjusted based on pile-up levels, measured by the number of reconstructed vertices, n_{vtx} . However, as pile-up increases,

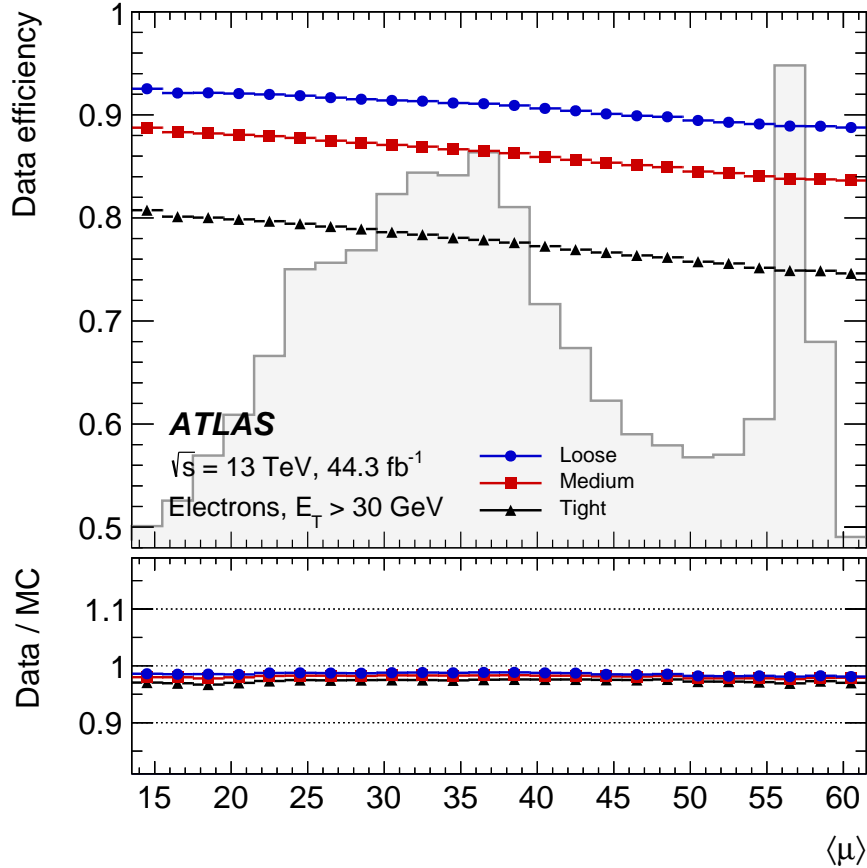


Fig. 5.2 The efficiency of electron identification in data for electrons with $E_T > 30$ GeV, presented as a function of the average number of interactions per bunch crossing. The analysis includes Loose, Medium, and Tight operating points. Efficiencies are derived from $Z \rightarrow ee$ events using data from 2017. The $\langle \mu \rangle$ distribution is depicted as a shaded histogram. The lower panel illustrates the ratio of data to simulation, including total uncertainties. Taken from Ref. [152].

the efficiency of signal detection diminishes, as demonstrated in Fig. 5.2, which shows the efficiency for electrons from Z boson decays.

The target efficiencies for these operating points mirror those of previous identification methods [152], proven effective in various analyses and topologies. The efficiencies average at 93%, 88%, and 80% for the Loose, Medium, and Tight points respectively, increasing with higher E_T . Although tighter criteria reduce efficiency, they significantly improve background rejection by factors of 2.0 and 3.5 for the Medium and Tight points, respectively, within the range $20 \text{ GeV} < E_T < 50 \text{ GeV}$. This background efficiency is evaluated in QCD two-to-two processes as detailed in Ref. [152]. The data shown in Fig. 5.3 reveal efficiency variations

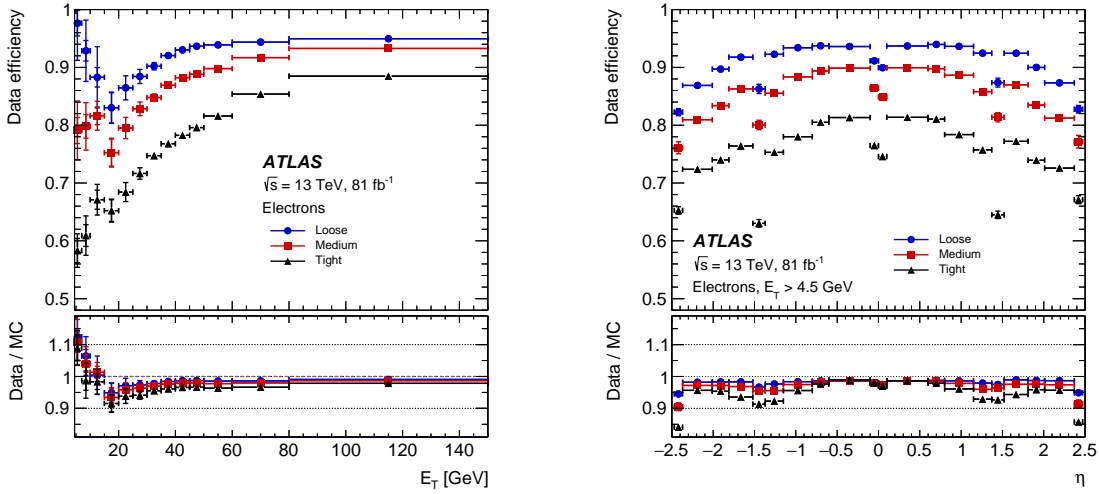


Fig. 5.3 Electron identification efficiency in $Z \rightarrow ee$ events as a function of E_T (left) and η (right) for Loose, Medium, and Tight operating points. Efficiency ratios from $J/\psi \rightarrow ee$ and $Z \rightarrow ee$ events are applied to $Z \rightarrow ee$ simulations. Inner uncertainties are statistical, and total uncertainties include both statistical and systematic components added in quadrature. The bottom panels in both plots show the data-to-simulation ratios. Adapted from Ref. [152].

from 58% at $E_T = 4.5$ GeV to 88% at $E_T = 100$ GeV for the Tight point, and from 86% at $E_T = 20$ GeV to 95% at $E_T = 100$ GeV for the Loose point. Variations in 2016 and 2017, compared to 2015, in the data are attributed to different gas mixtures from the Transition Radiation Tracker and residual pile-up dependencies.

The uncertainty in efficiency measurements is $\pm 7\%$ at $E_T = 4.5$ GeV, which decreases with higher transverse energy to below $\pm 1\%$ for $30 \text{ GeV} < E_T < 250 \text{ GeV}$. The systematic uncertainties, mainly from the subtraction of the background at low E_T , are detailed in Ref. [152]. For higher E_T , additional uncertainties of $\pm 0.5\%$, $\pm 1.0\%$, and $\pm 1.5\%$ are assigned for Loose, Medium, and Tight identifications, respectively, due to variations in efficiency, limiting overall precision.

5.4.2 Efficiency of the muon identification

The efficiency of muon identification is evaluated for the Loose, Medium, and Tight criteria using data from $J/\psi \rightarrow \mu\mu$ and $Z \rightarrow \mu\mu$ events. For muons with $p_T > 10$ GeV, the efficiencies are stable across all selection levels, with the data and MC predictions showing good agreement. However, efficiencies drop significantly for muons with $p_T < 5$ GeV, primarily because these muons often lack sufficient residual energy to reach the second station

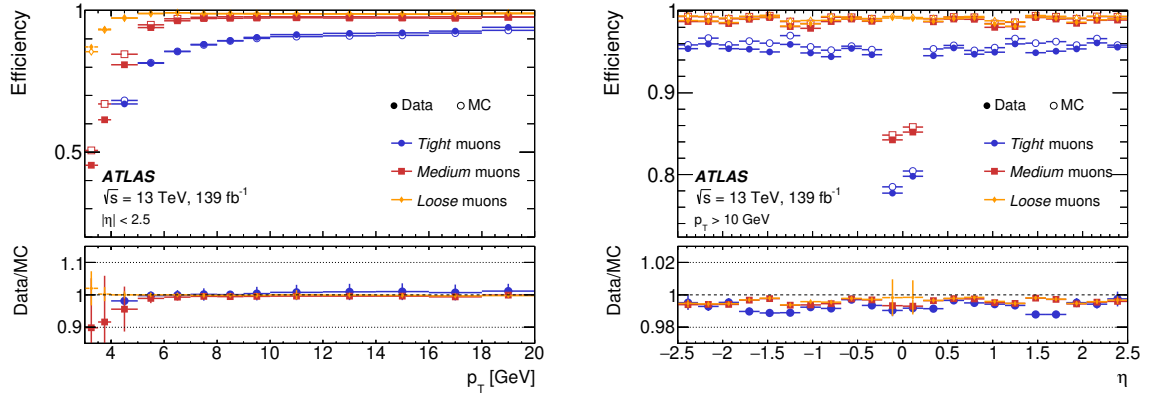


Fig. 5.4 Comparison of muon reconstruction and identification efficiencies for *Loose*, *Medium*, and *Tight* selection criteria. The left plot illustrates the efficiencies derived from the $J/\psi \rightarrow \mu\mu$ events as a function of p_T , while the right plot presents the efficiencies of the $Z \rightarrow \mu\mu$ events versus η for muons with $p_T > 10$ GeV. The predicted efficiencies are shown with open markers, and the results of the collision data are indicated by filled markers. Statistical uncertainties, when significant, are represented by error bars. The bottom panel shows the relationship between measured and predicted efficiencies, including both statistical and systematic uncertainties.

of precision MS chambers. As illustrated in Fig. 5.4, efficiencies measured in the $Z \rightarrow \mu\mu$ events as a function of η for muons with $p_T > 10$ GeV exhibit consistent performance in different regions of the detector.

The Medium identification criteria are further evaluated using a finer binning in the (η, ϕ) plane, as shown in Fig. 5.5, with scale factors (SFs) calculated for muons with $p_T > 15$ GeV. The detailed binning reflects the unique characteristics of the Medium WP, which is sensitive to the presence or absence of hits at various MS stations. The results demonstrate high efficiency, exceeding 95% for tracks within $0.1 < |\eta| < 2.5$ with slight variations due to detector performance and geometry. Discrepancies observed in the low p_T and specific η regions are attributed to temporary faults or inefficiencies in the muon chambers during data collection, highlighting the need for meticulous calibration and alignment procedures.

The efficiencies for the Loose and Medium criteria are characterised by similar performance throughout most of the detector, except in the region $|\eta| < 0.1$. Here, the Loose selection includes Combined Tracks and Segment-Tagged muons to fill gaps in MS coverage, resulting in an efficiency exceeding 98% for tracks with $0.1 < |\eta| < 2.5$. Conversely, the Tight selection shows slightly lower efficiency in this region, but still exceeds 95%, with differences between data and simulation within the 1% level or lower. These findings underscore the

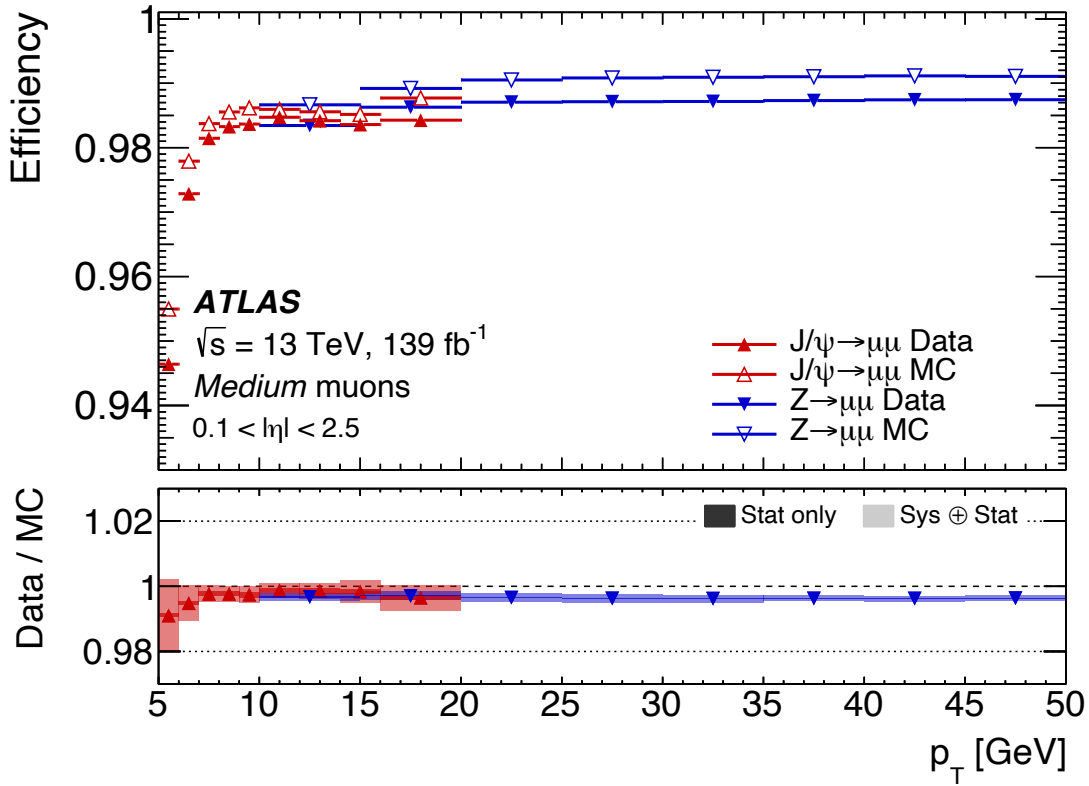


Fig. 5.5 Evaluation of muon reconstruction and identification efficiencies for *Medium* criteria using $J/\psi \rightarrow \mu\mu$ and $Z \rightarrow \mu\mu$ events, plotted as a function of p_T for muons within $0.1 < |\eta| < 2.5$. Statistical uncertainties are shown by error bars when they are not negligible. The bottom panel provides the ratio of the measured efficiencies to the predicted ones, accounting for both statistical and systematic uncertainties.

effectiveness of selection criteria in maintaining high identification efficiency in diverse detector conditions and pile-up scenarios.

Overall agreement between data and simulation across the (η, ϕ) plane is achieved with an average deviation of 0.5%, with about 9% of the measured SFs showing a deviation from unity greater than 1%, primarily in the $|\eta| < 0.1$ region. Specific inefficiencies are also observed in $|\eta| < 1.0$ around $\phi = -1.2$ and $\phi = -2.0$, corresponding to detector support structures that prevent complete coverage by the MS. Other localised efficiency drops are traced to temporary faults in the Cathode Strip Chambers during the 2017 data-taking period. Such detailed efficiency mapping and associated calibration efforts ensure the robustness of muon identification in high-precision physics analyses.

5.5 Event selection

5.5.1 Trigger configuration

The 4ℓ final state is highly sensitive to heavy resonances due to its exceptional mass resolution achieved through minimal experimental and theoretical uncertainties. To effectively analyse events with four leptons, a systematic categorisation is used into three distinct channels based on the lepton flavour: 4 muons (4μ), 2 electrons and 2 muons ($2e2\mu$), and 4 electrons ($4e$). The use of single-lepton, dilepton, and trilepton triggers, particularly dilepton and trilepton triggers that encompass electron(s)-muon(s) combinations, facilitates this classification. In particular, stricter 'medium' to 'tight' likelihood requirements were implemented for single-electron triggers, while 'loose' to 'medium' criteria sufficed for di- and tri-electron triggers. During the four years of data collection, the minimum trigger thresholds in p_T were adjusted in response to the increased peak luminosity experienced during these periods [153, 94]. The p_T thresholds for muon and electron triggers varied between 20 to 26 GeV and 24 to 26 GeV, respectively, in response to increasing luminosity, ensuring an overall trigger efficiency of approximately 98% for events that meet the final selection requirements.

5.5.2 Physics objects selection

In the construction of candidate quadruplets for each lepton-flavour combination, the process involves selecting two pairs of dileptons. These pairs are characterised by having identical flavours but opposite signs. To classify each quadruplet, the thresholds for the three highest p_T are set at: (20, 15, and 10) GeV. The classification of quadruplets is further refined by identifying the dilepton mass that most closely approximates the mass of the Z boson, referred to as m_{12} . This pair is designated as the primary dilepton, while the other pair, termed m_{34} , is considered secondary. The leptons that compose each pair must be of the same flavour. The selection criteria for the leading and subleading pairs are based not only on their mass but also on the lepton flavour within the quadruplet. The leading dilepton mass (m_{12}) was restricted to a window between 50 - 106 GeV. On the contrary, the mass of the subleading dilepton (m_{34}) is subject to a variable threshold that depends on the total mass of the quadruplet ($m_{4\ell}$). This threshold is initially set at 12 GeV when $m_{4\ell}$ is less than 140 GeV, progressively increasing to 50 GeV as $m_{4\ell}$ reaches 190 GeV, and stabilises beyond this point. To suppress contributions from J/ψ decays, channels with $4e$ or 4μ enforce an additional criterion: both alternative pairings of oppositely charged leptons within the quadruplet must exceed a specific mass threshold, that is 5 GeV.

Stringent kinematic and topological criteria are used to select genuine quadruplet candidates and suppress background contributions. The angular separation between the two pairs of leptons within a quadruplet must exceed 0.1 radians, ensuring minimal overlap with the final-state radiation (FSR) electrons. This requirement is stricter for pairs of opposite flavours in previous analyses, but the tighter FSR recovery method described later eliminates the need for that distinction. To minimise background contamination from heavy-flavour hadrons, rigorous measures were employed to assess the distance of each quadruplet lepton from the primary interaction point. This assessment involved the "transverse impact parameter significance," a metric indicating how far a charged particle's trajectory deviates from the collision origin relative to its expected uncertainty. For electrons, a significance threshold of 5 was implemented, whereas muons were held to a stricter limit of 3. These criteria effectively reduced the presence of heavy-flavor background particles within the analysis. Further background suppression is achieved through isolation criteria for each lepton. These track-based and calorimeter-based criteria, detailed in Section 5.7, target reducible backgrounds originating primarily from Z + jets and $t\bar{t}$ processes. Additionally, a vertex-based selection criterion improves the suppression of these backgrounds.

To further suppress background contributions, a vertex-based selection strategy was implemented, requiring all leptons within a quadruplet to originate from a common vertex. A carefully calibrated χ^2/Ndof (number of degrees of freedom) threshold was applied to the vertex fit, achieving a remarkable 99.5% signal efficiency while rejecting approximately one-quarter to one-third of both Z + jets and $t\bar{t}$ backgrounds. The specific threshold values differ between the 4μ channel ($\chi^2/\text{Ndof} < 6$) and other channels ($\chi^2/\text{Ndof} < 9$) due to variations in the resolution of the electron and muon tracks, which affects the fit quality.

First, the importance of $|d_0|/\sigma_{d_0}$, the transverse impact parameter significance, is central. Here, d_0 represents the transverse impact parameter, which measures the distance of closest approach of the lepton track to the primary vertex in the transverse plane, and σ_{d_0} is the uncertainty in this measurement. For muons and electrons, this parameter must remain below the thresholds of 3 and 5, respectively. To reduce the influence of background noise, isolation is assessed by integrating data from track and calorimeter analyses. The method focusing on track isolation considers tracks exceeding $p_T > 500$ MeV, located in proximity defined by a ΔR (distance in the η - ϕ plane) radius of 0.3 relative to the lepton. These tracks should be linked to the primary interaction point or have a longitudinal impact parameter below 3 mm. Importantly, for leptons with momenta surpassing 33 GeV, the cone radius shrinks, reaching a minimum of $\Delta R = 0.2$ for energies of 50 GeV and above. To ensure lepton isolation

(calorimeter-based), the sum of positive topological cluster energies within a radius defined by $\Delta R = 0.2$ is calculated, excluding the track of the lepton. This combined track-calorimeter isolation must be less than 16% of the lepton's p_T , with at least 40% of this isolation energy sum originating from the calorimeter. This criterion, named 'FixedCutPFlowLoose', effectively suppresses background events. Further background reduction is achieved through vertex reconstruction. A dedicated algorithm fits the quadruplet of charged leptons, ensuring their origin from a common vertex. This algorithm exhibits an impressive efficiency that exceeds 99% for signal channels, together with a goodness-of-fit requirement of $\chi^2/\text{Ndof} < 6$ for the 4μ channel and $\chi^2/\text{Ndof} < 9$ for other flavours.

In the analysis of Z boson decays, the reconstruction process incorporates photons from the FSR, identifiable in the electromagnetic calorimeter and accurately represented in simulations. This process involves the identification and inclusion of a singular FSR photon for each event, which is assumed to be emitted by one of the charged leptons in the leading pair. Incorporating FSR photons into the 4ℓ analysis, aligning with methodologies from Run 1 as cited in [154], involves identifying collinear FSR photons related specifically to muons, and non-collinear ones relevant to both muons and electrons, restricting to a single photon for each event. The four-momentum of the photon is then combined with that of the lepton pair, and events with more than one FSR photon are not included. Post this combination, a kinematic fit recalculates the four-momenta for each dilepton pair. This fitting process applies a Z -mass constraint, consistent with the approaches in [155]. It also includes a Breit–Wigner model for the Z boson lineshape and a Gaussian distribution for each lepton, adjusted for anticipated resolution, which helps in the precise reconstruction of the Z boson momentum response function in this scenario. Details of the selection of events for the final state 4ℓ are outlined in Section 5.5.3.

5.5.3 Selection criteria for physics objects

Physics Objects

Electrons

To select electrons, a loose-likelihood criterion is applied. This criterion requires a hit in the innermost layer, a transverse energy exceeding 7 GeV, and $|\eta|$ within 2.47. Furthermore, electrons must satisfy the interaction point criterion: the absolute value of $z_0 \times \sin \theta$ must be less than 0.5 mm, provided an ID track is present. Here, z_0 represents the longitudinal impact

parameter, which measures the distance of closest approach of the track to the primary vertex along the beam axis.

Muons

First, muons are loosely identified if their p_T exceeds 5 GeV and their $|\eta|$ is less than 2.7. Furthermore, calorimeter-tagged muons must have a p_T above 15 GeV and an $|\eta|$ less than 0.1. This pseudo-rapidity restriction also applies to segment-tagged muons. Stand-alone and silicon-associated forward muons are constrained to a specific region, where $|\eta|$ ranges from 2.5 to 2.7. Furthermore, a combined criterion is established for stand-alone and segment-tagged muons, stipulating a p_T greater than 5 GeV. The interaction point criteria for muons require that the absolute value of d_0 be less than 1 mm and the product of z_0 and $\sin\theta$ should be less than 0.5 mm, given that the ID track is accessible.

Jets

Only jets that pass the anti- k_T algorithm with bad-loose identification criteria are considered. These jets must have $p_T > 30$ GeV and are located within the $|\eta| < 4.5$ range.

Overlap Removal

Jets within a ΔR cone of 0.2 around an electron are discarded. Similarly, jets that fall within a ΔR cone of 0.1 around a muon are also excluded.

Vertex Considerations

To ensure the presence of a clear interaction point, events were required to have at least one detectable collision site (vertex) with two or more particles (tracks) originating from it. This key vertex, essential for calculating track impact parameters and other analyses, was identified based on the combined momentum squared ($\sum p_T^2$) of its associated tracks, prioritising the vertex with the highest total momentum squared.

Event Selection

Quadruplet Selection

This analysis focuses on identifying quadruplets, each composed of a pair each of oppositely charged electrons and muons. Within each quadruplet, the three highest- p_T leptons must surpass the momentum thresholds of 20 GeV, 15 GeV, and 10 GeV, respectively. Furthermore, each quadruplet is limited to a maximum of one muon of each type (calorimeter-tagged, stand-alone, or silicon-associated forward). The invariant mass of the leading dilepton (m_{12}) must fall within the range of 50-106 GeV. The mass of the subleading dilepton (m_{34}) must be greater than or equal to a predefined minimum threshold ($m_{threshold}$) and less than or equal

to 115 GeV. Additionally, all pairs of leptons within the quadruple must be separated by a minimum spatial distance, measured by $\Delta R = 0.10$. Finally, any quadruplet containing an alternative pair of opposite-charge leptons of the same flavour with a mass below 5 GeV is excluded. Quadruplets that meet all these criteria are retained for further analysis.

Isolation

In the process of isolation calculation for quadruplet leptons, the impact of other leptons within the same quadruplet is carefully deduced. Concurrently, FixedCutPFlowLoose WP is consistently applied across all leptons.

Impact Parameter Significance

To distinguish signal leptons from those originating from heavy-flavour decays, strict impact parameter criteria are applied to all electrons and muons within quadruplets. For electrons, the significance of d_0/σ_{d_0} must be less than 5. Similarly, muons must have a significance below 3.

Best Quadruplet Selection

The event with the highest probability of originating from a Higgs boson decay is selected among events with multiple candidate quadruplets of leptons. This prioritisation depends on the specific decay channel, which can involve four electrons, two electrons, and two muons in either pairing (electron-muon or muon-electron) or four electrons alone.

Vertex Selection

All leptons within a chosen quadruplet must share a common origin vertex. Additionally, in the 4μ decay channel, the chi-square per degree of freedom (χ^2/Ndof) must be less than 5, while other decay channels have a slightly higher threshold of 9.

5.6 The effects of pileup

5.6.1 Motivation

Pile-up, a term collectively used for additional pp collisions that are not the primary event of interest but occur at the same or adjacent bunch crossings, has progressively intensified.

The ATLAS detector has been crucial in observing pp interactions; however, a significant challenge in its operation is the phenomenon of pile-up. Pile-up refers to additional pp collisions that are not the primary event of interest but occur at the same or adjacent bunch crossings [156]. This phenomenon increasingly affects the quality of the data obtained from

high-luminosity runs of the LHC. During the Run 2 period, the ATLAS detector observed a consistent increase in the average number of pile-up interactions. The increasing average number of these interactions, observed during the Run 2 period, has increased from 13.4 interactions per bunch crossing in 2015 to 38.3 in 2018, with projections indicating a rise to more than 200 during the upcoming high-luminosity LHC operations after 2026 [157].

Pile-up can be categorized into five distinct components:

- *In-time pile-up*: This consists of additional pp collisions occurring within the same bunch crossing as the primary event.
- *Out-of-time pile-up*: Resulting from adjacent bunch crossings, these interactions pose a challenge due to the sensor electronics' integration time, often exceeding 25 ns, leading to a mixing of signals.
- *Cavern background*: Constituted by a diffuse gas of neutrons and photons, this background generates random hits within the detector.
- *Beam halo events*: Caused by protons scraping against an upstream collimator, leading to muon sprays parallel to the beamline.
- *Beam gas events*: The resulting product is from interactions between proton bunches and residual gases in the beam pipe, usually occurring off-centre in the detector.

The presence of pile-up introduces uncorrelated background signals, including soft calorimeter energy, which can impact various physics objects and measurements within ATLAS. Therefore, accurate modelling of these effects is crucial for data analysis and the extraction of physics results. Pile-up differs from the underlying event, which is caused by the remaining partons within colliding protons that did not participate in the primary hard scatter but could generate additional energy inside the isolation cones of particle detectors. These pile-up particles, originating from other vertices, may contaminate the isolation cones, affecting the analysis. As detailed in Section 5.7, particle isolation is calculated using an isolation cone in the η - ϕ plane, which collects any particle near the η and ϕ particles of interest. However, the pile-up particles, even though they come from a different vertex, can be close to each other in dimensions η and ϕ . Consequently, they may contaminate the isolation cone, introducing potential contamination despite spatial separation from the primary particle under consideration.

This section evaluates the influence of multiple pp collisions within the same bunch crossing (pile-up) on data from the mc16a and mc16d datasets. Although there are some differences

between these datasets, careful considerations have been made when merging them. Specifically, a weighted average based on both luminosity and pile-up conditions was applied to the pile-up profile over both years. The analysis concentrates on intermediate mass ranges (100-800 GeV) for the hypothesised heavy scalar boson. Each simulated event undergoes complete replication within the ATLAS detector using the dedicated $H4\ell$ framework, as detailed in Section 5.6.2.

5.6.2 The role of the analysis framework

For a physics group, the need for an analysis framework arises to aid in reducing the Analysis Object Data (AODs)/D3PDs/xAODs to a manageable size and format that can then be subsequently used to produce final results and graphs [158, 159]. This is accomplished by imposing specific analysis cuts and vetoing events that do not pass the full selection. Furthermore, in the final output, the framework saves only the variables needed for the final analysis and plotting. Section 5.5.3 summarises the cuts used by $H4\ell$ for its nominal analysis. These are designed to select events with 4ℓ that match the kinematic distribution of leptons originating from a $H \rightarrow ZZ^*$ decay. Furthermore, these cuts are also designed to reduce background events in which the final state is created by $pp \rightarrow ZZ^* \rightarrow 4\ell$ decays or $pp \rightarrow ZZ^* \rightarrow 2\ell 2q$ decays, where the jets are misidentified as leptons. In addition to the nominal cutflow, many other cutflows that contain slightly varied cuts are also implemented in a framework for this analysis. To estimate the background, control regions are created by inverting and relaxing isolation requirements, relaxing identification requirements on electrons, or selecting quadruplets with different charges and flavour compositions. The influence of systematic uncertainties on the final results is assessed by employing a dedicated procedure. The analysis utilises the same selection criteria as the nominal analysis, but with variations in the calibration and smearing of leptons and jets, following the recommendations provided by the CP group. Moreover, to derive resolution functions, $Z \rightarrow 2\ell$ events with similar preselection and isolation requirements are selected. Lastly, truth-level cutflows for MC events are used for fiducial studies. Once the events have been selected, the variables important for the final analysis are calculated and stored in minitrees. These variables range from calculating the invariant mass of selected objects to calculating boosted decision-tree scores to simply storing lepton-kinematic information. For MC events, weight variables for overall normalisation and truth-matched information are also calculated and saved in the final output.

5.6.3 Results

Event yields

Evaluating the impact of pileup on the $H \rightarrow 4\ell$ final state is essential to evaluate the efficacy of the selection criteria implemented on the Run 2 datasets, which include a total integrated luminosity of 139 fb^{-1} . This analysis focuses on the mass range of $100 \text{ GeV} < m_{4\ell} < 800 \text{ GeV}$ within the 4μ , $4e$, and $2\mu 2e$ decay channels. Table 5.1 presents the calculated event yields for the years 2015-2017, adhering to the standard selection criteria outlined in Section 5.5. These yields, which incorporate both statistical and systematic uncertainties, represent the number of observed weighted events that satisfy the defined selection requirements. For background estimation, MC simulations model the ZZ continuum contribution, while data-driven methods handle the reducible component. Reducible background refers to backgrounds that can be reduced or eliminated with appropriate selection criteria, such as those originating from misidentified jets or non-prompt leptons. In contrast, irreducible background refers to backgrounds that cannot be eliminated by selection criteria, typically consisting of processes that produce the same final states as the signal, such as production of ZZ . The mc16a and mc16d samples exhibit a consistent relative difference in the various decay channels, with an overall relative difference of approximately 1.03, indicating a variation of 3.77%. This consistency in the relative difference between the mc16a and mc16d samples points to the stable performance of the selection criteria over different data collection periods. Among the final states of 4μ and $4e$, the highest efficiency is observed for 4μ and the lowest efficiency for $4e$ due to the looser muon kinematic cuts compared to electrons. In the H mass region, the $2e2\mu$ or $2\mu 2e$ pair closest to the Z boson mass ($\approx 91 \text{ GeV}$) is selected. Hence, with both pairs on-shell, it is only the measurement resolution that tends to decide which way the pairing goes.³

An analysis of consistency in the selection of events within the mass range $60 \leq m_{Z_1} \leq 110 \text{ GeV}$ was conducted across different MC samples (mc16a and mc16d) by comparing their normalised event counts, taking into account their respective cross sections and luminosity values. All predictions shown here are selected using the properties of physics mentioned in Chapter 4 and the selection process in Section 5.5. Examination of the mass distributions for the final state of 4μ , shown in Fig. 5.6a for $m_{4\ell}$ and Fig. 5.6b for m_{Z_1} , indicates a peak around

³In the context of $2e2\mu$ final states, the configuration where two electrons form the sub-leading pair (equivalent to Z boson) is generally found to be more efficient than the one where two muons are the sub-leaders. This is attributed to the lower boost typically observed for leptons in the subleading pair compared to the leading pair, making them more susceptible to failing kinematic cuts.

Samples	4μ	$4e$	$2\mu 2e$	Overall
mc16a	249.92	157.76	398.38	805.76
mc16d	240.28	152.44	383.77	776.49
mc16a/mc16d	1.04	1.03	1.03	1.03
Rel. diff in %	4.01	3.52	3.81	3.77

Table 5.1 $H4\ell$ decay channel yields (2015-2017) post-selection, $m_{4\ell}$ range: 140-180 GeV. The event yields are weighted events.

91 GeV in the m_{Z_1} range, which aligns with the expected mass of the Z boson. The mc16a and mc16d simulations, compared in both figures, show alignment in this peak, confirming the mass resolution's accuracy for the Z boson in the 4μ final state. The overlap of the $m_{4\ell}$ distributions in Fig. 5.6a across different simulations denotes a consistent MC modelling. The extended tails past 500 GeV in the $m_{4\ell}$ distribution indicate a coherent selection of high-mass events. Minor discrepancies are observed in the lower mass region, under 200 GeV, are observed but are considered to be within the limits of statistical fluctuations, since the ratio graph maintains steady unity. The comparison of mc16a and mc16d samples in these figures reveals a good agreement within the estimated statistical and systematic uncertainties for both the m_{Z_1} and $m_{4\ell}$ distributions. This means that the simulation accurately captures the expected behaviour of the data within the calculated uncertainties.

Shape comparisons were also observed for other variables. Fig. 5.7 shows plots for the $4e$ final state with Fig. 5.7a showing events for the variable $m_{4\ell}$ and Fig. 5.7b showing events for the m_{Z_1} variable. No significant differences were found between the two MC samples. Figure 5.8 shows the distribution of the $2\mu 2e$ variable. Figure 5.8a presents the distribution of the invariant mass of four leptons ($m_{4\ell}$), while Fig. 5.8b focuses solely on the mass of the leading Z boson (m_{Z_1}). Again, there are no notable differences between the MC samples. These results suggest that there was no significant effect on pileup during Run 2, it neither increased nor decreased. New isolation cuts have been proposed in an attempt to reduce the pile-up effects while increasing the efficiency of lepton variables, and the results are included in the next section.

The $m_{4\ell}$ distribution in the $4e$ final state (Fig. 5.7) shows that although the mc16a dataset exhibited a slightly higher yield within the mass range considered, the overall shape closely mirrored that of the mc16d dataset. This observation suggests that the detection efficiencies for electrons in both sets of MC are well-modelled. Similarly, for the m_{Z_1} distribution in the $4e$ final state (Fig. 5.7a), the well-defined peak at the Z -mass indicated that the electron mass resolution remained consistent with the muon channel, although with a slightly broader peak

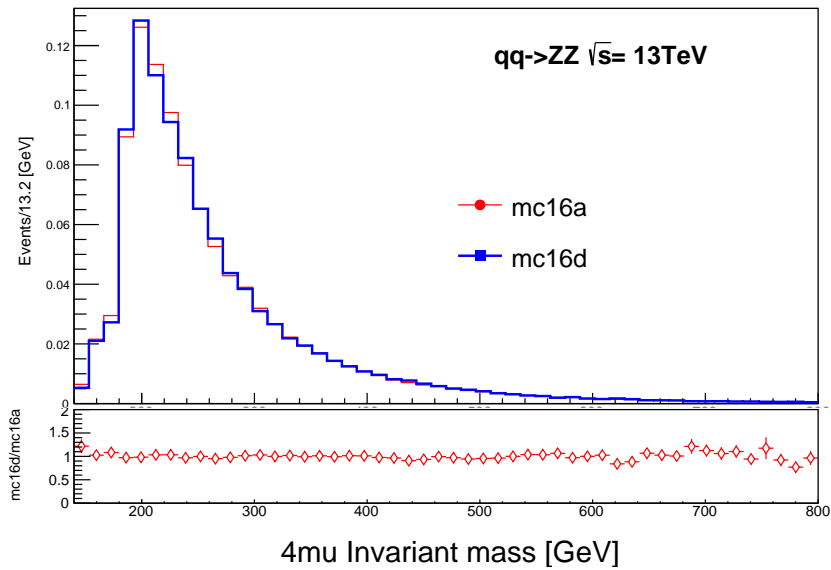
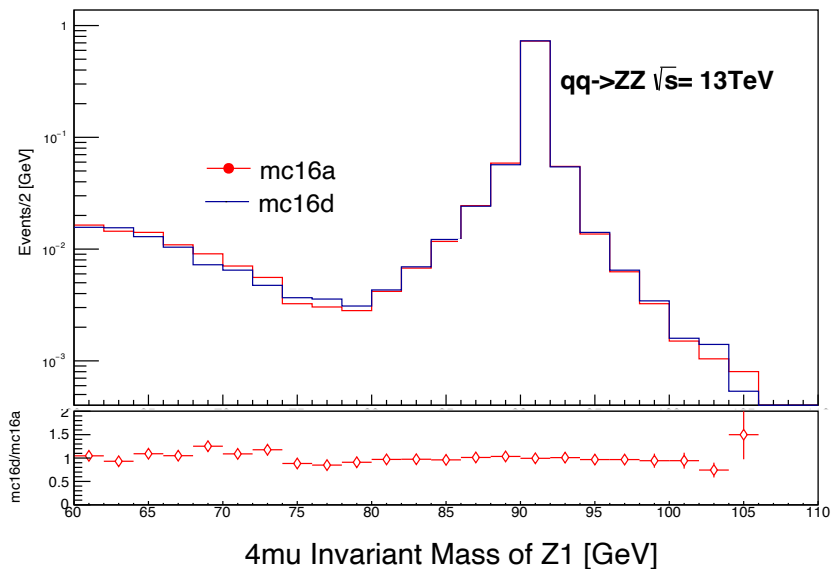
(a) Shape comparisons for $m_{4\ell}$ in the 4μ final state.(b) Shape comparisons for m_{Z_1} in the 4μ final state.

Fig. 5.6 Shape comparisons between mc16a and mc16d for m_{Z_1} and $m_{4\ell}$ for only the 4μ final state. The error bars in the ratio plots represent the statistical uncertainties in the ratio of the event counts.

that may suggest a marginal variation in the resolution of the electron channel or statistical fluctuations.

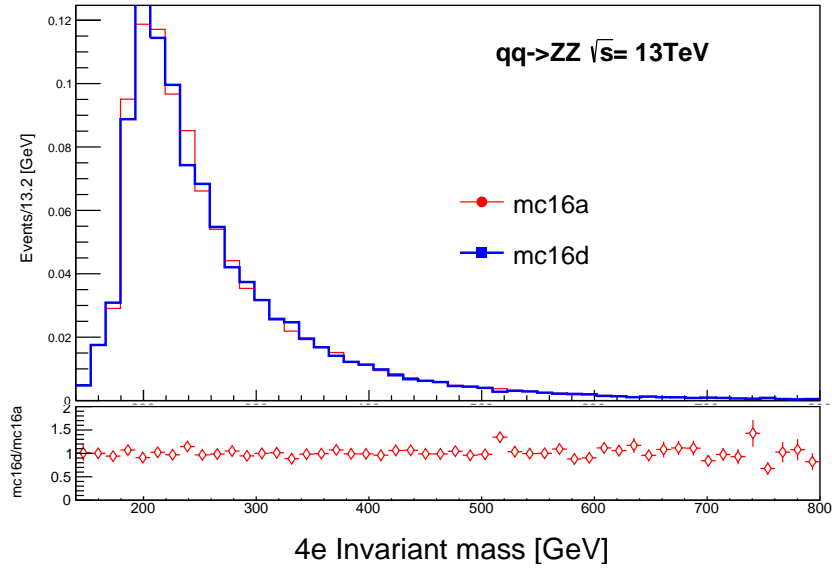
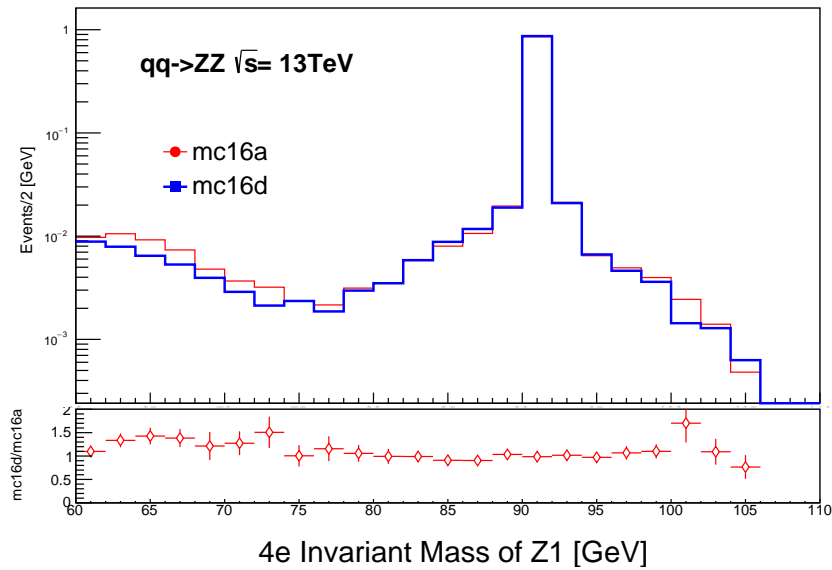
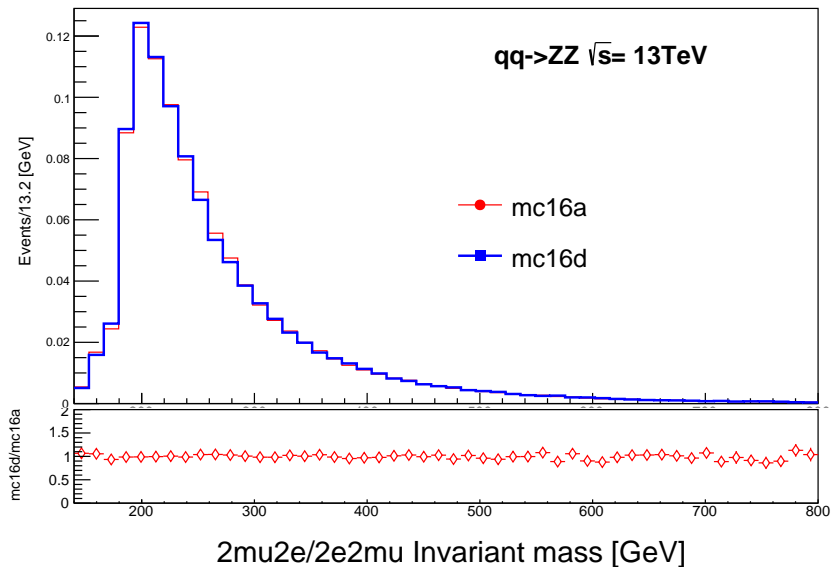
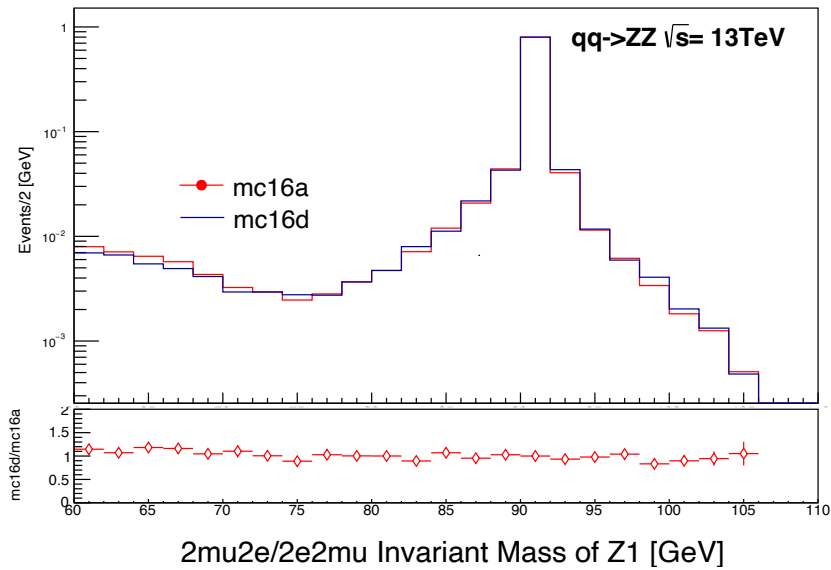
(a) Shape comparisons for m_{4e} in the $4e$ final state.(b) Shape comparisons for m_{Z_1} in the $4e$ final state.

Fig. 5.7 Shape comparisons between mc16a and mc16d for m_{4e} and m_{Z_1} for only the 4μ final state. The error bars in the ratio plots represent the statistical uncertainties in the ratio of the event counts.

Turning to the $2\mu 2e$ final state and examining the distributions of m_{4e} and m_{Z_1} in Fig. 5.8b, excellent agreement was observed between the mc16a and mc16d datasets for both variables.



(a) Shape comparisons for $m_{4\ell}$ in the $2\mu 2e$ final state.



(b) Shape comparisons for m_{Z_1} in the $2\mu 2e$ final state.

Fig. 5.8 Shape comparisons between mc16a and mc16d for m_{Z_1} and $m_{4\ell}$ for only the $2\mu 2e$ final state. The error bars in the ratio plots represent the statistical uncertainties in the ratio of the event counts.

This consistency across mixed final states underscores the reliability of cross-channel analysis, which often faces challenges in event reconstruction as a result of the distinct responses of

electrons and muons within the detector. The histograms reflect a high degree of consistency between the different MC samples and between the different decay channels. The peak positions for the Z mass are accurate, and the distributions' shapes suggest that the detector response and MC modelling are reliable. The absence of significant deviations suggests minimal systematic bias and excludes significant issues with the applied event selection criteria. These findings support the validity of the analysis framework and suggest that the pileup has been effectively managed, with no substantial influence observed on the mass resolution or event yield within the studied channels. This consistent performance across different final states and MC datasets reinforces confidence in the robustness of the analysis techniques and their potential to produce reliable physical interpretations.

5.7 Electron Isolation

5.7.1 Motivation

Most of the interesting physics signatures at the LHC require an accurate detection of leptons and photons that are prompt and non-fake, which is critical for exploring significant physics phenomena. Prompt particles are characterised by their origin and are distinct from products of hadron decay. The term non-fake refers to particles that are correctly identified; for instance, a true electron is not misidentified as another particle like a pion. Sources of incorrectly identified or non-prompt (fake) electrons include semi-leptonic decays of b and c quarks, photon conversions, and jets exhibiting substantial electromagnetic energy, leading to the formation of e^\pm or early showering events in the calorimeter. Several mechanisms can contribute to the presence of non-prompt or fake muons in the detector. These include semi-leptonic decays of bottom and charm quarks, decays of charged hadrons within the tracking volume or in hadronic showers, and punch-through particles originating from intense hadronic showers. Non-prompt or fake photons predominantly result from the decay of hadrons, particularly π^0 particles, or misidentified electrons. Prompt and non-fake leptons/photons typically exhibit isolation, meaning that they have minimal activity surrounding them. This necessitates defining a specific "isolation energy" to effectively separate them from non-prompt and misidentified objects. Photons, however, present a unique challenge in comparison to leptons. Prompt and non-fake photons can also be produced from quark fragmentation. The theoretical computation of such processes encounters limitations in the collinear limit, necessitating the application of some level of isolation in the theoretical computation. The isolation energy relies on data from both the tracker, which offers a more

pile-up-independent isolation, and the calorimeter, which detects neutral hadrons in addition to other particles. Typically, two separate isolation variables are computed using the data from these detectors. Many analyses employ one or both of these variables, with the latter being more powerful in most cases, except in highly boosted scenarios where calorimeter isolation becomes less reliable due to the limitations of cell size.

The particle flow algorithm, introduced not available in Run 1, combines tracker and calorimeter information, improving detection capabilities. Therefore, a particle flow isolation metric is also calculated for Run 2. Track isolation is more straightforward to handle because tracks can be readily associated with a specific particle and vertex. This allows for the subtraction of the lepton track and pile-up tracks. However, the subtraction of the lepton and pile-up in calorimeter isolation requires more complex adjustments, which are detailed in the following sections. During Run 1, isolation selection was individually optimised in each analysis, leading to a large number of efficiency estimations and data-MC SFs, calculated independently. However, in Run 2, a few central isolation WPs are provided, along with the associated efficiencies and SFs. Tools for recalculating these efficiency and SFs are also available for analyses that cannot use these predefined WPs.

This section explores reoptimisation studies aimed at reducing the pile-up dependence of lepton isolation variables. Specifically, this analysis considers two distinct regions of $m_{4\ell}$: a heavy Higgs boson mass (above 200 GeV) and low Higgs boson mass (in the range of 115-130 GeV).

5.7.2 Calorimeter-based isolation

The process of creating a calorimeter-based isolation variable begins with the identification of electron candidates, as detailed in Chapter 4. This involves the establishment of a cone, defined by a radius ΔR , centred on the location of the electron candidate cluster. In the initial stages of ATLAS operations, calorimeter-based isolation was determined by summing the transverse energies of cells within the calorimeters (including both electromagnetic and hadronic types), positioned within a cone aligned to the electron path. This sum excluded the energy contribution from the electron candidate itself. However, this approach proved to be ineffective against pile-up and exhibited inconsistencies between observed and simulated data. An improved method was developed that uses the transverse energies of topological clusters rather than individual cells, incorporating a noise reduction algorithm into the process [160].

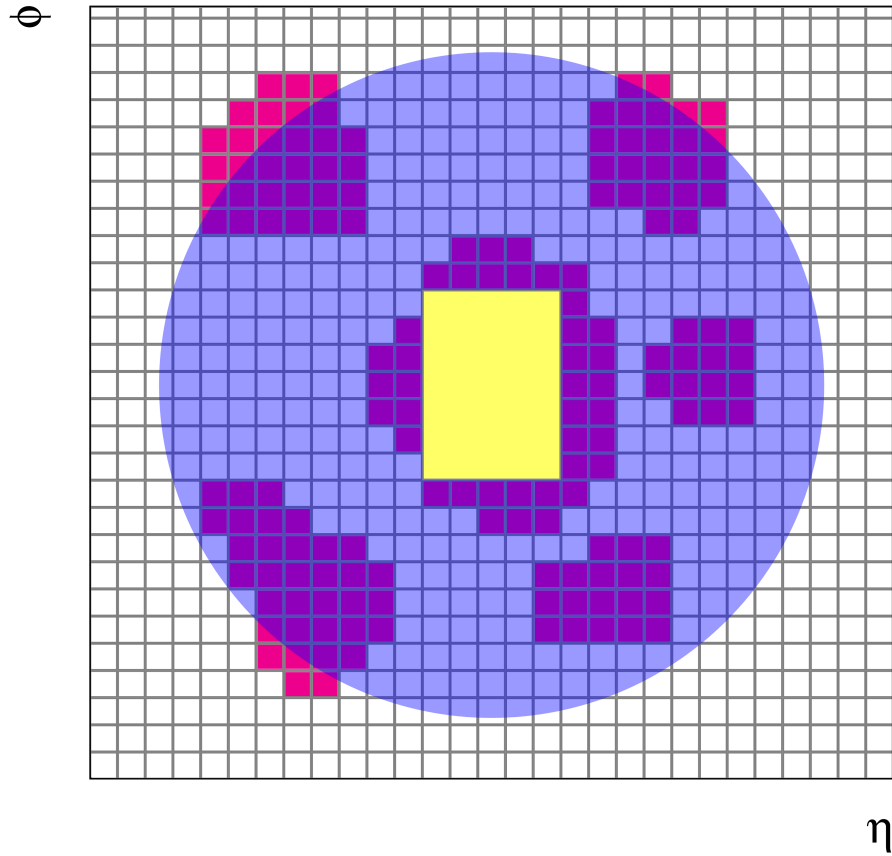


Fig. 5.9 E_T^{topocone} variable [161]. The grid depicts the second-layer calorimeter cells in η and ϕ coordinates. The central purple circle represents the lepton candidate, and the purple circle represents the isolation cone surrounding the lepton candidate. All topological clusters (red) with barycenters within this cone contribute to the isolation variable calculation. The yellow rectangle within the cone highlights the 5×7 core cell region (yellow) excluded in the core subtraction method.

Clusters of topological nature are identified as those surrounding cells where the energy scale of the electromagnetic interactions exceeds the anticipated noise levels by a factor greater than four, inclusive of both electronic noise and pile-up contributions. These clusters expand by incorporating neighbouring cells with energy over twice the noise threshold, extending through the various layers of the electromagnetic and hadronic calorimeters. This expansion continues until no adjacent cells meet the energy criteria, followed by the addition of a final layer of cells around the cluster. In particular, these clusters are employed in their raw form, based on the electromagnetic scale, without additional calibration. Calculating the isolation variable involves adding the energies of all topological clusters with positive energy and barycenters within the ΔR radius, as shown in Fig. 5.9.

The isolation energy, denoted as $E_{T,\text{raw}}^{\text{isol}}$, is composed of the candidate electron's core energy, $E_{T,\text{core}}$, which is subsequently removed. This removal is achieved by excluding the energy contribution within a predefined rectangular area (yellow in Fig. 5.9) ($\Delta\eta \times \Delta\phi = 0.125 \times 0.175$) surrounding the electron trajectory (central purple circle in Fig. 5.9). Although this subtraction approach is straightforward and is uniformly applied to both signal and background events, it has inherent limitations. Energy deposits by the candidate beyond the fixed rectangle may be erroneously attributed to activity, prompting the need for a leakage correction. This correction uses simulated single-electron samples to model the leakage energy profile using a Crystal Ball function. The Crystal Ball function is a probability density function that is used in high-energy physics to model the energy loss of particles. It combines a Gaussian core with a power-law tail, allowing for an accurate representation of the energy distribution, especially in the presence of tails. It was developed by the Crystal Ball Collaboration to fit the energy distribution of particles detected in their experiments. The most probable value of the function, μ_{CB} , is parameterized as a function of E_T to estimate the average leakage, $E_{\text{leakage}}(E_T)$, within individual η bins of the associated cluster.

5.7.3 Track-based Isolation

Electron candidates are identified and isolated on the basis of their surrounding activity in the tracker and calorimeter. Track-based isolation, termed p_T^{cone} , uses reconstructed tracks that pass specific criteria within a cone centred around the electron direction. The tracks must have a p_T exceeding 1 GeV and be confined within the active region of the ID, according to basic quality requirements. Selection optimisation used $t\bar{t}$ MC events containing candidate muons, prioritising tracks with minimal hits from the silicon detector and traversing the least number of inactive detector areas. To mitigate pile-up effects, a limit is imposed on the longitudinal impact parameter (z_0) relative to the reconstructed primary vertex. This limit, scaled by the polar angle of the track, restricts $|z_0 \sin \theta|$ to less than 3 mm. Figure 5.10 illustrates in detail the calculation of the pt cone.

Unlike calorimeter isolation, which is limited to cones larger than 0.2 radius due to cell size, the finer granularity of track information allows smaller cone sizes in the p_T^{cone} . However, in busy environments, some objects may be closely aligned with the lepton. To address this, a variable-size cone approach named p_T^{varcone} is adopted. This technique dynamically adjusts the cone radius based on the candidate's p_T , shrinking as p_T increases:

$$\Delta R = \min \left(\frac{10 \text{ GeV}}{p_T [\text{GeV}]}, R_{\text{max}} \right), \quad (5.1)$$

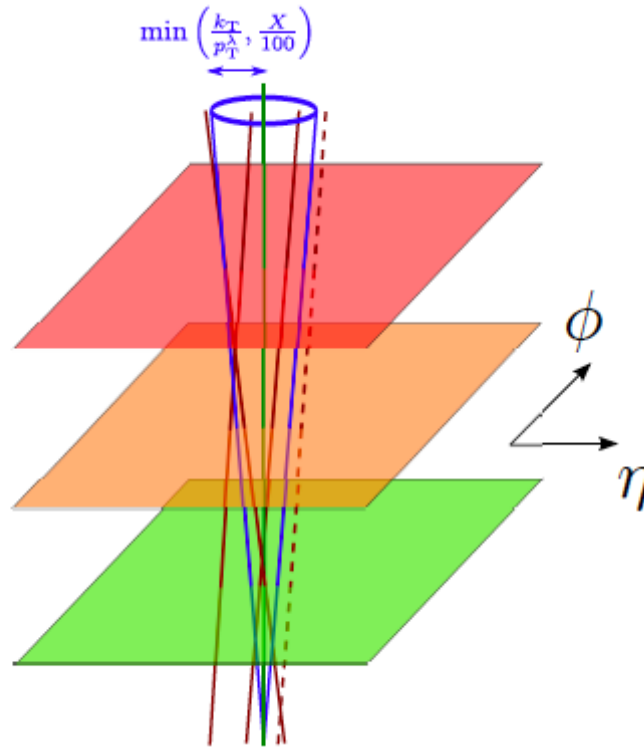


Fig. 5.10 A diagram of the p_T^{cone} variable. The cone is coloured blue, and all the favourable tracks (brown) around the object are selected. Objects that lie very far from the objects are not selected and are represented by the dotted lines. Taken from Ref. [162]

where R_{max} defines the upper limit for the cone size (typically 0.2 to 0.4). The 10 GeV value in the equation originates from simulations and aims to optimise background rejection. Note that ΔR is dimensionless, representing the angular separation in the $\eta - \phi$ plane.

5.7.4 Particle Flow Isolation

The particle flow algorithm was proposed to reconstruct all stable particles within the detector using tracker and calorimeter measurements. These include electrons, photons, muons, charged and neutral hadrons (the majority of which are pions, kaons, and neutrons). At low p_T , the tracker has shown better robust pile-up over the calorimeter and has also improved energy and momentum resolution. Therefore, it takes advantage of this by using the calorimeter's ability to reconstruct neutral particles simultaneously. To do this, a Boolean decision is made to use the tracker or calorimeter measurement for each particle, and if the tracker is used, the resulting particle energy should be subtracted from the calorimeter to avoid double counting. Details on the particle flow algorithm can be found in Ref. [163] and only a very short summary of the algorithm can be found here. In the first step, all detector components

are separated using standard reconstruction algorithms. The goal of an iterative tracking algorithm is to achieve high performance with a low false rate. First, select good quality tracks with $0.5 < p_T < 40$ GeV (above 40 GeV, the use of calorimeter measurement is more beneficial) [164, 163]. Since the particle algorithm is optimised for pions, electrons (with $p_T > 10$ GeV and passing a medium identification criterion) are omitted from the selection of tracks. Then one reconstructs topological clusters; it is important to note that these clusters are not intended to isolate energy deposits from various particles; they are meant to separate electromagnetic or hadronic energy showers of a different nature and to suppress noise. Therefore, a particle can produce multiple topological clusters most of the time, and one cluster can have contributions from several particles. Then, these topological clusters were optimised to react with pions. The tracks are then matched to clusters by extrapolating each track to the calorimeter. The distance $\Delta R'$ between the extrapolated track position and the barycenter cluster ($\Delta\eta$ and $\Delta\phi$), normalised by the expected standard deviation of cells in a cluster of pions σ_η and σ_ϕ , is calculated as follows:

$$\Delta R' = \sqrt{(\Delta\eta/\sigma_\eta)^2 + (\Delta\phi/\sigma_\phi)^2}. \quad (5.2)$$

The closest cluster with $E_{cluster}/p_{track} > 0.1$ in $\Delta R'$ is considered for subtraction. The energy of a cluster being below the anticipated $E_{cluster}/p_{track}$ ratio by an amount greater than the standard deviation of $E_{cluster}/p_{track}$ indicates that the particle's energy may be dispersed across multiple topological clusters. This ratio is established based on single-particle samples, classified according to η , the initial particle's energy, and the calorimeter's showering region. Under such circumstances, an ensemble of clusters, positioned within a radius of 0.2 around the track's extended path, are aggregated to adjust the energy calculation. Finally, if the closest cluster is further away than 1.64, no subtraction is made.

The next step is energy removal. If the energy of the matched clusters is less than predicted $E_{cluster}/p_{track}$, then the entire set is removed. In contrast, cell-by-cell subtraction is performed between selected cell rings in each layer by scaling down some of the ring cell energy to achieve the expected energy that should be removed. The remaining cells are also removed if they are compatible within 1.5 widths of the predicted $E_{cluster}/p_{track}$, or otherwise they are retained as the remaining cluster. The selected tracks (charged pflow objects) and remaining clusters (neutral pflow objects) should therefore represent the reconstructed event at the end of the algorithm, without double counting of energy. The particle flow isolation is made up of two parts: the charged component, which aligns with the track isolation detailed previously in Section 5.7.3 (that is, it does not require reconstruction and standard track isolation metrics

apply) and the neutral component, termed `nflowisol`. This neutral part is assembled using neutral energy flow objects. The methodology for constructing `nflowisol` parallels the approach to calorimeter isolation, as outlined in Section 5.7.2, although with the substitution of neutral energy flow objects for raw topological clusters.

5.7.5 Performance studies of the WPs

To identify the optimal isolation WP for the analysis, the focus was on maintaining equilibrium between signal efficiency, minimising background interference, and ensuring robustness against pile-up effects. A range of types of cuts was examined and categorised into three main groups. These groups were divided into two models to assess the trade-off between efficiency and statistical significance. The simplest of these models are the `TrackOnly` versions, which are preferred due to their enhanced resistance to pile-up, primarily when using track isolation over calorimeter isolation. The inclusion of two different models facilitates an evaluation of the trade-off between operational efficiency and statistical significance.

Subsequently, mixed WPs were explored. One such WP, known as `FixedCutLoose`, represented the standard approach used in previous studies. Looking for improvement, the analysis also evaluated `FixedCutHighMuLoose`, a modified variant that offers better pile-up resilience. Finally, the analysis introduced a novel WP named `FixedCutPflowLoose`, which utilises a triangular cut based on combined information from the transverse momentum variable within a cone (p_T^{varcone}) and the particle flow calorimeter isolation variable (`nflowisol`). This innovative approach was designed to optimise the trade-off between efficiency and pile-up mitigation. Optimising these cuts involved scanning for maximum significance, incorporating a significance measure that accounted for the reducible background uncertainty, set conservatively at 100% or 200%. The significance was calculated using the following equation shown below:

$$Z_A = \left[2 \left((s + b) \ln \left(\frac{(s + b)(b + \sigma_b^2)}{b^2 + (s + b)\sigma_b^2} \right) - \frac{b^2}{\sigma_b^2} \ln \left(1 + \frac{\sigma_b^2 s}{b(b + \sigma_b^2)} \right) \right) \right]^{1/2}, \quad (5.3)$$

where s represents the number of signal events, b represents the number of background events, and σ_b represents the uncertainty in the background estimate. Given that isolation selections are ineffective against the irreducible ZZ background, this factor was not included in the analysis.

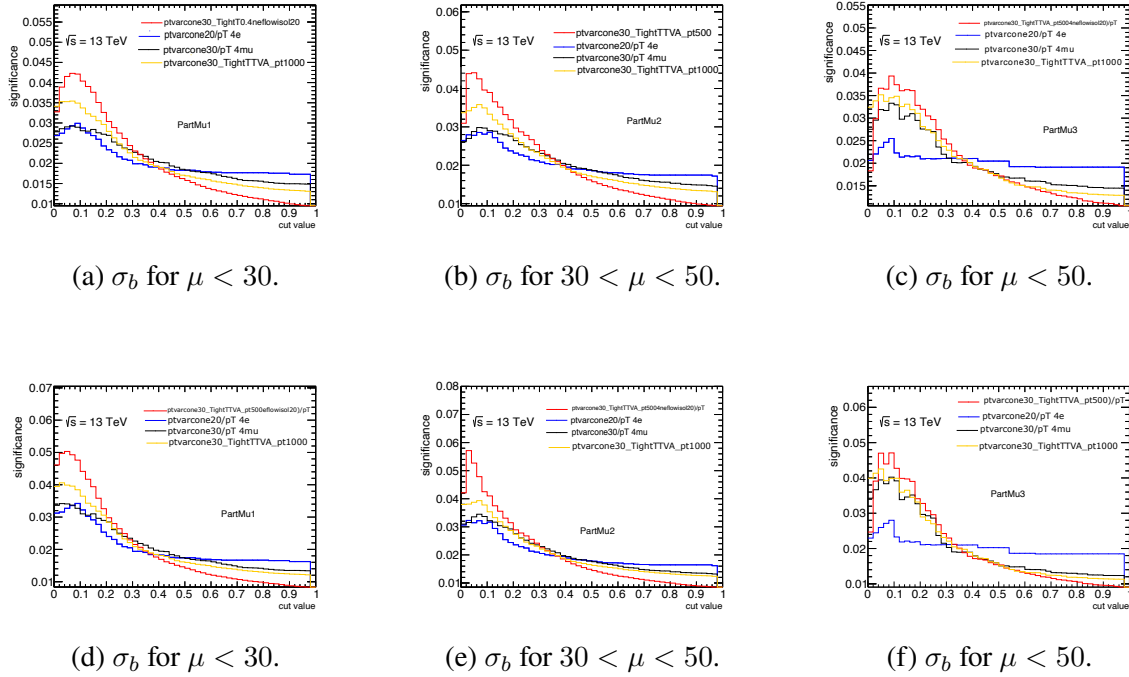


Fig. 5.11 Results of significance scans on the track isolation for ggH production for various values of the reducible background uncertainty and pileup (μ). Figures with 100% background uncertainty are shown in Figs. 5.11a, 5.11b, and 5.11c; those with 200% are shown in Figs. 5.11d, 5.11e, and 5.11f.

Given the significant impact of track isolation on simulated signal samples, particularly those representing primary signal types, the optimisation scan focused solely on this variable. Calorimeter isolation, with its relatively weak influence, was excluded from the scan. Figures 5.11 and 5.12 illustrate these scans for the production of ggH and ttH , respectively.⁴ The histograms illustrate the impact of varying levels of systematic uncertainty in the background (σ_b) on the statistical significance of signal detection. Each histogram corresponds to a different cut-off range for the variable μ , representing a specific characteristic of the signal. The levels of background uncertainty, represented by 100% and 200% of the μ value, were incorporated into the significance calculation to gauge the robustness of signal detection under different background conditions. The final category of isolation selections involved triangular cuts, which were derived through a two-dimensional scanning procedure plotting track and calorimeter isolation against each other. These cuts were derived from a two-dimensional scanning process, plotting the track against the calorimeter isolation. Two different isolating tracks methods are used: one is a robust pile-up version with a cut-off threshold of 0.5 GeV

⁴The 'cut value' on the x-axis is a dimensionless threshold from a 2D scan correlating track isolation (measured in GeV) and calorimeter isolation, used to optimise signal-to-background discrimination.

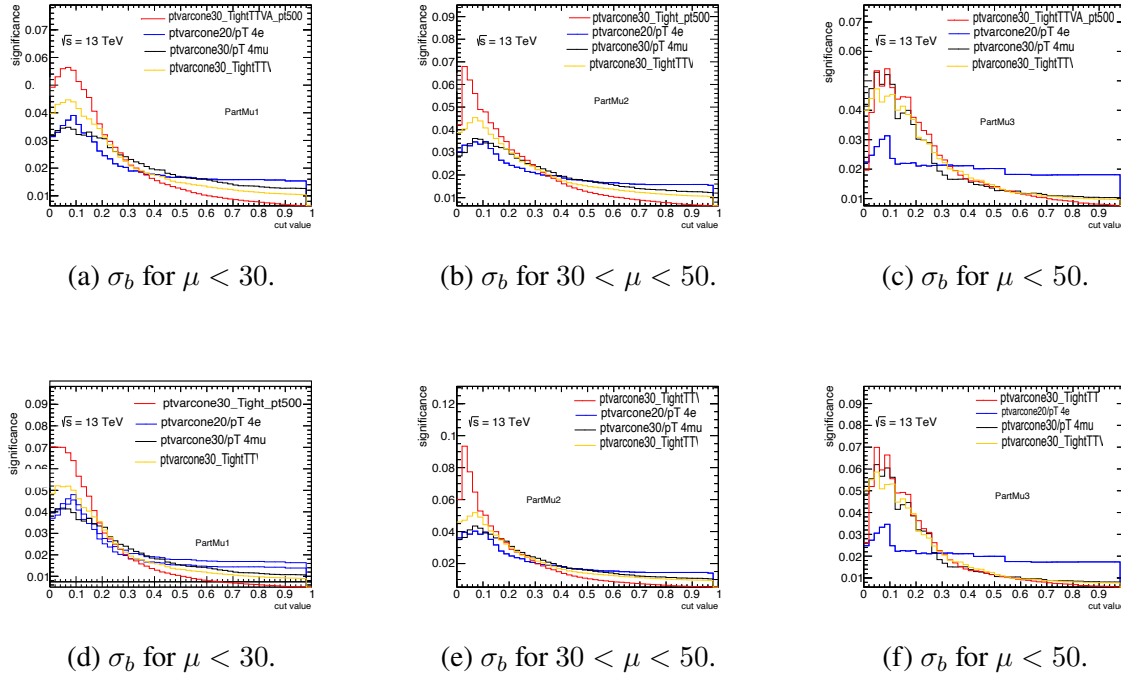


Fig. 5.12 Results of significance scans on the track isolation for ttH production for various values of the reducible background uncertainty and pileup with with 100% background uncertainty for Figs. 5.12a, 5.12b, and 5.12c and 200% for Figs. 5.12d, 5.12e, and 5.12f.

and a cone size of 0.3, while the other is a calorimeter isolation technique using E_T^{topocone} or particle flow with a cone size of 0.2.

Fig. 5.13 and Fig. 5.14 displays the example plots for each combination, specifically for muons. It should be noted that a separate study was conducted for electrons, but the results were so comparable that they were combined to obtain the final conclusion. These figures clearly demonstrate that signal distributions can be divided into two distinct components: a "bump" that can be effectively selected using a triangle cut of the type $\frac{1}{a} + \frac{1}{b} < 1$, where a and b represent the track isolation (p_T^{varcone}) and the calorimeter isolation (E_T^{topocone}), respectively. The "bar" component, on the other hand, requires a cut in calorimeter isolation alone, with the p_T^{varcone} being exactly zero. The methodology involves performing a two-dimensional significance scan to enhance the accuracy of the bump cut, followed by a one-dimensional scan to optimise the bar.

Figure 5.17 illustrates the effectiveness of various candidate selection criteria, presented as a function of the average number of interactions per bunch crossing ($\langle \mu \rangle$). These criteria demonstrate their potential to differentiate between signal and background events. However, finalising isolation selection demands a data-driven, comprehensive assessment of reducible

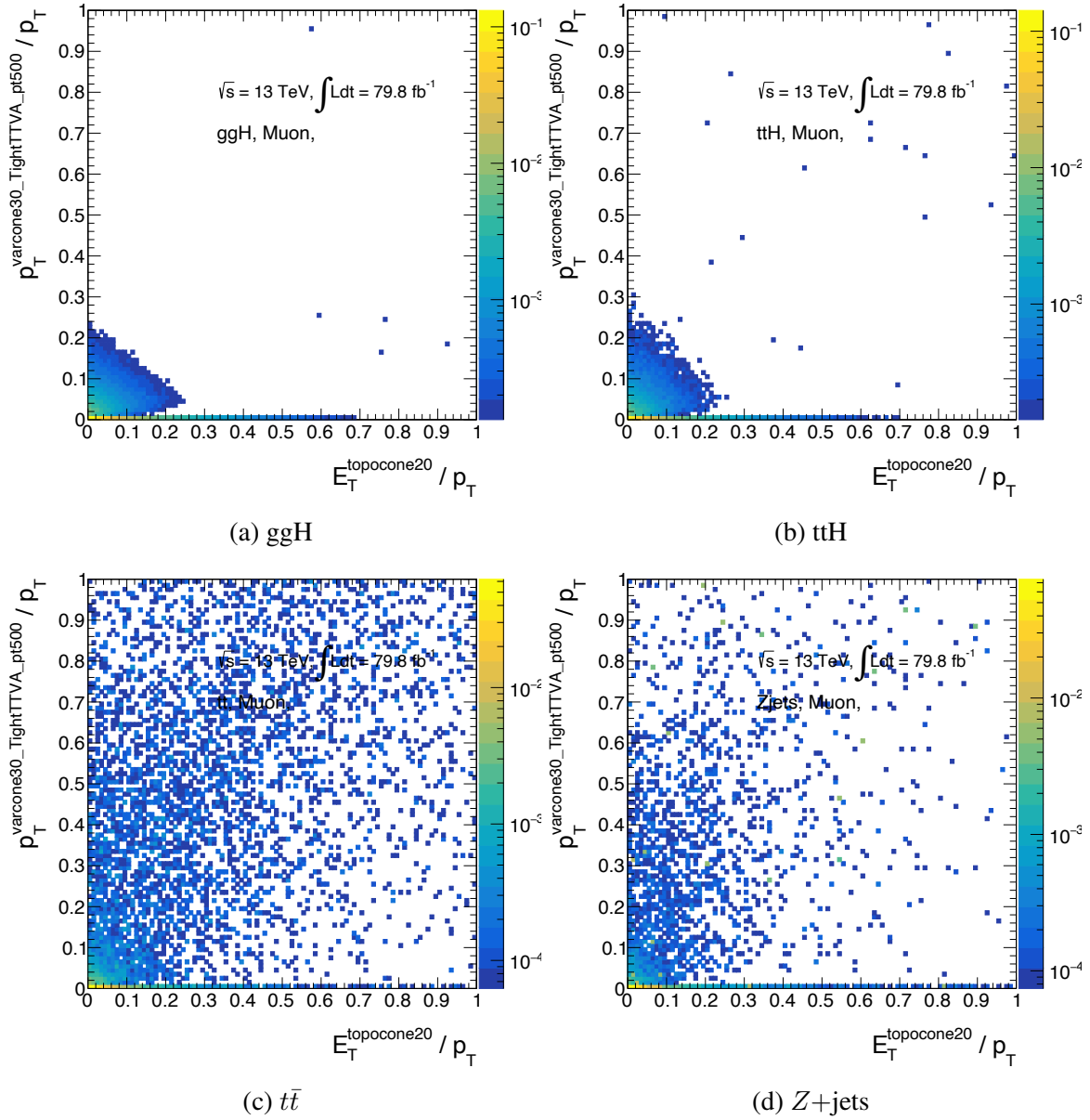


Fig. 5.13 Comparison of transverse momentum isolation within a cone of radius 0.3 ($p_T^{\text{varcone30}}$) to transverse energy in a cone of radius 0.2 ($E_T^{\text{topocone20}}$) for 4μ events in ggH, ttH, $t\bar{t}$, and Z+jets production processes.

backgrounds, which Section 6.3 elaborates on. While simulations aid in initial optimization, only the actual background calculation can precisely evaluate the impact of these selections. Since these are experimental WPs, they lack the overlap removal necessary to guarantee that a single lepton within a quadruplet doesn't contribute to the isolation of other quadruplet

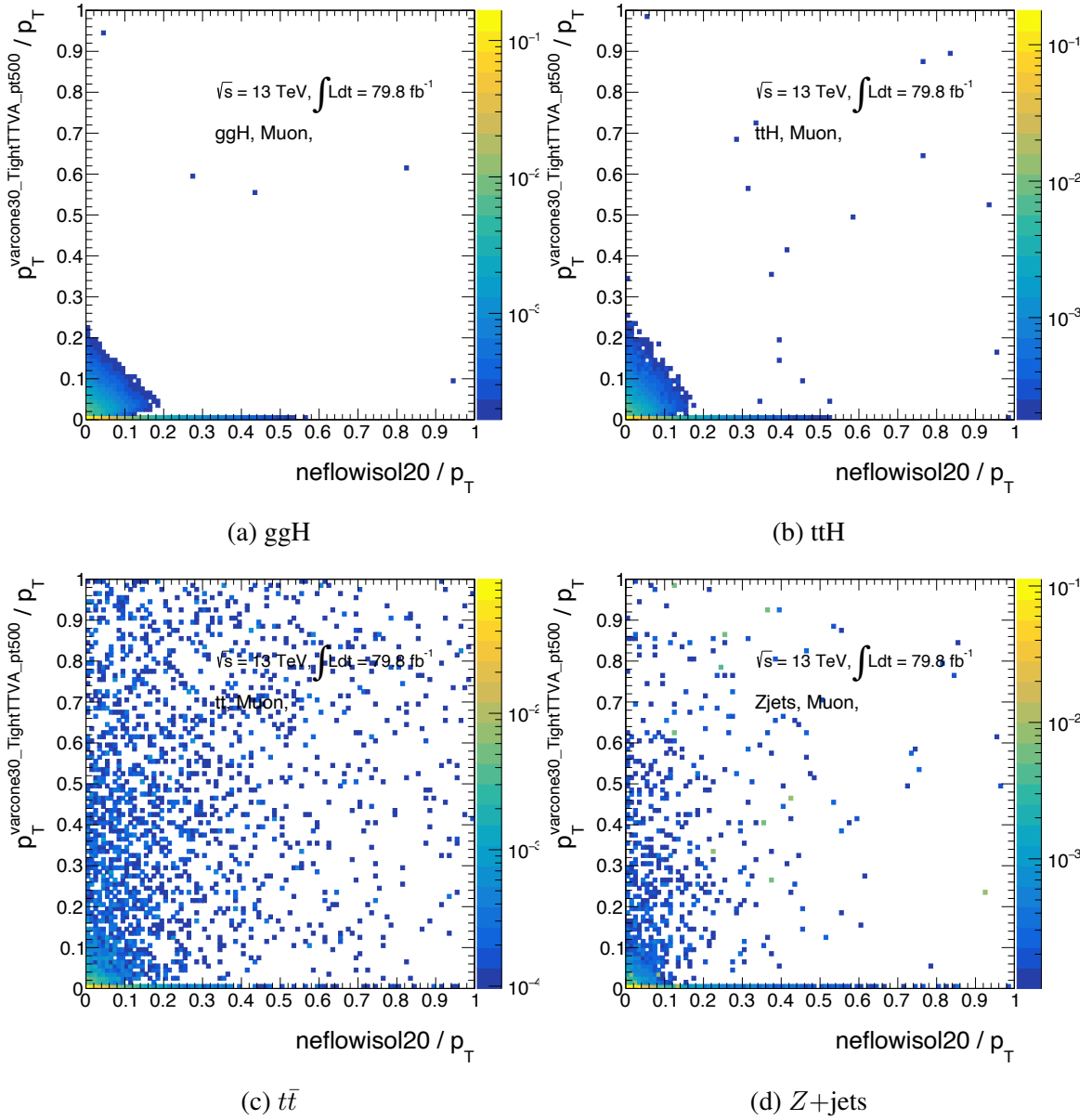


Fig. 5.14 Correlation between transverse momentum isolation within a cone of radius 0.3 ($p_T^{\text{varcone30}}$) and particle flow calorimeter isolation (neflowisol20) for 4μ channels in ggH , ttH , $t\bar{t}$, and Z + jets production.

members. To address this potential bias, a modified ΔR parameter, increased to 0.3, is utilized in this scenario potentially reducing overall efficiency, but ensuring a fair comparison between potential WPs.

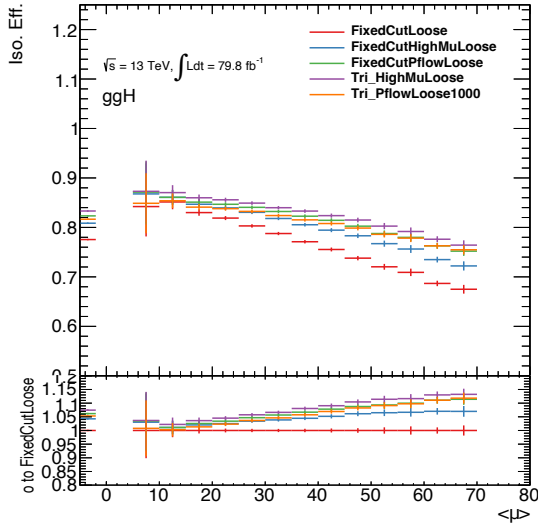


Fig. 5.15 ggH

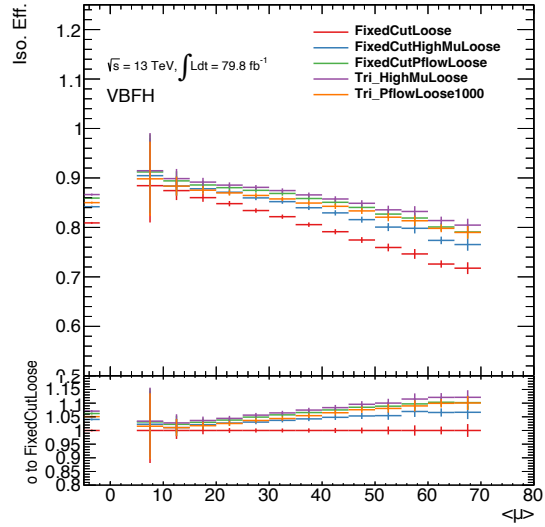


Fig. 5.16 VBF

Fig. 5.17 Efficiency vs. average number of interactions ($\langle\mu\rangle$) for signal and background samples for several isolation WPs for the ggH and VBF processes. The error bars in the ratio plot (bottom panel) represent the statistical uncertainty in the efficiency measurements relative to the FixedCutLoose working point.

Isolation selection	Signal	$qqZZ$	$t\bar{t}$	Z +jets	Significance
FixedCutLoose	34.027	15.108	0.260	1.230	6.754
FixedCutPflowLoose	35.811	16.945	0.329	1.841	6.897
FixedCutPflowLooseOp3	40.499	19.125	0.890	3.328	7.274
Tri_PflowLoose1000	35.488	16.628	0.258	1.588	6.898
Tri_HighMuLoose	35.995	16.999	0.219	1.731	6.935
TrackOnlyOp20	39.653	18.915	0.778	2.925	7.185

Table 5.2 Comparison of yields and significances for different isolation criteria, with reducible ($ll\mu\mu$) background calculated via Monte Carlo simulation and signal extracted from simulation.

Table 5.2 presents the reducible background yields and the corresponding significances for promising isolation selections within the $ll\mu\mu$ channel's $115 < m_{Al} < 130$ GeV mass range. Given the varying impact of isolation across categories with diverse activity levels, it is critical to confirm that WPs effective in the dominant 0-jet category translate to success in others. An extensive evaluation concluded that FixedCutPflowLoose WP demonstrated the best or near-best performance in all tests, securing its selection for further analysis.

5.7.6 Optimisation of isolation criteria and final results with scale factors

Although the above results guide the decision on the appropriate WP, a critical effect remains unaccounted for. Calculating significance after applying isolation selection implicitly assumes an equal impact on both the data and the MC simulation. However, this assumption is not entirely valid. A discrepancy was identified between the simulated and observed isolation efficiency. To address this, the final results incorporate SFs applied to the simulated events, effectively adjusting the simulated efficiency to match the values observed in the data.

This analysis leverages the tag-and-probe (T&P) technique, a well-established approach detailed in Ref. [165, 166], to directly measure the effectiveness of electron selection criteria. T&P relies on the decays of the Z boson into pairs of electrons. As described in Section 5.7.7, the method involves identifying one electron with strict criteria (the "tag"). The other electron (the "probe") serves as a benchmark for evaluating the selection efficiency. Both electrons must share an invariant mass consistent with the Z boson mass, and, when relevant, timing information from the reconstructed vertex is also considered. This method guarantees a fair sample, allowing each electron pair to contribute to the efficiency evaluation, where an electron may alternate between a probe and a tag in different pairs. Electron selection efficiency depends on multiple sub-efficiencies, each calculated relative to the preceding step. Both data and Monte Carlo simulations are used to evaluate these efficiencies. To account for discrepancies in electron modelling across different physics experiments, SFs are introduced. These factors represent the ratio of efficiencies between data and MC simulations. Electron efficiency varies with both transverse momentum and pseudo-rapidity. Therefore, SFs are measured as a two-dimensional array within the E_T - η space:

- 20 bins in η : [-2.47, -2.37, -2.01, -1.81, -1.52, -1.37, -1.15, -0.80, -0.60, -0.10, 0.00, 0.10, 0.60, 0.80, 1.15, 1.37, 1.52, 1.81, 2.01, 2.37, 2.47]
- 13 bins E_T : [4.5, 7, 10, 15, 20, 25, 30, 40, 45, 50, 60, 80, 150, 200, 250, 300, 350, 500] GeV

Dataset-specific variations in the electron isolation SFs were evaluated for each year from 2015 to 2018 in the context of the present analysis. To achieve a spectrum of signal efficiencies within the $H4\ell$ channel, three distinct WPs were implemented: Tight, Medium, and Loose. Notably, the stringent selection criteria inherent to the Tight WP naturally encompass the looser requirements of the Medium and Loose WPs.

5.7.7 Tag and Probe with $Z \rightarrow ee$

The Tag and Probe technique uses ZZ decays to create a dataset of "clean" $Z \rightarrow ee$ electron candidates with a E_T above 15 GeV. This dataset allows for assessing the effectiveness of electron identification across various operating points. However, substantial background contamination, especially for lower E_T ranges (< 25 GeV), necessitates statistical background subtraction. Two complementary approaches address this background challenge:

- **Mass-based method:** This method utilises the invariant mass of the tag-probe pair as a key variable to distinguish background events.
- **Isolation-based method:** This method contrasts the signal with the background based on the calorimetric isolation distribution of the probe electron.

Although seemingly different, these techniques can be viewed as variations of the common theme of measuring electron identification efficiency with systematic control of background contributions.

5.7.8 Discussion on experimental systematic uncertainties

Systematic uncertainties are critical to the accurate interpretation of electron identification efficiencies and scale factor results. These uncertainties can arise from several sources, including theoretical uncertainties associated with background processes and experimental uncertainties related to the reconstruction, identification, and measurement of electron energy and momentum.

The systemic uncertainties in this analysis were evaluated by comparing the nominal event yield with the yield after applying modified weights to the quantities of interest. The nominal yield, denoted as ΣA , is derived from the integral of the invariant mass ($m_{4\ell}$) spectrum after all weights are applied. The modified yield, ΣB , incorporates adjusted weights according to the agreement between data and MC. The relative systematic uncertainty is calculated as $|(\Sigma A - \Sigma B)/\Sigma A|$ and is expressed as a percentage. This method ensures that uncertainties reflect changes in the event yield due to systematic variations, providing symmetric uncertainties when comparing the yields with the ± 1 standard deviation (σ) from the nominal yield.

For instance, systematic uncertainty on the energy scale for electrons (or momentum scale for muons) was assessed by shifting the energy/momentum of leptons by a scale factor derived from data-MC agreement. This adjustment was made prior to event selection and the impact of

this scale factor on the number of events in the final state was then observed. This procedure, often referred to as “smearing,” involved applying a nominal scaling value and scaling values with $\pm 1\sigma$. In cases of electron or muon resolution, this shifting procedure accurately reflects potential calibration inaccuracies. Systematic uncertainties were calculated using the recommendations from the Combined Performance groups, encompassing a standard set of 195 nuisance parameters for high-mass analyses, which can be expanded to 353 nuisance parameters for mass analysis using the fully decorrelated E-Gamma model.

5.7.9 Efficiency and scale factor results

Single-electron isolation efficiencies are presented for two WPs in Figs. 5.18 and 5.19. These figures show estimates in one-dimensional form obtained from data collected between 2015 and 2018, together with the corresponding ratios of data to MC simulations. The efficiencies are shown as functions of E_T , η , and the number of interactions per bunch crossing. Details on isolation WPs can be found in Ref. [167]. Calorimeter isolation undergoes a pile-up correction that significantly reduces its dependence on isolation efficiency, decreasing it by approximately a factor of five. The results presented here are derived from a sample enriched with $Z \rightarrow ee$ events, where the electrons satisfy the Tight or Medium identification criteria for the first η bins.

When directly comparing the provided data and the output of the Monte Carlo simulation, the observed difference generally remains within a range of 1 - 5%. However, it is important to note that this value can fluctuate depending on the specific isolation WP used. However, there is a notable divergence in the low-electron E_T region ($E_T < 100$ GeV), while data and simulation converge at higher E_T values. Uncertainties in the overall scale factor range from approximately 5% for low- E_T electrons to less than 0. 5% at high E_T . For Medium and Tight WPs, the efficiencies exceed 70% for $E_T > 10$ GeV and approach 90% at higher E_T . Analysis of the FixedCutPFlowLoose WP revealed that while the event rate for electron-based events improves, the gains are largely offset by a reduction in the efficiency for specific categories. In particular, the event rate for 4e events decreased slightly due to the influence of the scale factor for low- p_T electrons on the efficiency of events with a subleading electron pair. Table 5.3 further illustrates this effect, showing the increase in the total ggF signal and each of the four final states with and without the applied SFs. Despite the slight decrease in 4ℓ events, the improvement remains beneficial due to the higher isolation efficiency of muons in the data compared to MC. This, along with the expected increase in improvement with higher pileup, highlights the potential of this WP in pileup-intensive conditions.

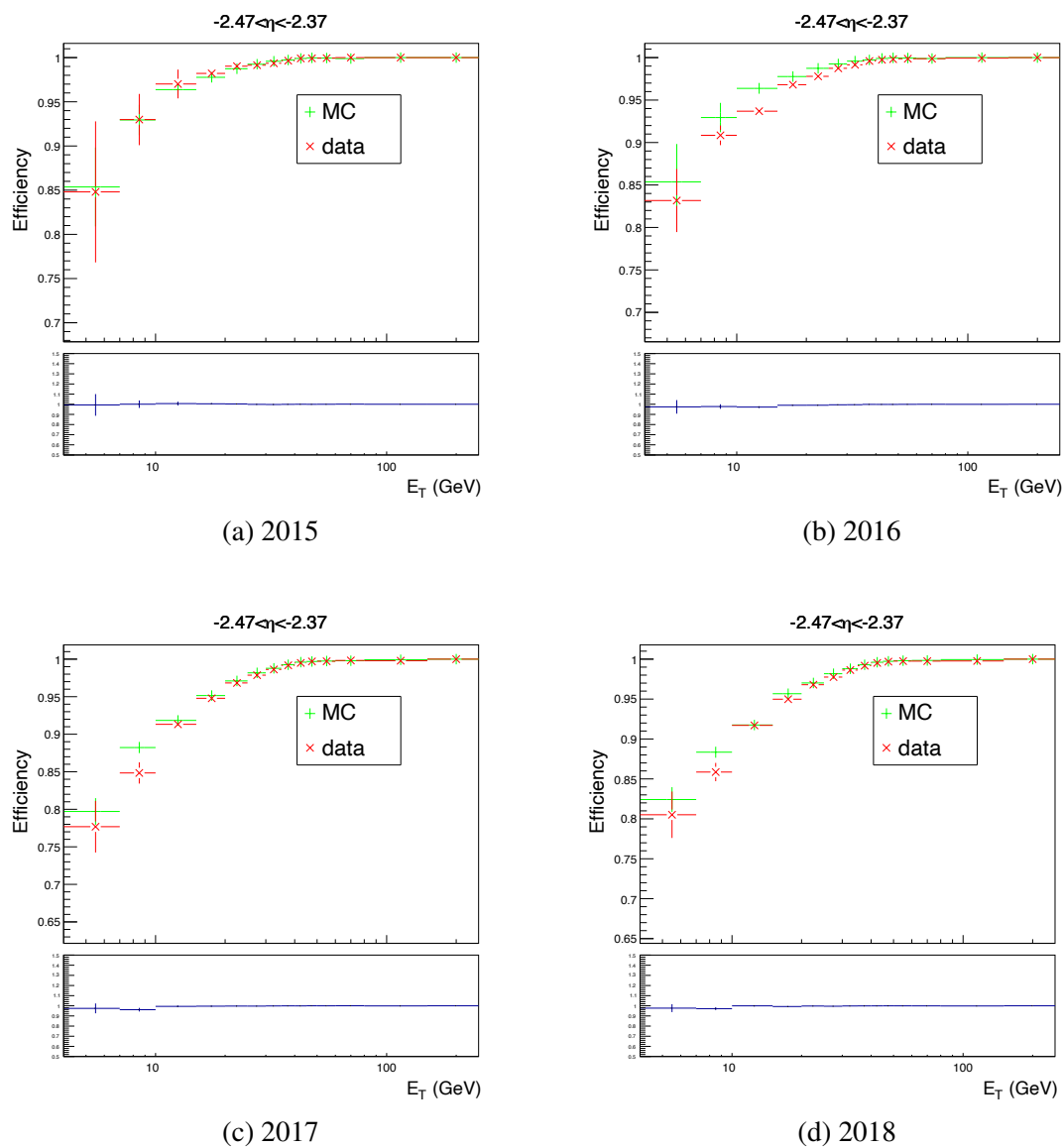


Fig. 5.18 Electron identification efficiencies $-2.47 < \eta < -2.37$, measured in $Z \rightarrow ee$ for 2015 - 2018 datasets using the Tight identification WP. The error bars in the ratio plot (bottom panel) represent the statistical uncertainty in the efficiency measurements.

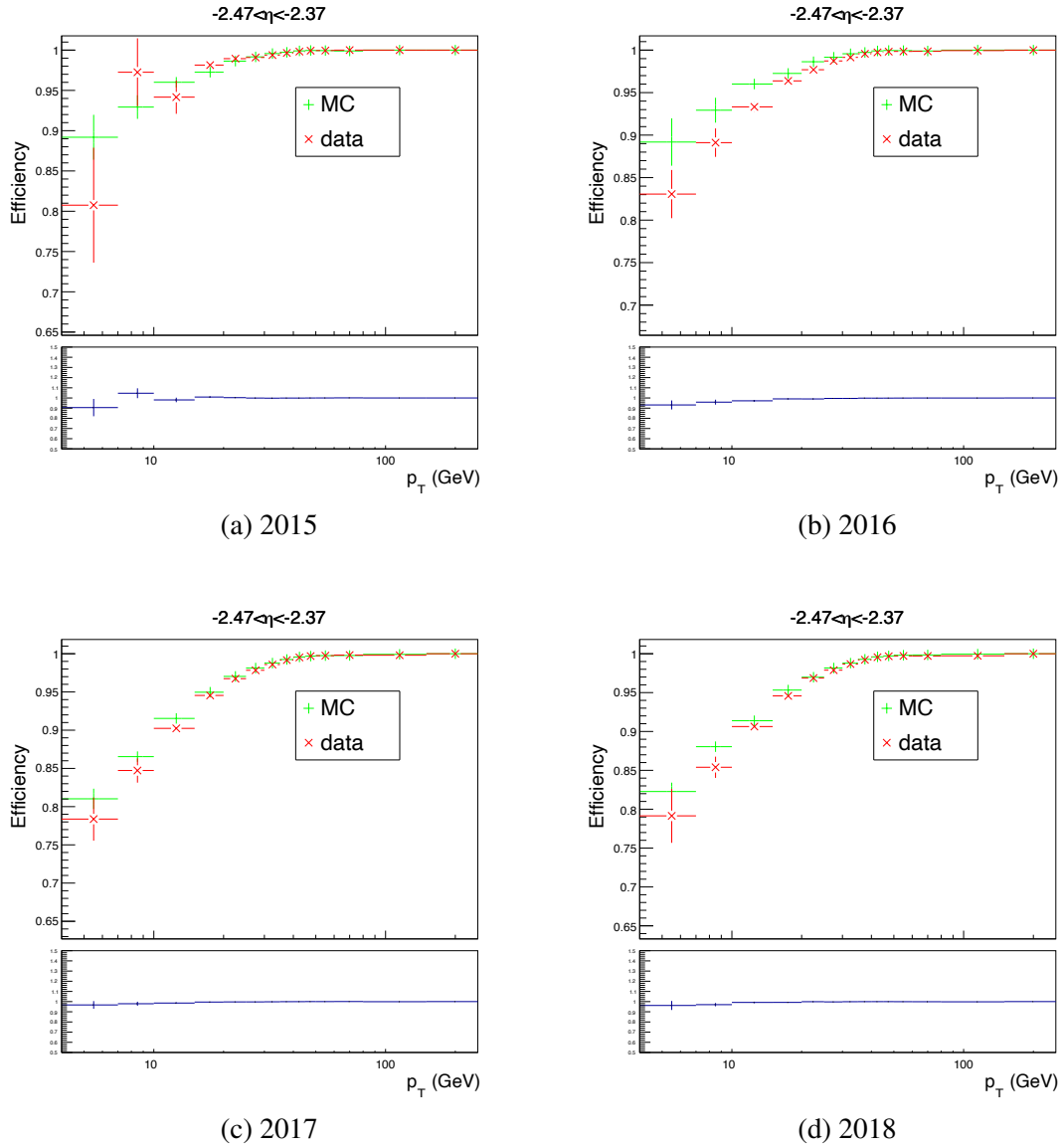


Fig. 5.19 Electron identification efficiencies $-2.47 < \eta < -2.37$, measured in $Z \rightarrow ee$ for 2015 - 2018 datasets using the Medium identification WP.

	Percent increase with scale factors			Percent increase without scale factors		
	mc16a	mc16d	mc16e	mc16a	mc16d	mc16e
all	3.0 ± 0.3	4.8 ± 0.5	5.6 ± 0.6	2.4 ± 0.2	4.6 ± 0.5	5.2 ± 0.5
4μ	6.8 ± 0.7	9.9 ± 1.0	10.2 ± 1.0	3.8 ± 0.4	6.9 ± 0.7	7.1 ± 0.7
4e	-1.8 ± 0.2	-1.6 ± 0.2	-0.1 ± 0.01	1.0 ± 0.1	2.5 ± 0.3	3.7 ± 0.4
$2\mu 2e$	0.4 ± 0.04	0.8 ± 0.08	2.4 ± 0.2	2.4 ± 0.2	3.7 ± 0.4	4.7 ± 0.5
$2e 2\mu$	3.3 ± 0.3	5.2 ± 0.5	5.4 ± 0.5	1.2 ± 0.1	3.4 ± 0.3	3.9 ± 0.4

Table 5.3 Change in the rate at which ggF events are reconstructed using the new ‘FixedCutPFlowLoose’ isolation WP for each MC simulation campaign, with and without the data-MC isolation efficiency scale factors. The error bars in the ratio plot (bottom panel) represent the statistical uncertainty in the efficiency measurements.

Chapter 6

Exploring higher-mass ZZ resonances in the 4ℓ final states

This chapter explores the potential decay of massive unknown particles ("heavy resonances") into pairs of Z bosons, ultimately leading to a final state with four leptons. The analysis uses a dataset of proton-proton collisions collected by the ATLAS detector at the LHC during 2015-2016. This dataset corresponds to roughly 36.1 fb^{-1} of data with a center-of-mass energy of 13 TeV. While Section 6.1 provides a general overview, Section 6.2 dives deeper into the specific criteria used to identify the necessary leptons. Subsequent sections tackle the challenge of background events: Section 6.3 evaluates their contributions, while Section 6.4 develops detailed models for both signal and background processes. A detailed analysis of the uncertainties arising from both experimental and theoretical sources is presented in Section 6.5. Finally, Sections 6.6 and 6.7 present the findings of the study, focusing on establishing limits on the production rates (cross sections) of hypothetical spin-0 and spin-2 resonances.

Indlovu ayisindwa ngumboko wayo.

E.W.M Mesatywa.

6.1 Research Analysis Outline

This chapter presents the combined results of a search for a hypothetical heavy resonance decaying into two Standard Model (SM) Z bosons, investigated through the $ZZ \rightarrow 4\ell$ and $ZZ \rightarrow 2\ell 2\nu$ final states. Although the focus is on the reconstructed 4ℓ channel, the analysis ultimately combines the results of both channels for better sensitivity. Higgs boson production is assumed to occur primarily via gluon-gluon fusion (ggF, sometimes referred to as $gg \rightarrow H$) and vector boson fusion (VBF, sometimes referred to as $qq \rightarrow H$), without assuming a specific model. Therefore, the results for $gg \rightarrow H$ and VBF production are interpreted separately. Events in both final states are classified into regions enriched with $gg \rightarrow H$ and VBF based on MC simulations, as described in detail here [122]. The search investigates a significant mass window, probing potential resonances from 200 GeV to 2000 GeV. The aim is to identify an excess in the distribution of $m_{4\ell}$, specifically within the 4ℓ channel. In the $\ell^+\ell^-\nu\bar{\nu}$ channel, where full reconstruction is not possible, the transverse mass (m_T) serves as the primary discriminant. The equation for m_T is given below:

$$m_T = \sqrt{\left[\sqrt{m_Z^2 + (p_T^{\ell\ell})^2} + \sqrt{m_Z^2 + (E_T^{miss})^2} \right]^2 - |\vec{p}_T^{\ell\ell} + \vec{E}_T^{miss}|^2}. \quad (6.1)$$

In this analysis, the potential existence of various resonance hypotheses is investigated. Firstly, a heavy scalar boson, denoted H , is examined within the framework of the Narrow Width Approximation (NWA). In this context, H is assumed to have a natural width comparable to that of the SM Higgs boson, which means that the resonance width is much smaller than the experimental resolution. Secondly, the study considers the Large Width Approximation (LWA), where H has a significant natural width. For LWA, the resonance width is a notable fraction of the mass, ranging from 1% to 15% of the Higgs boson mass, m_H . The fitting procedure accommodates different resonance widths by simultaneously fitting the mass spectra of various final states, ensuring that the fits account for the mass-dependent resolution and background variations. This approach allows for a comprehensive analysis of both narrow and broad resonances.

Within the Randall-Sundrum (RS) framework [168, 169], a spin-2 resonance emerges as a Kaluza-Klein (KK) excitation characterised by its mass, $m_{G_{KK}}$. This theoretical model addresses the hierarchy problem by introducing additional spatial dimensions where SM fields propagate, leading to a hierarchy of KK excitations, including spin-2 gravitons [170] at the TeV scale. The crucial parameter in the RS model is $k/\bar{M}_{\text{Planck}}$, the ratio of the extra-dimensional

curvature scale (k) to the reduced Planck mass ($\bar{M}_{\text{Planck}} = M_{\text{Planck}}/\sqrt{8\pi}$). Here, k represents the curvature of the extra dimension, which determines the separation of the KK modes. This study adopts a typical value of 1 for this parameter. Typically, RS model gravitons exhibit strong couplings to all SM fields, hindering their extra-dimensional propagation. However, this study employs a simplified "bulk RS" model in which SM fields extend into these extra dimensions, known as the "bulk". This approach significantly suppresses graviton couplings to light fermions, leading to reduced VBF production rates and lower branching fractions to leptons and photons. Consequently, ggF becomes the dominant production mode. In this simplified bulk RS model, $k/\bar{M}_{\text{Planck}}$ remains the only free parameter, typically set to 1. The lack of noticeable anomalies in both the $m_{4\ell}$ and m_T spectra establishes upper bounds on the product of the production cross section and branching fraction, denoted as $\sigma \times B(H \rightarrow ZZ)$, for heavy resonances. This scalar search primarily targets a heavy Higgs boson (H) produced via VBF and ggF processes. Although the relative contributions of these processes remain uncertain without a specific model, separate constraints are imposed on both $\sigma_{\text{VBF}} \times B(H \rightarrow ZZ)$ and $\sigma_{\text{ggF}} \times B(H \rightarrow ZZ)$ for a more comprehensive analysis. In the search for narrow resonances, the established upper bounds in $\sigma \times B(H \rightarrow ZZ)$ are converted into exclusion graphs based on the framework of the Two-Higgs-Doublet Model (2HDM), as discussed in Ref. [171]. Additionally, these constraints are applied to the RS model to limit the combined production cross section and branching fraction of a spin-2 graviton.

Based on a previous study [172] that identified two potential excesses in the 4ℓ channel, this analysis presents an updated search based on 2018 data with significantly improved sensitivity. The previous work detected events exceeding 3.6σ local significance at 240 and 700 GeV under the assumption of ggF production, with global significance of 2.2σ . These excesses showed a distinct channel dependence: the 240 GeV signal primarily concentrated in the $4e$ channel, while the 700 GeV signal appeared across all channels and categories. In particular, the $2\ell 2\nu$ search subsequently excluded the 700 GeV excess at 95% confidence level (CL), highlighting its greater sensitivity in that mass range. To provide more clarity on these findings, the present investigation significantly improves the 4ℓ search using several key advances. Initially, it used all the integrated luminosity data obtained during LHC Run 2, resulting in a substantial increase in the accessible dataset. Second, it employs a sophisticated multivariate approach for the categorisation of ggF and VBF event categorisation, replacing the previous cut-based definition. This refined approach improves signal sensitivity while simultaneously mitigating pile-up effects through enhanced lepton reconstruction and isolation techniques. Additionally, the analysis benefits from a pflow algorithm for improved jet reconstruction and

uses data-driven normalisation for the SM background instead of relying solely on predictions. Finally, the search range extends up to 2000 GeV for signal masses, allowing exploration of a broader theoretical landscape.

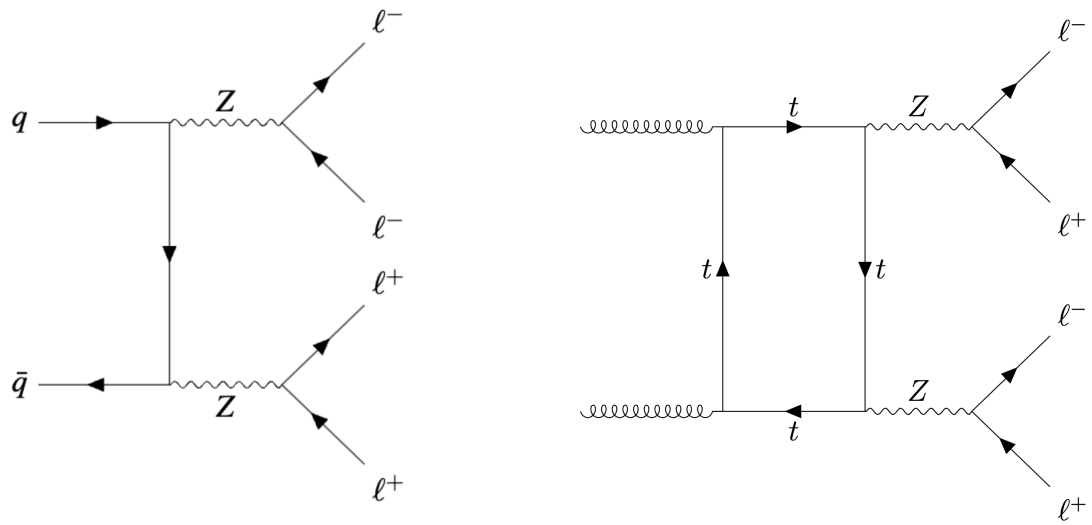
6.2 Event Selection

Pre-selection of candidate 4ℓ events for further analysis is achieved through a two-step process. First, a general model-independent criterion, as detailed in Chapter 5.5, identifies promising events based on predefined characteristics. This preselection identifies promising events for further analysis. Subsequently, the pre-selected events are categorised into distinct production modes, such as VBF and ggF. This categorisation uses multivariate classifiers to enhance sensitivity to NWA signals by exploiting specific correlations and patterns for each production mode. Typically, these multivariate classifiers are trained using a particular signal model, resulting in a level of dependence on the model. In addition, a cut-based event categorisation is taken into account for this analysis.

6.3 Background estimation

When considering the 4ℓ final state, the dominant source of background events is non-resonant ZZ production, contributing to 97% of anticipated events. The source of this background is primarily the interaction between the quark and the antiquark, which contributes to 86% of the cases. Furthermore, the processes initiated by the gluons play a significant role, making up 10% of the background. Electroweak vector boson scattering, though less prevalent, still contributes 1% to the background spectrum. In particular, the significance of the latter increases within the category enriched with VBF, reaching 20% of the total background. MC simulations effectively model these backgrounds (Section 5.2). The Z + jets and $t\bar{t}$ processes contribute an additional background at the percentage level; however, their impact is relatively minor. These backgrounds exhibit a steeper decrease in their contribution compared to non-resonant ZZ production as the $m_{4\ell}$ increases. Data-driven approaches are used for their estimation, using different techniques for final states containing a dimuon ($\ell\ell + \mu\mu$) or a dielectron ($\ell\ell + ee$) as the subleading pair, as detailed in Ref. [173]. Feynman diagrams that illustrate the two primary background processes of the SM are presented in Fig. 6.1.

Specific to the $\ell\ell + \mu\mu$ channel, non- ZZ backgrounds originate primarily from the $t\bar{t}$ and Z + jets processes. In these cases, the origin of muons is predominantly related to the semileptonic



(a) Feynman diagram of the process $q\bar{q} \rightarrow ZZ \rightarrow 4\ell$

(b) Feynman diagram of the process $gg \rightarrow ZZ \rightarrow 4\ell$.

Fig. 6.1 The lowest order Feynman diagrams of the SM processes $q\bar{q} \rightarrow ZZ$ and $gg \rightarrow ZZ$ in a pp collider.

decay processes of hadrons with heavy flavours. Furthermore, the decay of mesons such as π/K during flight also plays a role, although its contribution is relatively minor. The influence of single-top production in this context is considered minimal. To normalise the background associated with Z + jets and $t\bar{t}$, a method is used where the invariant mass distribution of the primary lepton pair is fitted within specific data control regions. In the case of the $\ell\ell + ee$ channel, the main sources of a non-prompt background are misidentified light-flavour jets that appear as electrons, the conversion of photons, and the semileptonic decay of hadrons rich in heavy flavours. The methodology for selecting a control region in the $\ell\ell + ee$ channel involves using electrons of the same charge in the secondary pair and applying relaxed identification and isolation criteria to the electron with lower transverse momentum (X). In the case of $\ell\ell + ee$ final states, data-driven estimates capture the WZ production process entirely. However, for the $\ell\ell + \mu\mu$ final states, simulated samples become the main source of information on the production of WZ . Both processes involving the pair production of top quarks (denoted as $t\bar{t}$) where the top quark decays to either a W or Z boson, and processes involving the production of three bosons (triboson), are considered negligible. Estimates of their contributions were obtained solely from computer simulations.

6.4 Signal and background simulation

The analysis of the $m_{4\ell}$ distribution relies on MC simulation to model both the signal and the dominant background from non-resonant ZZ production. This simulated distribution is then used to fit the observed data, allowing a statistically robust comparison between the expected and measured outcomes.

6.4.1 Signal simulation

The parameterisation of the signal depends on the nature of the resonance hypothesised.

Narrow-Width Scalar Signal

For a narrow scalar resonance, the $m_{4\ell}$ width reflects detector resolution, modelled by a Crystal Ball (C) function [174, 175] and a Gaussian (G) function, summed as a $C + G$ distribution:

$$P_s(m_{4\ell}) = f_C \times C(m_{4\ell}; \mu, \sigma_C, \alpha_C, n_C) + (1 - f_C) \times G(m_{4\ell}; \mu, \sigma_G), \quad (6.2)$$

where μ , representing the peak value, σ_C and σ_G , characterising the resolution parameters, and α_C and n_C governing the non-Gaussian tail shape. The function also uses a normalisation factor f_c . For illustration, only the combined $C + G$ function for ggF production is depicted because of the similarity of the spectra in the final states. Parameter determination proceeds by fitting simulated signal distributions for each final state. Subsequently, polynomial interpolation of these parameters between mass points is employed, with the optimal polynomial order chosen to minimise overfitting. However, this parameterisation approach introduces an inherent bias in both signal yield and m_H .

RS Graviton Signal

The Randall-Sundrum graviton searches target the mass range $600 < m_G < 2000$ GeV, where m_G is the lightest KK graviton excitation mass. Its width depends on the dimensionless coupling κ/M_{Pl} :

$$\Gamma_G \approx 1.44\kappa/(M_{\text{Pl}}^2)m_G. \quad (6.3)$$

Signal production uses the MADGRAPH [176] framework for event generation. Subsequently, these events undergo a parton shower within PYTHIA 8 [136] using the established A14 tune,

m_G [GeV]	DSID	Cross section [fb]
600	303327	7.875
800	303328	1.484
1000	303329	4.122×10^{-1}
1200	303330	1.424×10^{-1}
1400	303331	5.643×10^{-2}
1600	303332	2.465×10^{-2}
1800	303333	1.156×10^{-2}
2000	303334	5.721×10^{-3}

Table 6.1 List of RS graviton Monte Carlo samples.

as detailed in Ref. [177]. The parton distribution function chosen to simulate interaction dynamics is the NNPDF23 LO set. Table 6.1 provides a comprehensive overview of the MC samples used and their specific configurations.

6.4.2 Background Simulation

To accurately model the non-resonant background in the $m_{4\ell}$ spectrum originating from ZZ processes, a data-driven approach was adopted. Through MC simulations, dedicated $m_{4\ell}$ distributions were generated for each contributing production mode: quark-initiated ($q\bar{q} \rightarrow ZZ$), gluon-initiated ($gg \rightarrow ZZ$), and EW vector boson scattering ($q\bar{q} \rightarrow ZZ$ via EW interaction). This spectrum was parameterized using an empirical function, "Generalised Exp- β " ($GenExp - \beta'$), chosen for its versatility and smoothness, and is shown below:

$$f(m_{4\ell}) = C_0 H(m_0 - m_{4\ell}) f_1(m_{4\ell}) + H(m_{4\ell} - m_0) f_2(m_{4\ell}), \quad (6.4)$$

$$f_1(x) = \left(\frac{x - a_4}{a_3} \right)^{a_1 - 1} \left(1 + \left(\frac{x - a_4}{a_3} \right)^{-a_1 - a_2} \right), \quad (6.5)$$

$$f_2(x) = \exp \left[b_0 \left(\frac{x - b_4}{b_3} \right)^{b_1 - 1} \left(1 + \left(\frac{x - b_4}{b_3} \right)^{-b_1 - b_2} \right) \right]. \quad (6.6)$$

This function consists of two components, f_1 and f_2 , catering to different regions of the mass spectrum. The transition between these parts is regulated by Heaviside step functions, which change the functional form at a specified mass point, m_0 . For the $q\bar{q} \rightarrow ZZ$ process, the transition occurs at $m_0 = 260$ GeV, while for the $gg \rightarrow ZZ$ process, the switch point is set

at $m_0 = 350$ GeV. These points ensure the continuity of the function and optimise the fit performance. Parameters in f_1 and f_2 are determined by fitting the MC $m_{4\ell}$ spectra for each process.

The difference in the transition points reflects the varying kinematic properties of the processes initiated by $q\bar{q}$ and gg . The $q\bar{q} \rightarrow ZZ$ process typically dominates at lower masses due to its higher cross-section near the ZZ threshold, whereas the $gg \rightarrow ZZ$ process contributes more significantly at higher masses due to gluon-gluon fusion mechanisms. The combined approach ensures a smooth and accurate representation of the $m_{4\ell}$ spectrum across the entire mass range. To further clarify the fit procedure, the fitting process involves minimising the negative log-likelihood of the observed data given the model. The empirical functions f_1 and f_2 are adjusted to best match the shape of the $m_{4\ell}$ distribution for each production mode. Systematic uncertainties are incorporated by varying the fit parameters within their uncertainties and recalculating the fit to assess the impact on the final results. This approach ensures that the fits are robust and account for possible variations in the underlying distributions.

Furthermore, the reducible background is analysed separately for the $\ell\ell + \mu\mu$ and $\ell\ell + ee$ final states. The muon background comes primarily from heavy-flavour jets associated with a Z boson, whereas the electron background comes from light-flavour jets misidentified as electrons. To account for potential uncertainties associated with the chosen fitting model, the relative error is incorporated as an additional systematic uncertainty affecting the fitted distribution's shape. This uncertainty was quantified using a sampling technique. Multiple fits were performed with the model parameters varied according to a multivariate Gaussian distribution derived from the fit covariance matrix. The resulting distribution of fitted values for each mass point ($m_{4\ell}$) was used to construct a central interval encompassing 68.3% of the variations. This interval was then symmetrised and included as a systematic shape uncertainty in subsequent fits to the data.

6.5 Systematic uncertainties

The analysis presented in this chapter is subject to various systematic uncertainties. These uncertainties can be broadly classified into three categories: those that stem from the experimental configuration, those associated with the modelling of background contributions, and those that arise from theoretical limitations in the signal description. Throughout the subsequent statistical analysis, every systematic uncertainty is incorporated as a nuisance parameter (NP). A nuisance parameter is an additional parameter introduced into a statistical

model to account for uncertainty in the measurement process, allowing for more accurate estimation of the quantities of interest by effectively marginalising over these uncertainties.

6.5.1 Experimental systematic uncertainties

In the analysis presented, a comprehensive evaluation of systematic experimental uncertainties that affected signal and background estimations was carried out. These uncertainties are integrated as NPs in the statistical evaluation to obtain conclusive results. Notably, these uncertainties come from the calibration of energy/momentum as well as the efficiency of lepton and jet identification and reconstruction processes.

The evaluation involved a two-step approach:

- **Nominal Distribution:** The initial exploration of the $m_{4\ell}$ distribution involved standard weighting and a baseline configuration of nuisance parameters. This established the reference point for assessing the impacts of NP.
- **NP Variations:** Each NP was investigated by generating a $m_{4\ell}$ distribution with a standard device (1σ) variation applied in both the "up" and "down" directions $\pm 1\sigma$. For NPs that solely affected overall normalisation, the change in the total event yield under these modified distributions was compared directly with the reference yield of the nominal unmodified distribution. For shape-influencing NPs, additional assessments were made: relative changes in mean and root mean square (RMS) were evaluated, and these shape variations informed the analytical representation of the distribution, a key element in the construction of the workspaces.

6.5.2 Effect of systematic uncertainties on signal shape parameterisation

In the study of the $m_{4\ell}$ system within the 4μ and $4e$ channels, the influence of systematic experimental uncertainties has been thoroughly analysed. This analysis included different scenarios of ggF signaling, specifically at mass scales of 200 GeV, as depicted in Fig. 6.2. The influence of experimental systematics extends to the parameterisation of analytical signals, which particularly impacts the mean (μ) and combined standard deviations (σ_C and σ_G). This effect is quantified by varying each systematic uncertainty by $\pm 1\sigma$ within the MC $m_{4\ell}$ distributions. The mean and RMS of these varied distributions, compared to the nominal ones, provide information on the impacts on μ , σ_C , and σ_G . A detailed enumeration of the dominant experimental systematics for mass points of 200, 800, and 2000 GeV is provided in Table 6.2. In particular, these shape systematic uncertainties are of the order $O(0.001)$,

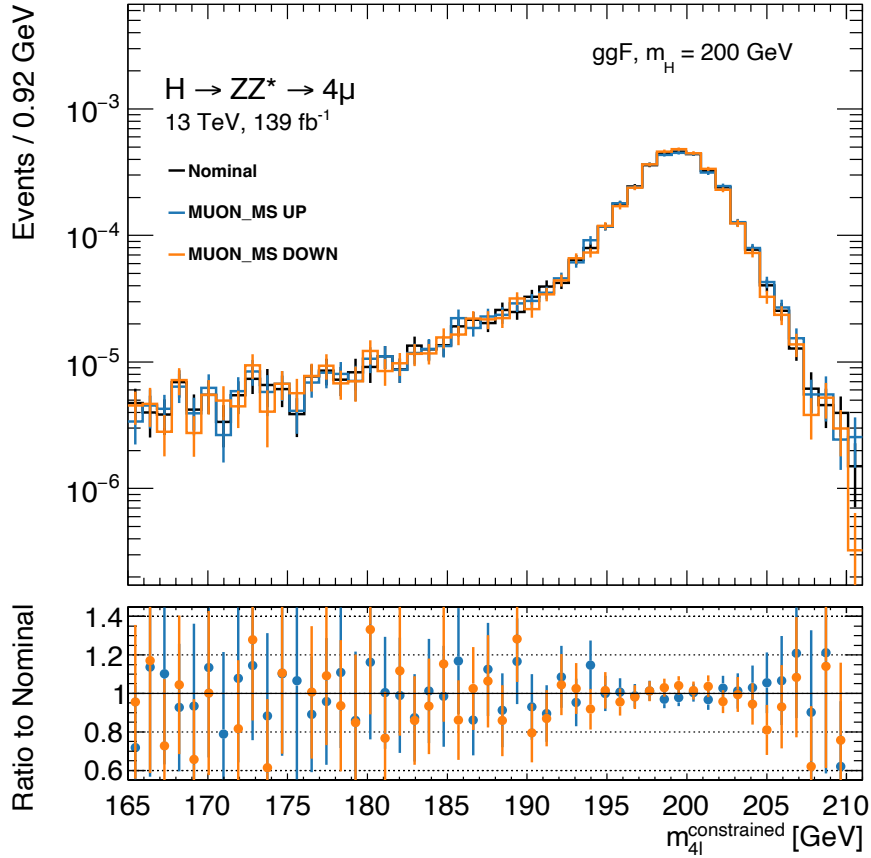


Fig. 6.2 Muon systematic effects for ggF signal with $m_H = 200$ GeV for the 4μ channel.

rendering their overall effect minimal compared to theoretical systematic uncertainties, and therefore are often considered negligible in this context.

6.5.3 Systematic assessment of theoretical uncertainties

In the evaluation of theoretical uncertainties related to both signal and background predictions, comprehensive and established methods were used. The uncertainties arising from PDFs were evaluated following the PDF4LHC prescription guidelines [178]. This included an analysis of variance within individual PDF sets and their respective internal error margins. To estimate the effects of higher-order QCD, variations in the factorisation and renormalisation scales were considered. The systematic uncertainty was determined by identifying the largest deviation in the results from the central value.

Effect on μ (%)	$m_H = 200$ GeV			$m_H = 800$ GeV			$m_H = 2000$ GeV		
	4μ	$4e$	$2\mu 2e$	4μ	$4e$	$2\mu 2e$	4μ	$4e$	$2\mu 2e$
MUON_SCALE	0.050	0.0	0.025	0.031	0.0	0.014	0.017	0.0	0.0076
EG_SCALE	0.0	0.10	0.053	0.0	0.44	0.22	0.0	0.60	0.30
Effect on σ_C and σ_G (%)									
MUON_ID	0.062	0.0	0.15	1.0	0.0	0.97	0.81	0.0	0.92
MUON_MS	0.23	0.0	0.086	1.3	0.0	0.94	1.75	0.0	2.0
MUON_SAGITTA_RESBIAS	0.19	0.0	0.068	4.0	0.0	3.1	7.5	0.0	4.9
MUON_SAGITTA_RHO	0.17	0.0	0.089	3.3	0.0	2.2	5.8	0.0	3.2
EG_RESOLUTION	0.0	0.23	0.26	0.0	1.4	0.54	0.0	2.2	0.26

Table 6.2 Summary of the effects of the experimental systematic uncertainties on the Crystal Ball + Gaussian parameters: μ (mean of the distribution), σ_G (standard deviation of the Gaussian component), and σ_C (standard deviation of the Crystal Ball component) for ggF production at $m_H = 200$ GeV, 800 GeV, and 2000 GeV. The errors are symmetrised for simplicity.

The uncertainties associated with parton showering were investigated by making various adjustments to the Pythia configuration. These adjustments included modifications to the AZNLO tune, the multi-parton interaction models, and the final-state radiation models. The AZNLO tune is a specific set of parameters in the Pythia generator that has been optimised to match experimental data more accurately for simulations involving next-to-leading-order (NLO) QCD calculations. This study evaluated the impact of different theoretical uncertainties on the selection efficiency of potential signal events (signal acceptance) and how these uncertainties affect the values of key features used to distinguish signals from background events (discriminant variables). In particular, the degree of sensitivity to these uncertainties varied significantly for signal acceptance. In regions of lower mass, the variation was less than 1%, while in areas of higher mass it increased to approximately 12% and 20% for the $2\ell 2\nu$ and 4ℓ final states, respectively.

To address uncertainties associated with the ZZ background, a novel approach was implemented that uses a variable normalisation factor. This factor, determined by simulation data, accounted for the relative contributions of the dominant $q\bar{q} \rightarrow ZZ$ and $gg \rightarrow ZZ$ processes. This strategy effectively incorporated theoretical uncertainties into the analysis through both the discriminant variable spectra and the relative yields of the simulated ZZ background. Furthermore, NLO EW corrections, obtained from the referenced studies [179–181], were applied, which affected the discriminant variables. These adjustments exhibited minimal influence, remaining below 1% on lower mass scales. However, their influence could reach 10% at higher mass scales, observed consistently across both the $2\ell 2\nu$ and 4ℓ final states. In particular, due to the significantly different energy scales investigated in the $2\ell 2\nu$ and 4ℓ

analyses, the theoretical uncertainties were considered independent. An alternative hypothesis assuming fully correlated uncertainties was also examined. However, comparative studies on expected limits suggested that the differences between these two scenarios were minimal.

6.6 Results

6.6.1 Statistical Approach and Systematic Uncertainty Analysis

This section extends the 7 TeV Higgs boson search framework detailed in previous work [182, 183] by employing a profile likelihood ratio statistic ($\Lambda(\alpha, \sigma)$) sensitive to the parameter of interest (α). Here, σ represents the standard deviation of the Gaussian distribution associated with the parameter estimates. This parameter (α) represents the product of the cross section, the branching ratio, and the scaling factors (θ). In particular, unlike previous reports [172], this analysis introduces novel normalisation factors for each final state. These factors mitigate theoretical and luminosity uncertainties by adjusting expected background counts, substantially reducing the overall normalisation uncertainty.

4 lepton final state:

Three different normalisation factors are used: $\mu_{ZZ}^{\text{VBF-MVA}}$, $\mu_{ZZ}^{\text{ggF-MVA-high}}$, and $\mu_{ZZ}^{\text{ggF-MVA-low}}$ for different categories.

2 lepton 2 neutrino final state:

A single normalisation factor, μ_{ZZ} , is used due to data limitations and a lower signal-to-background ratio.

6.6.2 Cut-Based Analysis

In the cut-based analysis, specific selection criteria are applied to identify events produced via the VBF production mode. This analysis categorises events based on having two or more jets with transverse momentum (p_T) greater than 30 GeV. Furthermore, the two leading jets must be well separated in pseudo-rapidity (η) with $\Delta\eta > 3.3$, and the invariant mass of the jet pair (m_{jj}) must exceed 400 GeV. These criteria were reviewed and confirmed to be suitable for the full Run-2 dataset.

Category	$qq \rightarrow ZZ$	EW prod. of $qq \rightarrow ZZ$	$gg \rightarrow ZZ$	$Z + \text{jets}, t\bar{t}$	$t\bar{t}V, VVV$	Total
ggF-2 μ 2e	1232.58 ± 26.776	11.13 ± 0.425	169.94 ± 13.141	6.59 ± 1.532	26.81 ± 0.606	1447.07 ± 26.839
ggF-4e	466.98 ± 10.144	4.39 ± 0.176	65.65 ± 5.078	3.04 ± 0.422	11.75 ± 0.306	551.81 ± 10.199
ggF-4 μ	779.87 ± 16.941	6.89 ± 0.290	103.06 ± 7.972	2.08 ± 0.353	16.35 ± 0.450	908.25 ± 16.907
VBF	43.52 ± 7.525	10.93 ± 0.946	11.55 ± 3.898	0.28 ± 0.083	3.03 ± 0.222	69.30 ± 8.306

Table 6.3 Simulated background event yields (weighted) and their systematic uncertainties in the 4ℓ channel, after fit to the background-only Asimov data.

Category	$qq \rightarrow ZZ$	$qq \rightarrow ZZEW$	$gg \rightarrow ZZ$	$Z + \text{jets}, t\bar{t}$	$t\bar{t}V, VVV$	Expected	Observed
ggF-2 μ 2e	1359.6 ± 3.0	11.1 ± 0.4	188.7 ± 14.5	6.68 ± 1.5	26.8 ± 0.6	1592.9 ± 28.1	1656.0
ggF4e	515.1 ± 10.7	4.4 ± 0.18	72.9 ± 5.6	3.1 ± 0.4	11.8 ± 0.3	607.2 ± 10.7	612.0
ggF4 μ	860.3 ± 17.9	6.9 ± 0.3	114.4 ± 8.8	2.09 ± 0.4	16.3 ± 0.4	1000 ± 17.7	932.0
VBF	47.7 ± 7.9	10.9 ± 0.9	13.1 ± 4.3	0.3 ± 0.1	3.0 ± 0.2	74.9 ± 8.6	75.0

Table 6.4 Background event estimates (weighted) after accounting for uncertainties, using the defined selection criteria.

6.6.3 Results for the cut-based analysis

Expected and observed events

The following section presents the results of the analysis using selection criteria, focusing on the validation procedures used before their application to real-world data. The Asimov data set, a pseudo-data set where the true values of the parameters are set to the expected values under the null hypothesis, served as a validation ground [184]. The production limits of ggF and VBF were calculated in a 95% CL using a dataset comprising 139 fb^{-1} of pp collision data across four distinct cut-based channels. Table 6.3 summarises the simulated background event yields in the 4ℓ channel after fitting to the background-only Asimov dataset. These yields are accompanied by their corresponding systematic uncertainties, which incorporate all relevant correlations among the background components. The systematic uncertainties considered include calibration of energy/momentum scales, identification efficiencies of leptons and jets, and modelling of background processes. Statistical errors are also taken into account. Similarly, Table 6.4 presents the background-only fit event yields extracted from the cut-based analysis, along with their respective systematic uncertainties. As with the Asimov data, the total background uncertainty accounts for all component correlations.

The look elsewhere effect

To explore the existence of an undiscovered particle with an undefined mass, a comprehensive evaluation of various mass values is essential. Anomalies in the data, specifically an increase

Final state	Normalisation factor	Fitted value
4ℓ	$\mu_{ZZ}^{\text{VBF-MVA}}$	0.9 ± 0.3
	$\mu_{ZZ}^{\text{ggF-MVA-high}}$	1.07 ± 0.05
	$\mu_{ZZ}^{\text{ggF-MVA-low}}$	1.12 ± 0.03
$\mu^+ \mu^- \nu \bar{\nu}$	μ_{ZZ}	1.04 ± 0.06

Table 6.5 Scaling factors for simulated ZZ events, derived from background-only fit and categorized by final state and signal region. Total uncertainties (statistical and systematic) included. MVA categories use the 4ℓ channel.

beyond the anticipated background levels at certain mass values, might suggest the existence of a novel resonance at that mass. Such a peak in the data could result from an authentic, novel signal, or simply be a statistical variation in the background data. The initial step in assessing the anomaly involves calculating the local probability, denoted as p_0 . This probability reflects the likelihood that the background alone generates a fluctuation at least as significant as the observed one. Local significance, expressed in terms of standard deviations, is given as Z_{local} . To account for the possibility of observing a similar excess elsewhere within the search range, the global probability is estimated using an asymptotic formula:

$$p_{\text{global}} = p_{\text{local}} \times \left(1 + \frac{\pi}{2} \times \mathcal{N} \times Z_{\text{local}} \right), \quad (6.7)$$

where, p_{global} represents the global p_0 , and \mathcal{N} signifies the count of occurrences where p_0 exceeds a predefined threshold. The threshold value of 0.71 is chosen based on statistical criteria to ensure meaningful significance levels, balancing the likelihood of detecting true signals against the rate of false positives. The factor adjusted for the effect of looking elsewhere, which is the ratio of global to local p_0 , increases with the range of hypotheses, the precision in mass resolution and the significance level of the excess. Detailed calculations of local p_0 s for varied signal hypotheses, following the NWA, are compiled and shown in Fig. 6.3. Furthermore, the summation of local p_0 s calculated independently for each category is also included. However, it is important to note that the global significance determined from this equation may not always be precisely accurate.

6.6.4 General Results

A total of 3275 events were observed in the 4ℓ final state with an invariant mass ($m_{4\ell}$) exceeding 200 GeV, while the $2\ell 2\nu$ final state produced 2794 events. These values represent the integer counts of observed events. To estimate the contributions of background processes,

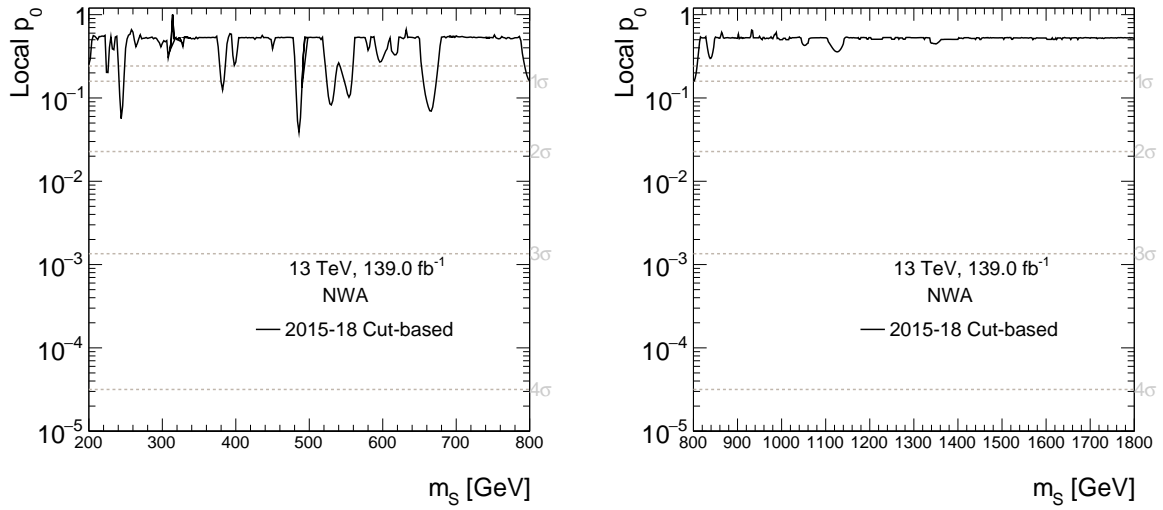


Fig. 6.3 The p_0 value as a function of m_S in the NWA for the cut-based analysis, combining all categories. The first plot covers the mass range from 200 to 800 GeV, while the second plot spans from 800 to 1800 GeV.

a simultaneous likelihood fit was performed for both final states, assuming the presence of background processes only. The results of this fit, including the normalisation factors for the SM ZZ background, are presented in Table 6.5. The expected background yields and the observed number of events with $m_{4\ell}$ greater than 200 GeV are summarised in Table 6.6. The analysis accounts for both statistical and systematic uncertainties, which include uncertainties in the normalisation factors for the SM ZZ background, as detailed in Table 6.5. Figure 6.4 shows the $m_{4\ell}$ spectrum, highlighting the effectiveness of background determination using a combined unbinned likelihood fit to the data under the background-only assumption.

The significance of the deviations between the data and the background-only hypothesis was assessed separately for NWA signals arising from the ggF and VBF production modes. For ggF production, the most significant deviation was observed around 240 GeV, with a local significance of 2.0 standard deviations and a global significance of 0.5 standard deviations. In the VBF production scenario, the maximum deviation, exceeding 2.4 standard deviations locally and 0.9 standard deviations globally, was found near 620 GeV. These findings align with previous observations around 240 GeV and 700 GeV in the 2015 and 2016 data [172], although those excesses are not confirmed with the full Run 2 dataset. The maximum deviation of the data from the background-only hypothesis is evaluated in the context of a NWA signal from both the ggF and the VBF production modes. The use of a combined

Process	VBF	4μ	ggF-MVA-high $2e2\mu$	$4e$	ggF-MVA-low
$q\bar{q} \rightarrow ZZ$	11 ± 4	232 ± 10	389 ± 17	154 ± 7	2008 ± 47
$gg \rightarrow ZZ$	3 ± 2	37 ± 6	64 ± 10	26 ± 4	247 ± 19
$ZZ(\text{EW})$	4.1 ± 0.4	4.5 ± 0.2	7.5 ± 0.4	3 ± 0.2	14.3 ± 0.7
$Z + \text{jets}, t\bar{t}$	0.08 ± 0.02	0.6 ± 0.1	1.7 ± 0.4	0.8 ± 0.1	8.8 ± 2.1
$t\bar{t}V, VVV$	0.96 ± 0.1	9.8 ± 0.2	17.5 ± 0.4	7.7 ± 0.2	21.9 ± 0.5
Total					
background	19 ± 5	284 ± 12	480 ± 20	192 ± 8	2300 ± 51
Observed	19	271	493	191	2301

Table 6.6 Comparison of observed (3275) vs. predicted 4ℓ events ($m_{4\ell} > 200$ GeV). The predictions assume a background-only scenario and incorporate uncertainties.

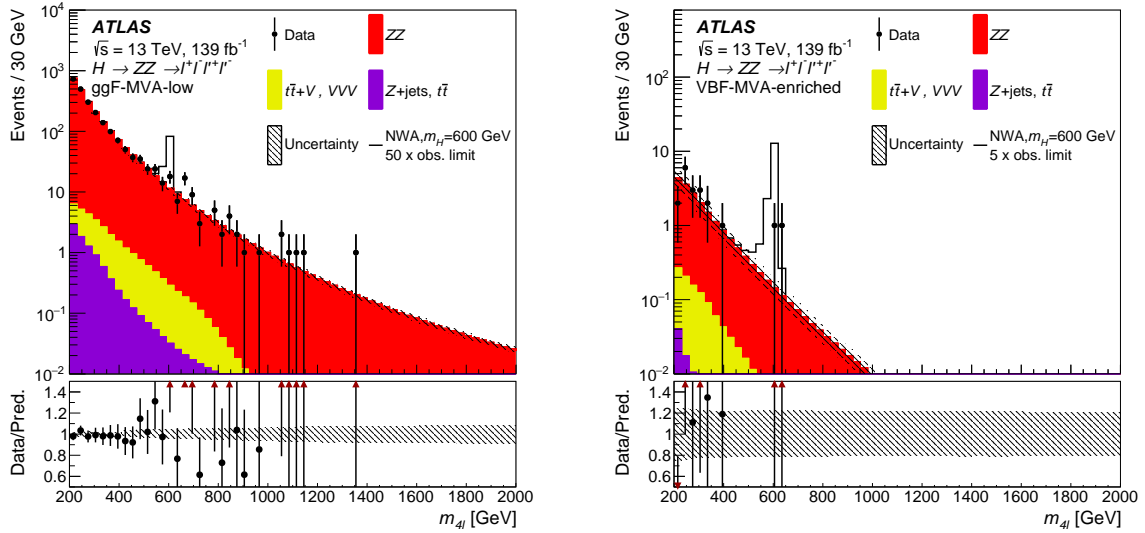


Fig. 6.4 Depictions of the $m_{4\ell}$ distributions in the 4ℓ background final states are presented for both the ggF-MVA-low classification and the 4ℓ final states within the VBF-MVA-enriched category. Figure taken from Ref. [122].

unbinned likelihood fit allows for a more accurate estimation of background contributions and highlights the robustness of the background determination methodology.

6.7 Interpretations

In the absence of significant deviations from the background expectations, the analysis focuses on the combined final states 4ℓ and $2\ell 2\nu$ to establish exclusion boundaries for various signal hypotheses. This approach takes advantage of the increased sensitivity of the combined

states, while maintaining the robustness of the exclusion limits. The detailed analysis of these exclusion boundaries is presented in the following sections.

6.7.1 Spin-0 Resonances

Spin-0 Resonances with NWA

This study aimed to establish upper bounds on the combined production rate and decay probability ($(\sigma \times B(H \rightarrow ZZ))$) for a theorised massive spin-0 resonance. The limits, which encompassed both final states (4ℓ and $2\ell 2\nu$), varied according to the mass of the resonance (m_H). Using the CL_s method with an asymptotic approximation (validated through pseudo-experiments with 4% precision) [184, 185], separate analyses were performed for the dominant ggF and VBF production mechanisms, treating the other process as a free variable within the model. Figure 6.5 presents the upper limits observed and expected 95% confidence level (CL) upper limits on $(\sigma \times B(H \rightarrow ZZ))$ for a narrow scalar resonance within the ggF and VBF production channels, together with the anticipated limits from the aforementioned searches. This is applicable to models where the resonance width is less than 0.5% of m_H . Combining data from both channels, the 95% CL upper limits ranged from 215 fb at $m_H = 240$ GeV to 2.0 fb at $m_H = 1900$ GeV for ggF, and from 87 fb at $m_H = 255$ GeV to 1.5 fb at $m_H = 1800$ GeV for VBF. These current expected limits represent reductions of 20% to 28% for ggF and 27% to 43% for VBF, compared to the expected limits for 139 fb^{-1} luminosity from a previous study, depending on the hypothesised mass.

Spin-0 resonances with LWA

This study used the Large-Width Approximation to constrain the product of the gluon-fusion production process cross section and the branching ratio ($\sigma_{ggF} \times B(H \rightarrow ZZ)$) of the heavy-scalar boson decaying into two Z bosons, considering various hypothetical widths of the boson. Figure 6.6 shows these constraints for the assumed widths of 1% and 5% of the boson mass. It is important to note that these limits were only calculated for m_H values greater than 400 GeV. This lower limit was chosen to mitigate potential instabilities in the LWA mass spectrum parameterisation and minimise interference effects, particularly those arising from the reduced mass of the signal poles. Consequently, the analysis solely focused on the ggF production process, as it is the dominant channel for investigating the influence of non-negligible intrinsic widths on the search for the massive scalar boson.

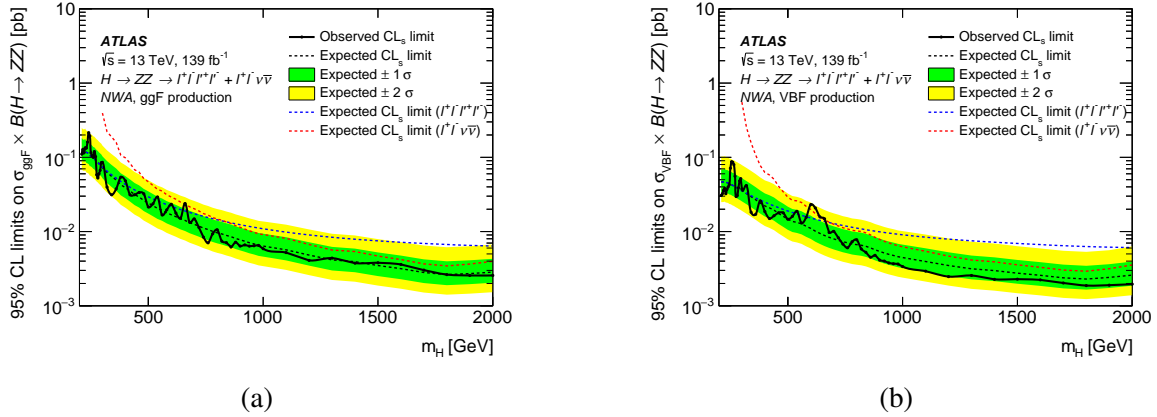


Fig. 6.5 Upper limits (95% CL). The solid black line represents the observed limits. The shaded areas in green and yellow indicate the one- and two-standard deviation uncertainties around the expected limits. The dashed lines represent the individual expected limits for each search channel. Refer to Figs. 6.5a and 6.5b for additional details on the ggF and VBF channels, respectively. Taken from Ref. [122]).

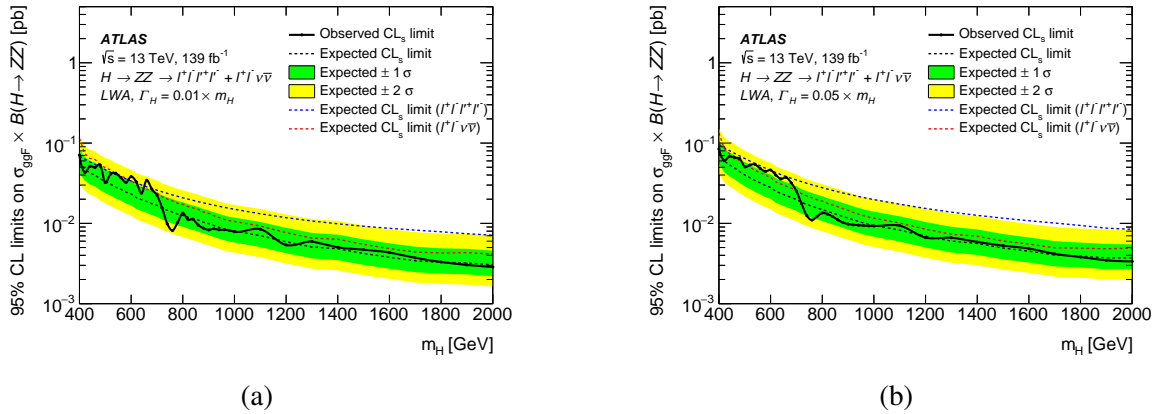


Fig. 6.6 Limits on $\sigma_{ggF} \times B(H \rightarrow ZZ)$ with additional heavy scalar (1%/5% width). Black: observed limit. Green/yellow bands: $\pm 1/\pm 2\sigma$ uncertainties. Dashed lines: individual search expectations. Taken from Ref. [122].

Two-Higgs-doublet model

In the CP-conserving 2HDM (Two-Higgs-Doublet Model), five Higgs bosons emerge following electroweak symmetry breaking: two CP-even (denoted as h and H), one CP-odd (A), and two charged (H^\pm). These particles are described by seven key parameters: the masses of the Higgs bosons (m_h, m_H, m_A, m_{H^\pm}), the ratio of the vacuum expectation values of the two Higgs doublets ($\tan \beta$), the mixing angle (α) and the soft \mathbb{Z}_2 -symmetry breaking parameter (m_{12}^2).

In the context of supersymmetry, $\tan \beta$ represents the ratio of the vacuum expectation values of the two Higgs fields, while α is the mixing angle between the two CP-even Higgs states. The parameter m_{12}^2 is associated with soft breaking of the \mathbb{Z}_2 symmetry that helps prevent flavour-changing neutral currents.

Different coupling schemes of the doublets Φ_1 and Φ_2 to quarks and leptons define the Type I and Type II models. In Type I models, only one Higgs doublet couples to fermions, while in Type II models, one doublet couples to up-type quarks and the other to down-type quarks and leptons. Variations like the "lepton-specific" and "flipped" models further adjust these couplings.

The coupling strength of the heavier CP-even Higgs boson to vector bosons is linked to $\cos(\beta - \alpha)$. When $\cos(\beta - \alpha) \rightarrow 0$, the lighter CP-even Higgs boson behaves like the Standard Model (SM) Higgs boson. For $H \rightarrow ZZ$ decays, the interpretations are valid primarily within Type I and Type II models, under the assumption that other Higgs bosons are too heavy to interfere with the decay channels of the heavy CP-even Higgs boson.

Figure 6.7 illustrates exclusion limits in the $\tan \beta$ versus $\cos(\beta - \alpha)$ plane for Type I and Type II 2HDMs with a 220 GeV heavy Higgs boson (m_H), highlighting the regions where the assumption of a heavy narrow Higgs boson holds. The parameter space is restricted to minimise interference, and limits are derived using the predicted gluon-gluon fusion (ggF) and vector boson fusion (VBF) production rates for the selected values of $\cos(\beta - \alpha)$ and $\tan \beta$.

6.7.2 Spin-2 resonances

Analysis within the RS model's bulk scenario $k/M_{\text{Pl}} = 1$ further explored the potential excitation of a Kaluza-Klein graviton G_{KK} through searches for excess graviton production. Using 95% CL upper limits in $\sigma \times B(G_{\text{KK}} \rightarrow ZZ)$ as a function of the KK graviton mass ($m(G_{\text{KK}})$), as shown in Fig. 6.8, the analysis compared them with theoretical predictions for the G_{KK} cross section. This comparison ruled out the presence of a spin-2 graviton for masses up to 1830 GeV.

6.8 Combined results

In the preceding analysis detailed in Section 6.7, while the data did not reveal any statistically significant excess leading to the establishment of upper limits on the production cross-section

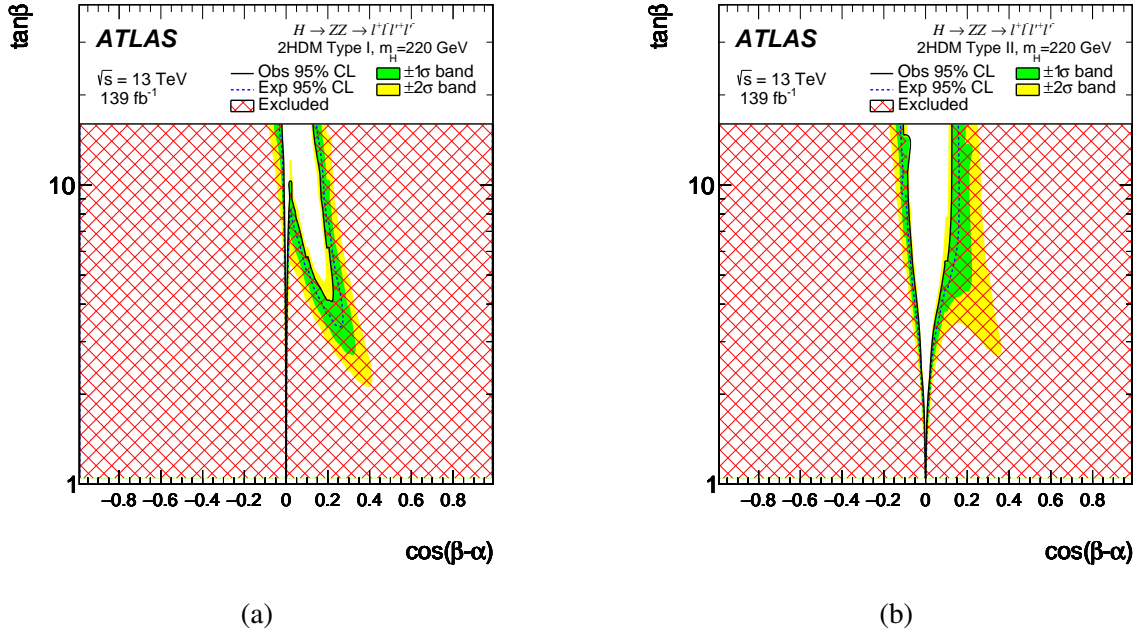


Fig. 6.7 Exclusion contours for 2HDM Type-I/II vs. $\cos(\beta - \alpha)$ and $\tan\beta$ at $m_H = 220$ GeV. The bands represent predicted uncertainty ($\pm 1\sigma, \pm 2\sigma$), shaded area denotes observed exclusion. Taken from Ref. [122].

for both spin-0 and spin-2 resonances. Notably, a subsequent study combined ATLAS Run 2 results for the ggF process (Ref. [122]) with inclusive CMS Run 2 data (Ref. [186]). The combined plot is presented in Fig. 6.9.

Furthermore, the ATLAS VBF process is depicted for both Run 2 (Ref. [122]) and Run 3 data (Ref. [187]) in blue and red, respectively. Interestingly, the combined ATLAS and CMS plot in Fig. 6.9. reveals a 2.4σ peak around 250 - 260 GeV, situated within the window of interest for the final state of the 4 lepton. Investigations, as expounded in Section 1.6, have been devoted to the scrutiny of multi-lepton anomalies observed at the LHC. These studies may provide crucial insights into the underlying processes at play, potentially pointing towards BSM phenomena.

¹Plot generated by Srimoy Bhattacharya (private communication).

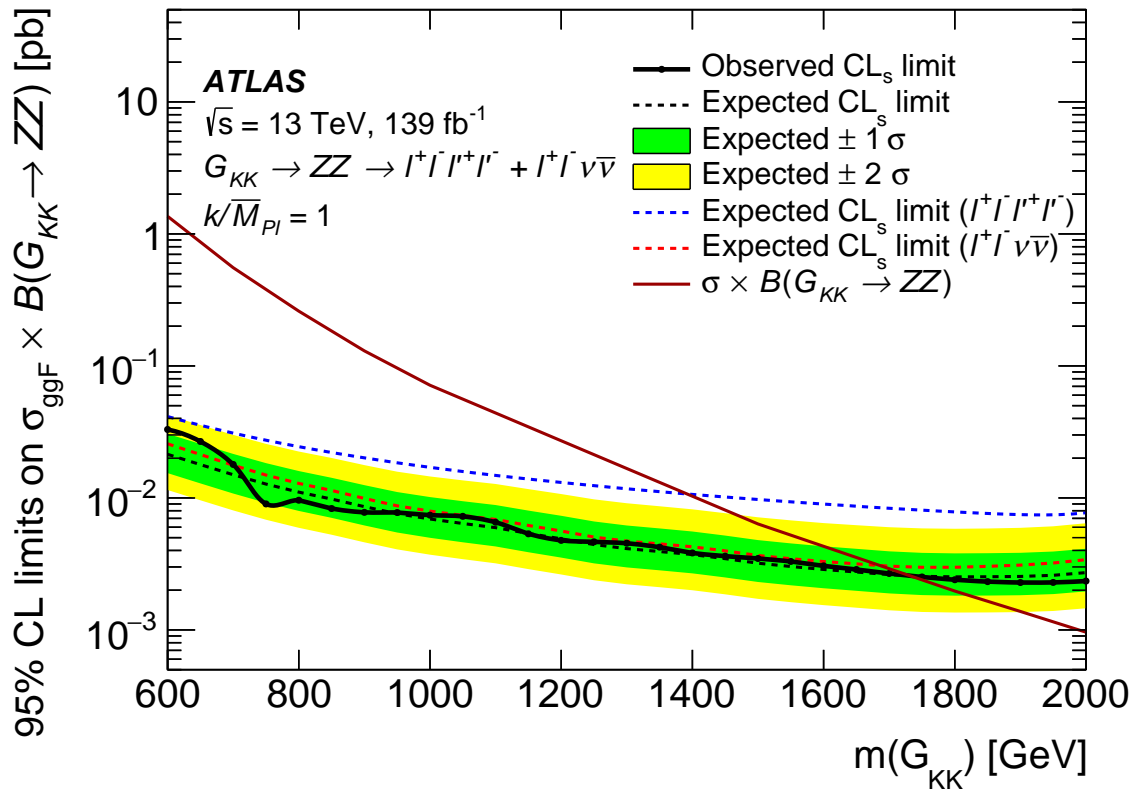


Fig. 6.8 This figure displays the upper limit of the cross section times branching fraction at a 95% confidence level. The black line represents the observed constraints, while the shaded regions in green and yellow depict the one and two standard deviation uncertainty ranges, respectively. Additionally, a red line shows the theoretical predictions for the mass of the Kaluza-Klein graviton, $m(G_{KK})$. Taken from Ref. [122].

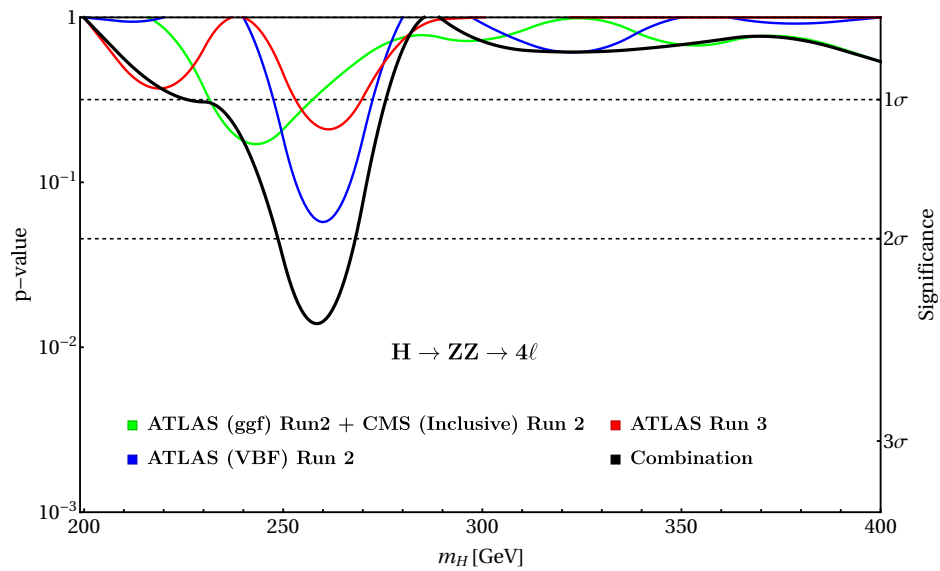


Fig. 6.9 The p -values for ATLAS (Run 2 and Run 3) and CMS (Run 2) data and their combined analysis, presented for the 4 lepton final state channels.¹

Chapter 7

Heavy Resonance Searches in 4ℓ and E_T^{miss} /Jets final state

A search is presented for a new heavy boson, produced by ggF and decaying to 4ℓ with E_T^{miss} or jets. Using pp collision data collected by the ATLAS detector at the LHC, the analysis delves into 139 fb^{-1} of data gathered at 13 TeV between 2015 and 2018. Two specific decay channels are investigated: $R \rightarrow SH$ and $A \rightarrow ZH$, where R and A are CP-even and CP-odd bosons, respectively, while H represents a CP-even boson that decays into invisible particles that can potentially constitute DM. Subsequently, H itself decays to ZZ . The structure of the chapter unfolds as follows: Section 7.1 outlines the analysis strategy, followed by Section 7.2 which delves into the selection of four-lepton events. Section 7.3 details the additional selection criteria implemented. The signal and background modelling for these events is described in Section 7.4. Section 7.5 presents the results of the analysis, which establish upper bounds for the cross section times branching ratio of the heavy resonances with a 95% confidence level.

Yakun' imvula kuhlokoma neendlela.

E.W.M Mesatywa.

7.1 Analysis Overview

In the analysis presented in Chapter 6, certain areas within the parameter space of the 2HDM were not included, and the examination of E_T^{miss} in the final states was overlooked. Furthermore, the presence of a 4ℓ final state, coupled with E_T^{miss} , was not analysed within the scope of the ATLAS experiment. Consequently, the present study delves into the generation of massive resonances through the gluon-gluon fusion (ggF) process, linked to E_T^{miss} , specifically in the domain where heavy bosons exhibit a mass surpassing 200 GeV. The investigation is anchored in the analysis of pp collision data, which encompasses a CM energy of 13 TeV and a cumulative luminosity of 139 fb^{-1} , collected via the ATLAS detector between 2015 and 2018 at the LHC. The findings are interpreted under two theoretical constructs.

Predominantly, the first model examines the decay of a heavy resonance (H), conjoined with the missing energy among four leptons E_T^{miss} , which is the result of the subsequent decay of a scalar boson (S) [188]. This model is based on processes such as $R \rightarrow SH \rightarrow 4\ell + E_T^{\text{miss}}$ [38, 189], and $A \rightarrow ZH \rightarrow 4\ell + X$ [38, 190]. Note that in this context, 'H' refers to a heavy Higgs boson from the 2HDM and not the Standard Model Higgs boson.

The original model was limited to a heavy resonance H and another scalar S . To encompass a wider spectrum of scenarios with varying levels of missing energy, the model has been expanded by including an extra heavy scalar particle, known as R . In this extension, R undergoes decay processes, leading to the production of H and S , thus constituting a 2HDM+S+R model. The Feynman diagram in Fig. 7.1 depicts the first model where R is a scalar boson that decays to two lighter scalar bosons S and H . Subsequently, S decays into DM particles ($S \rightarrow \text{invisible}$), while H decays into four leptons. Fixing the mass of the mediator particle, S , at 160 GeV serves as a control parameter, allowing exploration of the impact of varying the masses of the other two particles, R and H , on the E_T^{miss} . It should be noted that the choice of the S mass, initially suggested to be around 150 GeV, as indicated in Ref. [40], does not have a significant impact on the kinematic properties of the $R \rightarrow SH \rightarrow 4\ell + E_T^{\text{miss}}$ signal, provided that it remains below 200 GeV [40]. Feynman diagrams illustrating the generation of heavy bosons through ggF at leading order (LO) are shown in Fig. 7.1a, Fig. 7.1a represents the process $R \rightarrow SH \rightarrow 4\ell + E_T^{\text{miss}}$, and Figs. 7.1b and 7.1c represent $A \rightarrow ZH \rightarrow 4\ell + X$, where X includes $j/\ell^-/\nu$ and $\bar{j}/\ell^+/\bar{\nu}$.

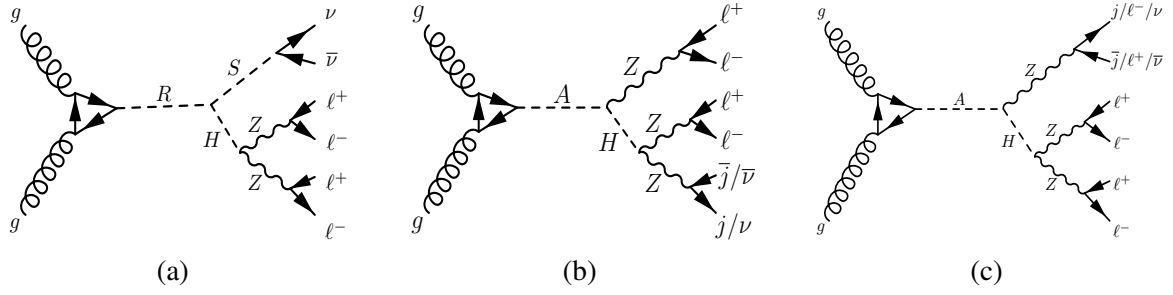


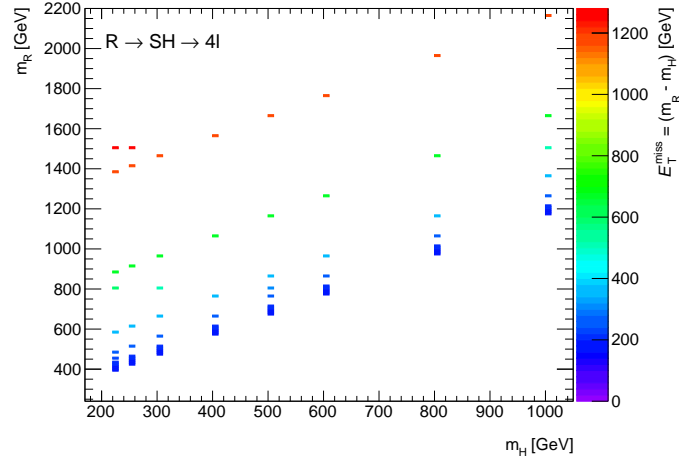
Fig. 7.1 Heavy boson generation through ggF. Figure 7.1a represents the process $R \rightarrow SH \rightarrow 4\ell + E_T^{\text{miss}}$, and Figs. 7.1b and 7.1c represent $A \rightarrow ZH \rightarrow 4\ell + X$, where X encompasses $j\bar{j}/\ell^\pm\ell^\pm/\nu\bar{\nu}$. Image taken from Ref. [191].

7.2 Data and simulated event samples

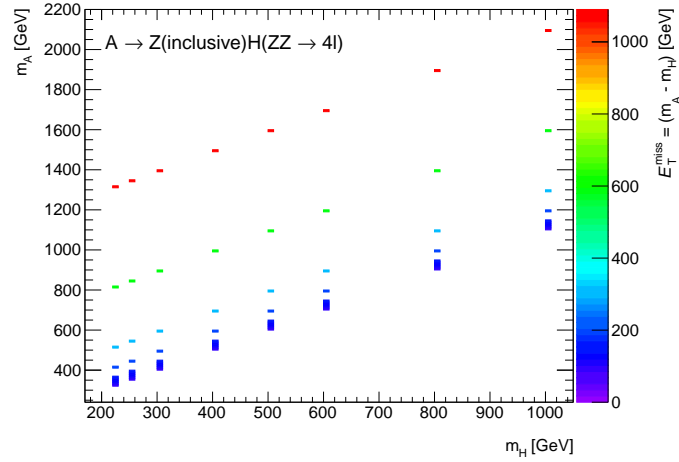
The selection of events with four leptons is performed by implementing the standard four-lepton selection criteria, as discussed in Chapter 5.5. The background modelling followed in this study is identical to that described in Chapter 5.3.2. This study examines two BSM models: the $R \rightarrow SH \rightarrow 4\ell + E_T^{\text{miss}}$ and $A \rightarrow ZH \rightarrow 4\ell + X$ scenarios. Both explore the hypothesis of H decaying into a pair of Z bosons, and the gluon-gluon fusion (ggF) production mechanism was chosen for simulation. Both involve the narrow-width approximation (NWA). The $R \rightarrow SH \rightarrow 4\ell + E_T^{\text{miss}}$ process was modelled using Pythia8 [136] with the A14 tune [192] and the NNPDF23LO PDF set [140]. A constant S mass of 160 GeV was employed, while the H mass was varied across a 220-1000 GeV range.

Furthermore, the mass of R is calculated using a mass gap variable, m_{Gap} , defined as the difference between the mass of R and the sum of the masses of H and S . Specifically, m_{Gap} is explored over a span from 10 to 1000 GeV. Evaluation of the R 's mass is restricted by the condition $m_R \geq m_H + m_S(160 \text{ GeV}) + m_{\text{Gap}}$. Figure 7.2a shows all the signal mass points generated, where the mass difference, $m_R - m_H$, is shown on the z -axis. These distributions indicate that the kinematics of the $R \rightarrow SH \rightarrow 4\ell + E_T^{\text{miss}}$ signal is not affected when the S mass is below 200 GeV. This is because below 200 GeV, the mass of S is small enough so that its variations do not significantly affect the overall energy distribution and kinematics of the final state particles.

The simulation of the $A \rightarrow Z(\rightarrow X)H(\rightarrow 4\ell)$ and $A \rightarrow Z(\rightarrow 2\ell)H(\rightarrow 2\ell + X)$ signals was carried out using MadGraph5_aMC@NLO [176] with the A14 tune and the NNPDF23LO PDF set. The parton shower and hadronization processes were performed using Pythia8. The mass of A was calculated using the same mass gap of the model $R \rightarrow SH \rightarrow 4\ell + E_T^{\text{miss}}$



(a)



(b)

Fig. 7.2 Two-dimensional plots showing the mass differences of the (a) $R \rightarrow SH \rightarrow 4\ell + E_T^{\text{miss}}$ and (b) $A \rightarrow Z(\rightarrow X)H(\rightarrow 4\ell)$ and $A \rightarrow Z(\rightarrow 2\ell)H(\rightarrow 2\ell)$ models. The mass differences are represented by the z -axis as $m_R - m_H$ or $m_A - m_H$. The z -axis also represents E_T^{miss} for these models, indicating that the signal is not varying when the mass of S is below 200 GeV. Different colors represent different values of the missing transverse energy.

as $m_A \geq m_H + m_Z(90 \text{ GeV}) + m_{\text{Gap}}$. The assumption that $m_A = m_H$ in this analysis is not valid, since the difference between m_A and m_H is currently being investigated. For the $A \rightarrow Z(\rightarrow X)H(\rightarrow 4\ell)$ signal, X represents everything ($j\bar{j}/\ell\ell/\nu\bar{\nu}$), except 2ℓ in the $A \rightarrow Z(\rightarrow 2\ell)H(\rightarrow 2\ell + X)$ signal. The mass points of the generated signals are shown in Figure 7.2b.

7.3 Analysis Strategy

After the initial pre-selection process described in Section 5, events must satisfy the condition $m_{4\ell} > 200$ GeV. Depending on the signal model, additional selection criteria are applied. This section details the selection criteria and optimisation strategies used in the analysis. The effectiveness of these optimisations is evaluated using two distinct significance formulae:

$$Z_{\text{sig1}} = \frac{s}{\sqrt{k \cdot b}}, \quad \text{and} \quad Z_{\text{sig2}} = \frac{s}{\sqrt{s + k \cdot b}}, \quad (7.1)$$

where s represents the signal events, b represents the background events, and k signifies the fraction applied to the background to isolate the background events within the signal peak. For example, for the signal characterised by $(m_R, m_H) = (390, 220)$ GeV, k is 19.9%. This value is derived from the proportion of events within a range of ± 10 GeV of the signal peak to the total events in the $m_{4\ell}$ spectrum above 200 GeV. Optimisation strategies are adapted for each signal hypothesis, as elaborated in the following sections.

7.3.1 $R \rightarrow SH \rightarrow 4\ell + E_T^{\text{miss}}$ Signal Optimisation

To simplify, four signal samples were chosen to compare their shapes with SM backgrounds for specific kinematic distributions. Two signals showed lower E_T^{miss} around 50 GeV, while the other had higher E_T^{miss} above 600 GeV, as shown in Figure 7.3. The E_T^{miss} significance, used instead of E_T^{miss} and object-based E_T^{miss} significance [191], is defined by:

$$E_T^{\text{miss}} \text{ significance} = \frac{E_T^{\text{miss}}}{\sqrt{\sum E_T}}. \quad (7.2)$$

This significance metric was applied in optimisation, as it provided a better distinction between signals and background. Events were classified into zero and at least one central jets regions, using p_T^{miss} and E_T^{miss} significance for signal-background discrimination via a 2D scan with $(m_R, m_H) = (390, 220)$ GeV. The use of a low E_T^{miss} sample captured signals with high E_T^{miss} , although this under-represented the high E_T^{miss} sample's peak of SM backgrounds (see Figure 7.3).

Optimal points were identified at E_T^{miss} significance > 2.0 and $p_T^{\text{miss}} > 20.0$ GeV, resulting in a significance of 3.08 for the zero central jets region, shown in Figure 7.4a. The significance calculation using Z_{Sig} , as described in Equation 7.2, was contrasted with other points of lower significance (2.47). Low missing transverse energy scans were performed after removing

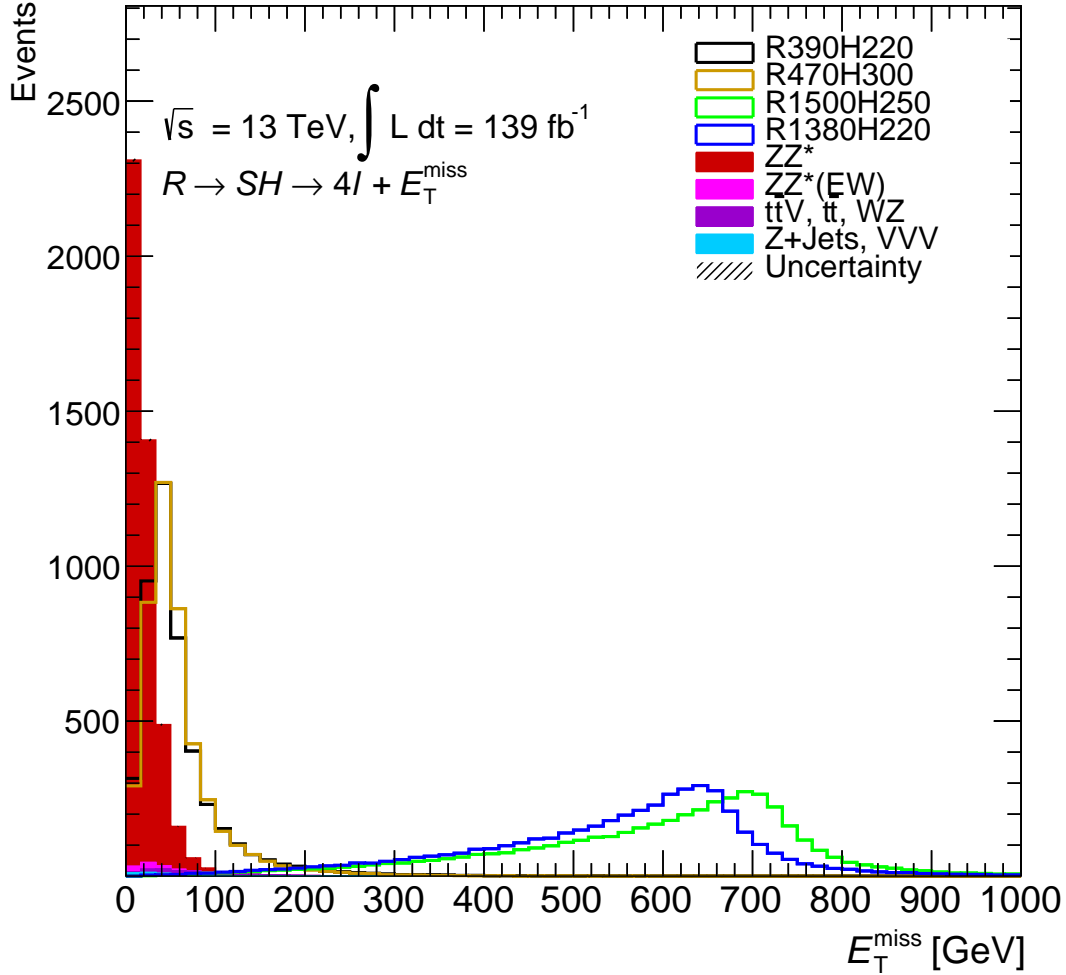


Fig. 7.3 Distribution for the $R \rightarrow SH \rightarrow 4\ell + E_T^{\text{miss}}$ signal comparing to the different background components of the Missing transverse energy. Each signal is normalised to the total number of background to get better comparison with the background.

these points, resulting in E_T^{miss} significance > 1.5 and $p_T^{\text{miss}} > 10.0$ GeV with significance values of 0.78 and 0.73, as shown in Figures 7.4b and 7.4d.

The low E_T^{miss} scan of at least one central jets region gave the best cuts at $p_T^{\text{miss}} > 2.5$ GeV and E_T^{miss} significance > 2.5 , using Z_{Sig1} . However, $p_T^{\text{miss}} > 0$ GeV was preferred for its higher overall significance. The combined significance for the $R \rightarrow SH \rightarrow 4\ell + E_T^{\text{miss}}$ signal, excluding the low- E_T^{miss} zero central jets region, was 6.85.

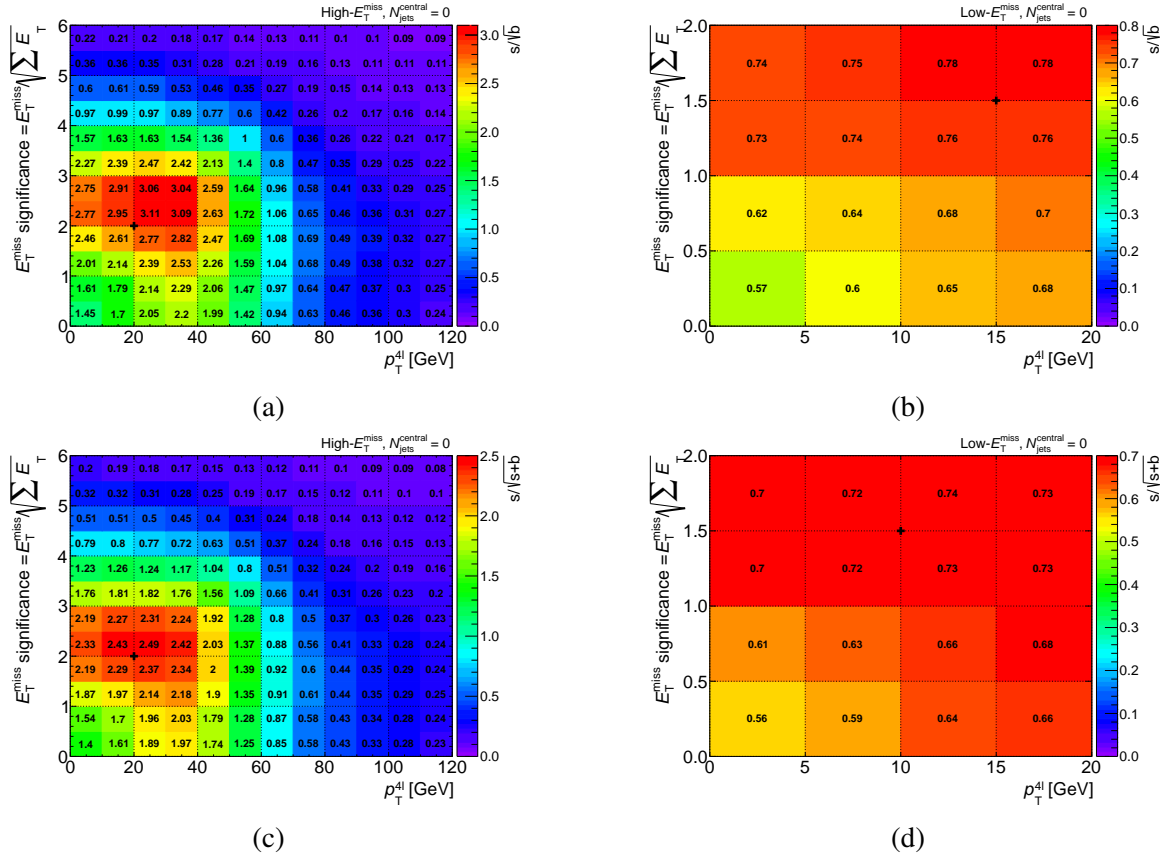


Fig. 7.4 Figure 7: Two-dimensional scan of the $p_T^{4\ell}$ and E_T^{miss} significance for the $R \rightarrow SH \rightarrow 4\ell + E_T^{\text{miss}}$ signal in the zero central jets region. The z-axis shows the significance calculated using s/\sqrt{b} (top) and $s/\sqrt{s+b}$ (bottom). The High- E_T^{miss} scans are displayed on 7.4a and 7.4c, and Low- E_T^{miss} on 7.4b) and 7.4d.

7.4 Signal and Background modelling

As elucidated in Chapter 5.3.2, simulation techniques were used to model and parameterize the $m_{4\ell}$ distribution for SM backgrounds. The signal shapes for the processes $R \rightarrow SH \rightarrow 4\ell + E_T^{\text{miss}}$ and $A \rightarrow ZH \rightarrow 4\ell + X$ were extracted directly from the MC simulation. Production included seventy-seven mass points for $R \rightarrow SH \rightarrow 4\ell + E_T^{\text{miss}}$ and seventy-two for $A \rightarrow ZH \rightarrow 4\ell + X$. The signal forms were extended throughout a wider mass spectrum using a linear interpolation technique, as explained in Ref. [193]. The focus was on the combinations of masses in (m_R, m_H) and (m_A, m_H) . The signal interpolation process is a two-step process that depends on (m_R, m_H) or (m_A, m_H) masses. In the initial step, the mass of H was kept constant while interpolating the mass parameters $(m_R - m_H)$ or $(m_A - m_H)$ and the mass R or A . The results of the preliminary interpolation step served as

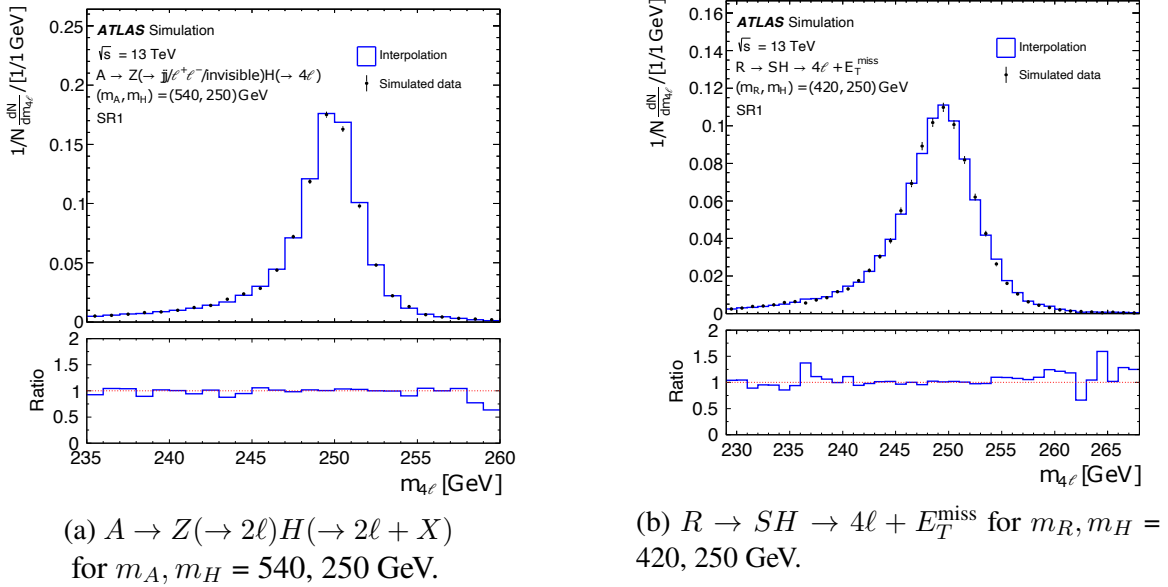


Fig. 7.5 The $m_{4\ell}$ distributions of the interpolated (blue) and simulated (black-filled point) signals. The lower panels show the ratio between the interpolated and simulated histograms. The plots are only shown in SR1 for illustrative purposes. The upper panels display the normalised distribution to compare the shapes, and the lower panels display the ratio, which should ideally be close to 1 if the interpolation is accurate. Taken from Ref. [191].

the basis for a further phase of interpolation. In this subsequent phase, the masses of R or A remained constant, while incremental adjustments were made to the mass of H , with each adjustment being 10 GeV. To validate the interpolation method, an analysis was performed in which the distributions of the simulated and interpolated signals at selected mass points were compared. This comparison is exemplified in Fig. 7.5 for the $A \rightarrow ZH \rightarrow 4\ell + X$ and $R \rightarrow SH \rightarrow 4\ell + E_T^{\text{miss}}$ signal processes. Although minor discrepancies appeared in the signal tails, they were identified as sources of potential systematic errors. However, it was established that these systematic errors had a minimal effect on the overall findings and, consequently, this uncertainty was excluded from further analysis.

7.5 Results

Table 7.1 presents the event yields on seven SRs as described in Section 7.3. A combined binned maximum likelihood analysis was performed, assuming only background contributions, to determine the observed and expected event counts in each SR. Furthermore, to explore potential deviations from the SM background, fits that incorporate both the signal and the background were performed on the $m_{4\ell}$ distribution, employing the statistical framework

	SR1	SR2	SR3	SR4	SR5	SR6	SR7
$q\bar{q} \rightarrow ZZ$	132 ± 12	17 ± 6	42 ± 7	40 ± 7	156 ± 13	549 ± 70	86 ± 11
$gg \rightarrow ZZ$	32 ± 6	3.2 ± 3.1	8.3 ± 3.1	6.6 ± 2.8	22.1 ± 3.7	102 ± 70	9.4 ± 4.2
VVV	7.5 ± 0.4	4.77 ± 0.34	14.9 ± 0.19	0.19 ± 0.04	1.59 ± 0.11	1.59 ± 0.13	0.50 ± 0.07
Other backgrounds	5.5 ± 0.9	7.1 ± 1.1	3.6 ± 0.7	2.47 ± 0.30	17.5 ± 0.8	11.3 ± 0.8	3.76 ± 2.3
Total background	177 ± 13	32 ± 6	55 ± 7	49 ± 7	197 ± 14	664 ± 26	134 ± 12
Observed	177	32	55	49	197	664	135
μ_{ZZ}^{norm}	1.15 ± 0.15	1.3 ± 0.6	0.96 ± 0.22	0.90 ± 0.17	0.80 ± 0.08	1.02 ± 0.13	1.4 ± 0.3

Table 7.1 Event yields following fit adjustment for $m_{A\ell} > 200$ GeV, encompassing uncertainties and comparing observed values with predicted values. Normalisation factor μ_{ZZ}^{norm} applies to $q\bar{q} \rightarrow ZZ$ and $gg \rightarrow ZZ$ backgrounds. Additional backgrounds such as $q\bar{q} \rightarrow ZZ$ (EW), $t\bar{t}$, $t\bar{t} + Z$, $t\bar{t} + jets$, and WZ , along with the VVV process, were fixed to their SM predictions.

outlined in Chapter 6.6.1. For the $R \rightarrow SH \rightarrow 4\ell + E_T^{\text{miss}}$ ($A \rightarrow ZH \rightarrow 4\ell + X$) search, mass ranges of 390–1300 GeV (320–1300 GeV for m_A) for m_R and 220–1000 GeV for m_H were scanned in 10 GeV steps. This approach generated 4187 (m_R, m_H) and 4740 (m_A, m_H) mass points within the NWA for each SR. Test statistics, including p -values and significance estimates, were used to assess the compatibility of the observed data with the background-only expectation and to search for evidence of potential deviations that could indicate new physical phenomena. The distributions of $m_{A\ell}$ for the $R \rightarrow SH \rightarrow 4\ell + E_T^{\text{miss}}$ search with the $(m_R, m_H) = (500, 300)$ GeV mass point are presented in Fig. 7.6 across three distinct SRs. These diagrams exhibit a fit to the dataset that exclusively considers the background, onto which signal data has been superimposed following scaling in accordance with the maximal observed limit of the cross section. A noticeable aspect in these diagrams is the prevalence of statistical fluctuations, particularly in the area where $m_{A\ell}$ reaches higher values. The determination of bin widths in these graphs has been guided by the need for consistent and reliable upper limit estimations in the cross section for both the $R \rightarrow SH \rightarrow 4\ell + E_T^{\text{miss}}$ and $A \rightarrow ZH \rightarrow 4\ell + X$ signals. While the computation of upper limits was conducted using bins of a uniform 5 GeV width, the representations in the graphs employ variable bin sizes for improved clarity and visual interpretation.

However, the observational data predominantly align with the expected background of the SM. Localised two-sigma excesses appear at several mass points within the $R \rightarrow SH \rightarrow 4\ell + E_T^{\text{miss}}$ and $A \rightarrow ZH \rightarrow 4\ell + X$ signal processes. The analysis identified an excess of events consistent with the $A \rightarrow ZH \rightarrow 4\ell + X$ signal at the mass coordinates $(m_A, m_H) = (510, 380)$ GeV. This excess corresponds to a statistical significance of 2.5 standard deviations above the background expectation. Further analysis was performed to assess the role of systematic uncertainties, especially in their influence on a critical factor, the optimal cross

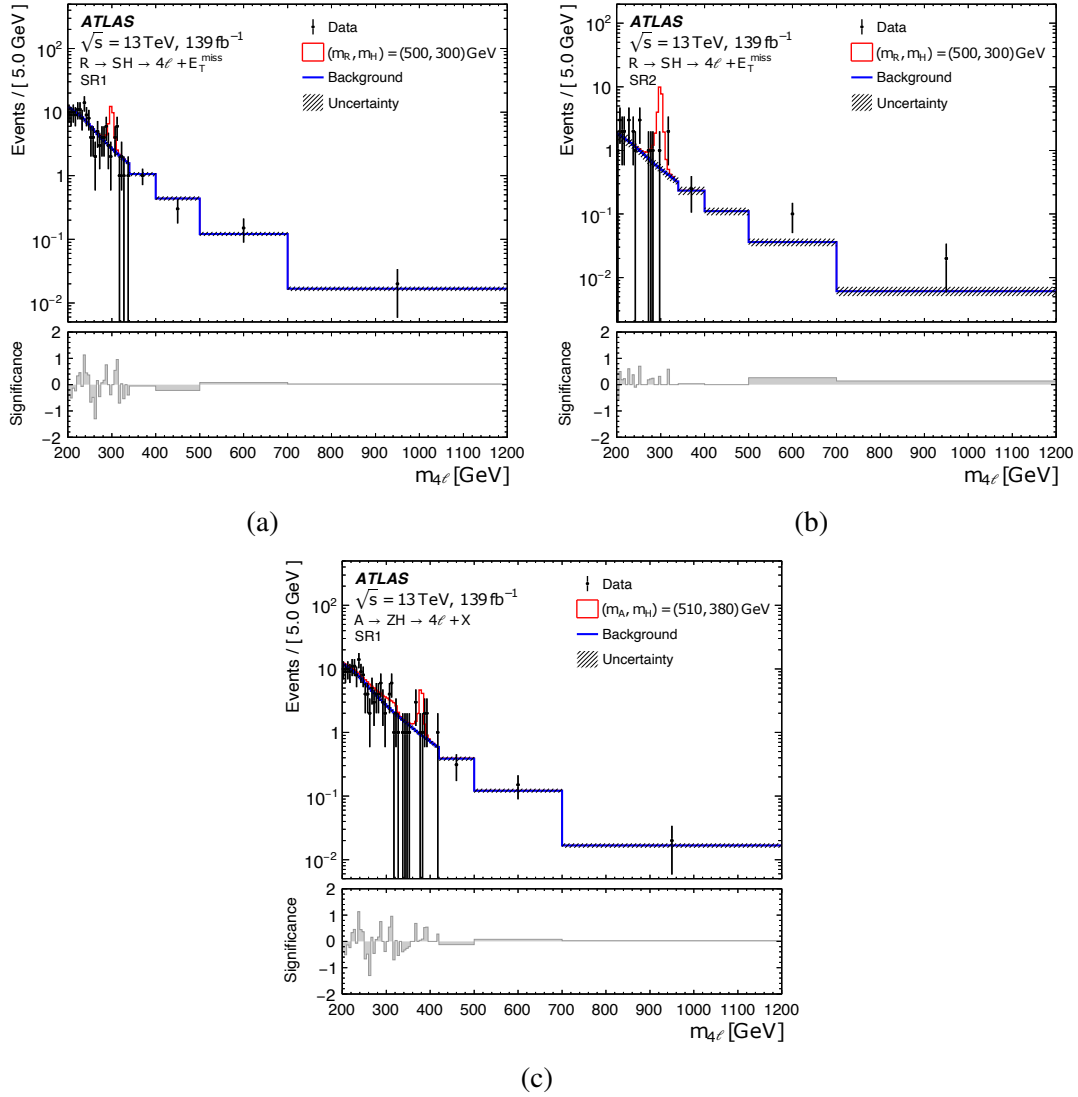


Fig. 7.6 Search for $R \rightarrow SH \rightarrow 4\ell + E_T^{\text{miss}}$ across SRs: background (blue) vs. potential signal (red, 500 GeV RH-neutrino, 300 GeV Higgs, upper limit 25.0 fb). Error bars: statistical, hatched areas: systematic uncertainties. Lower panel: Bin-by-bin significance. Taken from Ref. [191].

section value, in both the $R \rightarrow SH \rightarrow 4\ell + E_T^{\text{miss}}$ and $A \rightarrow ZH \rightarrow 4\ell + X$ processes. The magnitude of impact of these uncertainties was observed to vary when different mass pairs, either (m_R, m_H) or (m_A, m_H) , are considered.

Table 7.2 presents the five main sources of uncertainty that affect the optimal value of σ for three chosen mass configurations within each signal category. The influence of these factors was assessed using Asimov datasets, where the signal cross section was set to correspond to the anticipated exclusion limits at specific mass configurations of (m_R, m_H) or (m_A, m_H) .

$R \rightarrow SH \rightarrow 4\ell + E_T^{\text{miss}}$			$A \rightarrow ZH \rightarrow 4\ell + X$		
(m_R, m_H) [GeV]	Uncertainty source	$\Delta\sigma/\sigma$ [%]	(m_A, m_H) [GeV]	Uncertainty source	$\Delta\sigma/\sigma$ [%]
(390, 220)	Composition of Jet Flavours	6.2	(320, 220)	Parameterisation of Other Backgrounds in SR7	5.0
	Response of Jet Flavours	4.8		$q\bar{q} \rightarrow ZZ$ parameterisation SR7	3.9
	Jet energy scale	4.2		Composition of Jet Flavours	3.9
	Reweighting for Pile-up Effects	4.0		Luminosity	3.7
	CKKW parton showering ($gg \rightarrow ZZ$) SR2	3.8		$gg \rightarrow ZZ$ parameterisation SR6	3.6
(500, 300)	CKKW parton showering ($gg \rightarrow ZZ$) SR2	3.1	(510, 380)	Luminosity	2.4
	QSF parton showering ($gg \rightarrow ZZ$) SR2	3.0		Composition of Jet Flavours	2.4
	$q\bar{q} \rightarrow ZZ$ parameterisation SR2	2.0		Jet energy scale	1.7
	Reweighting for Pile-up Effects	1.9		Jet energy resolution	1.5
	VVV parameterisation SR2	1.9		Signal PDF	1.4
(1300, 1000)	$q\bar{q} \rightarrow ZZ$ parameterisation SR2	9.3	(1300, 1000)	CKKW parton showering ($gg \rightarrow ZZ$) SR2	3.3
	Composition of Jet Flavours	7.3		QSF parton showering ($gg \rightarrow ZZ$) SR2	3.3
	Response of Jet Flavours	3.5		Parameterisation of Other Backgrounds in SR2	2.6
	Reweighting for Pile-up Effects	2.9		$q\bar{q} \rightarrow ZZ$ parameterisation SR5	2.1
	CKKW parton showering ($gg \rightarrow ZZ$) SR2	2.9		VVV parameterisation SR2	2.1

Table 7.2 Relative impact of major uncertainty components on the final signal cross section values determined through model fitting. The table presents results for three mass points in the context of the $R \rightarrow SH \rightarrow 4\ell + E_T^{\text{miss}}$ and $A \rightarrow ZH \rightarrow 4\ell + X$ signal analyses. Each bar represents the sum of squared upward and downward variations ($\Delta\sigma$) in the cross section due to a specific uncertainty, divided by the best fit cross section value (σ) for that particular signal.

This was done under the assumption that the R or A and H bosons have narrow widths. In particular, in the analysis of the $R \rightarrow SH \rightarrow 4\ell + E_T^{\text{miss}}$ process, jet-related uncertainties, especially those concerning jet flavour composition, had a substantial influence. This was particularly evident, as they were the first and second most significant at the mass points $(m_R, m_H) = (390, 220)$ GeV and $(m_R, m_H) = (1300, 1000)$ GeV. The limitations associated with jet characteristics significantly impacted the assessments of both $R \rightarrow SH \rightarrow 4\ell + E_T^{\text{miss}}$ and $A \rightarrow ZH \rightarrow 4\ell + X$ searches. Although some mass points exhibited localised deviations exceeding two standard deviations, in general no statistically significant deviations from the predicted background were observed. Figures 7.7a and 7.7b show these localised excesses for the respective searches. Given the absence of a substantial background excess, upper limits were calculated for the production cross sections of hypothetical signals. These limits account for relevant branching fractions and employ the CL_s method with an asymptotic approximation. Optimisation of nuisance parameter probability functions for each mass hypothesis resulted in limits on specific cross section and branching ratio combinations. Figures 7.8a and 7.8b present observed and expected upper limits for the first search, ranging from 6.8 fb to 119.2 fb and 7.7 fb to 70.3 fb, respectively. Similarly, Figs. 7.8c and 7.8d show observed and expected limits for the second search, ranging from 2.1 fb to 32.3 fb and 2.9 fb to 18.8 fb, respectively.

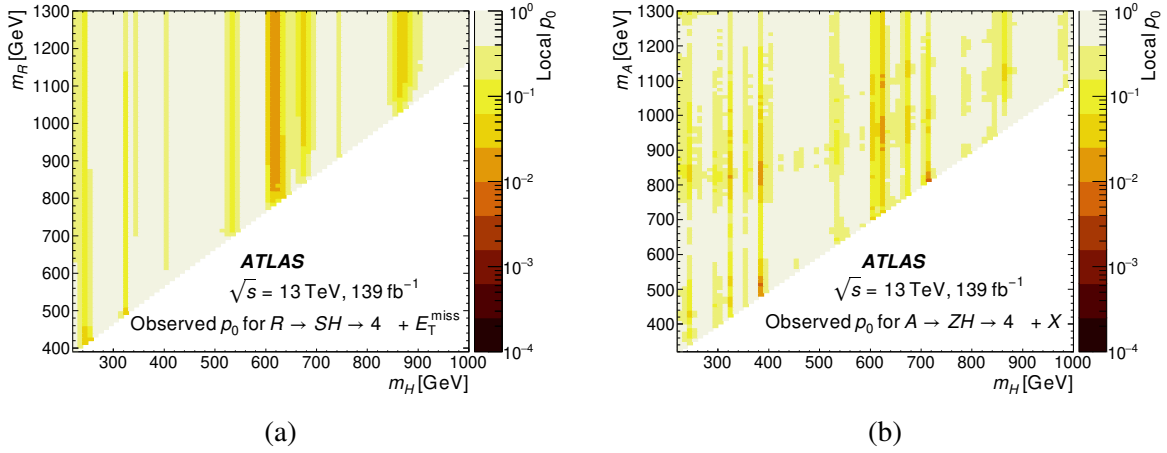


Fig. 7.7 **a** presents local p_0 -values in the plane of (m_H, m_R) for the decay process $R \rightarrow SH \rightarrow 4\ell + E_T^{\text{miss}}$, with m_S at 160 GeV. **b** illustrates the same in the (m_H, m_A) plane for the decay $A \rightarrow ZH \rightarrow 4\ell + X$. Taken from Ref. [191].

It should be noted that pseudo-experiments confirmed the validity of the asymptotic upper limits used across various mass points in the analysis [184, 185]. This study focused on heavy resonances with NWA for the A and H bosons produced by ggF in both the $A \rightarrow ZH \rightarrow 4\ell + X$ and $R \rightarrow SH \rightarrow 4\ell + E_T^{\text{miss}}$ processes. However, the impact of LWA on the analysis was also investigated. The analysis considered two signal scenarios with mass points similar to the NWA for the $A \rightarrow ZH \rightarrow 4\ell + X$ process. The chosen mass points were 320 GeV and 220 GeV for the lower mass scenario and 1190 GeV and 600 GeV for the higher mass scenario. Due to the significant natural widths of the A and H bosons relative to their masses, the upper limits were calculated for the case of LWA. These upper limits exhibited a positive correlation with the assumed natural width. For example, when the natural widths of the A and H bosons were set at 15% and 5% of their true masses, the LWA upper limits were 1.4 and 1.7 times larger than the corresponding NWA upper limits, respectively, for the low and high mass scenarios. Similarly, increasing natural widths to 30% and 10% resulted in LWA upper limits that were 1.7 and 1.9 times larger than NWA upper limits, respectively. A comprehensive comparison of the width assumptions, mass points and upper limits for both the LWA and NWA scenarios is provided in Table 7.3.

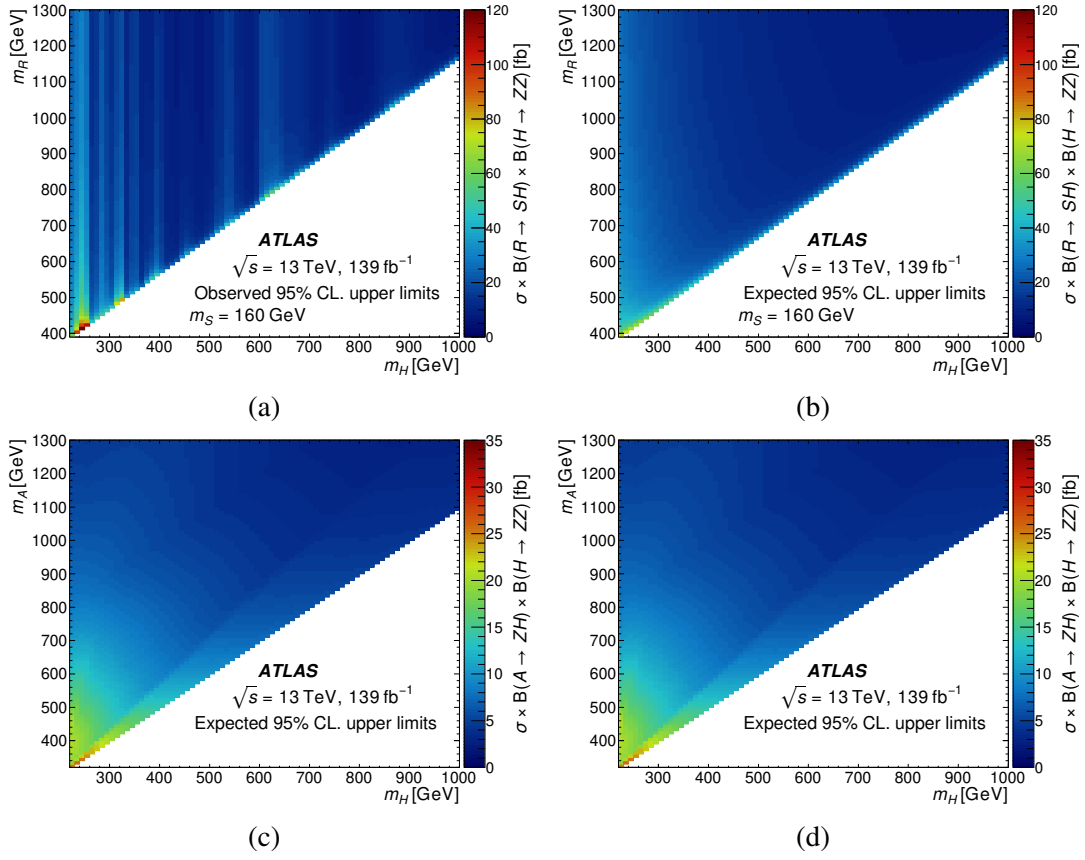


Fig. 7.8 Comparing observed (left) and expected (right) limits on $gg \rightarrow R/A \rightarrow 4\ell$ searches, with $m_S = 160$ GeV. Solid/dashed lines show 95% confidence limits for $R \rightarrow SH$ and $A \rightarrow ZH$ across the $(m_H, m_{R/A})$ planes.

Width assumptions	Mass points [GeV]	Upper limits in the $\sigma(gg \rightarrow A)$ [fb]		Ratio w.r.t Narrow width
		Observed	Expected	
Narrow width	$(m_A, m_H) = (320, 220)$	19.6	25.1	1.0
	$(m_A, m_H) = (1190, 600)$	4.8	3.5	1.0
$(\Gamma_A/m_A, \Gamma_H/m_H) = (15\%, 5\%)$	$(m_A, m_H) = (320, 220)$	31.5	36.2	1.4
	$(m_A, m_H) = (1190, 600)$	8.3	6.0	1.7
$(\Gamma_A/m_A, \Gamma_H/m_H) = (30\%, 10\%)$	$(m_A, m_H) = (320, 220)$	38.9	42.5	1.7
	$(m_A, m_H) = (1190, 600)$	8.9	6.6	1.9

Table 7.3 Observed and expected upper limits at 95% CL on the product of three cross sections: $\sigma(gg \rightarrow A)$, $\mathcal{B}(A \rightarrow ZH)$, and $\mathcal{B}(H \rightarrow ZZ)$, for various LWA signals. These results are compared with the NWA.

Chapter 8

Conclusions

Imbila yaswel'umsila ngokuyalezela

E.W.M Mesatywa.

Numerous theoretical models beyond the Standard Model posit the existence of additional heavy resonances resembling the Higgs boson. If present, these resonances could be detected at the TeV scale by hadron colliders like the Large Hadron Collider (LHC). Operating at unprecedented luminosities, the ATLAS and CMS detectors, designed for diverse physics measurements at the LHC, offer exceptional sensitivity to both high-precision Standard Model measurements and potential new discoveries. This dissertation presented two searches for heavy resonances conducted using the ATLAS detector. The first search targeted final states containing four leptons, while the second expanded to include events with missing transverse momentum or jets. These analyses used proton-proton collision data collected by ATLAS at the LHC between 2015 and 2018, a total integrated luminosity of 139 fb^{-1} . Additionally, an overview of the integrator panel's operation within the Prometeo software for the ATLAS Tile calorimeter is presented.

8.1 The Integrator Panel on the Prometeo Software

The Phase II Upgrade of the LHC is poised to substantially increase its instantaneous luminosity, with an expected enhancement factor ranging between 5 and 10. This increase requires significant adjustments in electronics, both in terms of their capacity to withstand elevated radiation doses and their ability to handle a surge in data throughput. The time frame for this undertaking is 2025 to 2027. In the context of our research, Prometeo, a key

element discussed in Chapter 3, assumes a critical role in certifying the performance of Phase II front-end electronics within TileCal. The Prometeo offers a comprehensive suite of test capabilities. Its development mirrors an iterative approach, with each component (including new GUI panels, Integrator, and LED systems) undergoing a thorough testing before integration. Verification through system testing has confirmed its functionality, and subsequently been incorporated into the final design. The test bench has successfully conducted pulse, LED shape and charge injection tests, demonstrating its readiness for a comprehensive electronic evaluation. Concurrent with the demonstrator's development, additional tests are continuously being developed and evaluated. This ongoing effort paves the way for robust and reliable electronics for the TileCal detector in the HL-LHC era.

8.2 Isolation Studies for 4ℓ searches

The impact of pile-up on the 4ℓ final state was evaluated for the 2015 + 2016 and 2017 datasets, employing a weighted pile-up profile throughout these years (Chapter 5.6). Focusing on the 100-800 GeV mass range for the heavy scalar boson, fully simulated events generated within the H 4ℓ framework were analysed. Comparison of the data revealed the expected yield results, with 4μ events demonstrating the highest efficiency. In particular, although the event results were higher for 2015 + 2017, the overall difference remained marginal (3.77%). Shape comparisons yielded ratios close to unity between the datasets, indicating a minimal influence of pileup on mass resolution and energy/momentum scale. Subsequently, electron isolation studies were carried out to optimise the discrimination between signal decay products and the background (Chapter 5.7.5). The evaluation process involved a variety of types of cuts, each aiming to achieve an equilibrium among key parameters: signal efficiency, the ability to distinguish the signal from background noise, and the resilience against pile-up. The FixedCutPflowLoose WP emerged as the most promising candidate due to its superior or near-superior performance in all tests. However, scaling factors applied to correct for simulated isolation efficiencies revealed a significant attenuation of the initial gains observed for electron-triggered events. In particular, as expected, the benefit of the FixedCutPflowLoose WP was amplified with a higher pile-up, demonstrating its robustness under such conditions. This optimised isolation strategy ultimately formed the basis for the analyses presented in Chapters 6 and 7.

8.3 Searches for heavy resonances in the 4ℓ final state

Building on the 4ℓ final state analysis detailed in Chapter 6, a comprehensive search for heavy resonances decaying into ZZ pairs across a mass spectrum of 200-2000 GeV was conducted. Within the SM framework, no significant deviations were observed. Focusing on a hypothetical heavy-scalar resonance (dominant production modes: ggF and VBF), narrow- and large-width scenarios were investigated. For the narrow-width case, 95% Confidence Level (CL) upper limits on the production rate (combining both final states) were established: 215-2.0 fb for ggF and 87-1.5 fb for VBF, depending on the mass range (240-1900 GeV and 255-1800 GeV, respectively). Furthermore, interpretations within two-Higgs doublet models (Types I and II) produced exclusion contours in the $\tan \beta$ versus $\cos(\beta - \alpha)$ (for $m_H = 220$ GeV) and $\tan \beta$ versus $\tan \beta$ planes. Furthermore, the Randall-Sundrum model with an extra dimension was probed, resulting in a 95% CL exclusion limit of $m(G_{kk}) < 1830$ GeV for the graviton excitation spin-2 resonance.

8.4 Searches for heavy resonances in the 4ℓ final state and E_T^{miss} or jets

This thesis builds on the search outlined in Chapter 6 by comprehensively investigating new heavy resonances in the final state of four leptons accompanied by either missing transverse momentum or a jet. The study focused on two specific signal processes:

- $R \rightarrow SH \rightarrow 4\ell + E_T^{\text{miss}}$: This process involves a hypothetical heavy boson, R , decaying into an invisible S boson and a SM Higgs boson (H). The Higgs boson subsequently decays into two Z bosons, ultimately resulting in 4ℓ final state.
- $A \rightarrow ZH \rightarrow 4\ell + X$: This process features the decay of a heavy boson, A , into a Z boson and a H boson. Two scenarios for the associated production of Z and H bosons were explored:
 1. $A \rightarrow Z(\rightarrow jj/\ell^+\ell^-/\text{invisible})H(\rightarrow 4\ell)$
 2. $A \rightarrow Z(\rightarrow 2\ell)H(\rightarrow 2\ell + jj/\text{invisible})$

Both searches investigated hypothetical bosons (A and R) with mass ranges of 320-1300 GeV (A) and 390-1300 GeV (R), while the mass of the S boson was fixed at 160 GeV. Neither analysis observed any significant deviations from the expected Standard Model background.

Upper limits on production cross sections and branching ratios were established at 95% confidence level (CL). These findings complement prior searches for the $A \rightarrow ZH$ process (discussed in Chapter 5) and offer valuable insights into the behaviour of these hypothetical bosons. The $R \rightarrow SH \rightarrow 4\ell + E_T^{\text{miss}}$ analysis expands on existing searches by exploring a broader phase space and incorporating the potential for missing transverse momentum.

In conclusion, while the results presented align with the SM predictions, a recent combined analysis of the ATLAS and CMS Run 2 and Run 3 data, presented in Figure 6.9, reveals a tentative excess in the 250 - 260 GeV range. This 2.4σ resides precisely within the anticipated mass spectrum for the phenomena that produce a final state of 4 leptons. This finding underscores the importance of ongoing experimental efforts to elucidate any potential deviations from the Standard Model and potentially pave the way for discoveries beyond our current understanding.

References

- [1] Helge Kragh. Rutherford, radioactivity, and the atomic nucleus, 2012. arXiv:1202.0954, <https://arxiv.org/abs/1202.0954>.
- [2] G. Aad et al. Observation of a new particle in the search for the Standard Model Higgs boson with the ATLAS detector at the LHC. *Phys. Lett.*, B716:1–29, 2012.
- [3] S. Chatrchyan et al. Observation of a New Boson at a Mass of 125 GeV with the CMS Experiment at the LHC. *Phys. Lett.*, B716:30–61, 2012.
- [4] E. Fernandez. Collider Physics. *PoS*, silafae-III:008, 2000.
- [5] M. E. Peskin and D. V. Schroeder. *An Introduction to quantum field theory*. Addison-Wesley, Reading, USA, 1995.
- [6] M. D. Schwartz. *Quantum Field Theory and the Standard Model*. Cambridge University Press, 2014.
- [7] J. Iliopoulos. Symmetries and the Weak Interactions, 1 2011.
- [8] A. Salam. Weak and Electromagnetic Interactions. *Conf. Proc.*, C680519:367–377, 1968.
- [9] S. Weinberg. A Model of Leptons. *Phys. Rev. Lett.*, 19:1264–1266, 1967.
- [10] C. Yang and R. L. Mills. Conservation of Isotopic Spin and Isotopic Gauge Invariance. *Phys. Rev.*, 96:191–195, 1954. [,150(1954)].
- [11] Wikimedia Commons webpage. Standard model of particle physics–most complete diagram. https://commons.wikimedia.org/w/index.php?title=File:Standard_Model_Of_Particle_Physics--Most_Complete_Diagram.png&oldid=285432513, 2018. Last accessed 23 January 2020.
- [12] M. Gell-Mann. A Schematic Model of Baryons and Mesons. *Phys. Lett.*, 8:214–215, 1964.
- [13] G. Zweig. An SU(3) model for strong interaction symmetry and its breaking. Version 2, 2 1964.
- [14] O. W. Greenberg. Spin and Unitary Spin Independence in a Paraquark Model of Baryons and Mesons. *Phys. Rev. Lett.*, 13:598–602, 1964.

- [15] H. D. Politzer. Asymptotic Freedom: An Approach to Strong Interactions. *Phys. Rept.*, 14:129–180, 1974.
- [16] R. Aaij et al. First Observation of a Doubly Charged Tetraquark and Its Neutral Partner. *Phys. Rev. Lett.*, 131(4):041902, 2023.
- [17] R. Aaij et al. Observation of the resonant character of the $Z(4430)^-$ state. *Phys. Rev. Lett.*, 112(22):222002, 2014.
- [18] R. Aaij et al. Observation of $J/\psi p$ Resonances Consistent with Pentaquark States in $\Lambda_b^0 \rightarrow J/\psi K^- p$ Decays. *Phys. Rev. Lett.*, 115:072001, 2015.
- [19] G. Arnison et al. Experimental Observation of Lepton Pairs of Invariant Mass Around 95-GeV/c² at the CERN SPS Collider. *Phys. Lett.*, 126B:398–410, 1983. [7.55(1983)].
- [20] P. Bagnaia et al. Evidence for $Z_0 \rightarrow e^+e^-$ at the CERN anti-p p Collider. *Phys. Lett.*, 129B:130–140, 1983. [7.69(1983)].
- [21] G. Arnison et al. Experimental Observation of Isolated Large Transverse Energy Electrons with Associated Missing Energy at $\sqrt{s} = 540$ -GeV. *Phys. Lett.*, 122B:103–116, 1983. [6.11(1983)].
- [22] M. Banner et al. Observation of Single Isolated Electrons of High Transverse Momentum in Events with Missing Transverse Energy at the CERN anti-p p Collider. *Phys. Lett.*, 122B:476–485, 1983. [7.45(1983)].
- [23] K. A. Olive et al. Review of Particle Physics. *Chin. Phys.*, C38:090001, 2014.
- [24] F. Englert and R. Brout. Broken Symmetry and the Mass of Gauge Vector Mesons. *Phys. Rev. Lett.*, 13:321–323, 1964. [1.57(1964)].
- [25] P. W. Higgs. Broken Symmetries and the Masses of Gauge Bosons. *Phys. Rev. Lett.*, 13:508–509, 1964. [1.60(1964)].
- [26] G. S. Guralnik, C. R. Hagen, and T. W. B. Kibble. Global Conservation Laws and Massless Particles. *Phys. Rev. Lett.*, 13:585–587, 1964. [1.62(1964)].
- [27] Riebesell Janosh. Tikz example: Mexican hat, 2024. Accessed: 2024-05-23.
- [28] J. Goldstone, A. Salam, and S. Weinberg. Broken Symmetries. *Phys. Rev.*, 127:965–970, 1962.
- [29] D. de Florian et al. Handbook of LHC Higgs Cross Sections: 4. Deciphering the Nature of the Higgs Sector, 10 2016. arXiv:1610.07922, <https://arxiv.org/abs/1610.07922>.
- [30] J. T. Seeman. The stanford linear collider. *Annual Review of Nuclear and Particle Science*, 41(1):389–428, 1991.
- [31] CERN. LEP Design Report: Vol.2. The LEP Main Ring, 6 1984.
- [32] TeVI Group. Design Report Tevatron 1 project, 1984.

- [33] G. Aad et al. Combined Measurement of the Higgs Boson Mass in pp Collisions at $\sqrt{s} = 7$ and 8 TeV with the ATLAS and CMS Experiments. *Phys. Rev. Lett.*, 114:191803, 2015.
- [34] R. Barate et al. Search for the standard model Higgs boson at LEP. *Phys. Lett. B*, 565:61–75, 2003.
- [35] A. Tumasyan et al. A portrait of the Higgs boson by the CMS experiment ten years after the discovery. *Nature*, 607(7917):60–68, 2022. [Erratum: *Nature* 623, (2023)].
- [36] O. Fischer et al. Unveiling hidden physics at the LHC. *Eur. Phys. J. C*, 82(8):665, 2022. arXiv:2109.06065, <https://arxiv.org/abs/2109.06065>.
- [37] S. von Buddenbrock et al. The compatibility of LHC Run 1 data with a heavy scalar of mass around 270 GeV, 2015. arXiv:1506.00612, <https://arxiv.org/abs/arXiv:1506.00612>.
- [38] S. von Buddenbrock et al. Phenomenological signatures of additional scalar bosons at the LHC. *Eur. Phys. J.*, C76(10):580, 2016.
- [39] S. von Buddenbrock, A.S. Cornell, M. Kumar, and B. Mellado. The Madala hypothesis with Run 1 and 2 data at the LHC. *J. Phys. Conf. Ser.*, 889(1):012020, 2017.
- [40] S. von Buddenbrock et al. Multi-lepton signatures of additional scalar bosons beyond the Standard Model at the LHC. *J. Phys.*, G45(11):115003, 2018.
- [41] S. von Buddenbrock, A.S. Cornell, E.D.R. Iarilala, M. Kumar, B. Mellado, X. Ruan, and E.M. Shrif. Constraints on a 2HDM with a singlet scalar and implications in the search for heavy bosons at the LHC. *J. Phys. G*, 46(11):115001, 2019.
- [42] S. Buddenbrock, A.S. Cornell, Y. Fang, A.F Mohammed, M. Kumar, B. Mellado, and K.G. Tomiwa. The emergence of multi-lepton anomalies at the LHC and their compatibility with new physics at the EW scale. *JHEP*, 10:157, 2019.
- [43] D. Sabatta, A.S. Cornell, A. Goyal, M. Kumar, B. Mellado, and X. Ruan. Connecting muon anomalous magnetic moment and multi-lepton anomalies at LHC. *Chin. Phys. C*, 44(6):063103, 2020.
- [44] Y. Hernandez, M. Kumar, A.S. Cornell, S.E. Dahbi, Y. Fang, B. Lieberman, B. Mellado, K. Monnagogtla, X. Ruan, and S. Xin. The anomalous production of multi-lepton and its impact on the measurement of Wh production at the LHC. *Eur. Phys. J. C*, 81(4):365, 2021.
- [45] S. von Buddenbrock, R. Ruiz, and B. Mellado. Anatomy of inclusive $t\bar{t}W$ production at hadron colliders. *Phys. Lett. B*, 811:135964, 2020.
- [46] A.M. Sirunyan et al. Search for a standard model-like Higgs boson in the mass range between 70 and 110 GeV in the diphoton final state in proton-proton collisions at $\sqrt{s} = 8$ and 13 TeV. *Phys. Lett. B*, 793:320–347, 2019.
- [47] S. Banik, G. Coloretti, A. Crivellin, and B. Mellado. Uncovering New Higgses in the LHC Analyses of Differential $t\bar{t}$ Cross Sections, 8 2023.

- [48] G. Aad et al. Inclusive and differential cross-sections for dilepton $t\bar{t}$ production measured in $\sqrt{s} = 13$ TeV pp collisions with the ATLAS detector. *JHEP*, 07:141, 2023.
- [49] M. Aaboud et al. Measurement of fiducial and differential W^+W^- production cross-sections at $\sqrt{s} = 13$ TeV with the ATLAS detector. *Eur. Phys. J. C*, 79(10):884, 2019.
- [50] A.M. Sirunyan et al. Search for heavy Higgs bosons decaying to a top quark pair in proton-proton collisions at $\sqrt{s} = 13$ TeV. *JHEP*, 04:171, 2020. [Erratum: *JHEP* 03, 187 (2022)].
- [51] G. Aad et al. Observation of four-top-quark production in the multilepton final state with the ATLAS detector. *Eur. Phys. J. C*, 83(6):496, 2023.
- [52] A. Hayrapetyan et al. Observation of four top quark production in proton-proton collisions at $s=13$ TeV. *Phys. Lett. B*, 847:138290, 2023.
- [53] CMS Collaboration. Measurement of Higgs boson production in association with a W or Z boson in the $H \rightarrow WW$ decay channel, 2021.
- [54] G. Aad et al. Observation of WWW Production in pp Collisions at $\sqrt{s} = 13$ TeV with the ATLAS Detector. *Phys. Rev. Lett.*, 129(6):061803, 2022.
- [55] A. Tumasyan et al. Measurements of the Higgs boson production cross section and couplings in the W boson pair decay channel in proton-proton collisions at $\sqrt{s} = 13$ TeV. *Eur. Phys. J. C*, 83(7):667, 2023.
- [56] A. Crivellin and B. Mellado. Anomalies in Particle Physics, 9 2023. arXiv:2309.03870, <https://arxiv.org/abs/2309.03870>.
- [57] A. Crivellin, Y. Fang, O. Fischer, S. Bhattacharya, M. Kumar, E. Malwa, B. Mellado, N. Rapheeha, X. Ruan, and Q. Sha. Accumulating evidence for the associated production of a new Higgs boson at the LHC. *Phys. Rev. D*, 108(11):115031, 2023.
- [58] G. Aad et al. CP Properties of Higgs Boson Interactions with Top Quarks in the $t\bar{t}H$ and tH Processes Using $H \rightarrow \gamma\gamma$ with the ATLAS Detector. *Phys. Rev. Lett.*, 125(6):061802, 2020.
- [59] A.M. Sirunyan et al. Measurements of Higgs boson production cross sections and couplings in the diphoton decay channel at $\sqrt{s} = 13$ TeV. *JHEP*, 07:027, 2021.
- [60] G. Aad et al. Measurements of Higgs boson production cross-sections in the $H \rightarrow \tau^+\tau^-$ decay channel in pp collisions at $\sqrt{s} = 13$ TeV with the ATLAS detector. *JHEP*, 08:175, 2022.
- [61] ATLAS Collaboration. Search for diphoton resonances in the 66 to 110 GeV mass range using 140 fb^{-1} of 13 TeV pp collisions collected with the ATLAS detector. Technical report, CERN, Geneva, 2023.
- [62] A. Tumasyan et al. Searches for additional Higgs bosons and for vector leptoquarks in $\tau\tau$ final states in proton-proton collisions at $\sqrt{s} = 13$ TeV. *JHEP*, 07:073, 2023.

- [63] S. Bhattacharya, G. Coloretti, A. Crivellin, S.E Dahbi, Y. Fang, M. Kumar, and B. Mellado. Growing Excesses of New Scalars at the Electroweak Scale, 6 2023.
- [64] M. Chabab, M. C. Peyranère, and L. Rahili. Probing the Higgs sector of $Y = 0$ Higgs Triplet Model at LHC. *Eur. Phys. J. C*, 78(10):873, 2018.
- [65] P. Fileviez, HH. Patel, and AD. Plascencia. On the W mass and new Higgs bosons. *Phys. Lett. B*, 833:137371, 2022.
- [66] Y. Cheng, X. He, F. Huang, J. Sun, and Z. Xing. Electroweak precision tests for triplet scalars. *Nucl. Phys. B*, 989:116118, 2023.
- [67] T. Chen, C. Chiang, and K. Yagyu. Explanation of the W mass shift at CDF II in the extended Georgi-Machacek model. *Phys. Rev. D*, 106(5):055035, 2022.
- [68] J. de Blas, M. Pierini, L. Reina, and L. Silvestrini. Impact of the Recent Measurements of the Top-Quark and W-Boson Masses on Electroweak Precision Fits. *Phys. Rev. Lett.*, 129(27):271801, 2022.
- [69] T. Aaltonen et al. High-precision measurement of the W boson mass with the CDF II detector. *Science*, 376(6589):170–176, 2022.
- [70] S. Schael et al. Electroweak Measurements in Electron-Positron Collisions at W-Boson-Pair Energies at LEP. *Phys. Rept.*, 532:119–244, 2013.
- [71] A. Djouadi, P. Gambino, and Bernd A. Kniehl. Two loop electroweak heavy fermion corrections to Higgs boson production and decay. *Nucl. Phys. B*, 523:17–39, 1998.
- [72] CERN. CERN Annual Personnel Statistics 2022, 2022. CERN Annual Personnel Statistics 2022.
- [73] R. Assmann, M. Lamont, and S. Myers. A brief history of the LEP collider. *Nucl. Phys. Proc. Suppl.*, 109B:17–31, 2002. [17(2002)].
- [74] M. Jacob, editor. *Proceedings, ECFA-CERN Workshop on large hadron collider in the LEP tunnel*, 1984.
- [75] O. Buning, P. Collier, P. Lebrun, S. Myers, R. Ostojic, J. Poole, and P. Proudlock. LHC Design Report. 2. The LHC infrastructure and general services, 11 2004.
- [76] E. Lopienska. The CERN accelerator complex, layout in 2022. Complexe des accélérateurs du CERN en janvier 2022, 2022. General Photo.
- [77] S. Holmes, R. S. Moore, and V. Shiltsev. Overview of the Tevatron Collider Complex: Goals, Operations and Performance. *JINST*, 6:T08001, 2011.
- [78] L. Rossi. The LHC superconducting magnets, 2003. Published in: Conf.Proc.C 030512 (2003) 141. Contribution to: Particle Accelerator Conference (PAC 03). Report numbers: PAC03-TOAB001, CERN-LHC-PROJECT-REPORT-660. View in: CERN Document Server, <https://cds.cern.ch/record/630341>.
- [79] V. Duvivier. Cross section of LHC dipole.. Dipole LHC: Coupe transversale. AC Collection. Legacy of AC. Pictures from 1992 to 2002., 2001.

- [80] G. Aad et al. The ATLAS Experiment at the CERN Large Hadron Collider. *JINST*, 3:S08003, 2008.
- [81] S. Chatrchyan et al. The CMS Experiment at the CERN LHC. *JINST*, 3:S08004, 2008.
- [82] A. Augusto Alves, Jr. et al. The LHCb Detector at the LHC. *JINST*, 3:S08005, 2008.
- [83] O. Adriani et al. The LHCf detector at the CERN Large Hadron Collider. *JINST*, 3:S08006, 2008.
- [84] V. A. Mitsou. The MoEDAL experiment at the LHC: status and results. *J. Phys. Conf. Ser.*, 873(1):012010, 2017.
- [85] Run-2 luminosity public results. <https://twiki.cern.ch/twiki/bin/view/AtlasPublic/LuminosityPublicResultsRun2>, 2020. Last accessed 08 October 2023.
- [86] J. Pequeno. Computer generated image of the whole ATLAS detector, Mar 2008. CERN-GE-0803012, <https://cds.cern.ch/record/1095924>.
- [87] J. Pequeno and P. Schaffner. How ATLAS detects particles: diagram of particle paths in the detector, Jan 2013. CERN-EX-1301009, <https://cds.cern.ch/record/1505342>.
- [88] Georges Aad et al. Alignment of the ATLAS Inner Detector in Run-2. *Eur. Phys. J. C*, 80(12):1194, 2020.
- [89] M. Capeans, G. Darbo, K. Einsweiler, M. Elsing, T. Flick, M. Garcia-Sciveres, C. Gemme, H. Pernegger, O. Rohne, and R. Vuillermet. ATLAS Insertable B-Layer Technical Design Report, 9 2010.
- [90] ATLAS Collaboration. Track Reconstruction Performance of the ATLAS Inner Detector at $\sqrt{s} = 13\sim\text{TeV}$, 7 2015. ATL-PHYS-PUB-2015-018, <https://cds.cern.ch/record/2052552>.
- [91] Joao Pequeno. Computer generated image of the ATLAS Muons subsystem, 2008. View in: CERN Document Server, <https://cds.cern.ch/record/1095929>.
- [92] T. Colombo. Data-flow performance optimisation on unreliable networks: the atlas data-acquisition case. *Journal of Physics: Conference Series*, 608:012005, 05 2015.
- [93] A. Pozo and E. Mikel. The ATLAS Data Acquisition System in LHC Run 2. *Journal of Physics: Conference Series*, 898:032017, Oct 2017.
- [94] ATLAS Collaboration. Trigger Menu in 2016. Technical Report ATL-DAQ-PUB-2017-001, CERN, Geneva, Jan 2017.
- [95] G. Aad et al. The ATLAS Experiment at the CERN Large Hadron Collider. *JINST*, 3:S08003, 2008.
- [96] G. Aad et al. Readiness of the ATLAS Tile Calorimeter for LHC collisions. *Eur. Phys. J. C*, 70:1193–1236, 2010.
- [97] TileCal webpage. Published Tilecal Figures. <https://twiki.cern.ch/twiki/bin/view/AtlasPublic/TilecalPublishedTilecalFigures>, 2024. Accessed: 2024-01-17.

- [98] ATLAS collaboration. Technical Design Report for the Phase-II Upgrade of the ATLAS Tile Calorimeter, 2017. View in: CERN Document Server, <https://cds.cern.ch/record/2137105>.
- [99] University of Chicago webpage. Tilecal Front-end Electronics 3-IN-1 Card . <https://hep.uchicago.edu/atlas/tilecal/pmt/3in1v30diag.pdf>, 2024. Accessed: 2024-01-18.
- [100] F.I. Zurbano et al. High-Luminosity Large Hadron Collider (HL-LHC): Technical design report, 12 2020. CERN-2020-010. <https://doi.org/10.23731/CYRM-2020-0010>.
- [101] P. Starovoitov. Upgrade of ATLAS Hadronic Tile Calorimeter for the High-Luminosity LHC. *Instruments*, 6(4):54, 2022.
- [102] P. Moreno et al. A new portable test bench for the ATLAS Tile calorimeter front-end electronics. *JINST*, 8(02):C02046, 2013.
- [103] S. Muschter, K. Anderson, C. Bohm, D. Eriksson, M. Oreglia, and F. Tang. Development of a readout link board for the demonstrator of the ATLAS Tile calorimeter upgrade. *JINST*, 8:C03025, 2013.
- [104] F. Tang, H. Akerstedt, K. Anderson, C. Bohm, K. Hildebrand, S. Muschter, and M. Oreglia. Design of main board for atlas tilecal demonstrator. In *2014 19th IEEE-NPSS Real Time Conference*, pages 1–3, 2014.
- [105] R. Bonnefoy, M. Crouau, C. Fayard, M.L. Mercier, D Pallin, E Sahuc, and F Vazeille. Active Dividers for the Tile Calorimeter of the ATLAS detector. Technical report, CERN, Geneva, 2014.
- [106] RCB1200 Series Datasheet. https://www.cdiweb.com/datasheets/enedo/ds_rcb1200_rev07.pdf, 2024. Accessed: 2024-01-01.
- [107] J. S. Kapustinsky, R. M. DeVries, N. J. DiGiacomo, W. E. Sondheim, J. W. Sunier, and H. Coombes. A fast timing light pulser for scintillation detectors. *Nucl. Instrum. Meth. A*, 241(2-3):612–613, 1985.
- [108] D. Bullock, F. Carrió, M. Govender, I. Hofsjager, B. Mellado, P. Moreno, R. Reed, X. Ruan, C. Sandrock, S.C. Solans, R. Suter, G. Usai, and A. Valero. Prometeo: A portable test-bench for the upgraded front-end electronics of the atlas tile calorimeter. In *Technology and Instrumentation in Particle Physics 2014 (TIPP2014) - Poster Session 11*, page 409, 07 2015.
- [109] O. Mtintsilana, J. Abdallah, P. Tsotskolauri, and B. Mellado. Implementation of the LED Integrator panel for the Prometeo system in the ATLAS Tile Calorimeter. In *The Proceedings of SAIP2022, the 66th Annual Conference of the South African Institute of Physics*, pages 517–522, 2022. Best Poster Presentation Award Winner.
- [110] W. Lampl, S. Laplace, D. Lelas, P. Loch, H. Ma, S. Menke, S. Rajagopalan, D. Rousseau, S. Snyder, and G. Unal. Calorimeter clustering algorithms: Description and performance, 5 2008.
- [111] G. Aad et al. Topological cell clustering in the ATLAS calorimeters and its performance in LHC Run 1. *Eur. Phys. J.*, C77:490, 2017.

- [112] ATLAS Collaboration. Electron and photon reconstruction and performance in ATLAS using a dynamical, topological cell clustering-based approach, 12 2017. ATL-PHYS-PUB-2017-022, <https://cds.cern.ch/record/2298955>.
- [113] ATLAS Collaboration. Optimisation of the ATLAS b -tagging performance for the 2016 LHC Run, 2016. ATL-PHYS-PUB-2016-012, <https://cds.cern.ch/record/2209121>.
- [114] ATLAS Collaboration. Electron efficiency measurements with the ATLAS detector using the 2015 LHC proton-proton collision data, 6 2016.
- [115] A.M. Sirunyan et al. Electron and photon reconstruction and identification with the CMS experiment at the CERN LHC. *JINST*, 16(05):P05014, 2021.
- [116] G. Aad et al. Muon reconstruction performance of the ATLAS detector in proton-proton collision data at $\sqrt{s} = 13$ TeV. *Eur. Phys. J.*, C76(5):292, 2016.
- [117] G. Aad et al. Measurement of the muon reconstruction performance of the ATLAS detector using 2011 and 2012 LHC proton-proton collision data. *Eur. Phys. J.*, C74(11):3130, 2014.
- [118] G. Aad et al. Muon reconstruction performance of the ATLAS detector in proton-proton collision data at $\sqrt{s} = 13$ TeV. *Eur. Phys. J. C*, 76(5):292, 2016.
- [119] Henning Kirschenmann and On behalf of the CMS collaboration. Jet Energy Scale performance in 2011. *J. Phys.: Conf. Ser.*, 404:012013, 5 2012.
- [120] M. Cacciari, G. P. Salam, and G. Soyez. The anti- k_t jet clustering algorithm. *JHEP*, 04:063, 2008.
- [121] M. Aaboud et al. Jet energy scale measurements and their systematic uncertainties in proton-proton collisions at $\sqrt{s} = 13$ TeV with the ATLAS detector. *Phys. Rev.*, D96(7):072002, 2017.
- [122] G. Aad et al. Search for heavy resonances decaying into a pair of Z bosons in the $\ell^+\ell^-\ell'^+\ell'^-$ and $\ell^+\ell^-\nu\bar{\nu}$ final states using 139 fb^{-1} of proton-proton collisions at $\sqrt{s} = 13$ TeV with the ATLAS detector. *Eur. Phys. J. C*, 81(4):332, 2021.
- [123] Morad Aaboud et al. Jet reconstruction and performance using particle flow with the ATLAS Detector. *Eur. Phys. J. C*, 77(7):466, 2017.
- [124] M. Aaboud et al. Jet energy scale measurements and their systematic uncertainties in proton-proton collisions at $\sqrt{s} = 13$ TeV with the ATLAS detector. *Phys. Rev. D*, 96(7):072002, 2017.
- [125] ATLAS Collaboration. Tagging and suppression of pileup jets, 5 2014.
- [126] G. Aad et al. Performance of pile-up mitigation techniques for jets in pp collisions at $\sqrt{s} = 8$ TeV using the ATLAS detector. *Eur. Phys. J. C*, 76(11):581, 2016.
- [127] M. Aaboud et al. Performance of missing transverse momentum reconstruction with the ATLAS detector using proton-proton collisions at $\sqrt{s} = 13$ TeV. *Eur. Phys. J.*, C78(11):903, 2018.

- [128] Georges Aad et al. The performance of missing transverse momentum reconstruction and its significance with the ATLAS detector using 140 fb^{-1} of $\sqrt{s} = 13 \text{ TeV}$ pp collisions, 2 2024.
- [129] G. Aad et al. ATLAS data quality operations and performance for 2015–2018 data-taking. *JINST*, 15(04):P04003, 2020. arXiv:1911.04632, <https://arxiv.org/abs/1911.04632>.
- [130] G. Aad et al. The ATLAS Experiment at the CERN Large Hadron Collider: A Description of the Detector Configuration for Run 3, 5 2023.
- [131] ATHENA: The ATLAS software framework. <https://atlassoftwaredocs.web.cern.ch/athena/athena-intro/>, 2020. Last accessed 08 October 2023.
- [132] ATLAS Collaboration. Luminosity determination in pp collisions at $\sqrt{s} = 13 \text{ TeV}$ using the ATLAS detector at the LHC, 6 2019.
- [133] G. Aad et al. The ATLAS Simulation Infrastructure. *Eur. Phys. J. C*, 70:823–874, 2010.
- [134] S. Agostinelli et al. GEANT4—a simulation toolkit. *Nucl. Instrum. Meth. A*, 506:250–303, 2003.
- [135] P. Nason and G. Zanderighi. W^+W^- , WZ and ZZ production in the POWHEG-BOX-V2. *Eur. Phys. J. C*, 74(1):2702, 2014.
- [136] T. Sjostrand, S. Mrenna, and P.Z. Skands. A Brief Introduction to PYTHIA 8.1. *Comput. Phys. Commun.*, 178:852–867, 2008.
- [137] D. J. Lange. The EvtGen particle decay simulation package. *Nucl. Instrum. Meth. A*, 462:152–155, 2001.
- [138] H.L. Lai, M. Guzzi, J. Huston, Z. Li, P.M. Nadolsky, J. Pumplin, and C.-P. Yuan. New parton distributions for collider physics. *Phys. Rev. D*, 82:074024, 2010.
- [139] J. Alwall, R. Frederix, S. Frixione, V. Hirschi, F. Maltoni, O. Mattelaer, H. S. Shao, T. Stelzer, P. Torrielli, and M. Zaro. The automated computation of tree-level and next-to-leading order differential cross sections, and their matching to parton shower simulations. *JHEP*, 07:079, 2014.
- [140] R.D. Ball et al. Parton distributions for the LHC Run II. *JHEP*, 04:040, 2015.
- [141] S. Schumann and F. Krauss. A Parton shower algorithm based on Catani-Seymour dipole factorisation. *JHEP*, 03:038, 2008.
- [142] S. Hoeche, F. Krauss, M. Schonherr, and F. Siegert. QCD matrix elements + parton showers: The NLO case. *JHEP*, 04:027, 2013.
- [143] T. Gleisberg and S. Hoeche. Comix, a new matrix element generator. *JHEP*, 12:039, 2008.
- [144] F. Buccioni, J.N. Lang, J.M. Lindert, P. Maierhöfer, S. Pozzorini, H. Zhang, and M.F. Zoller. OpenLoops 2. *Eur. Phys. J. C*, 79(10):866, 2019.

- [145] F. Cascioli, P. Maierhofer, and S. Pozzorini. Scattering Amplitudes with Open Loops. *Phys. Rev. Lett.*, 108:111601, 2012.
- [146] A. Denner, S. Dittmaier, and L. Hofer. Collier: a fortran-based Complex One-Loop Library in Extended Regularizations. *Comput. Phys. Commun.*, 212:220–238, 2017.
- [147] T. Sjostrand, S. Mrenna, and P.Z. Skands. PYTHIA 6.4 Physics and Manual. *JHEP*, 05:026, 2006.
- [148] P.Z. Skands. Tuning Monte Carlo Generators: The Perugia Tunes. *Phys. Rev. D*, 82:074018, 2010.
- [149] P. Golonka and Z. Was. PHOTOS Monte Carlo: A Precision tool for QED corrections in Z and W decays. *Eur. Phys. J. C*, 45:97–107, 2006.
- [150] S. Jadach, Z. Was, R. Decker, and Johann H. Kuhn. The tau decay library TAUOLA: Version 2.4. *Comput. Phys. Commun.*, 76:361–380, 1993.
- [151] P. Golonka, B. Kersevan, T. Pierzchala, E. Richter-Was, Z. Was, and M. Worek. The Tauola photos F environment for the TAUOLA and PHOTOS packages: Release. 2. *Comput. Phys. Commun.*, 174:818–835, 2006.
- [152] Georges Aad et al. Electron and photon performance measurements with the ATLAS detector using the 2015–2017 LHC proton-proton collision data. *JINST*, 14(12):P12006, 2019.
- [153] ATLAS Collaboration. 2015 start-up trigger menu and initial performance assessment of the ATLAS trigger using Run-2 data. Technical report, CERN, Geneva, 2016.
- [154] G. Aad et al. Search for an additional, heavy Higgs boson in the $H \rightarrow ZZ$ decay channel at $\sqrt{s} = 8$ TeV in pp collision data with the ATLAS detector. *Eur. Phys. J. C*, 76(1):45, 2016.
- [155] G. Aad et al. Measurement of the Higgs boson mass from the $H \rightarrow \gamma\gamma$ and $H \rightarrow ZZ^* \rightarrow 4\ell$ channels with the ATLAS detector using 25 fb^{-1} of pp collision data. *Phys. Rev. D*, 90(5):052004, 2014.
- [156] O.S. Bruning. LHC challenges and upgrade options. *J. Phys. Conf. Ser.*, 110:112002, 2008.
- [157] ATLAS Collaboration. Letter of Intent for the Phase-II Upgrade of the ATLAS Experiment, 2012. Report Number: CERN-LHCC-2012-022, LHCC-I-023. Pages: 1-136.
- [158] O. Mtintsilana and T. Lagouri. Studying the Effects of Pileup on the Leptonic Properties in the $H \rightarrow ZZ \rightarrow 4\ell$ Channel Using the ATLAS Detector. In Japie Engelbrecht, editor, *The Proceedings of SAIP2018, the 63rd Annual Conference of the South African Institute of Physics*, pages 110–115, 2018. Best Poster Presentation Award Winner.
- [159] S.H Abidi. Run II Analysis Framework and Initial Validation Studies for $H \rightarrow ZZ^* \rightarrow 4\ell$ Analysis. Bachelor thesis, Toronto U., 4 2015.

- [160] G. Aad et al. Topological cell clustering in the ATLAS calorimeters and its performance in LHC Run 1. *Eur. Phys. J. C*, 77:490, 2017.
- [161] M. Aaboud et al. Electron reconstruction and identification in the ATLAS experiment using the 2015 and 2016 LHC proton-proton collision data at $\sqrt{s} = 13$ TeV. *Eur. Phys. J.*, C79(8):639, 2019.
- [162] J.B De Vivie De Regie et al. ATLAS electron, photon and muon isolation in Run 2. Technical report, CERN, Geneva, 2017.
- [163] M. Aaboud et al. Jet reconstruction and performance using particle flow with the ATLAS Detector. *Eur. Phys. J. C*, 77(7):466, 2017.
- [164] O. Mtintsilana, T. Lagouri, and B. Mellado. Electron isolation studies in $H \rightarrow ZZ \rightarrow 4\ell$ analysis using the ATLAS detector. Submitted for publication, 2019.
- [165] ATLAS Collaboration. Electron efficiency measurements with the ATLAS detector using the 2012 LHC proton-proton collision data, 2014. ATLAS-CONF-2014-032, <https://cds.cern.ch/record/1706245>.
- [166] N. Kerschen and A. Schaffer. Electron performance of the ATLAS detector using the $J/\psi \rightarrow e^+e^-$ decays. Technical Report ATL-PHYS-INT-2010-124, CERN, Geneva, Nov 2010.
- [167] J.B. de Vivie De Regies. Isolationselectiontool. <https://twiki.cern.ch/twiki/bin/viewauth/AtlasProtected/IsolationSelectionTool>, 2019. Last accessed 23 December 2019.
- [168] L. Randall and R. Sundrum. A Large mass hierarchy from a small extra dimension. *Phys. Rev. Lett.*, 83:3370–3373, 1999.
- [169] H. Davoudiasl, J. L. Hewett, and T. G. Rizzo. Bulk gauge fields in the Randall-Sundrum model. *Phys. Lett. B*, 473:43–49, 2000.
- [170] K. Agashe, H. Davoudiasl, G. Perez, and A. Soni. Warped Gravitons at the LHC and Beyond. *Phys. Rev. D*, 76:036006, 2007.
- [171] G. C. Branco, P. M. Ferreira, L. Lavoura, M. N. Rebelo, Marc Sher, and Joao P. Silva. Theory and phenomenology of two-Higgs-doublet models. *Phys. Rept.*, 516:1–102, 2012.
- [172] M. Aaboud et al. Search for heavy ZZ resonances in the $\ell^+\ell^-\ell^+\ell^-$ and $\ell^+\ell^-\nu\bar{\nu}$ final states using proton–proton collisions at $\sqrt{s} = 13$ TeV with the ATLAS detector. *Eur. Phys. J. C*, 78(4):293, 2018.
- [173] G. Aad et al. Measurements of Higgs boson production and couplings in the four-lepton channel in pp collisions at center-of-mass energies of 7 and 8 TeV with the ATLAS detector. *Phys. Rev. D*, 91(1):012006, 2015.
- [174] M. Oreglia et al. A Study of the Reaction $\psi\text{-prime} \rightarrow \gamma\gamma J/\psi$. *Phys. Rev. D*, 25:2259, 1982.

- [175] J. Gaiser et al. Charmonium Spectroscopy from Inclusive ψ -prime and J/ψ Radiative Decays. *Phys. Rev. D*, 34:711, 1986.
- [176] Johan Alwall, Michel Herquet, Fabio Maltoni, Olivier Mattelaer, and Tim Stelzer. MadGraph 5 : Going Beyond. *JHEP*, 06:128, 2011.
- [177] ATLAS collaboration. Summary of ATLAS Pythia 8 tunes, 8 2012. ATL-PHYS-PUB-2012-003, <https://cds.cern.ch/record/1474107>.
- [178] J. Butterworth et al. PDF4LHC recommendations for LHC Run II. *J. Phys. G*, 43:023001, 2016.
- [179] B. Biedermann, A. Denner, S. Dittmaier, L. Hofer, and B. Jäger. Electroweak corrections to $pp \rightarrow \mu^+ \mu^- e^+ e^- + X$ at the LHC: a Higgs background study. *Phys. Rev. Lett.*, 116(16):161803, 2016.
- [180] B. Biedermann, A. Denner, S. Dittmaier, L. Hofer, and B. Jager. Next-to-leading-order electroweak corrections to the production of four charged leptons at the LHC. *JHEP*, 01:033, 2017.
- [181] S. Kallweit, J.M. Lindert, P. Maierhöfer, S. Pozzorini, and M. Schönherr. NLO electroweak automation and precise predictions for W +multijet production at the LHC. *JHEP*, 04:012, 2015.
- [182] ATLAS and CMS Collaboration. Procedure for the LHC Higgs boson search combination in Summer 2011, 8 2011. ATL-PHYS-PUB-2011-011, <https://cds.cern.ch/record/1375842>.
- [183] G. Aad et al. Combined search for the Standard Model Higgs boson in pp collisions at $\sqrt{s} = 7$ TeV with the ATLAS detector. *Phys. Rev. D*, 86:032003, 2012.
- [184] Glen Cowan, Kyle Cranmer, Eilam Gross, and Ofer Vitells. Asymptotic formulae for likelihood-based tests of new physics. *Eur. Phys. J. C*, 71:1554, 2011. [Erratum: *Eur.Phys.J.C* 73, 2501 (2013)].
- [185] A.L. Read. Presentation of search results: The CL(s) technique. *J. Phys.*, G28:2693–2704, 2002. [,11(2002)].
- [186] Albert M Sirunyan et al. Measurements of production cross sections of the Higgs boson in the four-lepton final state in proton–proton collisions at $\sqrt{s} = 13$ TeV. *Eur. Phys. J. C*, 81(6):488, 2021.
- [187] Georges Aad et al. Measurement of ZZ production cross-sections in the four-lepton final state in pp collisions at $\sqrt{s} = 13.6$ TeV with the ATLAS experiment, 11 2023. arXiv:2311.09715, <https://arxiv.org/abs/2311.09715>.
- [188] H. Tlou, A. Fadol, B. Mellado, O. Mtintsilana, and X. Ruan. Search for heavy resonances in the $\ell^+ \ell^- \ell^+ \ell^-$ final state in association with missing transverse energy using pp collisions at $\sqrt{s} = 13$ TeV with the ATLAS detector. In *in The Proceedings of SAIP2021, the 65th Annual Conference of the South African Institute of Physics*, pages 126–131, 2021.

-
- [189] M. Muhlleitner, M.O.P. Sampaio, R. Santos, and J. Wittbrodt. The N2HDM under Theoretical and Experimental Scrutiny. *JHEP*, 03:094, 2017.
- [190] G. C. Dorsch, S. J. Huber, K. Mimasu, and J. M. No. Echoes of the Electroweak Phase Transition: Discovering a second Higgs doublet through $A_0 \rightarrow ZH_0$. *Phys. Rev. Lett.*, 113(21):211802, 2014.
- [191] ATLAS Collaboration. Search for heavy resonances in final states with four leptons and missing transverse momentum or jets in pp collisions at $\sqrt{s} = 13$ TeV with the ATLAS detector, 2024. arXiv:2401.04742, <https://arxiv.org/abs/2401.04742>.
- [192] ATLAS Collaboration. ATLAS Pythia 8 tunes to 7 TeV data, 11 2014.
- [193] A.L. Read. Linear interpolation of histograms. *Nucl. Instrum. Meth. A*, 425:357–360, 1999.

